

SEISMIC INTERFEROMETRY FOR TEMPORAL MONITORING

by

Norimitsu Nakata

© Copyright by Norimitsu Nakata, 2013

All Rights Reserved

A thesis submitted to the Faculty and the Board of Trustees of the Colorado School of Mines in partial fulfillment of the requirements for the degree of Doctor of Philosophy (Geophysics).

Golden, Colorado

Date \_\_\_\_\_

Signed: \_\_\_\_\_

Norimitsu Nakata

Signed: \_\_\_\_\_

Dr. Roel Snieder  
Thesis Advisor

Golden, Colorado

Date \_\_\_\_\_

Signed: \_\_\_\_\_

Dr. Terence K. Young  
Professor and Head  
Department of Geophysics

## ABSTRACT

Seismic interferometry, where one computes coherency of waves between two or more receivers and averages over many sources, is a technique of signal processing to reconstruct wavefields. This technique is used in geophysics, especially exploration geophysics and seismology. After more than a half century from the first study related to seismic interferometry (although the name of seismic interferometry has been used for approximately the last 15 years), researchers have developed this technique for many aspects: using multiples for increasing illuminations, enhancement of survey areas, ambient-noise analysis, and removal of the imprint of a complicated overburden. In this dissertation, I focus on the advantages of seismic interferometry for time-lapse measurements.

Measurements of temporal changes yield beneficial information of fluid flow, crustal deformation, temperature, and/or stress. Estimation of temporal changes using active sources is, however, technically and economically challenging. Because seismic interferometry reconstruct waves that would have been recorded with a repeatable active sources using only receivers, this technique is appropriate for temporal monitoring. With seismic interferometry, one obtains some advantages that include canceling the complexity of wave propagation to a virtual source, creating virtual shear-wave (S-wave) sources (active S sources are expensive), and using waves that are not usable for active sources (e.g., ambient noise and multiples).

I seek applications of seismic interferometry in a variety of topics (i.e., seismology, structural engineering, and exploration geophysics), and develop and/or modify several techniques of seismic interferometry for each application. Some chapters focus on developing techniques of seismic interferometry, and other chapters aim to estimate and interpret temporal changes with the developed techniques.

For passive seismic sources, deconvolution-based seismic interferometry has better repeatability than crosscorrelation-based interferometry. Also, I can estimate attenuation of media with deconvolution interferometry using the amplitude decay of deconvolved waveforms. In higher-dimensional elastic cases, deconvolution interferometry allows me to obtain PP, PS, SP, and SS reflected waves without any unwanted crosstalk of P and S waves. Higher-dimensional data are more challenging for seismic interferometry, and I employ techniques such as wavefield decomposition, multi-dimensional analysis, time windowing, and time reversal to improve deconvolved waveforms obtained from earthquakes.

The main discoveries in the seismological applications in addition to the techniques are that I successfully estimate near-surface S-wave velocities and azimuthal anisotropy all over Japan with deconvolution interferometry using earthquake data, that the velocities in the near surface decrease when large earthquakes occur, and that S-wave velocities at the soft-rock sites negatively correlate with precipitation. Using interferometry, I find that the 2011  $M_W$  9.0 Tohoku-Oki earthquake significantly changed near-surface S-wave velocities and S-wave splitting in Japan. In the applications of structural engineering, the velocities of traveling waves in a building estimated from earthquakes vary greater than those in the near surface because the response of the building often includes nonlinearity caused by the shaking of the building itself. I can estimate linear responses of the building with ambient-noise data, and nonlinear and linear mixed responses from earthquake data.

## TABLE OF CONTENTS

ABSTRACT . . . . .	iii
LIST OF FIGURES . . . . .	xi
LIST OF TABLES . . . . .	xxviii
ACKNOWLEDGMENTS . . . . .	xxix
CHAPTER 1 INTRODUCTION . . . . .	1
CHAPTER 2 ESTIMATING NEAR-SURFACE SHEAR-WAVE VELOCITIES IN JAPAN BY APPLYING SEISMIC INTERFEROMETRY TO KIK-NET DATA . . . . .	7
2.1 Summary . . . . .	7
2.2 Introduction . . . . .	8
2.3 KiK-net data . . . . .	9
2.4 Retrieval of the wavefield between receivers . . . . .	12
2.5 Data processing . . . . .	13
2.5.1 Estimating the shear-wave velocity . . . . .	14
2.5.2 Computing the average and standard deviation of the annual or monthly stacks . . . . .	15
2.5.3 Comparison between cross-correlation and deconvolution interferometry . . . . .	15
2.5.4 Shear-wave splitting . . . . .	16
2.6 Retrieved near-surface shear-wave velocities in Japan . . . . .	18
2.6.1 Annual and monthly stacks . . . . .	18
2.6.2 Shear-wave splitting . . . . .	20

2.7	Interpretation of shear-wave velocities and shear-wave splitting . . . . .	22
2.7.1	Influence of major earthquakes . . . . .	22
2.7.2	Influence of precipitation . . . . .	26
2.7.3	Shear-wave splitting and the direction of the plate motion . . . . .	28
2.8	Conclusions . . . . .	31
2.9	Acknowledgments . . . . .	31
2.A	1D seismic interferometry . . . . .	31
2.B	Shear-wave splitting . . . . .	33
2.C	Fourier coefficients . . . . .	35
CHAPTER 3 NEAR-SURFACE WEAKENING IN JAPAN AFTER THE 2011 TOHOKU-OKI EARTHQUAKE . . . . .		37
3.1	Summary . . . . .	37
3.2	Introduction . . . . .	37
3.3	KiK-net . . . . .	38
3.4	Computing methods . . . . .	39
3.4.1	Deconvolution interferometry . . . . .	39
3.4.2	Enhancing time resolution . . . . .	40
3.4.3	Estimating the angle of incidence . . . . .	40
3.5	Determining shear-wave velocities throughout northeastern Japan . . . . .	40
3.6	Discussion and Conclusions . . . . .	46
3.7	Acknowledgments . . . . .	48
CHAPTER 4 TIME-LAPSE CHANGE IN ANISOTROPY IN JAPAN'S NEAR SURFACE CAUSED BY THE 2011 TOHOKU-OKI EARTHQUAKE . . . . .		49
4.1	Summary . . . . .	49

4.2	Introduction . . . . .	49
4.3	Earthquake records and the analyzing method . . . . .	51
4.3.1	KiK-net . . . . .	51
4.3.2	Seismic interferometry . . . . .	51
4.4	The change in anisotropy caused by the Tohoku-Oki earthquake . . . . .	53
4.5	Comparing the changes in anisotropy and static stress . . . . .	59
4.6	Conclusions . . . . .	62
4.7	Acknowledgments . . . . .	62
CHAPTER 5 COMBINATION OF HI-NET AND KIK-NET DATA FOR DECONVOLUTION INTERFEROMETRY . . . . .		63
5.1	Summary . . . . .	63
5.2	Introduction . . . . .	63
5.3	Comparison of observed waveforms of Hi-net and KiK-net . . . . .	66
5.4	Deconvolution interferometry using Hi-net and KiK-net data . . . . .	71
5.4.1	Deconvolution interferometry . . . . .	71
5.4.2	Discussion of dynamic resolution . . . . .	73
5.4.3	Short-time moving-window seismic interferometry . . . . .	75
5.5	Conclusions . . . . .	78
5.6	Acknowledgments . . . . .	78
5.A	Example of another earthquake . . . . .	78
CHAPTER 6 MONITORING A BUILDING USING DECONVOLUTION INTERFEROMETRY. I: EARTHQUAKE-DATA ANALYSIS . . . . .		82
6.1	Summary . . . . .	82
6.2	Introduction . . . . .	83

6.3	Building and earthquakes . . . . .	85
6.4	Deconvolution with an arbitrary receiver . . . . .	87
6.5	Crosscorrelation and crosscoherence interferometry . . . . .	94
6.5.1	Crosscorrelation . . . . .	94
6.5.2	Crosscoherence . . . . .	95
6.5.3	Comparison of deconvolution, crosscorrelation, and crosscoherence . . . . .	97
6.6	Deconvolved waveforms generated from an earthquake . . . . .	102
6.7	Monitoring a building using 17 earthquakes . . . . .	107
6.8	Conclusions . . . . .	112
6.9	Acknowledgments . . . . .	113
6.A	Normal-mode analysis of deconvolution interferometry . . . . .	113
6.B	Amplitude of crosscorrelation interferometry . . . . .	114
6.C	Applying crosscorrelation and crosscoherence interferometry to real data . . . . .	115
CHAPTER 7 MONITORING A BUILDING USING DECONVOLUTION INTERFEROMETRY. II: AMBIENT-VIBRATION ANALYSIS . . . . .		117
7.1	Summary . . . . .	117
7.2	Introduction . . . . .	118
7.3	Deconvolution analysis using ambient vibration . . . . .	119
7.3.1	Observed records . . . . .	119
7.3.2	Pre-processing . . . . .	121
7.3.3	Deconvolution analysis using two-week ambient vibration . . . . .	122
7.4	Discussion of the deconvolved waveforms . . . . .	124
7.4.1	One source inside the building . . . . .	124

7.4.2	Multiple sources . . . . .	127
7.5	Monitoring the building using ambient vibration . . . . .	131
7.6	Conclusions . . . . .	133
7.7	Acknowledgments . . . . .	136
7.A	Eigenfunctions and eigenfrequencies of the string model . . . . .	136
CHAPTER 8 BODY-WAVE INTERFEROMETRY USING REGIONAL EARTHQUAKES WITH MULTI-DIMENSIONAL DECONVOLUTION AFTER WAVEFIELD DECOMPOSITION AT FREE SURFACE . . . . .		
8.1	Summary . . . . .	139
8.2	Introduction . . . . .	139
8.3	Upgoing/Downgoing P/S wavefield decomposition . . . . .	141
8.4	Earthquake data . . . . .	146
8.4.1	Data set and previous studies . . . . .	146
8.4.2	Observed data . . . . .	148
8.4.3	Wavefield decomposition . . . . .	150
8.5	Application of seismic interferometry to earthquake data . . . . .	154
8.5.1	Trace-by-trace deconvolution . . . . .	155
8.5.2	Trace-by-trace crosscoherence . . . . .	162
8.5.3	Multi-dimensional deconvolution . . . . .	164
8.6	Discussion of velocities . . . . .	167
8.7	Conclusions . . . . .	168
8.8	Acknowledgments . . . . .	168
CHAPTER 9 CONCLUSIONS . . . . .		
		169

REFERENCES CITED . . . . .	173
APPENDIX - COPYRIGHT AND PERMISSIONS . . . . .	190
A.1 Journals' permission and copyright information . . . . .	190
A.1.1 Journal of Geophysical Research . . . . .	190
A.1.2 Geophysical Research Letters . . . . .	190
A.1.3 Bulletin of the Seismological Society of America . . . . .	190
A.2 Co-authors' permission . . . . .	191
A.2.1 Seiichiro Kuroda, <i>National Institute for Rural Engineering</i> . . . . .	191
A.2.2 Takao Aizawa and Shunichiro Ito, <i>Suncoh Consultants Co., Ltd.</i> . . . .	192
A.2.3 Takashi Kunimi, <i>Akebono Brake Industry Co., Ltd.</i> . . . . .	192

## LIST OF FIGURES

Figure 2.1	<p>KiK-net stations (December, 2010). The black dots on the map represent the locations of the stations. The dark gray shows the area analyzed in section 2.7.1. The light gray illustrates the area where we apply the analysis for seasonal change (section 2.7.2). The rectangle area in panel (a) is magnified in panel (b). The large black circle indicates station <i>NIGH13</i>, which we use for examples of analysis in Figures 2.2, 2.4, 2.5, 2.6, 2.9, and 2.10. The black crosses depict the epicenters of three significant earthquakes that occurred in the vicinity. . . . .</p>	10
Figure 2.2	<p>An earthquake recorded at all channels of station <i>NIGH13</i> (latitude 37.0514°N and longitude 138.3997°E). This earthquake occurred at 14:59:19.56, 27 October 2004. The epicenter is at latitude 37.2204°N and longitude 138.5608°E and the depth is 11.13 km. The magnitude of this earthquake is <math>M_{JMA}4.2</math>. <i>UD</i> represents the vertical component, <i>NS</i> the north-south direction horizontal component, <i>EW</i> the east-west direction horizontal component, <i>1</i> the borehole seismograph, and <i>2</i> the surface seismograph. (a) The bandpass-filtered (1-13 Hz) time series. (b) The power spectra of the unfiltered records. . . . .</p>	11
Figure 2.3	<p>Quadratic interpolation. Using the three largest amplitude points (crosses), we interpolate the highest amplitude point (circle) by estimating the quadratic curve through the three highest amplitude points. . . . .</p>	15
Figure 2.4	<p>Annual-stacked wavefields by using (a) cross correlation and (b) deconvolution interferometry at station <i>NIGH13</i>. The surface and borehole receiver orientation directions are north-south. Epicenter locations are illustrated in Figure 2.5. . . . .</p>	16
Figure 2.5	<p>Epicenters used in Figure 2.4 from 2000 to 2004 (a) and from 2005 to 2010 (b) at station <i>NIGH13</i>. At the right in each panel, we show the number of earthquakes we use to obtain the waveforms in Figure 2.4 in each year. The size of each circle refers the magnitude of each earthquake and the color indicates the depth. The white triangle illustrates the location of station <i>NIGH13</i>. Because of the proximity of events, many circles overlap. . . . .</p>	17

Figure 2.6	Annual-stacked wavefields (curves) with the interpolated largest amplitude (circles) at station <i>NIGH13</i> . The horizontal line at around 0.15 s is the shear-wave arrival time determined from logging data. From left to right, we show annual stacks from 2000 to 2010. The source and receiver polarization directions are the north-south direction. . . . .	19
Figure 2.7	Shear-wave velocities obtained from logging data ( <i>Log</i> ) and estimated by annual-stacked seismic interferometry using earthquake data at the north-south polarization (excerpted 2000, 2002, 2005, 2008, and 2010). The blue dots on a map represent the station locations which we use to make the map. We interpolate velocities between stations by triangle-based cubic interpolation [Lawson, 1984]. The longitude and latitude belong to the map in the upper-left. The number of right-upper side of each map shows the year of data. . . . .	21
Figure 2.8	Crossplot of velocities computed from logging data and by seismic interferometry in 2008. The black line indicates equal velocities. . . . .	22
Figure 2.9	Monthly-stacked wavefields (curves) with the interpolated largest amplitude (circles) at station <i>NIGH13</i> . The horizontal line at around 0.15 s is the shear-wave arrival time obtained from logging data. From left to right, we depict monthly stacks from January to December. Each trace is stacked over the 11 years (January 2000–2010, February 2000–2010, ..., and December 2000–2010). The source and receiver polarization directions are the north-south direction. . . . .	23
Figure 2.10	(a) Cross correlograms along every 10-degree polarization direction in 2010 at station <i>NIGH13</i> . Each trace is plotted at an angle equal to the polarization direction used to construct that trace. The dashed circle indicates the peak-amplitude time of the north-south direction, and the thick solid line represents the peak-amplitude time for each polarization direction. (b) Shear-wave velocities computed from the thick solid line in panel (a). Black circles represent the quadratic-interpolated fast and slow polarization shear-wave velocities. . . . .	24

Figure 2.11	<p>(a) The isotropic component of the shear-wave velocity (Fourier coefficient <math>v_0</math>) averaged over one year before and three months after three major earthquakes. (b) The direction of the fast shear-wave polarization averaged over same intervals. All data are computed for stations in the Niigata prefecture (the dark shaded area in Figure 2.1). In each panel, the label of the year is placed in the middle of each year. The dashed arrows in panel (a) and the vertical dashed lines in panel (b) indicate the times of the three major earthquakes shown with the black crosses in Figure 2.1. The numbers at the left and right of dashed arrows (a) and lines (b) are the number of earthquakes we use for determining velocities and polarizations before and after the major earthquakes, respectively. In panel (a), each velocity is the velocity variation <math>\Delta v</math> in equation 2.4. The horizontal extent of each box depicts the time interval used for averaging (one year before and three months after the major earthquakes). The vertical extent of each box represents the standard deviation of the velocity in the area computed by the method in section 2.5.2. The horizontal line in each box indicates average velocity <math>\Delta v</math> in each time interval, and the vertical line the center of each time interval. In panel (b), we use only the stations with significant anisotropy (<math>(v_{fast} - v_{slow})/v_{fast} \geq 1\%</math>). We select 11 stations from 19 stations and depict the fast shear-wave polarization directions with different symbols or lines. Each symbol is placed at the center of each time period. . . . .</p>	25
Figure 2.12	<p>Seasonal dependence of shear-wave velocity. (a) Variation of the average monthly-velocities stacked over the period 2000 through 2010 in southern Japan (the light gray area in Figure 2.1). We use the stations with the 15% slowest velocities in the area. The horizontal extent of each box shows time interval used for averaging, and the vertical extent the standard deviations of all receivers in the time interval computed by the method in section 2.5.2. The horizontal line in each box indicates average velocity <math>\Delta v</math> in each time interval, and the vertical line the center of each time interval. (b) Crossplot between monthly precipitation (provide by JMA) and the average velocity <math>\Delta v</math> with error bars. (c) Crossplot between monthly precipitation and the average velocity <math>\Delta v</math> with error bars using the stations with the 85% fastest velocities in the area. . . . .</p>	27
Figure 2.13	<p>(a) Fast shear-wave polarization directions (black lines) and the direction of the plate motion (gray lines) estimated from GPS data ]2000sagiya at the stations with significant anisotropy (<math>(v_{fast} - v_{slow})/v_{fast} \geq 1\%</math>). (b) Extracted stations from panel (a) with shear-wave velocity faster than 600 m/s. . . . .</p>	29

Figure 2.14	Crossplot between the direction of the plate motion and the fast shear-wave polarization directions. We use the stations which have faster than 600 m/s shear-wave velocity. Red indicates there are many points. The north-south direction is 0 degrees, and the east-west direction 90 degrees. . . . .	30
Figure 2.A1	Geometry of an earthquake and a KiK-net station, where $\mathbf{r}_s$ is the surface receiver (black triangle), $\mathbf{r}_b$ the borehole receiver (white triangle), and $\mathbf{s}$ the epicenter of earthquake (gray star). . . . .	32
Figure 2.B1	Projection of fast and slow velocity directions, where $\hat{\mathbf{p}}_f$ is the fast polarization direction, $\hat{\mathbf{p}}_s$ the slow polarization direction, $\hat{\mathbf{p}}$ an arbitrary direction, and $\phi$ the angle between the fast direction and arbitrary direction. $\hat{\mathbf{p}}$ , $\hat{\mathbf{p}}_f$ , and $\hat{\mathbf{p}}_s$ are unit vectors. Dashed arrows show the projection, which is shown in equation 2.B1. . . . .	34
Figure 3.1	(a) Deconvolved waveforms of individual earthquakes from 1 January 2011 to 26 May 2011 at station FKSH18. This station recorded 25 earthquakes from 1 January 2011 to 10 March 2011 (black curves), the Tohoku-Oki earthquake of 11 March 2011 (magenta thick curve), 5 other earthquakes on 11 March 2011 (red curves), and 96 earthquakes from 12 March 2011 to 26 May 2011 (blue curves). Circles, marked by the same color as the waveforms (blue replaces cyan), represent the interpolated arrival times of waves. The waveforms are ordered by the origin times of earthquakes in the vertical axis. (b) Epicenters of two time intervals: 1 January 2011 to 10 March 2011 and 12 March 2011 to 26 May 2011. The size of each circle indicates the magnitude of each earthquake and the color denotes the depth. The white triangle points to the location of station FKSH18. . . . .	41
Figure 3.2	Short-time moving-window seismic interferometry of the ground motion caused by the Tohoku-Oki earthquake. (a) The earthquake record observed at the north-south horizontal component borehole seismometer of station FKSH18. Gray bars indicate the 20-s time windows for seismic interferometry with 10-s overlap. Black circles are the center of each window. (b) Deconvolved waveforms of each time window. Each waveform is aligned with the center time of the employed time window. Black circles illustrate the interpolated arrival times. . . . .	43

Figure 3.3	Shear-wave velocity variations in the upper 100 m at station FKSH18. By using the arrival times of waves (the circles in Figure 3.1), we compute the velocity variations from 1 January 2011 to 26 May 2011. The color of each dot is the same as in Figure 3.1. Black vertical line indicates the origin time of the Tohoku-Oki earthquake. Orange line depicts the average velocity (before the Tohoku-Oki earthquake) and the logarithm curve determined by least-squares fitting of the velocity after the earthquake. We do not include the Tohoku-Oki earthquake data point (magenta dot) in the data fit. . . . .	44
Figure 3.4	Averaged waveforms of Figure 3.1 before (from 1 January 2011 to 10 March 2011; black solid curve) and after (from 12 March 2011 to 26 May 2011; blue solid curve) the Tohoku-Oki earthquake at station FKSH18. Circles denote the interpolated arrival times of averaged waves. Black and blue dashed curves represent the averaged waveforms from 1 January to 10 March and from 12 March to 26 May over 11 years (from 2000 to 2010), respectively. . . . .	45
Figure 3.5	Shear-wave velocities estimated from deconvolved waveforms before (upper-left) and after (middle) the Tohoku-Oki earthquake. Blue dots on these two maps show the KiK-net stations used in this study. The map on the lower-right gives the relative change in shear-wave velocity before and after the event. The longitude and latitude belong to the map in the upper-left. Locations and magnitude of the earthquakes from 1 January 2011 to 26 May 2011 are shown as circles, relative to the map on the lower-right. The size of each circle indicates the magnitude of each earthquake and the color represents the depth. The yellow star denotes the location of the Tohoku-Oki earthquake. The dashed black lines show the locations of MTL and ISTL ]1996ito. . . . .	47
Figure 4.1	Number of earthquakes used in the study at each station before (left: 1 January 2011 to 10 March 2011) and after (right: 12 March 2011 to 26 May 2011) the Tohoku-Oki earthquake. The color represents the number of earthquakes. Three stations (FKSH12, IWTH03, and TYMH04) used in Figure 4.2 and Figure 4.3 are pointed. . . . .	53

Figure 4.2	Variation in shear-wave velocity and anisotropy coefficient from 1 May 2010 to 31 December 2011 at station FKSH12. The top panel depicts the isotropic velocity of each earthquake (black dot) and its nine-point moving average (blue line). The bottom panel indicates the anisotropy coefficient computed from fast and slow shear-wave velocities (black cross) and its nine-point moving average (blue line). The velocity and the anisotropy coefficient estimated from the main event are illustrated by magenta symbols. Green vertical lines denote the origin time of the event. Red horizontal lines and gray shaded areas are the mean values and the mean values $\pm$ the standard deviations of the measurements of all used earthquakes during each period. We show the number of earthquakes used and mean values of each period at the bottom. The range of each value is the 95% confidence interval of the mean. The bars at the top of the figure illustrate the time intervals used in Figure 4.4. . . . . .	54
Figure 4.3	Variation in shear-wave velocity and anisotropy coefficient from 1 January 2011 to 26 May 2011 at (a) station IWTH03 and (b) station TYMH04 (see Figure 4.1 for locations of the stations). In each panel, the top and bottom subpanels illustrate the isotropic velocity (black dot) and the anisotropy coefficient (black cross) of each earthquake, respectively. The velocity and the anisotropy coefficient estimated from the main event are illustrated by magenta symbols. The green vertical lines denote the origin time of the event. The red horizontal lines are the mean values of all used earthquakes in each period. . . . .	55
Figure 4.4	Changes in shear-wave velocity and anisotropy coefficient after the Tohoku-Oki earthquake. Each map has a label at upper-right: anisotropy coefficients before (Before: 1 January 2011 to 10 March 2011) and after (After: 12 March 2011 to 26 May 2011) the Tohoku-Oki earthquake, its change, defined as $(AC_{after} - AC_{before})/AC_{before}$ (Anisotropy change), and the change in the isotropic shear-wave velocity (Velocity change). Dark blue (before) and light blue (after) arrows on the Before, After, and Anisotropy-change maps represent the direction of fast shear-wave polarization. We plot polarization-direction arrows without the change in the anisotropy coefficient in Figure 4.5. The longitude and latitude pertain to the leftmost map. The dashed black lines show the locations of major tectonic lines (the Median Tectonic Line and the Itoigawa-Shizuoka Tectonic Line) [1996ito]. Locations and magnitude of the earthquakes from 1 January 2011 to 26 May 2011 are shown as circles and relative to the rightmost map. The size of each circle indicates the magnitude of each earthquake and the color represents its depth. The yellow star denotes the epicenter of the Tohoku-Oki earthquake. The small Japanese map at the top shows four regions for interpretation in Figure 4.6. . . . .	58

Figure 4.5	Directions of fast shear-wave polarization before (blue arrow: 1 January 2011 to 10 March 2011) and after (red arrow: 12 March 2011 to 26 May 2011) the Tohoku-Oki earthquake. . . . .	59
Figure 4.6	Crossplot of the changes in shear-wave velocity and anisotropy coefficient in the regions. Each symbol indicates the data of each station. The numbers in the corners of each panel show the fraction of stations in each quadrant of all stations in each region. . . . .	60
Figure 4.7	(a) Anisotropy change in Figure 4.4 with the largest principal stress direction (from Figure 3 in ), before (red arrows) and after (blue arrows) the Tohoku-Oki earthquake. The arrows are estimated in each 0.5°-grid area. Black dashed lines indicate the locations of the major tectonic lines. A-M areas denote the interpreted regions in panel (b) as well as . (b) Crossplot of the changes in the largest principal stress direction ]2012yoshida and the anisotropy coefficient in each area shown in panel (a). The change in the anisotropy coefficient is the mean value for each 0.5° grid. Asterisk indicate the areas on the west side of the tectonic lines. The blue and red dashed circles indicate two groups which have a correlation between the changes in the largest principle stress direction and in the anisotropy coefficient. . . . .	61
Figure 5.1	(a) Observed Hi-net waveform of one earthquake recorded in the NS horizontal component at H.HTAH (37.2139°N and 140.5736°E). This earthquake occurred at 18:17:59, 12 January 2012 (JST). The epicenter is at 37.595°N and 141.616°E, and the depth is 42.9 km. (b,c) Integral (displacement) and derivative (acceleration) of the waveform shown in panel (a). (d) Acceleration waveform computed from the waveform in panel (a) with the correction of the receiver response (equation 5.1). (e,f) Observed waveforms recorded by the co-located KiK-net receivers (FKSH12) in the borehole and at the surface. Units of each waveform are shown at top-right of each panel. . . . .	67
Figure 5.2	(a) Comparison of amplitude spectra computed from the waveforms in Figures 5.1c (derivative of Hi-net: dashed black), 5.1d (response-corrected Hi-net: solid black), and 5.1e (KiK-net: gray). (b) The ratios of amplitude spectra (Hi-net/KiK-net). The gray line is computed from the amplitude spectra of the waveforms in Figures 5.1c and 5.1e (the ratio of the gray and dashed black lines in panel (a)), and the black line from Figures 5.1d and 5.1e (the ratio of the gray and solid black lines in panel (a)). (c) The differences of phase spectra (Hi-net – KiK-net). The gray and black dots are computed from the waveforms used for the gray and black lines in panel (b). Because of the display, some dots are shown around 360°. . . . .	68

Figure 5.3	Comparison of the waveforms shown in Figures 5.1d (Hi-net: black) and 5.1e (KiK-net: gray) at different time intervals. Note that the amplitude scales of each panel are different. The unit of vertical axes is acceleration ( $\text{cm/s}^2$ ). . . . .	70
Figure 5.4	Comparison of deconvolved waveforms obtained from the earthquake shown in Figure 5.1 using only KiK-net records (gray: equation 5.2) and the combination of KiK-net and Hi-net records (black: equation 5.3). For the combination, I deconvolve the KiK-net record at the surface with the response-corrected Hi-net record at the borehole. Panel (a) is the unfiltered waveforms, and panel (b) the bandpass-filtered (1–13 Hz) waveforms. Note that panel (b) also shows black and gray lines. . . . .	72
Figure 5.5	Synthetic observed waveforms recorded at the (a) surface and (b) borehole receivers. The gray and black lines show the original and synthetic KiK-net waveforms, respectively. (c) Deconvolved waveforms computed from the synthetic KiK-net records (simulated $D_{KK}(S, B, t)$ ). (d) Deconvolved waveforms computed from the synthetic KiK-net (surface) and Hi-net (borehole) records (simulated $D_{KH}(S, B, t)$ ). The gray lines in panels (c,d) are deconvolved waveforms computed from the original waveforms. The waveforms are applied the same bandpass filter used in Figure 5.4. . . . .	74
Figure 5.6	(a) Observed waveforms recorded at the KiK-net borehole receiver (the same waveforms shown in Figure 5.1e). Gray lines indicate the 20-s time windows for SMSI with a 10-s overlap. Black circles are the center of each time window. (b) Deconvolved waveforms at each time interval using only KiK-net records. (c) Deconvolved waveforms computed from the combination of KiK-net (surface) and Hi-net (borehole) records. (d) S/N of KiK-net (gray) and receiver-response corrected Hi-net records (black) computed by the RMS amplitude at each time interval divided by the RMS amplitude of background noise. Waveforms in panels (b) and (c) are applied the same bandpass filter used in Figure 5.4. Waveforms and circles in panels (b,c,d) are aligned with the center time of the employed time window shown in panel (a). . . . .	77

Figure 5.A1	(a) Comparison of amplitude spectra computed from waveforms generated by an earthquake, which occurred at 21:48:43, 4 January 2012 (JST). The epicenter is at 36.574°N and 141.148°E, and the depth is 32.9 km. The station is the same as used in Figure 5.1 (H.HTAH and FKSH12). The gray line illustrates the amplitude spectra of the KiK-net borehole record, the dashed black line the derivative of the Hi-net record, and the solid black line the response-corrected Hi-net record. (b) The ratios of amplitude spectra (Hi-net/KiK-net). The gray line is computed from the amplitude spectra shown in the gray and dashed black lines in panel (a), and the black line from the gray and solid black lines in panel (a). (c) The differences of phase spectra (Hi-net – KiK-net). The gray and black dots are computed from the waveforms used for the gray and black lines in panel (b). Because of the display, some dots are shown around 360°. . . . .	79
Figure 5.A2	Comparison of the waveforms between the response-corrected Hi-net records (black) and KiK-net records (gray) at different time intervals of the earthquake used in Figure 5.A1. Note that amplitude scales of each panel are different. The unit of vertical axes is acceleration (cm/s <sup>2</sup> ). . . .	80
Figure 5.A3	(a) Observed waveforms recorded at the KiK-net borehole receiver obtained from the earthquake used in Figure 5.A1. Gray lines indicate the 20-s time windows for SMSI with a 10-s overlap. Black circles are the center of each time window. (b) Deconvolved waveforms at each time interval using only KiK-net records. (c) Deconvolved waveforms computed from the combination of KiK-net (surface) and Hi-net (borehole) records. (d) S/N of KiK-net (gray) and response-corrected Hi-net records (black) computed by the RMS amplitude at each time interval divided by the RMS amplitude of background noise. Waveforms in panels (b) and (c) are applied the same bandpass filter used in Figure 5.4. Waveforms and circles in panels (b,c,d) are aligned with the center time of the employed time window shown in panel (a). . . .	81
Figure 6.1	The building (rectangle, not to scale) and epicenters of earthquakes used (crosses). Numbers beside of crosses correspond to the sequential numbers in Table 6.1. The lower-right map indicates the location of the magnified area. . . . .	86
Figure 6.2	The (left) EW and (right) NS vertical cross sections of the building and the positions of receivers (triangles). Elevations denote the height of each floor from ground level. We put receivers on stairs 0.19 m below each floor except for the basement (on the floor) and the first floor (0.38 m below). Receiver M2 is located between the first and second floors. Horizontal-receiver components are aligned with the EW and NS directions. . . . .	88

Figure 6.3	<p>Unfiltered waveforms of earthquake No. 5 recorded at the building in (a) the EW component and (b) the NS component, and (c, d) their power spectra. (e, f) Spectrogram computed with continuous-wavelet transformed waveforms recorded at the fourth floor. Time 0 s represents the origin time of the earthquake. We preserve relative amplitudes of the EW and NS components. . . . .</p>	89
Figure 6.4	<p>Displacement of the first three horizontal normal modes for earthquake No. 5 estimated from the real part of the Fourier spectra at different floors. Each mark indicates the displacement of a receiver. The center frequency of each mode is shown at the top of each panel. Black horizontal lines and the numbers on the lines show the amplitude ratio among modes, and the box depicts the height of the building (R2 in Figure 6.2). The zero displacement is at the right side of each box. . . . .</p>	90
Figure 6.5	<p>Schematic shapes of the fundamental mode retrieved by using seismic interferometry. (a) Fundamental mode retrieved by deconvolving wavefields with a motion recorded at <math>z_a</math> (equation 6.3). (b) Fundamental mode retrieved by deconvolving wavefields with a motion recorded at the first floor (equation 6.9). . . . .</p>	92
Figure 6.6	<p>(a) Synthetic waveforms based on equation 6.1. We numerically calculate waveforms with an impulse response (<math>S(\omega) = 1</math>) at <math>t = 0</math> s at 0 m, <math>R(\omega) = 0.5</math>, <math>Q = 3000</math>, <math>H = 100</math> m, and <math>c = 200</math> m/s. Interferometric waveforms by computing deconvolution (panel b: equation 6.9), crosscorrelation (panel c: equation 6.12), and crosscoherence (panel d: equation 6.16) using waveforms shown in panel (a). The virtual source for interferometry is at the 0-m receiver. We apply a bandpass filter 0.5-1-30-40 Hz after computing each waveform. The circles in each panel highlight four waves which are discussed in the main text. The numbers near each arrow indicate the ratio of the amplitude difference between two waves highlighted by the circles apart from the attenuation expected from the traveling distance at the correct velocity. To estimate the ratio of amplitude in panel (d), we ignore wavefields which attenuate faster than <math>e^{-6\gamma k (H-z)}</math>, and <math>CH_1 = 2/(4 - e^{-4\gamma k (H-z)} - e^{-4\gamma k H})</math> where <math>z = 40</math> m. Amplitudes in each panel are normalized by the amplitude of the first highlighted wave (at <math>t=0.2</math> s). The gray line in panel (d) shows the wave which propagates at 66.67 m/s. . . . .</p>	100

Figure 6.7	Deconvolved waveforms, in which the virtual source is at the first floor, of earthquake No. 5 after applying a bandpass filter 0.4-0.5-45-50 Hz in the (a) EW and (b) NS components. Gray lines indicate the arrival time of traveling waves with the velocity that is estimated from the least-squares fitting of the first upgoing and downgoing waves. We repeat the gray lines after the second traveling waves based on equation 6.9. Solid gray lines highlight the waves in the positive polarization and dashed gray lines the waves in the negative polarization. . . . .	103
Figure 6.8	(a) Deconvolved waveforms, in which the virtual source is at the fourth floor, of earthquake No. 5 after applying a bandpass filter 0.4-0.5-45-50 Hz in the EW component. The gray lines indicate the travel paths expected from the velocity 195 m/s and equation 6.3. Solid gray lines highlight the waves in the positive polarization and dashed gray lines the waves in the negative polarization. The circle indicates the point where the positive and negative polarization waves cancel. (b) The same waveforms shown in panel (a) but omitting deconvolved waveforms lower than the fourth floor. When we focus on the cut-off building above the fourth floor, the reflection coefficient at the circle is $-1$ . . . . .	104
Figure 6.9	Deconvolved waveforms, in which the virtual source is at the eighth floor, of earthquake No. 5 after applying a bandpass filter 0.4-0.5-12-16 Hz in the EW component. The gray lines show the travel time of the waves propagating at 210 m/s. The positions of the lines are estimated from equation 6.3. The thick lines have positive polarization and the dashed line negative polarization. . . . .	106
Figure 6.10	Natural logarithm of the envelopes (thin line) and linear fitting using the least-squares method (thick line). We show envelopes at only the middle-second to eighth floors because the first floor is a virtual source and the basement floor has a different physical condition. . . . .	107
Figure 6.11	The waveforms of each earthquake in the EW component after deconvolution with the waves recorded on the first floor in the time domain (left panel), and the power spectra of the waveforms (right panel). We apply a bandpass filter 0.4-0.5-45-50 Hz. We show the traces from the first floor to the eighth floor in each earthquake. . . . .	108

Figure 6.12	(a) Velocities estimated from traveling waves (black) and by coda-wave interferometry using the stretching method (gray) of each earthquake. The error bars of the velocities estimated from traveling waves (black) are one standard deviation of individual arrival times, and the bars in the stretching method are calculated by $\sqrt{\sigma_s^2 + \sigma_{\delta v}^2}$ . We illustrate only velocities which have smaller than 10% velocity uncertainty (for traveling waves) or are estimated from more than three traces which have a correlation coefficient greater than 0.9 (for the stretching method). (b) Crossplot of estimated velocities with maximum acceleration observed at the first floor. . . . .	110
Figure 6.13	(a) Correlation coefficient (CC) as a function of $\alpha$ (equation 6.22) between deconvolved waveforms computed from earthquakes No. 5 and No. 9 at the eighth floor. Dashed arrows point to the maximum CC value and its value of $\alpha$ . For computing CC, we use only the waveforms from 1.0 s to 3.0 s. (b) Deconvolved waveforms at the eighth floor of earthquakes No. 5, No. 9, and No. 9 with stretching for $\alpha = 0.21$ (see panel (a)). . . . .	111
Figure 6.C1	Waveforms obtained by applying (a,c) crosscorrelation and (b,d) crosscoherence interferometry, in which the virtual source is at the first floor, to the records of earthquake No. 5 in the EW component. These waveforms are applied bandpass filters (a,b) 0.4-0.5-45-50 Hz, (c) 1.3-1.6-45-50 Hz, and (d) 1.4-2-45-50 Hz. Note that the bandpass filter for panels (a) and (b) is the same filter as for Figure 6.7. The amplitude scales in each panel are different. The solid gray lines in panel (c) and (d) are the positive-polarity traveling waves with the velocity estimated from Figure 6.7a based on equations 6.12 and 6.16. The dashed gray line in panel (d) indicates the wave that propagates at one third of the velocity of Figure 6.7a. . . . .	116
Figure 7.1	The building (rectangle, not to scale) and epicenters of earthquakes used in Part I (crosses). The lower-right map indicates the location of the magnified area. . . . .	120
Figure 7.2	The (left) EW and (right) NS vertical cross sections of the building and the positions of receivers (triangles). Elevations denote the height of each floor from ground level. Receivers are located on stairs 0.19 m below each floor except for the basement (on the floor) and the first floor (0.38 m below). Receiver M2 is located between the first and second floors. Horizontal-receiver components are aligned with the EW and NS directions. . . . .	121

Figure 7.3	RMS amplitude of the records observed at each floor. The labels of the date are placed at the start of days (midnight). Each trace indicates the RMS amplitude, and the positive axis of amplitude for each trace is upward (dashed horizontal grids describe zero amplitude at each floor).	122
Figure 7.4	Deconvolved waveforms obtained from ambient vibrations in the EW component (expression 7.1). Ambient vibrations observed at Floor 1 is used for the denominator in expression 7.1. The waveforms are averaged over two weeks and applied a bandpass filter 1.3-1.5-15-20 Hz. The shear velocity is estimated from the downgoing waves in the positive time and the upgoing waves in the negative time marked by arrows. Gray lines show the arrival times of the waves propagating with a velocity equal to 270 m/s. . . . .	123
Figure 7.5	(a) Synthetic waveforms obtained from one source inside a building (expressions 7.2 and 7.3) and (b) waveforms of panel (a) after deconvolution with the waves observed at $z = 0$ m. The source is located at $z_s = 13$ m and excites waves at $t = 0.2$ s. The gray lines in panel (b) show the arrival times of the traveling waves based on expressions 7.4 and 7.5. The solid and dashed gray lines respectively illustrate the terms $e^{ik(z-2z_s)}e^{-\gamma k (z-2z_s)}$ and $Re^{ikz}e^{-\gamma k z}$ , and their reverberations. The amplitudes of panels (a) and (b) are normalized after applying the same bandpass filter as used in Figure 7.4. . . . .	126
Figure 7.6	Displacement of radiation damping of the string model. The density of the light string ( $\rho$ ; $z > 0$ ; thin line) is much smaller than that of the heavy string ( $\rho_g$ ; $z < 0$ ; thick line). . . . .	128
Figure 7.7	Synthetic deconvolved waveforms using three-hour random vibrations as sources after applying the same bandpass filter as in Figure 7.4. Panels (a)–(i) are computed by adopting different quality factors $Q$ and reflection coefficients $R$ (see lower-left of each panel). Gray lines indicate the arrival time of the traveling wave with the velocity used for the modeling ( $c = 270$ m/s). The scale of the amplitudes at each panel is the same. . . . .	130
Figure 7.8	Convergence test of ambient-vibration interferometry based on RMS misfits (equation 7.13) as a function of the stacking duration. (a) RMS misfits with respect to the stacked waveform over two-week ambient vibrations recorded in both daytime (8AM–6PM) and nighttime (6PM–8AM). The shaded areas correspond to nighttimes. We show the misfits at second, fourth, and eighth floors. (b) RMS misfits with respect to the same waveforms as panel (a) but using only daytime data. We show the RMS misfits for 122 hours (52 hours of daytime and 70 hours of nighttime) in panel (a) and 52 hours in panel (b). . . . .	132

Figure 7.9	(Left) Time-lapse deconvolved waveforms averaged over 96 hours with a 48-hour overlap using ambient vibrations recorded in both daytime and nighttime. We have applied the same bandpass filter as used in Figure 7.4. (Right) Shear-wave velocities estimated from the traveling waves in the left panel. The width of each box indicates one standard deviation of estimated velocities at each floor. . . . .	134
Figure 7.10	(Left) Time-lapse deconvolved waveforms averaged over 40 hours with a 20-hour overlap using ambient vibration recorded in daytime only. We have applied the same bandpass filter as used in Figure 7.4. (Right) Shear-wave velocities estimated from the traveling waves in the left panel. The width of each box indicates one standard deviation of estimated velocities at each floor. . . . .	135
Figure 8.1	Plane-wave reflection system and coordinates for the wavefield decomposition in section 8.3. The horizontal gray line shows the free surface (indicated by $\sphericalangle$ ), and the downward triangle on the line is a receiver. The black arrows near the receiver define the positive directions of observed records. The dashed lines illustrate portions of plane waves of upgoing/downgoing P/S waves. The black arrows near the dashed lines describe the positive directions of each vector wavefield. Solid black lines connected to dashed lines indicate the ray paths of each wavefield, and the triangles on the solid lines the direction of propagation. The angles $\theta_P$ and $\theta_S$ are the angles of incidence for P and S waves, respectively. . . . .	143
Figure 8.2	Geometry of receivers (triangles). We use records observed at the receivers shown by red triangles for this study. Survey lines 1 and 2 contain receivers 1–15 and 42–55, respectively. The circle on the top-right map shows the location of magnified area. The gray scale illustrates topography. . . . .	146
Figure 8.3	Geometry of earthquakes (yellow dots) and receivers (red triangles). We use an earthquake swarm (embraced by black circle) for the interferometry study. Triangles indicate the locations of receivers No. 1 and 55. The gray scale illustrates topography. . . . .	147
Figure 8.4	Example of observed records from an earthquake in the North-South horizontal component after applying a bandpass filter, 0.4–0.5–7–9 Hz. Time 0 s is the origin time of the earthquake. Trace numbers correspond with the receiver numbers in Figure 8.2. The white arrows show the receivers used for survey lines 1 and 2. . . . .	149

Figure 8.5	Space-interpolated observed record in (a) vertical and (b) radial components in line 1 (after rotating the horizontal components in the radial direction) from the same earthquake used in Figure 8.4. Trace number is assigned after the space interpolation, and traces 1–14 correspond to traces 42–55 in Figure 8.4. We apply the same bandpass filter used in Figure 8.4 to waveforms in all panels. The pink and yellow lines indicate the picked arrival times for the largest energy of direct P and S waves, respectively. Amplitudes are normalized separately at each panel. . . . .	150
Figure 8.6	Particle motion of observed wavefields in the vertical and radial components (Figure 8.5) at around (top row) P- and (bottom row) S-wave arrivals after applying the same bandpass filter used in Figure 8.4. Red (0 s in the color bar) indicates the times at the pink line for P waves and the yellow line for S waves in Figure 8.5. Blue lines illustrate the particle motion based on the angle of incidence estimated by ray tracing. Top-left numbers at each panel describe trace numbers of each motion. . . . .	151
Figure 8.7	Upgoing/downgoing P/S waves after applying wavefield decomposition (equation 8.11) to the wavefields in Figure 8.5. We employ the same bandpass filter used in Figure 8.4 in all panels. The colors in panel (a) indicate the time windows we use in this study to separate direct (pink for P and yellow for S) and reflected waves (blue for P and green for S). The arrival times represented by the pink/yellow lines in Figure 8.5 locate the interfaces between pink/yellow and blue/green, respectively. Amplitudes are normalized separately at each panel. . . . .	152
Figure 8.8	Comparison between upgoing P and S wavefields in Figures 8.7a and 8.7b at around (a) P-wave and (b) S-wave arrival times. Although in both panels upgoing P and S waves are shown in black and red, respectively, we change the order of wavefields; upgoing P is behind in panel (a) and upgoing S is behind in panel (b). Amplitude ratios between upgoing P/S waves are preserved. . . . .	153
Figure 8.9	Particle motion of upgoing P and S wavefields at around (top row) P- and (bottom row) S-wave arrivals after applying the same bandpass filter used in Figure 8.4. Red (0 s in the color bar) indicates the times at the pink line for P wave and the yellow line for S waves in Figure 8.5. Blue lines illustrate the ideal particle motion of P (top row) and S (bottom row) waves in the case when wavefields are perfectly separated and no converted waves are generated. Top-left numbers at each panel describe trace numbers of each motion. Note that in contrast to Figure 8.6, the axes denote the upgoing P- and S-wave components. . . . .	154

Figure 8.10	Wavefields at line 1 obtained by applying trace-by-trace deconvolution to observed vertical (black) and radial (red) components (equation 8.12). We apply a bandpass filter 0.4–0.5–7–9 Hz to wavefields in the vertical component and 0.4–0.5–4–6 Hz to wavefields in the radial component. Offset 0 km is the location of the virtual source. . . . .	156
Figure 8.11	Schematic plane-wave propagation. Receivers (triangles) are deployed at the free surface (indicated by $\swarrow\swarrow$ ), and a plane wave (the black arrow at lower-left) propagates with angle $\theta$ of the incidence. Dashed lines, all of which are parallel, indicate the portions of plane waves. The red arrow illustrates the ray path for the different portion of the same plane wave as the black arrow. The model contains one horizontal layer and a half space below the layer. The thickness of the layer is $h$ . Gray lines and receivers show unfolded imaginary layers and receivers to understand reflected plane waves based on Snell’s law. Distance $h_d$ corresponds with the difference of the travel distance between direct upgoing waves to receivers $A$ and $B$ , and $h_r$ is the travel distance of the reflected waves from $A$ to $B$ . We do not show converted waves in this figure. . . . .	157
Figure 8.12	Wavefields in survey line 1 obtained by applying trace-by-trace deconvolution to upgoing P (black) and S (red) waves (equation 8.14). The solid lines show the dip of P (black) and S (red) plane waves in survey line 1, and the dashed lines in survey line 2. We apply the same bandpass filters used in Figure 8.10. Offset 0 km is the location of the virtual source. . . . .	158
Figure 8.13	Relationship of upgoing/downgoing P/S wavefields and Green’s functions between receivers $A$ and $B$ . The free surface is indicated by $\swarrow\swarrow$ . The direction of arrows represents the direction of causality. Upgoing waves are reflected waves (direct upgoing waves are not shown). . . . .	160
Figure 8.14	Reflected plane waves retrieved by trace-by-trace deconvolution after time windowing. We compute (a) $D_p^d(B)/U_p^r(A) (\approx G_{pp}^*)$ , (b) $D_p^d(B)/U_s^r(A) (\approx G_{ps}^*)$ , (c) $D_s^d(B)/U_p^r(A) (\approx G_{sp}^*)$ , and (d) $D_s^d(B)/U_s^r(A) (\approx G_{ss}^*)$ . We apply bandpass filters with (a,b) 0.4–0.5–7–9 Hz and (c,d) 0.4–0.5–4–6 Hz. Red lines indicate the dip for slant stacking, and the rightmost trace at each panel is the stacked trace. The reference trace for the deconvolution is the trace at offset 0 km (virtual source). The amplitudes in panels (c,d) are multiplied by a factor 2.5 compared with those in panels (a,b), and the amplitudes in panels (a,b) are the same . . . . .	161

Figure 8.15 Reflected plane waves retrieved by trace-by-trace crosscoherence after time windowing. We compute (a)  $D_p^d(B)U_p^{r*}(A)/|D_p^d(B)||U_p^r(A)|$  ( $\approx G_{pp}^*$ ), (b)  $D_p^d(B)U_s^{r*}(A)/|D_p^d(B)||U_s^r(A)|$  ( $\approx G_{ps}^*$ ), (c)  $D_s^d(B)U_p^{r*}(A)/|D_s^d(B)||U_p^r(A)|$  ( $\approx G_{sp}^*$ ), and (d)  $D_s^d(B)U_s^{r*}(A)/|D_s^d(B)||U_s^r(A)|$  ( $\approx G_{ss}^*$ ). We apply the same bandpass filters as used in Figure 8.14. Red lines indicate the dip for slant stacking, and the rightmost trace at each panel is the stacked trace. The reference trace for the interferometry is the trace at offset 0 km (virtual source). The amplitudes in panels (c,d) are multiplied by a factor 2.5 compared with those in panels (a,b), and the amplitudes in panels (a,b) are the same. . . . . 164

Figure 8.16 Reflected plane waves retrieved by multi-dimensional deconvolution after time windowing. (a)  $G_{pp}^*$ , (b)  $G_{ps}^*$ , (c)  $G_{sp}^*$ , and (d)  $G_{ss}^*$ . We apply the same bandpass filters as used in Figure 8.14. Red lines indicate the dip for slant stacking, and the rightmost trace at each panel is the stacked trace. The red arrows on the rightmost traces in panels (a,b,d) point at the waves that we interpret. The reference trace for the interferometry is the trace at offset 0 km (virtual source). The amplitudes in panels (c,d) are multiplied by a factor 2.5 compared with those in panels (a,b), and the amplitudes in panels (a,b) are the same. 166

## LIST OF TABLES

Table 5.1	Specifications of KiK-net and Hi-net systems. . . . .	65
Table 6.1	Origin times, magnitudes, and hypocenter locations of recorded earthquakes estimated by the Japan Meteorological Agency (JMA). The earthquakes are numbered sequentially according to their origin times. Maximum acceleration is the observed maximum amplitude of the MEMS accelerometers at the first floor in the 120 s following the origin time of each earthquake. . . . .	87
Table 6.2	Amplitudes of traveling waves obtained from observed records and computed by seismic interferometry based on deconvolution, crosscorrelation, and crosscoherence for $z_a = 0$ (equations 6.1, 6.9, 6.12, and 6.16). We compute the amplitudes of crosscorrelation interferometry in Appendix B. For crosscoherence interferometry we ignore wavefields which attenuate faster than $e^{-6\gamma k (H-z)}$ . . . . .	98
Table 8.1	Notations of physical parameters and wavefields. . . . .	142

## ACKNOWLEDGMENTS

My thesis work and personal life were supported by numerous people, and I am pleased to have a chance to show my appreciation here. Although it is difficult to fully express my gratitude in words, I hope readers understand it. My acknowledgments to people who supported me to prepare each part of my PhD study are shown at the end of each chapter.

In this acknowledgment, the order of people is not important, except the first person; my advisor Prof. Roel Snieder. I first visited Center for Wave Phenomena (CWP), Colorado School of Mines (CSM) in January 2009 as a part of my Master's degree, and he was my advisor at CSM. Although I then had serious problems with my English, I enjoyed staying and studying here because Roel always tried to understand what I wanted to say. My English communication problems were largely overcome during my second visit to CWP. Roel encouraged and supported me to go to take English classes to improve my English. He always considers my long-term career (note: at that time, I was not his official student), and his suggestion to go to take English classes was, no doubt, worthwhile. After visiting twice, I returned to CWP as a PhD student in January 2012.

I really like Roel's advising style. I am sure if he had not been my advisor, I would not have come to the US. One-on-one weekly meetings with Roel smoothly guided my research, and served as a good metronome for my research. Before each meeting, I tried to summarize what I did in one week, why I have done it, and what I need to do next. Roel is a treasure house of ideas, and after each meeting I got ideas for which I needed more than one week to implement. He always looks at the big picture of research. I learned the importance of considering the meaning of equations and connection between mathematics and physics. I know that our relationship will continue after I graduate as a friend, a colleague, and an adviser (not advisor).

I appreciate the help of committee members Prof. Mike Mooney, Prof. Paul Sava, Prof. David Wald, and Prof. Masami Nakagawa. They understood my situation, in which I wanted to graduate soon, and assisted me to achieve a quick graduation. Also, I have gotten quite a few valuable comments during the defense sessions and committee meetings. I enjoyed taking Paul Sava's migration class. In his class, I learned what imaging is and how to use Madagascar (which is an open-source package for multidimensional data analysis), and I found my next research topics. I want to acknowledge Prof. Toshifumi Matsuoka and Prof. Takeshi Tsuji, who are my former advisors at Kyoto University. Since I moved to CSM, they have continuously asked about my PhD progress. Also, Toshi is the person who introduced seismic interferometry to me. Discussion with Dr. Rie Kamei, who is an alumnus of Kyoto University, has given me a lot of research ideas. Prof. Terry Young provided me a chance to teach a class, Advanced Engineering Mathematics. Terry continuously told me that "teaching is simply communication," and communication is a fun challenge. He taught me how interesting teaching is during the period I taught the class. I would like to be as great a teacher as he is.

One of the reasons why I moved to CSM is to receive support for writing papers and presenting our research. Writing interesting papers is possibly the most important part for a professional career, as is presenting attractive talks for fellow researchers. Writing and presenting are the two abilities I improved most during my PhD studies. Diane Witters is the key person for the improvement, and I greatly appreciate her help to prepare all of my manuscripts. Dr. Ken Larner has also revised my manuscripts. Diane and Ken taught me how interesting writing is, how I should carefully choose words, and how unpredictable English is.

I am also grateful to Roel and Diane for assisting me to improve my presentation skills. CWP has a project review meeting every year, and students rehearse their talks in front of students and faculty. During my first rehearsal in 2011, Roel encouraged me to overcome my monotone voice by practicing to say "amaaaaazing," which was a turning point to construct

my presentation style. After two years, I can now use my voice as a tool of emphasis. To obtain the presentation style, Diane has taught how to control voice tones and corrected my pronunciation. During rehearsals, Prof. Dave Hale and Prof. Ilya Tsvankin also gave me important advice to enhance the quality of my talks.

I thank Pamela Kraus, Shingo Ishida, John Stockwell, Michelle Szobody, and other support staff in the Department of Geophysics to prepare an environment where I could perfectly concentrate on research. My PhD studies were financially supported by the Consortium Project on Seismic Inverse Methods for Complex Structures at the CWP. My research is not in the main stream of CWP, but CWP students and faculty understand my interests and support me from both a technical stand point and as friends. I would like to appreciate all my friends inside and outside CWP. I have no doubt that our friendship will not end after I graduate. I especially thank Hidemichi Yonezawa and Blanca Pina. I have shared a lot of unforgettable time with them in the US, Spain, and Japan.

I am grateful to my parents, brothers, and sister in Japan. I have not had contact with them very often, but they have believed in me to get my PhD and continuously encouraged me to get it. I also appreciate Rie Mukai and her parents to give me a hearty cheer. It might have taken a few more years to complete the PhD program if I did not live with Darlene Wilson, who is my host mother. She has cheered me on, supported me, and made me happy.

# CHAPTER 1

## INTRODUCTION

The interest in monitoring temporal changes using geophysical techniques has increased because the changes provide us with information about, for example, fluid flow and structural deformation (Snieder et al., 2007). In petroleum engineering, the changes in seismic velocities or locations of microseismic events can improve the understanding reservoir conditions (Koster et al., 2000; Lumley, 2001; Herwanger and Horne, 2005; Vasco et al., 2008; Maxwell et al., 2010; Verdon et al., 2010). Continuous measurements of the velocities, anisotropy, and hypocenters of microtremors are important for earthquake seismology to estimate the damage due to large earthquakes (Reasenber and Aki, 1974; Nishimura et al., 2000; Crampin and Peacock, 2008; Allmann and Shearer, 2009). This monitoring could potentially contribute to finding precursors of large earthquakes (Aki, 1985; Peacock et al., 1988; Kato et al., 2012), although earthquake prediction is a challenging research topic (Panakkat and Adeli, 2008). One can also discover the change inside volcanoes (e.g., magma flow) by monitoring volcanic tremors (Aki and Ferrazzini, 2000; Aki, 2004; Snieder and Hagerty, 2004). Geophysical measurements are also useful for monitoring the stability of CO<sub>2</sub> during carbon capture and storage (Arts et al., 2004; Chadwick et al., 2010). In civil engineering, estimation of time-lapse changes of structure strength has a critical role for evaluating the safety of structures (Fuhr et al., 1992; Farrar and Worden, 2007).

For time-lapse monitoring, the source must be repeatable. Two ways can achieve this; either one has a repeatable physical source, or one uses interferometry to create a virtual source. Multiplets (repeating earthquakes) are one of the physical passive sources, which can be used for temporal monitoring (Poupinet et al., 1984; Schaff and Beroza, 2004; Arrowsmith and Eisner, 2006). Using these earthquakes, one can estimate the change in velocities along the ray path from the hypocenters to receivers. The other technique is using seismic interfer-

ometry for redatuming the waves generated by passive sources into virtual-source wavefields (Sens-Schönfelder and Wegler, 2006; Brenguier et al., 2008a; Schuster, 2009). Seismic interferometry is a data reconstruction technique, which allows us to extract information from complicated wavefields (e.g., ambient noise). The properties of such a virtual source depend on the location and orientation of receivers, and on the statistical properties of complex waves. When these are repeatable, the virtual source is repeatable. Note that seismic interferometry and coda-wave interferometry (Snieder et al., 2002; Snieder, 2006) are different techniques. Coda-wave interferometry is a technique to detect small changes of materials using physical or virtual repeating sources (e.g., using multiplet: Snieder and Vrijlandt, 2005, and using virtual source: Sens-Schönfelder and Wegler, 2006).

With seismic interferometry, one can retrieve the signals from observed waves generated by earthquakes, microtremors, cultural noise, or artificial seismic sources with scattering and attenuation. Most seismic-interferometry studies apply this technique to surface waves because extracting surface waves is easier than reconstructing body waves due to the strong energy of surface waves (e.g., Campillo and Paul, 2003; Shapiro et al., 2005; Bensen et al., 2007; Prieto and Beroza, 2008; Curtis et al., 2009; Lin et al., 2009; Forghani and Snieder, 2010). Some studies successfully retrieve body waves (e.g., P waves: Draganov et al., 2007, 2009; Tonegawa et al., 2009, and S waves: O’Connell, 2007; Miyazawa et al., 2008; Nakata et al., 2011).

The extraction of the Green’s function with seismic interferometry based on crosscorrelation between two sensors can be derived from normal modes (Lobkis and Weaver, 2001), representation theorems (Wapenaar, 2004; Wapenaar and Fokkema, 2006), principle of time reversal (Roux and Fink, 2003), and stationary-phase analysis (Snieder, 2004a; Snieder et al., 2006b). After computing crosscorrelation, one can recognize that a receiver serves as a virtual source for waves recorded by other receivers, which leads to a pseudo shot gather for many receivers (Bakulin and Calvert, 2004; Mehta et al., 2007a; van der Neut and Bakulin, 2009; Ruigrok et al., 2010). The first application of seismic interferometry was based on

crosscoherence (Aki, 1957), and the wide-spread algorithm in seismic interferometry is based on crosscorrelation (Claerbout, 1968; Wapenaar, 2003; Bakulin and Calvert, 2004; Schuster et al., 2004). Another proposed algorithm is based on deconvolution, where the source signal is removed by means of spectral division. The mathematical theory of deconvolution interferometry has been derived by Snieder et al. (2006a) and Vasconcelos and Snieder (2008a), and the method has been applied to field data (Snieder and Şafak, 2006; Vasconcelos and Snieder, 2008b; Vasconcelos et al., 2008). Wapenaar et al. (2008a,b) extend the deconvolution interferometry based on multi-dimensional analysis and overcome some limitations of trace-by-trace deconvolution interferometry. The various methods have both advantages and disadvantages (Table 1 of Snieder et al., 2009). In this dissertation, I apply seismic interferometry based on deconvolution to a variety of targets to explore the advantages of using seismic interferometry for time-lapse measurements.

In Chapters 2–5, I use data observed by seismological networks in Japan. The National Research Institute for Earth Science and Disaster Prevention (NIED) operates four large seismometer networks which cover throughout Japan: Hi-net, F-net, K-NET, and KiK-net (Okada et al., 2004). The number of seismometers in Japan has drastically increased since the  $M_W$  6.8 Kobe earthquake in 1995. K-NET contains more than 1000 strong-motion sensors with a 20-km spatial interval deployed at the surface (Aoi et al., 2004). KiK-net is the other strong-motion network and contains approximately 700 stations (Aoi et al., 2004). Uniquely, each KiK-net station has two three-component receivers at the surface and downhole. The depth of the boreholes is mostly about 100–210 m. Hi-net is a high-sensitivity seismograph network co-located with the KiK-net downhole receivers (Obara et al., 2005). F-net includes about 80 broadband receivers with a 100-km spatial interval (Okada et al., 2004). Although K-NET and KiK-net are triggering systems to record earthquake waves, Hi-net and F-net observe continuous data including earth tides and ambient noise.

Many researchers use these networks to study source properties of earthquakes or earth structure (Obara, 2002; Ito et al., 2007; Kimura et al., 2010). In Chapter 2, I propose

techniques to estimate shear-wave velocities and shear-wave splitting in the near surface using the data observed by KiK-net. I apply deconvolution interferometry to the earthquake records at each station to extract the traveling waves from the borehole receiver to the surface sensor. After applying interferometry to all KiK-net stations, I create annual shear-wave velocity maps. Because KiK-net has recorded strong-motion seismograms continuously since the end of 1990s, the data are available for time-lapse measurements. Measuring time-lapse changes of the shallow subsurface is important for civil engineering and for estimating the site response to earthquakes.

In Chapters 3 and 4, I use deconvolution interferometry developed in Chapter 2 to detect and measure the changes in shear-wave velocities and splitting in the near surface after the  $M_W$  9.0 Tohoku-Oki earthquake occurred at the east coast of Japan on March 11, 2011. This earthquake is the fourth largest earthquake in the world since 1900, and ground motions caused by foreshocks, mainshock, and aftershocks are recorded by the networks mentioned above. In Chapter 5, I improve the deconvolution interferometry in Chapter 2 by using the combination of KiK-net and Hi-net data. Because Hi-net has a better signal-to-noise ratio and higher sensitivity than KiK-net, I obtain deconvolved waveforms with better quality.

I apply a similar technique of deconvolution interferometry from Chapter 2 to wavefields observed inside a building (Chapters 6 and 7). I analyze earthquake data and ambient-vibration data in Chapters 6 and 7, respectively, to estimate traveling-wave velocities, normal-mode frequencies, and attenuation of the building. Although the response of a building to an earthquake has been studied since the early 1900s and researchers estimate normal-mode frequencies and quality factors of a building from recorded earthquake and ambient-noise data (e.g., Biot, 1933; Trifunac, 1972; Clinton et al., 2006), the frequencies estimated from observed records depend on both the building itself and the soil-structure coupling (Trifunac et al., 2001a,b). Snieder and Şafak (2006) applied deconvolution interferometry to earthquake records observed in a building and mathematically interpreted the deconvolved waveforms. Based on their study, one can separate the soil-structure coupling

from the building response with deconvolution interferometry. My studies in Chapters 6 and 7 are an extension of Snieder and Şafak (2006), and I apply the deconvolution technique to earthquake and ambient-noise data to retrieve the impulse response of a building.

In Chapter 8, I improve the deconvolved waveforms reconstructed by seismic interferometry using multi-dimensional analyses and wavefield decomposition at the free surface. Note that because multi-dimensional deconvolution interferometry requires the separation of wavefields depending on the direction of wave propagation, no studies have yet applied this interferometry to earthquake data observed at the surface to extract body waves. By applying seismic interferometry to wavefields generated from a cluster of earthquakes, I reconstruct reflected plane body waves. Chapter 9 contains general conclusions and final remarks of this dissertation.

The work in this dissertation is documented in the following publications:

**Chapter 2:** Nakata, N. and R. Snieder, 2012, Estimating near-surface shear-wave velocities in Japan by applying seismic interferometry to KiK-net data: *J. Geophys. Res.*, 117, B01308.

**Chapter 3:** Nakata, N. and R. Snieder, 2011, Near-surface weakening in Japan after the 2011 Tohoku-Oki earthquake: *Geophys. Res. Lett.*, 38, L17302

**Chapter 4:** Nakata, N. and R. Snieder, 2012, Time-lapse change in anisotropy in Japan's near surface after the 2011 Tohoku-Oki earthquake: *Geophys. Res. Lett.*, 39, L11313.

**Chapter 5:** Nakata, N., 2013, Combination of Hi-net and KiK-net data for deconvolution interferometry: *Bull. Seismol. Soc. Am.* (*submitted*).

**Chapter 6:** Nakata, N., R. Snieder, S. Kuroda, S. Ito, T. Aizawa, and T. Kunimi, 2013, Monitoring a building using deconvolution interferometry. I: Earthquake-data analysis: *Bull. Seismol. Soc. Am.*, 103 (*in press*).

**Chapter 7:** Nakata, N. and R. Snieder, 2013, Monitoring a building using deconvolution interferometry. II: Ambient-vibration analysis: Bull. Seismol. Soc. Am. (*submitted*).

**Chapter 8:** Nakata, N., R. Snieder, and M. Behm, 2013, Body-wave interferometry using regional earthquakes with multi-dimensional deconvolution after wavefield decomposition at free surface: Geophys. J. Int. (*to be submitted*).

CHAPTER 2  
ESTIMATING NEAR-SURFACE SHEAR-WAVE VELOCITIES IN JAPAN BY  
APPLYING SEISMIC INTERFEROMETRY TO KIK-NET DATA

Published in *Journal of Geophysical Research* (2012): 117, B01308

Nori Nakata<sup>1</sup> and Roel Snieder<sup>1</sup>

## 2.1 Summary

We estimate shear-wave velocities in the shallow subsurface throughout Japan by applying seismic interferometry to the data recorded with KiK-net, a strong-motion network in Japan. Each KiK-net station has two receivers; one receiver on the surface and the other in a borehole. By using seismic interferometry, we extract the shear wave that propagates between these two receivers. Applying this method to earthquake-recorded data at all KiK-net stations from 2000 to 2010 and measuring the arrival time of these shear waves, we analyze monthly and annual averages of the near-surface shear-wave velocity all over Japan. Shear-wave velocities estimated by seismic interferometry agree well with the velocities obtained from logging data. The estimated shear-wave velocities of each year are stable. For the Niigata region, we observe a velocity reduction caused by major earthquakes. For stations on soft rock, the measured shear-wave velocity varies with the seasons, and we show negative correlation between the shear-wave velocities and precipitation. We also analyze shear-wave splitting by rotating the horizontal components of the surface sensors and borehole sensors and measuring the dependence on the shear-wave polarization. This allows us to estimate the polarization with the fast shear-wave velocity throughout Japan. For the data recorded at the stations built on hard-rock sites, the fast shear-wave polarization directions correlate with the direction of the plate motion.

---

<sup>1</sup>Center for Wave Phenomena, Colorado School of Mines

## 2.2 Introduction

Seismic interferometry is a powerful tool to obtain the Green's function that describes wave propagation between two receivers (e.g., Aki, 1957; Claerbout, 1968; Lobkis and Weaver, 2001; Roux and Fink, 2003; Schuster et al., 2004; Wapenaar et al., 2004; Bakulin and Calvert, 2006; Snieder et al., 2006; Wapenaar and Fokkema, 2006). Seismic interferometry is applied to ambient noise (e.g., Hohl and Mateeva, 2006; Draganov et al., 2007, 2009; Brenguier et al., 2008; Stehly et al., 2008; Lin et al., 2009), traffic noise (e.g., Nakata et al., 2011), production noise (e.g., Miyazawa et al., 2008; Vasconcelos and Snieder, 2008), earthquake data (e.g., Larose et al., 2006, Sens-Schönfelder and Wegler, 2006; Snieder and Şafak, 2006; Ma et al., 2008; Ruigrok et al., 2010), and active sources (e.g., Bakulin and Calvert, 2004; Mehta et al., 2008).

In Japan, large seismometer networks, such as Hi-net, F-net, K-NET, and KiK-net (Okada et al., 2004), are deployed. By using these networks for seismic interferometry, Tonegawa et al. (2009) extract the deep subsurface structure of the Philippine Sea slab. These data have also been used to observe time-lapse changes in small regions (Wegler and Sens-Schönfelder, 2007; Sawazaki et al., 2009; Wegler et al., 2009; Yamada et al., 2010). Each KiK-net station has two receivers, one on the ground surface and the other at the bottom of a borehole. One can estimate the body-wave velocity between two receivers by using seismic interferometry (Trampert et al., 1993; Snieder and Şafak, 2006; Mehta et al., 2007c; Miyazawa et al., 2008).

By applying seismic interferometry to KiK-net data, we analyze near-surface velocities throughout Japan. Because KiK-net has recorded strong-motion seismograms continuously since the end of 1990s, the data are available for time-lapse measurements. Measuring time-lapse changes of the shallow subsurface is important for civil engineering and for estimating the site response to earthquakes. Previous studies extracted time-lapse changes caused by earthquakes (Li et al., 1998; Vidale and Li, 2003; Schaff and Beroza, 2004; Wegler and Sens-Schönfelder, 2007; Brenguier et al., 2008a). Interferometry applied to a single KiK-net

station has also been used to measure time-lapse change due to earthquakes (Sawazaki et al., 2009; Yamada et al., 2010). Interferometric studies have shown changes in the shear-wave velocity caused by precipitation (Sens-Schönfelder and Wegler, 2006) and have measured shear-wave splitting (Bakulin and Mateeva, 2008; Miyazawa et al., 2008). We study the annual and monthly averages of the shear-wave velocity and the fast shear-wave polarization directions for stations all over Japan, and the temporal change in shear-wave velocity in the Niigata prefecture for three major earthquakes.

This paper presents data processing of KiK-net data with seismic interferometry. We first introduce the properties of KiK-net. Next, we show the data analysis method. Then we present near-surface shear-wave velocities in every part of Japan. Finally, we interpret these velocities to study time-lapse changes, which are related to major earthquakes and precipitation, and present measurements of shear-wave splitting.

### **2.3 KiK-net data**

About 700 KiK-net stations are distributed in Japan (Figure 2.1). The stations are operated by the National Research Institute for Earth Science and Disaster Prevention (NIED). Each station has a borehole and two seismographs which record strong motion at the bottom and top of the borehole. Each seismograph has three components: one vertical component and two horizontal components. Although the two horizontal components of the surface seismograph are oriented in the north-south and east-west directions, respectively, the horizontal components of the borehole seismograph are not always aligned with the north-south and east-west directions because of technical limitations. Therefore, we rotate the directions of the borehole seismograph north-south and east-west directions before data processing. The depth of about 25% of the boreholes is 100 m, and the other boreholes are at greater depth. Since our target is the near surface, we use the stations with a depth less than 525 m, which accounts for 94% of the stations. The sampling interval is either 0.005 or 0.01 s, depending on the station and the recording date.

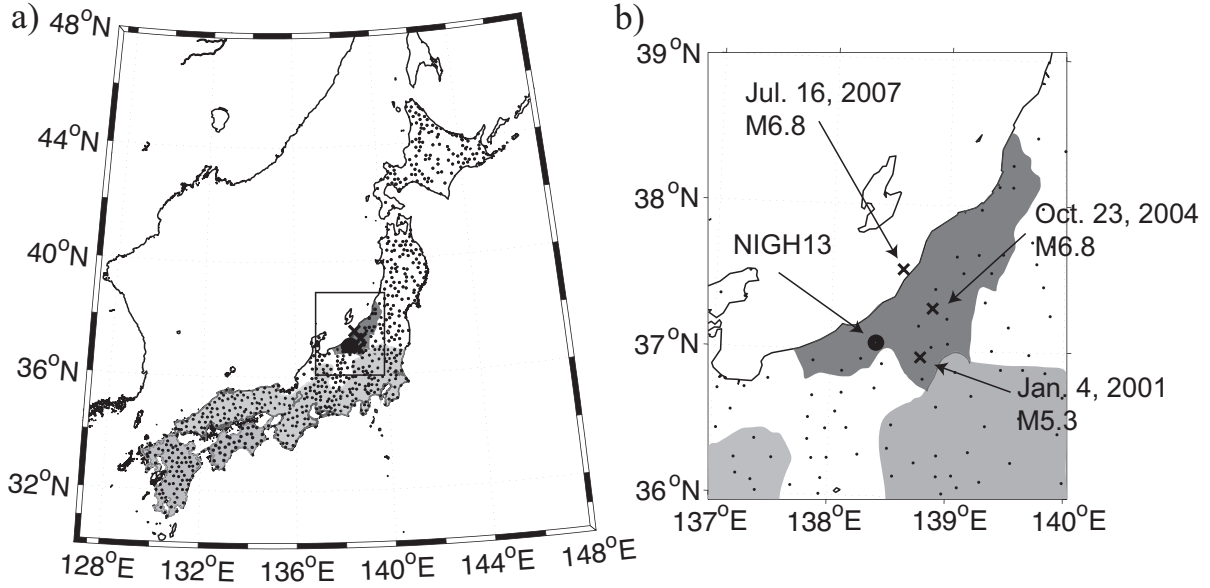


Figure 2.1. KiK-net stations (December, 2010). The black dots on the map represent the locations of the stations. The dark gray shows the area analyzed in section 2.7.1. The light gray illustrates the area where we apply the analysis for seasonal change (section 2.7.2). The rectangle area in panel (a) is magnified in panel (b). The large black circle indicates station *NIGH13*, which we use for examples of analysis in Figures 2.2, 2.4, 2.5, 2.6, 2.9, and 2.10. The black crosses depict the epicenters of three significant earthquakes that occurred in the vicinity.

We show example records of an earthquake in Figure 2.2. Figure 2.2a illustrates bandpass-filtered time series, and Figure 2.2b the power spectra of the unfiltered data. As shown in Figure 2.2b, most energy is confined to 1-13 Hz, and we apply a bandpass filter over this frequency range for all data processing. In Figure 2.2, *UD* denotes the vertical component, *NS* the north-south direction horizontal component, and *EW* the east-west direction horizontal component. In Figure 2.2a, the P wave arrives at around 7 s, and the shear wave arrives at around 14 s.

All the used events are at a depth greater than 10 km. Because of this large depth compared to the depth of the boreholes and the low velocity in the near surface, the waves that travel between the sensors at each station propagate in the near-vertical direction as plane waves. We compute the angle of the incoming wave at the borehole receiver by using one-dimensional ray tracing to confirm that the wave propagating between the borehole and

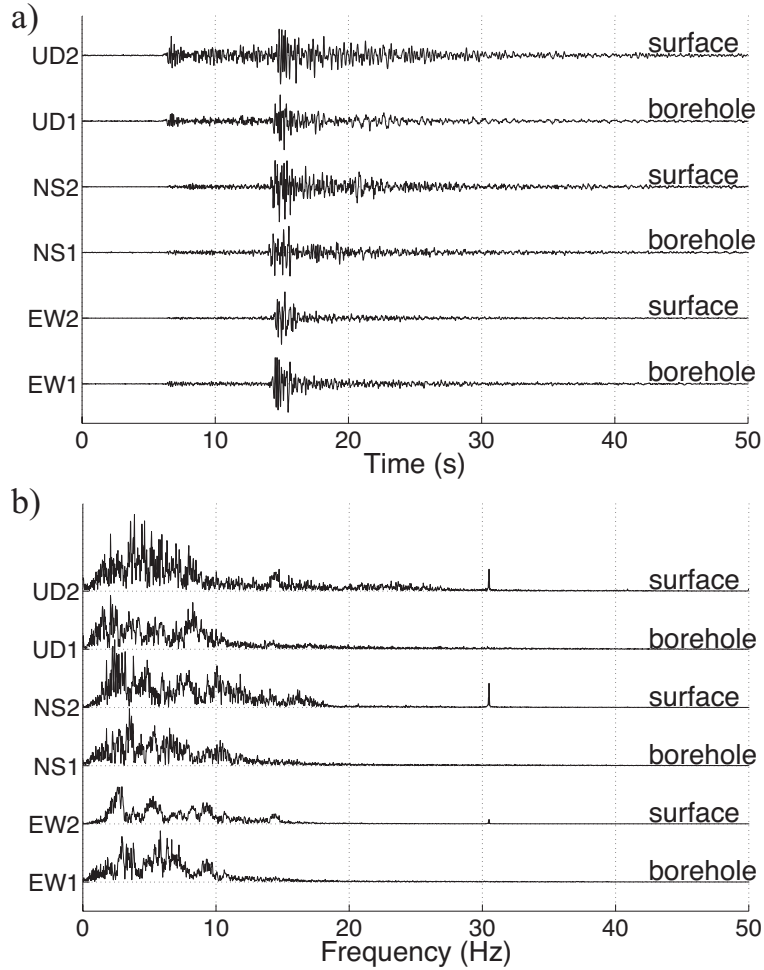


Figure 2.2. An earthquake recorded at all channels of station *NIGH13* (latitude  $37.0514^{\circ}\text{N}$  and longitude  $138.3997^{\circ}\text{E}$ ). This earthquake occurred at 14:59:19.56, 27 October 2004. The epicenter is at latitude  $37.2204^{\circ}\text{N}$  and longitude  $138.5608^{\circ}\text{E}$  and the depth is 11.13 km. The magnitude of this earthquake is  $M_{JMA}4.2$ . *UD* represents the vertical component, *NS* the north-south direction horizontal component, *EW* the east-west direction horizontal component, *1* the borehole seismograph, and *2* the surface seismograph. (a) The bandpass-filtered (1-13 Hz) time series. (b) The power spectra of the unfiltered records.

surface seismometers, propagates in the near-vertical direction. We use the velocity model of Nakajima et al. (2001) to determine the ray parameter  $p$  of the ray between each earthquake and the borehole sensor. The angle of incidence  $\theta$  of the wave propagating from the borehole receiver to the surface receiver is given by  $\cos \theta = \sqrt{1 - p^2 v^2}$ , where  $v$  is the average shear-wave velocity between these sensors as determined in this study. A bias in the velocity estimation due to non-vertical propagation depends on the deviation of  $\cos \theta$  from its value for vertical incidence,  $\cos 0^\circ = 1$ .

## 2.4 Retrieval of the wavefield between receivers

We apply seismic interferometry to the recorded earthquake data of each station for retrieving the wavefield where the borehole receiver behaves as a virtual source. Several algorithms have been used in seismic interferometry to obtain the wavefield. These include cross correlation (e.g., Claerbout, 1968; Bakulin and Calvert, 2004), deconvolution (e.g., Trampert et al., 1993; Snieder and Şafak, 2006), cross coherence (e.g., Aki, 1957; Prieto et al., 2009), and multidimensional deconvolution (e.g., Wapenaar et al., 2008; Minato et al., 2011).

We introduce the cross-correlation and deconvolution algorithms. We denote the wavefield, excited at source location  $\mathbf{s}$  that strikes the borehole receiver at location  $\mathbf{r}_b$  by  $u(\mathbf{r}_b, \mathbf{s}, \omega) = S(\mathbf{r}_b, \mathbf{s}, \omega)$ , where  $S(\mathbf{r}_b, \mathbf{s}, \omega)$  is the incoming wavefield that includes the source signature of the earthquake and the effect of propagation such as attenuation and scattering, in the frequency domain. The corresponding wavefield recorded at the surface receiver at location  $\mathbf{r}_s$  is given by

$$u(\mathbf{r}_s, \mathbf{s}, \omega) = 2G(\mathbf{r}_s, \mathbf{r}_b, \omega)S(\mathbf{r}_b, \mathbf{s}, \omega), \quad (2.1)$$

where the factor 2 is due to the presence of the free surface at  $\mathbf{r}_s$ . Because the wavefield striking the borehole receiver is close to a vertically propagating plane wave,  $G(\mathbf{r}_s, \mathbf{r}_b, \omega)$  is the plane wave Green's function that accounts for the propagation from the borehole

seismometer to the surface seismometer.

The cross-correlation approach to retrieve the wavefield in one dimension is given by Wapenaar et al. (2010a)

$$|S(\mathbf{r}_b, \mathbf{s}, \omega)|^2 G(\mathbf{r}_s, \mathbf{r}_b, \omega) = \frac{2j\omega}{\rho c} u(\mathbf{r}_s, \mathbf{s}, \omega) u^*(\mathbf{r}_b, \mathbf{s}, \omega), \quad (2.2)$$

where  $\rho$  is the mass density of the medium,  $c$  the wave propagation velocity,  $j$  the imaginary unit, and  $*$  the complex conjugate. The regularized deconvolution, which is similar to cross correlation, is given by

$$G(\mathbf{r}_s, \mathbf{r}_b, \omega) = \frac{u(\mathbf{r}_s, \mathbf{s}, \omega)}{u(\mathbf{r}_b, \mathbf{s}, \omega)} \approx \frac{u(\mathbf{r}_s, \mathbf{s}, \omega) u^*(\mathbf{r}_b, \mathbf{s}, \omega)}{|u(\mathbf{r}_b, \mathbf{s}, \omega)|^2 + \epsilon}, \quad (2.3)$$

where  $\epsilon$  is a regularization parameter (Mehta et al., 2007c,b). The deconvolution is potentially unstable due to the spectral division, and we avoid divergence by adding a positive constant  $\epsilon$  to the denominator (equation 2.3). Note that the deconvolution eliminates the imprint of waveform  $S(\mathbf{r}_b, \mathbf{s}, \omega)$ , which is incident on the borehole receiver. We derive the features of cross-correlation and deconvolution interferometry in Appendix 2.A.

## 2.5 Data processing

We use 111,934 earthquake-station pairs that are recorded between 2000 and 2010. The magnitude range is confined between 1.9 and 8.2. The cosine of the angle of incidence  $\cos \theta$  of the wave propagating between the receivers at each station is greater than 0.975, even for the events that are the furthest away. The bias introduced by non-vertical propagation thus is less than 2.5 %, and for most measurements it is much smaller. First, we check the data quality and drop some seismograms by a visual inspection using the signal-to-noise ratio as a criterion. Additionally, we discard stations with a borehole seismometer at a depth greater than 525 m because we focus this study on the near surface. We remove the DC component of the data by subtracting the average of each seismogram. For aligning the directions of the borehole receiver to the exact north-south and east-west directions, we

rotate the borehole receiver using the rotation angle provided by NIED (Shiomi et al., 2003). Because the sampling interval is not small compared to the travel time of P waves between the borehole and surface seismometers, we focus on the shear wave and only analyze the horizontal components.

We first apply deconvolution interferometry to the motion in the north-south direction of each surface-borehole pair. In this study, for reasons explained below, deconvolution interferometry gives more consistent estimates of the Green’s function than does cross-correlation interferometry. We choose  $\epsilon$  in equation 2.3 to be 1% of the average power spectrum of the borehole receiver in the frequency range 1-13 Hz because we find empirically that this is the smallest regularization parameter to obtain stable wavefields. We apply a band-pass filter from 1-13 Hz after applying deconvolution interferometry.

In this paper, we average in three ways to interpret the wavefields. The first method is the *annual stack*, where we average the deconvolved waveforms over the earthquakes recorded in each year. In the second averaging method, we average the deconvolved waves over all earthquakes recorded in each month over the 11 years (January 2000–2010, February 2000–2010, ..., and December 2000–2010). We call this average the *monthly stack*. In the third method, which we use for analyzing the influence of major earthquakes, we average over three months after a significant earthquake.

### 2.5.1 Estimating the shear-wave velocity

Before we apply annual stacking or monthly stacking, we resample the data from 0.005-s interval to 0.01-s interval if the data that are stacked include both 0.005-s and 0.01-s sampling-interval data. After stacking, we estimate the arrival time by seeking the three adjacent samples with the largest values and apply quadratic interpolation to find the time at which the deconvolved data have a maximum amplitude (Figure 2.3). This time is the travel time for a shear wave that propagates between the borehole and surface sensors. We use this travel time to compute the shear-wave velocity of the region between the two receivers.

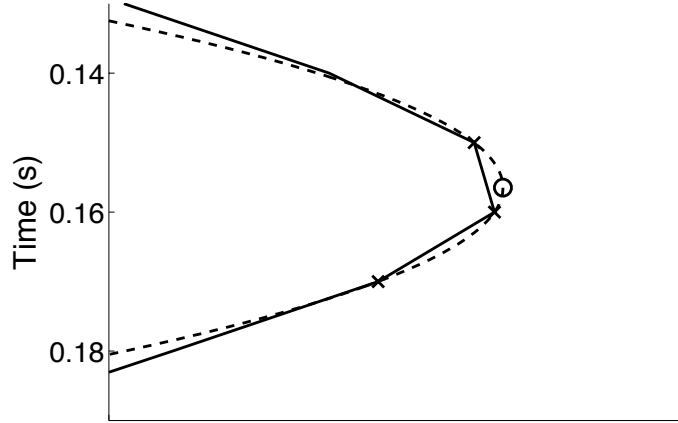


Figure 2.3. Quadratic interpolation. Using the three largest amplitude points (crosses), we interpolate the highest amplitude point (circle) by estimating the quadratic curve through the three highest amplitude points.

### 2.5.2 Computing the average and standard deviation of the velocity of the annual or monthly stacks

To interpret time-lapse variations in the velocities, we need to compute the average and standard deviation of the velocities within a region. Let us denote the estimated velocity by  $v_i(m, y)$ , where  $v_i$  is the shear-wave velocity at station  $i$ , in month  $m$ , and year  $y$ . This velocity is already averaged over each month. Each station has a different velocity. In order to quantify the time-lapse variations of the velocity, we subtract the average value of each station before calculating temporal variation in the annual or monthly average:

$$\Delta v_i(m, y) = v_i(m, y) - \bar{v}_i, \quad (2.4)$$

where  $\bar{v}_i$  is an average velocity of station  $i$  over all months and years. Then we compute either the annual or monthly average of the velocity variation over stations  $\Delta v$ , and we also compute the standard deviation of this quantity.

### 2.5.3 Comparison between cross-correlation and deconvolution interferometry

We compare the cross-correlation and deconvolution approaches using the annual-stacked wavefields (Figure 2.4). We show the locations of the epicenters of the used earthquakes in

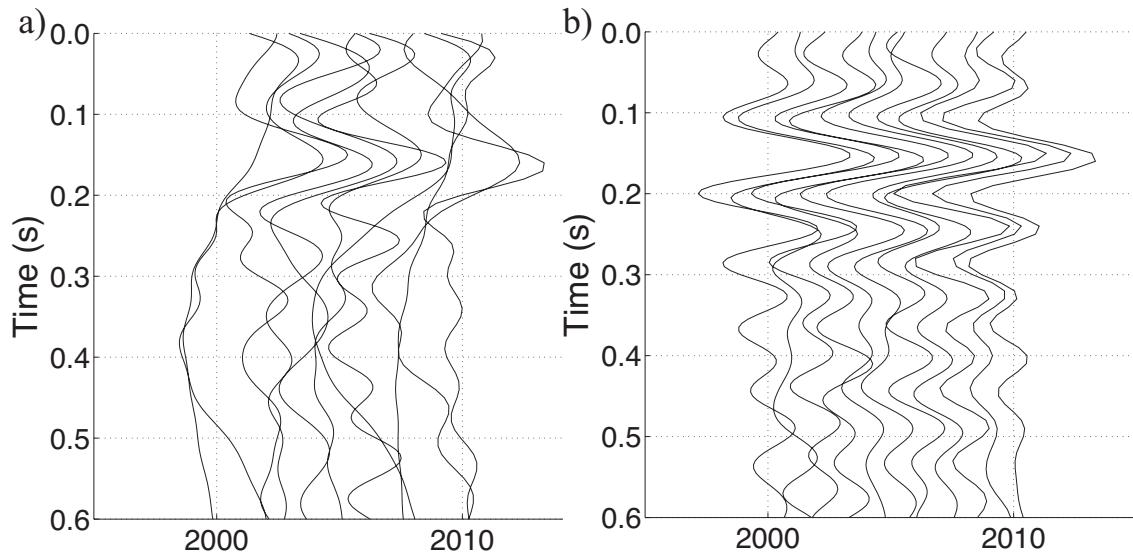


Figure 2.4. Annual-stacked wavefields by using (a) cross correlation and (b) deconvolution interferometry at station *NIGH13*. The surface and borehole receiver orientation directions are north-south. Epicenter locations are illustrated in Figure 2.5.

Figure 2.5. The annual stacks of the waveforms obtained by cross correlation are shown in Figure 2.4a. These waveforms are not repeatable from year to year and often do not show a pronounced peak at the arrival time of the shear wave at around  $t = 0.15$  s. We attribute the variability in these waveforms to variations in the power spectrum  $|S(\mathbf{r}_b, \mathbf{s}, \omega)|^2$  of the waves incident at the borehole receiver (equation 2.A1). In contrast, the annual stacks of the waveforms obtained by deconvolution shown in Figure 2.4b are highly repeatable and show a consistent peak at the arrival time of the shear wave. The consistency of these waveforms is due to the deconvolution that eliminates the imprint of the incident wave  $S(\mathbf{r}_b, \mathbf{s}, \omega)$  (equation 2.A2). Consistent with earlier studies (Trampert et al., 1993; Snieder and Şafak, 2006), we use deconvolution to extract the waves that propagate between the seismometers at each KiK-net station.

#### 2.5.4 Shear-wave splitting

We investigate shear-wave splitting by measuring the shear-wave velocity as a function of the polarization. We rotate both surface and borehole receivers from 0 to 350 degrees using

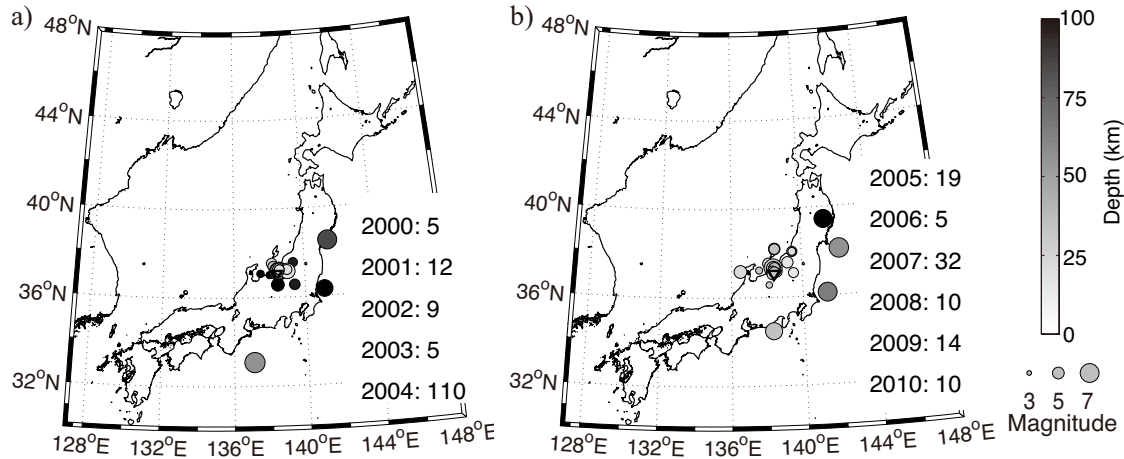


Figure 2.5. Epicenters used in Figure 2.4 from 2000 to 2004 (a) and from 2005 to 2010 (b) at station *NIGH13*. At the right in each panel, we show the number of earthquakes we use to obtain the waveforms in Figure 2.4 in each year. The size of each circle refers the magnitude of each earthquake and the color indicates the depth. The white triangle illustrates the location of station *NIGH13*. Because of the proximity of events, many circles overlap.

a 10-degree interval. The north-south direction is denoted by 0 degrees, and the east-west direction by 90 degrees. Because a rotation over 180 degrees does not change the polarization, the 0- to 170-degree wavefields are the same as the 180- to 350-degree data. We apply deconvolution interferometry to the rotated wavefields, located at the surface and borehole receivers with the same polarizations, for determining the velocity of each polarization. Because the velocity for each polarization is related to the velocities of the fastest and slowest shear waves (Appendix 2.B), we can estimate shear-wave splitting from the velocity difference. We cross-correlate the deconvolved wavefield for every used polarization (from 0 to 350 degrees in 10-degree intervals) with the deconvolved wavefield obtained from the motion in the north-south direction. This allows us to quantify the polarization dependence of the shear-wave velocity. Similar to the process described in section 2.5.1, we compute annual stacks of cross-correlated wavefields and pick the peak amplitudes of stacked wavefields by using quadratic interpolation.

We can separate the velocity  $v(\phi)$  as a function of polarization direction  $\phi$  into the isotropic and anisotropic terms using a Fourier series expansion (Appendix 2.C):

$$v(\phi) = v_0 + v_1 \cos 2\phi + v_2 \sin 2\phi. \quad (2.5)$$

In this expression,  $v_0$  is the isotropic component of the velocity, and  $\sqrt{v_1^2 + v_2^2}$  the anisotropy. We assume the splitting time to be much smaller than the period of the wavefield. Because the wavefields of each polarization data are symmetric by 180 degrees, the anisotropy depends on polarization through a dependence of  $2\phi$ .

## 2.6 Retrieved near-surface shear-wave velocities in Japan

Using deconvolution interferometry at each station, we obtain the wavefield that corresponds to a plane wave propagating in the near-vertical direction ( $\cos \theta > 0.975$ ) between the borehole receiver and surface receiver at each station. In this section, we show the wavefields of the annual stack, monthly stack, and shear-wave splitting.

### 2.6.1 Annual and monthly stacks

Figure 2.6 shows the annual-stacked wavefields at station *NIGH13* represented by the large black circle in Figure 2.1. At this station, the sampling interval is 0.005 s until 2007 and is 0.01 s after 2008. In Figure 2.6, the deconvolved wavefields have good repeatability and a pronounced peak amplitude. After we apply quadratic interpolation (section 2.5.1), the determined arrival times (the black circles in Figure 2.6) correlate well with the travel time which is obtained from logging data (the horizontal line in Figure 2.6). The logging data is measured using a logging tool and by Vertical Seismic Profiling (VSP). The seismic source of VSP is a vertical-component vibrator. For finite offsets this source generates shear waves. We determine the average velocity from the logging data by computing the depth average of the slowness, because this quantity accounts for the vertical travel time. Because of the quadratic interpolation, the measured travel times show variations smaller than the original sampling time.

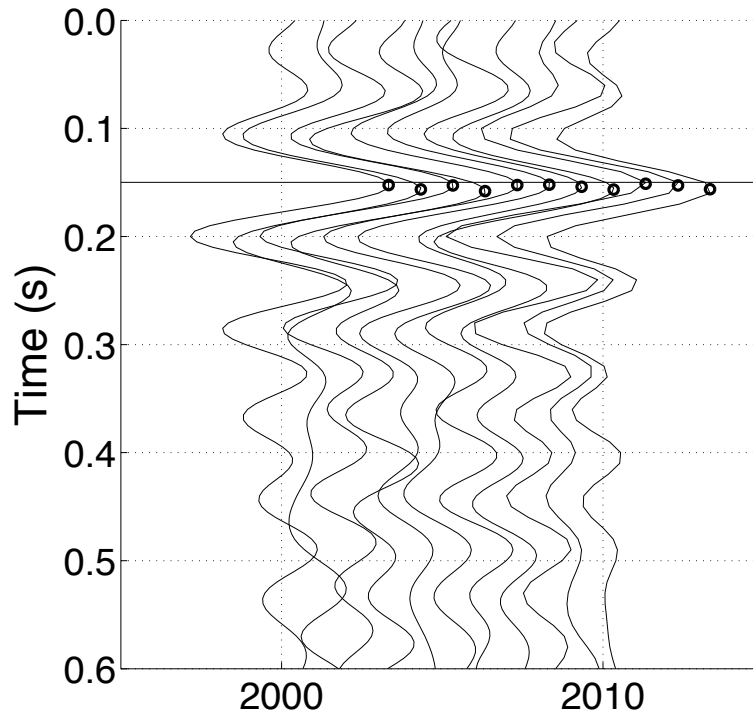


Figure 2.6. Annual-stacked wavefields (curves) with the interpolated largest amplitude (circles) at station *NIGH13*. The horizontal line at around 0.15 s is the shear-wave arrival time determined from logging data. From left to right, we show annual stacks from 2000 to 2010. The source and receiver polarization directions are the north-south direction.

After determining the arrival times of all stations, we compute the shear-wave velocities by using the known depth of the boreholes. Applying triangle-based cubic interpolation (Lawson, 1984) between stations, we create the shear-wave velocity map of Japan in each year (Figure 2.7). To reduce the uncertainty of the velocity estimation we use only the stations which give deconvolved waves with an arrival time greater than 0.1 s. Thus, we obtain the near-surface shear-wave velocities throughout Japan by applying seismic interferometry to KiK-net data. The shear-wave velocity obtained from logging data is shown in the top left in Figure 2.7. Note that the velocities measured in different years are similar. In Figure 2.8, we crossplot the velocities estimated by interferometry in 2008 and obtained from logging data. The data are concentrated along the black line, which indicates the degree of correlation between the shear-wave velocity obtained from logging data and from seismic interferometry.

We also analyze seasonal changes and show the monthly-stacked wavefields at station *NIGH13* in Figure 2.9. The monthly stacked wavefields also have good repeatability between different months.

### 2.6.2 Shear-wave splitting

In Figure 2.10a, we show the wavefields of the shear-wave splitting analysis at station *NIGH13* in 2010 that are obtained by the sequence of deconvolution and cross correlation described in section 2.5.4. Each trace is plotted at the angle that is equal to the shear-wave polarization used to compute that trace. The thick solid line in Figure 2.10a shows the interpolated maximum amplitude time of each waveform. The dashed circle shows the arrival time for the wave polarized in the north-south direction. For the polarizations where the thick solid line is outside of the dashed circle, the shear-wave velocity is slower. The fast and slow shear polarization directions in Figure 2.10a are 22 degrees and  $-71$  degrees clockwise from the north-south direction, respectively. The angle between these fast and slow directions is 93 degrees, which is close to 90 degrees as predicted by theory (Crampin (1985) and Appendix 2.C). The 3-degree discrepancy could be caused by data noise or discretization errors. At station *NIGH13* in 2010, the fast polarization shear-wave velocity  $v_{fast}$  is 638 m/s,

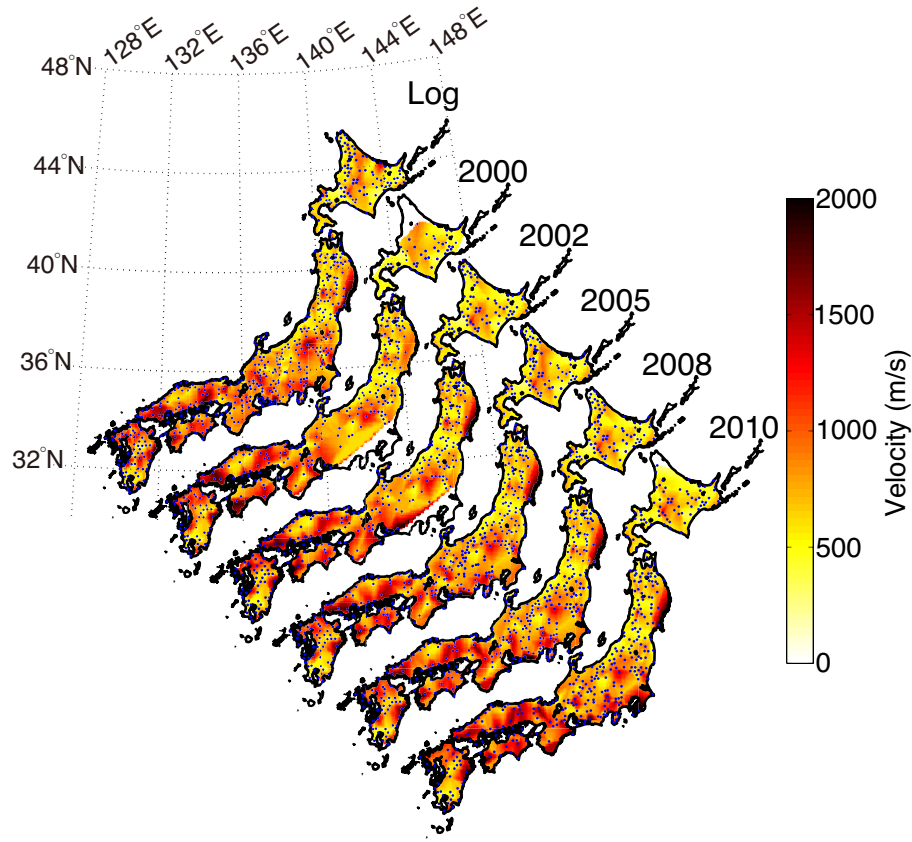


Figure 2.7. Shear-wave velocities obtained from logging data (*Log*) and estimated by annual-stacked seismic interferometry using earthquake data at the north-south polarization (excerpted 2000, 2002, 2005, 2008, and 2010). The blue dots on a map represent the station locations which we use to make the map. We interpolate velocities between stations by triangle-based cubic interpolation (Lawson, 1984). The longitude and latitude belong to the map in the upper-left. The number of right-upper side of each map shows the year of data.

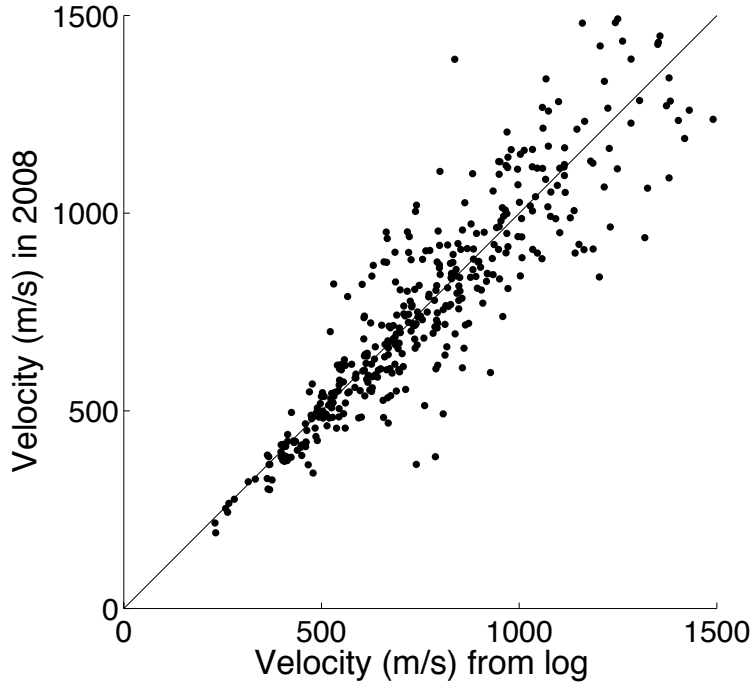


Figure 2.8. Crossplot of velocities computed from logging data and by seismic interferometry in 2008. The black line indicates equal velocities.

the slow velocity  $v_{slow}$  is 593 m/s, and the anisotropy parameter  $(v_{fast} - v_{slow})/v_{fast}$  is 7% (see Figure 2.10b). The difference of the arrival times between the fast- and slow-polarization velocity wavefields is much smaller than the period of a wavefield when the borehole depth is less than 525 m.

## 2.7 Interpretation of shear-wave velocities and shear-wave splitting

### 2.7.1 Influence of major earthquakes

The near-surface shear-wave velocity in Japan is similar between years (see Figure 2.7), which means the near-surface structure is basically stable. In this section, we focus on a small region. We use  $\Delta v$  (calculated by the method presented in section 2.5.2) and the fast shear-wave polarizations shown in Figure 2.11 to analyze the influence of major earthquakes in the Niigata prefecture (the dark shaded area in Figure 2.1). Three significant earthquakes, shown by the dashed arrows in each panel, occurred during the 11 years.

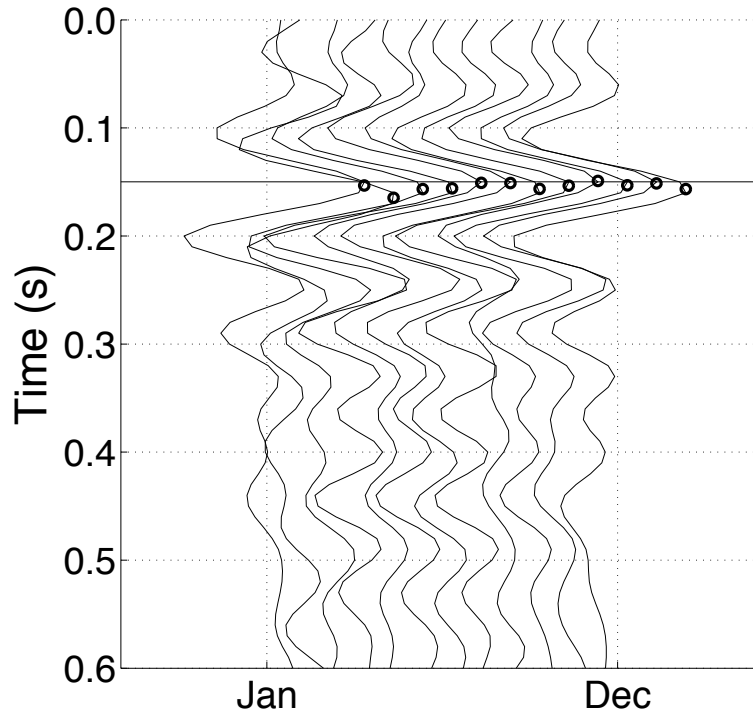


Figure 2.9. Monthly-stacked wavefields (curves) with the interpolated largest amplitude (circles) at station *NIGH13*. The horizontal line at around 0.15 s is the shear-wave arrival time obtained from logging data. From left to right, we depict monthly stacks from January to December. Each trace is stacked over the 11 years (January 2000–2010, February 2000–2010, ..., and December 2000–2010). The source and receiver polarization directions are the north-south direction.

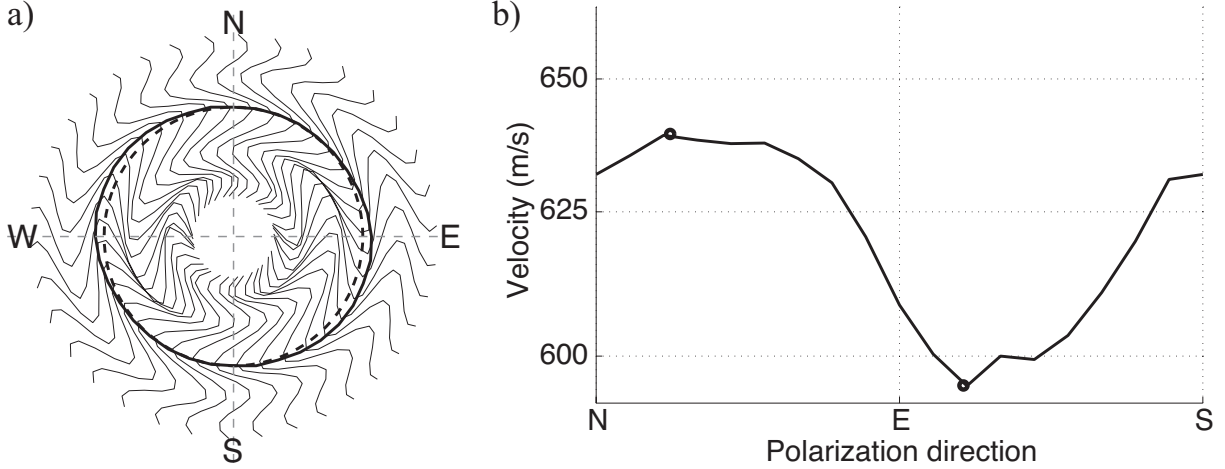


Figure 2.10. (a) Cross correlograms along every 10-degree polarization direction in 2010 at station *NIGH13*. Each trace is plotted at an angle equal to the polarization direction used to construct that trace. The dashed circle indicates the peak-amplitude time of the north-south direction, and the thick solid line represents the peak-amplitude time for each polarization direction. (b) Shear-wave velocities computed from the thick solid line in panel (a). Black circles represent the quadratic-interpolated fast and slow polarization shear-wave velocities.

Figure 2.11a shows the velocity variation  $\Delta v$  for the isotropic component  $v_0$  computed by equation 2.5 compiled over periods one year before and three months after the major earthquakes. We use all stations in the Niigata prefecture and compute the average over the stations. Each box depicts the time range (horizontal extent) and the error in the average velocity over that time interval (vertical length). The error in the velocity is given by the standard deviation of measurements from different earthquakes in each time interval (section 2.5.2). In Figure 2.11a, these average velocities show significant velocity reduction after the major earthquakes. The average isotropic velocity of all stations in the region from 2000 to 2010 is 662 m/s, and the relative velocity change of each earthquake is around 3-4%. Similar velocity variations caused by major earthquakes were reported earlier; for example, Sawazaki et al. (2009) analyze the variations caused by the 2000 Western-Tottori Earthquake, Yamada et al. (2010) analyze the variations caused by the 2008 Iwate-Miyagi Nairiku earthquake using KiK-net stations, while Nakata and Snieder (2011) observe a velocity reduction of about 5% after the 2011 Tohoku-Oki earthquake. To increase the temporal resolution of the velocity

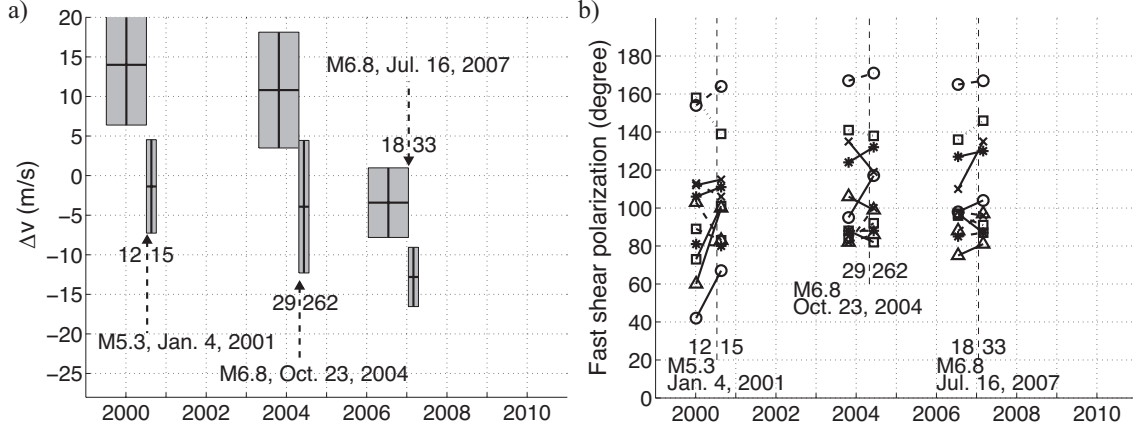


Figure 2.11. (a) The isotropic component of the shear-wave velocity (Fourier coefficient  $v_0$ ) averaged over one year before and three months after three major earthquakes. (b) The direction of the fast shear-wave polarization averaged over same intervals. All data are computed for stations in the Niigata prefecture (the dark shaded area in Figure 2.1). In each panel, the label of the year is placed in the middle of each year. The dashed arrows in panel (a) and the vertical dashed lines in panel (b) indicate the times of the three major earthquakes shown with the black crosses in Figure 2.1. The numbers at the left and right of dashed arrows (a) and lines (b) are the number of earthquakes we use for determining velocities and polarizations before and after the major earthquakes, respectively. In panel (a), each velocity is the velocity variation  $\Delta v$  in equation 2.4. The horizontal extent of each box depicts the time interval used for averaging (one year before and three months after the major earthquakes). The vertical extent of each box represents the standard deviation of the velocity in the area computed by the method in section 2.5.2. The horizontal line in each box indicates average velocity  $\Delta v$  in each time interval, and the vertical line the center of each time interval. In panel (b), we use only the stations with significant anisotropy ( $(v_{fast} - v_{slow})/v_{fast} \geq 1\%$ ). We select 11 stations from 19 stations and depict the fast shear-wave polarization directions with different symbols or lines. Each symbol is placed at the center of each time period.

change, we compute velocity changes averaged over periods one year before and three months after the major earthquakes (Figure 2.11a) because Sawazaki et al. (2009) found that the velocity reduction is sustained over a period of at least three months after an earthquake.

The stations on soft-rock sites have a greater velocity reduction than those on hard-rock sites. (We define soft- and hard-rock sites from the estimated shear-wave velocity; hard-rock sites have a shear-wave velocity greater than 600 m/s, while soft-rock sites have a shear-wave velocity less than 600 m/s.) For the used event-station pairs, the velocity reduction does not change measurably with the distance from the epicenter. This is an indication that the

velocity reduction depends mostly on the local geology. The velocity reduction can be due either to the opening and closing of existing fractures, to the creation of new fractures, or to the change in the shear modulus caused by changes in the pore fluid pressure because of shaking-induced compaction (Das, 1993, Figure 4.24).

The relative velocity reduction is smaller than the reduction found by Wu et al. (2009) because of the averaging over stations and over earthquakes recorded over a period of three months. Wu et al. (2009) use a single station located on a soft-rock site and do not average over several months. Wegler et al. (2009) estimate the velocity reduction in deeper parts of the subsurface, and the velocity reduction they find is small (0.3-0.5 %). From this we infer that the velocity reduction due to a major earthquake is most pronounced in near surface, especially for soft-rock sites.

We also obtain the polarization directions of the fast shear waves before and after the major earthquakes by averaging over the same time intervals as used in Figure 2.11a (Figure 2.11b). The direction of the fast shear-wave polarization does not show a significant change after the earthquakes, hence it seems to be unaffected by these earthquakes. The average standard deviation of the polarization direction of all stations in the Niigata prefecture between 2000 and 2010 is 15 degrees, which represents the accuracy of the fast shear-wave velocity polarization direction.

### **2.7.2 Influence of precipitation**

We compute the monthly-averaged shear-wave velocities of the north-south polarization (Figure 2.12a) to investigate a possible seasonal velocity variation related to precipitation. We use only the data in southern Japan (the light shaded area in Figure 2.1) because that region has a more pronounced seasonal precipitation cycle than northern Japan. Figure 2.12a illustrates a significant velocity difference between spring/summer and fall/winter. We calculate the average velocities over the stations with the 15% slowest shear-wave velocities in the area because these stations are located at soft-rock sites and are therefore influenced more by precipitation than the station at hard-rock sites. We compare the monthly-averaged

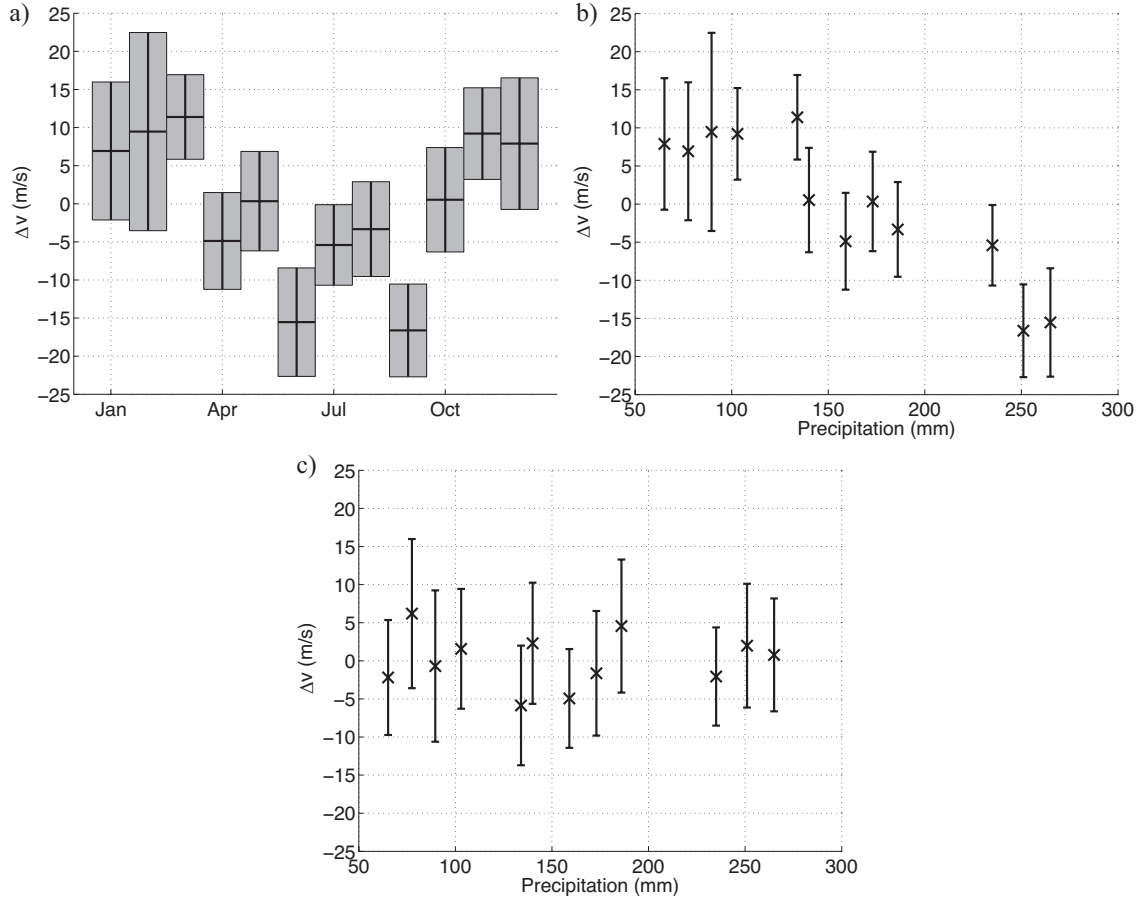


Figure 2.12. Seasonal dependence of shear-wave velocity. (a) Variation of the average monthly-velocities stacked over the period 2000 through 2010 in southern Japan (the light gray area in Figure 2.1). We use the stations with the 15% slowest velocities in the area. The horizontal extent of each box shows time interval used for averaging, and the vertical extent the standard deviations of all receivers in the time interval computed by the method in section 2.5.2. The horizontal line in each box indicates average velocity  $\Delta v$  in each time interval, and the vertical line the center of each time interval. (b) Crossplot between monthly precipitation (provide by JMA) and the average velocity  $\Delta v$  with error bars. (c) Crossplot between monthly precipitation and the average velocity  $\Delta v$  with error bars using the stations with the 85% fastest velocities in the area.

velocities with the monthly average of precipitation (observed by the Japan Meteorological Agency (JMA)) computed from precipitation records over 30 years (Figure 2.12b). Note the negative correlation between the shear-wave velocity and precipitation (i.e., when it rains, the velocity decreases), which is consistent with the findings of Sens-Schönfelder and Wegler (2006).

For comparison, for the stations with the 85% fastest shear-wave velocities in the area (Figure 2.12c) the shear-wave velocity does not vary with precipitation. The cause of the velocity reduction is the decreased effective stress of the soil due to the infiltration of water that increases the pore pressure (Das, 1993, Section 4.19; Chapman and Godin, 2001; Snieder and van den Beukel, 2004). We assume that for soft-rock sites most of the velocity change is caused by the effective stress change because Snieder and van den Beukel (2004) show that the relative density change with pore pressure is much smaller than the relative change in the shear modulus.

### 2.7.3 Shear-wave splitting and the direction of the plate motion

Using shear-wave splitting analysis, we determine fast shear-wave polarization directions of every station (illustrated by the black arrows in Figure 2.13a). These directions are averaged over all years from 2000 to 2010 because the temporal changes in the direction are small (see Figure 2.11b). We plot the directions of all stations which have an anisotropy parameter  $(v_{fast} - v_{slow})/v_{fast} \geq 1\%$  because the uncertainty in the direction of the fast shear polarization is large when the anisotropy is small. In Figure 2.13a, we also plot the direction of the plate motion at each station (the gray arrows), estimated from GPS data (Sagiya et al., 2000). Each arrow is normalized to the same length.

In Figure 2.13b, we plot only the stations which have an anisotropy parameter larger than 1% and a north-south polarization shear-wave velocity faster than 600 m/s; these stations are located on hard-rock sites. The average absolute angle between the directions of fast shear polarization and the plate motion in these stations is 16 degrees, and this average angle of the stations which have a shear-wave velocity less than 600 m/s is 36 degrees. Therefore, the

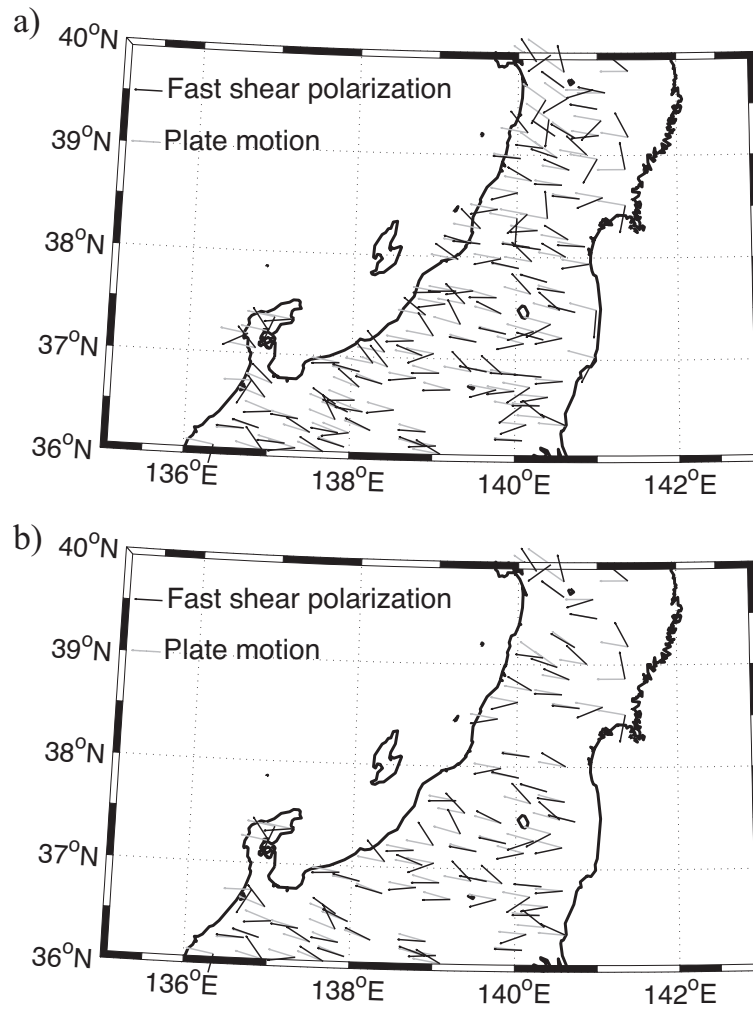


Figure 2.13. (a) Fast shear-wave polarization directions (black lines) and the direction of the plate motion (gray lines) estimated from GPS data (Sagiya et al., 2000) at the stations with significant anisotropy ( $(v_{fast} - v_{slow})/v_{fast} \geq 1\%$ ). (b) Extracted stations from panel (a) with shear-wave velocity faster than 600 m/s.

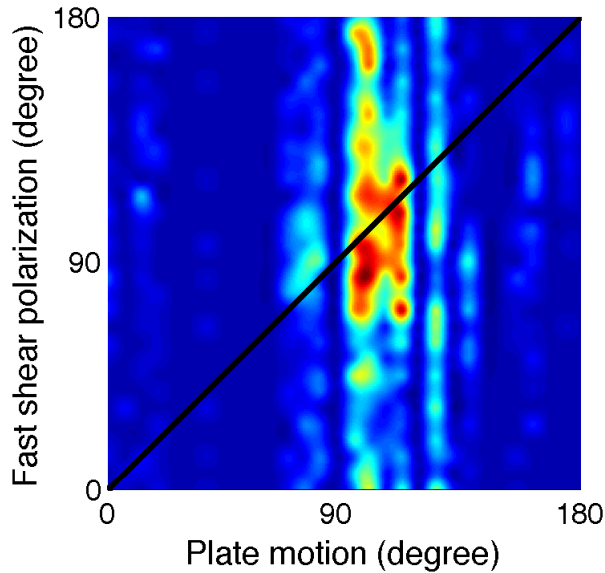


Figure 2.14. Crossplot between the direction of the plate motion and the fast shear-wave polarization directions. We use the stations which have faster than 600 m/s shear-wave velocity. Red indicates there are many points. The north-south direction is 0 degrees, and the east-west direction 90 degrees.

fast shear-wave polarization on hard-rock sites correlates more strongly with the direction of the plate motion than the polarization on soft-rock sites. The 16-degree angle is close to the 15-degree standard deviation angle of each station computed in section 2.7.1. The near-surface polarization in the western part of Figure 2.13b correlates well with observations of the shear-wave polarization at greater depth (Okada et al., 1995; Nakajima and Hasegawa, 2004; Nakajima et al., 2006), but this agreement does not hold in the regions further east.

We present a crossplot of the directions of the fast shear-wave polarization and the plate motion for stations all over Japan (Figure 2.14), where we only used the stations which have an anisotropy parameter greater than 1% and a shear-wave velocity faster than 600 m/s. The red area in Figure 2.14 indicates that for most stations the direction of the plate motion is between 90 and 140 degrees, and that this direction correlates with the polarization direction of the fast shear wave. The near-surface stress directions on hard-rock sites is presumably related to the plate motion because the stress field related to the plate motion changes the

properties of fractures. Note that the used shear waves sample the shallow subsurface (down to about several hundreds of meters). It is remarkable that the shear-wave velocities in the near surface at hard-rock sites correlate with tectonic process (plate motion) that extends several tens of kilometers into the subsurface.

## **2.8 Conclusions**

We obtain annual and monthly averaged near-surface shear-wave velocities throughout Japan by applying seismic interferometry to KiK-net data. Deconvolution interferometry yields more repeatable and higher resolution wavefields than does cross-correlation interferometry. Because picked arrival times in waveforms are generally stable over time and consistent with logging data, the near-surface has a stable shear-wave velocity. After three strong earthquakes in the Niigata prefecture, however, the shear-wave velocity is reduced. By computing the monthly-stacked velocity, we observe a velocity variation on stations placed on soft rock that has a negative correlation with precipitation. We also observe shear-wave splitting. The fast shear-wave polarization direction on a hard-rock site correlates with the direction of the plate motion. Because the shear-wave velocity is related to ground soil strength, these velocities are useful for civil engineering, site characterization, and disaster prevention.

## **2.9 Acknowledgments**

We are grateful to NIED for providing us with the KiK-net data and to JMA for precipitation data. We thank Diane Witters for her professional help in preparing this manuscript. We are grateful to the assistant editor, Kaoru Sawazaki, and one anonymous reviewer for suggestions, corrections, and discussions.

### **2.A 1D seismic interferometry**

We explain in this appendix why deconvolution interferometry is suitable for this study. Figure 2.A1 illustrates the model of interferometry using a KiK-net station and an earth-

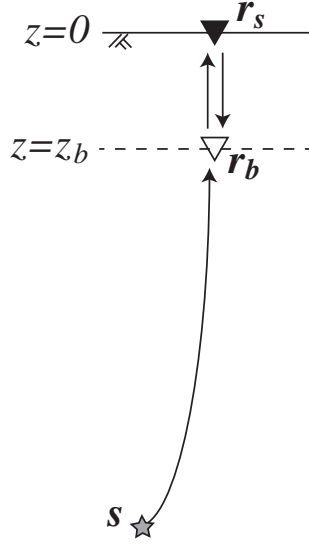


Figure 2.A1. Geometry of an earthquake and a KiK-net station, where  $\mathbf{r}_s$  is the surface receiver (black triangle),  $\mathbf{r}_b$  the borehole receiver (white triangle), and  $\mathbf{s}$  the epicenter of earthquake (gray star).

quake. The incoming wavefield  $S(\mathbf{r}_b, \mathbf{s}, \omega)$ , propagating from source  $\mathbf{s}$  to receiver  $\mathbf{r}_b$ , is given by  $G(\mathbf{r}_b, \mathbf{s}, \omega)W(\mathbf{s}, \omega)$ , where  $G$  is the Green's function including any unknown complex effect of wave propagation such as scattering and attenuation, and  $W$  the source signature in the frequency domain. Assuming that the subsurface is homogeneous between the receivers, the received wavefield at surface receiver  $\mathbf{r}_s$  is  $2S(\mathbf{r}_b, \mathbf{s}, \omega)e^{jkz_b}e^{-\gamma z_b}$ , where  $\gamma$  is the attenuation coefficient and  $k$  the wave number. Because of the free surface, the amplitude of the wavefield at the surface is multiplied by a factor 2. We assume that there are no multiples between the two receivers. The reflected wavefield from the surface at the borehole receiver  $\mathbf{r}_b$  is  $S(\mathbf{r}_b, \mathbf{s}, \omega)e^{2jkz_b}e^{-2\gamma z_b}$ , and the total wavefield at  $\mathbf{r}_b$  is  $S(\mathbf{r}_b, \mathbf{s}, \omega) + S(\mathbf{r}_b, \mathbf{s}, \omega)e^{2jkz_b}e^{-2\gamma z_b}$ . Applying cross-correlation interferometry to these wavefields yields

$$\begin{aligned} u(\mathbf{r}_s, \mathbf{s}, \omega)u^*(\mathbf{r}_b, \mathbf{s}, \omega) &= 2S(\mathbf{r}_b, \mathbf{s}, \omega)e^{jkz_b}e^{-\gamma z_b} \left[ S^*(\mathbf{r}_b, \mathbf{s}, \omega) + S^*(\mathbf{r}_b, \mathbf{s}, \omega)e^{-2jkz_b}e^{-2\gamma z_b} \right] \\ &\approx 2|S(\mathbf{r}_b, \mathbf{s}, \omega)|^2 e^{jkz_b}e^{-\gamma z_b} \end{aligned} \quad (2.A1)$$

when we consider only the first arrival. Using deconvolution interferometry, we obtain

$$\begin{aligned} \frac{u(\mathbf{r}_s, \mathbf{s}, \omega)}{u(\mathbf{r}_b, \mathbf{s}, \omega)} &= \frac{2S(\mathbf{r}_b, \mathbf{s}, \omega)e^{jkz_b}e^{-\gamma z_b}}{S(\mathbf{r}_b, \mathbf{s}, \omega) + S(\mathbf{r}_b, \mathbf{s}, \omega)e^{2jkz_b}e^{-2\gamma z_b}} \\ &\approx 2e^{jkz_b}e^{-\gamma z_b}, \end{aligned} \quad (2.A2)$$

where we also only retain the first arrival. The plane-wave Green's function excited at  $\mathbf{r}_b$  and received at  $\mathbf{r}_s$  is equal to  $2e^{jkz_b}e^{-\gamma z_b}$  in the frequency domain. Let us compare equations 2.A1, 2.A2, and the Green's function. The wavefield retrieved by cross-correlation interferometry is complicated because equation 2.A1 includes the power spectrum  $|S(\mathbf{r}_b, \mathbf{s}, \omega)|^2$ . This term is different for different earthquakes. In contrast, deconvolution interferometry eliminates the incoming wave  $S(\mathbf{r}_b, \mathbf{s}, \omega)$ , and thus provides a more accurate estimate of the Green's function. When we stack deconvolved wavefields over earthquakes, the accuracy of this estimate is improved. Because the deconvolved waves do not depend on the power spectrum of the incident wave  $|S(\mathbf{r}_b, \mathbf{s}, \omega)|^2$ , the deconvolved wavefields are more reproducible than those obtained from cross correlation.

## 2.B Shear-wave splitting

Usually, shear-wave splitting is analyzed with Alford rotation (Alford, 1986; Thomsen, 1988). This procedure is based on the use of two independent orthogonal sources in the horizontal direction. In our study, the virtual source in the borehole has the polarization of the incident wave. The two horizontal components of the virtual source therefore are not independent, so that Alford rotation cannot be applied.

The angle of the fast and slow shear-wave polarization directions is 90 degrees because we assume the incoming wave is a plane wave (Crampin, 1985). A wavefield with polarization  $\hat{\mathbf{p}}$ , which is a unit vector, can be expressed in the polarization of the fast and slow shear waves:

$$\hat{\mathbf{p}} = \hat{\mathbf{p}}_f \cos \phi + \hat{\mathbf{p}}_s \sin \phi, \quad (2.B1)$$

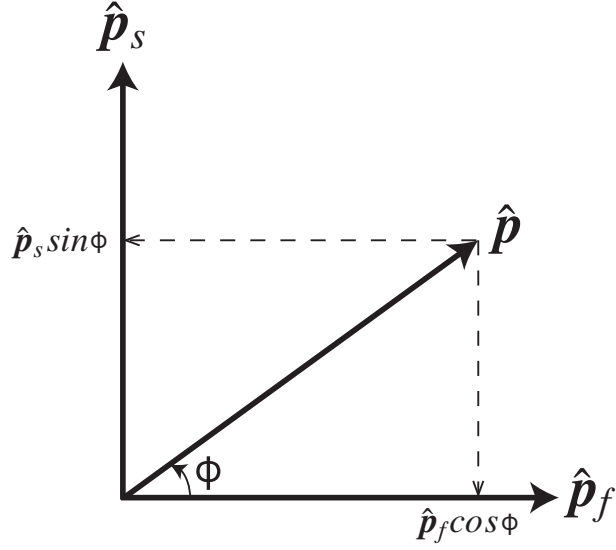


Figure 2.B1. Projection of fast and slow velocity directions, where  $\hat{\mathbf{p}}_f$  is the fast polarization direction,  $\hat{\mathbf{p}}_s$  the slow polarization direction,  $\hat{\mathbf{p}}$  an arbitrary direction, and  $\phi$  the angle between the fast direction and arbitrary direction.  $\hat{\mathbf{p}}$ ,  $\hat{\mathbf{p}}_f$ , and  $\hat{\mathbf{p}}_s$  are unit vectors. Dashed arrows show the projection, which is shown in equation 2.B1.

where  $\phi$  is the polarization angle in the arbitrary wavefield relative to the direction of the fast shear-wave polarization, and  $\hat{\mathbf{p}}_f$  and  $\hat{\mathbf{p}}_s$  are the unit vectors of the fast and slow velocity wavefields, respectively (see Figure 2.B1).

The incoming wavefield  $\mathbf{u}_b$  at the borehole receiver is

$$\mathbf{u}_b = S(t)\hat{\mathbf{p}} = S(t)\hat{\mathbf{p}}_f \cos \phi + S(t)\hat{\mathbf{p}}_s \sin \phi, \quad (2.B2)$$

where  $S(t)$  is the incoming wavefield, and  $t$  the time. The wavefield at surface receiver  $\mathbf{u}_s$  is given by

$$\mathbf{u}_s = S\left(t - \frac{z_b}{v_f}\right)\hat{\mathbf{p}}_f \cos \phi + S\left(t - \frac{z_b}{v_s}\right)\hat{\mathbf{p}}_s \sin \phi, \quad (2.B3)$$

where  $v_f$  is the fast velocity,  $v_s$  the slow velocity, and  $z_b$  the distance between the top and bottom receivers.

The component of  $\mathbf{u}_s$  along  $\hat{\mathbf{p}}$  is

$$\begin{aligned}
u_s(\phi) &= (\hat{\mathbf{p}} \cdot \mathbf{u}_s) = S \left( t - \frac{z_b}{v_f} \right) (\hat{\mathbf{p}} \cdot \hat{\mathbf{p}}_f) \cos \phi + S \left( t - \frac{z_b}{v_s} \right) (\hat{\mathbf{p}} \cdot \hat{\mathbf{p}}_s) \sin \phi \\
&= S \left( t - \frac{z_b}{v_f} \right) \cos^2 \phi + S \left( t - \frac{z_b}{v_s} \right) \sin^2 \phi.
\end{aligned} \tag{2.B4}$$

We express  $v_f$  and  $v_s$  in the average velocity  $v_0$  and the difference  $\delta$ :

$$\frac{1}{v_f} = \frac{1}{v_0} - \delta, \quad \frac{1}{v_s} = \frac{1}{v_0} + \delta, \tag{2.B5}$$

and assume the splitting time  $z_b\delta$  is much smaller than the period. We insert expression 2.B5 into equation 2.B4 and expand using first-order Taylor expansion in  $\delta$ :

$$\begin{aligned}
u_s(\phi) &= S \left( t - \frac{z_b}{v_0} + z_b\delta \right) \cos^2 \phi + S \left( t - \frac{z_b}{v_0} - z_b\delta \right) \sin^2 \phi \\
&= S \left( t - \frac{z_b}{v_0} \right) (\sin^2 \phi + \cos^2 \phi) + S' \left( t - \frac{z_b}{v_0} \right) z_b\delta (\cos^2 \phi - \sin^2 \phi) \\
&= S \left( t - \frac{z_b}{v_0} \right) + S' \left( t - \frac{z_b}{v_0} \right) z_b\delta \cos 2\phi \\
&= S \left( t - \frac{z_b}{v_0} + z_b\delta \cos 2\phi \right),
\end{aligned} \tag{2.B6}$$

where  $S'$  is the time derivative of  $S$ . Thus, using Taylor expansion, we obtain the velocity for a shear wave with the polarization of equation 2.B1:

$$v(\phi) = \frac{v_0}{1 - v_0\delta \cos 2\phi}, \tag{2.B7}$$

or to first order in  $v_0\delta$ :

$$v(\phi) = v_0(1 + v_0\delta \cos 2\phi). \tag{2.B8}$$

## 2.C Fourier coefficients

We describe the meaning of  $v_0$ ,  $v_1$ , and  $v_2$  in equation 2.5. Expression 2.B8 gives the velocity for a polarization  $\phi$  relative to the polarization of the fast shear wave. When the azimuth of the fast shear-wave polarization is given by  $\psi$ , the angle  $\phi$  in equation 2.B8 must

be changed into  $\phi \rightarrow \phi - \psi$ . Denoting  $v_0^2 \delta$  by  $V$ , these changes turn equation 2.B8 into

$$v(\phi) = v_0 + V \cos 2(\phi - \psi). \quad (2.C1)$$

This can also be written as

$$v(\phi) = v_0 + v_1 \cos 2\phi + v_2 \sin 2\phi; \quad (2.C2)$$

with

$$v_0 = \frac{1}{2\pi} \int_{-\pi}^{\pi} v(\phi) d\phi, \quad v_1 = \frac{1}{\pi} \int_{-\pi}^{\pi} v(\phi) \cos 2\phi d\phi, \quad v_2 = \frac{1}{\pi} \int_{-\pi}^{\pi} v(\phi) \sin 2\phi d\phi,$$

$$V = \sqrt{v_1^2 + v_2^2}, \quad \psi = \frac{1}{2} \arctan \left( \frac{v_2}{v_1} \right).$$

In expression 2.C2,  $v_0$ ,  $v_1$ , and  $v_2$  are the Fourier coefficients of the velocity  $v(\phi)$ . Because  $v_0$  does not depend on  $\phi$ ,  $v_0$  represents the isotropic velocity. Expression 2.C1 shows that  $v(\psi)$  and  $v(\psi + \pi/2)$  are the fastest and slowest velocities, respectively. Therefore,  $V$  is the anisotropic velocity and the angle between the fast and slow polarization directions is 90 degrees, which corresponds to shear-wave splitting of a plane wave (Crampin, 1985).

CHAPTER 3  
NEAR-SURFACE WEAKENING IN JAPAN AFTER THE 2011 TOHOKU-OKI  
EARTHQUAKE

Published in *Geophysical Research Letters* (2011): 38, L17302

Nori Nakata<sup>1</sup> and Roel Snieder<sup>1</sup>

### 3.1 Summary

The magnitude ( $M_W$ ) 9.0 Tohoku-Oki earthquake on 11 March 2011 was one of the largest in recent history. Ground motion caused by the seismicity around the time of the main shock was recorded by *KiK-net*, the strong-motion network that covers most of Japan. By deconvolving waveforms generated by earthquakes that are recorded at the surface and in a borehole at KiK-net station FKSH18, we detect a reduction of shear-wave velocity in the upper 100 m of about 10%, and a subsequent healing that varies logarithmically with time. Using all available borehole and surface records of more than 300 earthquakes that occurred between 1 January 2011 and 26 May 2011, we observe a reduction in the shear-wave velocity of about 5% in the upper few hundred meters after the Tohoku-Oki earthquake throughout northeastern Japan. The area of the velocity reduction is about 1,200 km wide, which is much wider than earlier studies reporting velocity reductions following other larger earthquakes. The reduction of the shear-wave velocity is an indication that the shear modulus, and hence the shear strength, is reduced over a large part of Japan.

### 3.2 Introduction

The Tohoku-Oki earthquake ( $M_W$ 9.0) of 11 March 2011 is one of the largest earthquakes in recent times. The subduction of the Pacific Plate at a velocity of 8-8.5 cm/year (DeMets

---

<sup>1</sup>Center for Wave Phenomena, Colorado School of Mines

et al., 2010) has resulted in many  $M_W$  7+ earthquakes (Miyazawa and Mori, 2009). Before and after the Tohoku-Oki earthquake, many smaller earthquakes occurred. We use ground motion excited by seismicity recorded by KiK-net (the strong-motion network operated by the National Research Institute for Earth Science and Disaster Prevention (NIED)) to estimate time-lapse changes of the shear-wave velocities in the shallow subsurface throughout northeastern Japan after the Tohoku-Oki earthquake.

To measure shear-wave velocities, we use *seismic interferometry*, developed over the last 10 years (Claerbout, 1968; Trampert et al., 1993; Lobkis and Weaver, 2001; Roux and Fink, 2003; Schuster et al., 2004; Wapenaar, 2004; Bakulin and Calvert, 2006; Snieder et al., 2006b) to determine the arrival time of waves that propagate between two sensors. This technique has been applied to earthquake data in various ways, such as measuring shear-wave velocity (e.g., Snieder and Şafak, 2006; Sawazaki et al., 2009) and estimating deep subsurface structure (e.g., Tonegawa et al., 2009; Ruigrok et al., 2010).

In this paper, we present the time-lapse change of the near-surface shear-wave velocity throughout the east half of Japan after the Tohoku-Oki earthquake. First, we introduce the use of KiK-net data based on seismic interferometry and time interpolation. Then we show the waveforms of one KiK-net station retrieved by seismic interferometry. Finally, we present a shear-wave velocity-change map throughout northeastern Japan.

### **3.3 KiK-net**

About 700 KiK-net stations are distributed across Japan (Okada et al., 2004). Each station has a borehole with three-component strong-motion seismographs at the bottom and top of the borehole. The sampling interval of KiK-net stations is 0.01 s.

We use all available KiK-net stations and seismicity from 1 January 2011 to 26 May 2011. The depths of borehole seismometers are between 100 m and 337 m (91% of the seismometers are at a depth less than 210 m). Magnitude of seismicity is between 2.8 and 9.0. The observed record, as used for seismic interferometry, ranges from 60 s to 300 s depending on the earthquake.

All the used events are at a depth greater than 7 km, which is a relatively large depth compared to the depth of the boreholes. The velocity in the near surface is much slower than it is at greater depths. Because of the depth of events and slow velocities in the near surface, the waves that travel between the sensors at each station propagate in the near-vertical direction. Hence we assume the incoming waves at the receivers are locally near-vertical plane waves. In this study, we use only the north-south horizontal component. Before the data processing, we apply a bandpass filter from 1 to 13 Hz for all earthquake data.

### 3.4 Computing methods

#### 3.4.1 Deconvolution interferometry

Seismic interferometry is a technique to obtain the Green's function that accounts for wave propagation between two stations (Claerbout, 1968; Lobkis and Weaver, 2001; Roux and Fink, 2003; Wapenaar, 2004; Bakulin and Calvert, 2006; Snieder et al., 2006b). Although the widest applied algorithm in seismic interferometry is based on cross correlation (e.g., Claerbout, 1968; Wapenaar, 2004; Bakulin and Calvert, 2004; Schuster et al., 2004), we use the algorithm based on deconvolution (e.g., Trampert et al., 1993; Snieder and Şafak, 2006; Vasconcelos and Snieder, 2008). In deconvolution interferometry, we can suppress the complicated imprint of the structure (e.g., attenuation and scattering) incurred as the waves travel from the hypocenter to the borehole seismogram (Snieder et al., 2009). We denote the wavefield excited by an earthquake at location  $\mathbf{s}$  that strikes the borehole receiver at location  $\mathbf{r}_b$  by  $u(\mathbf{r}_b, \mathbf{s}, \omega)$ , and the wavefield recorded at the surface receiver at location  $\mathbf{r}_s$  by  $u(\mathbf{r}_s, \mathbf{s}, \omega)$  in the frequency domain. The deconvolved waveform is given by

$$D(\omega) = \frac{u(\mathbf{r}_s, \mathbf{s}, \omega)}{u(\mathbf{r}_b, \mathbf{s}, \omega)} \approx \frac{u(\mathbf{r}_s, \mathbf{s}, \omega)u^*(\mathbf{r}_b, \mathbf{s}, \omega)}{|u(\mathbf{r}_b, \mathbf{s}, \omega)|^2 + \epsilon}, \quad (3.1)$$

where  $*$  is the complex conjugate and  $\epsilon$  the regularization parameter that stabilized the deconvolution (Snieder and Şafak, 2006; Mehta et al., 2007c).  $D(\omega)$  is the frequency-domain waveform that propagates from the borehole sensor to the surface sensor (Snieder and Şafak,

2006; Mehta et al., 2007c; Sawazaki et al., 2009; Yamada et al., 2010). We choose  $\epsilon$  to be 1% of the average power spectrum of the wavefield at the borehole receiver because we find experimentally this is the smallest value of the regularization parameter that produces stable deconvolved wavefields.

### 3.4.2 Enhancing time resolution

Because the sampling time of KiK-net seismometers is larger than the changes in the travel time that we seek to measure, we interpolate the deconvolved waveforms and enhance the time resolution. We estimate the arrival time by selecting the three adjacent samples with the largest amplitude and quadratically interpolate between these points. We use the time of the maximum amplitude of the parabola thus obtained as the arrival time of the deconvolved wave. This makes it possible to measure the arrival time with a resolution better than the sampling time. We refer to this procedure as *quadratic interpolation*.

### 3.4.3 Estimating the angle of incidence

We compute the angle of the incoming wave at the borehole receiver by using one-dimensional ray tracing to confirm whether the wave propagating between the borehole and surface sensors propagates vertically. We use the velocity model of Nakajima et al. (2001) to determine the ray parameter  $p$  of the ray that connects each earthquake with the borehole sensor. The angle of incidence  $\theta$  of the wave that propagates between the borehole and surface seismometers is then given by  $\cos \theta = \sqrt{1 - p^2 v^2}$ , where  $v$  is the average shear-wave velocity between these sensors as determined in this study. A bias in the velocity estimation due to non-vertical propagation depends on the deviation from  $\cos \theta$  from its value for vertical incidence,  $\cos 0^\circ = 1$ .

## 3.5 Determining shear-wave velocities throughout northeastern Japan

Figure 3.1a shows deconvolved waveforms of earthquakes between 1 January 2011 and 26 May 2011 for KiK-net station FKSH18 in the Fukushima prefecture at a distance of about

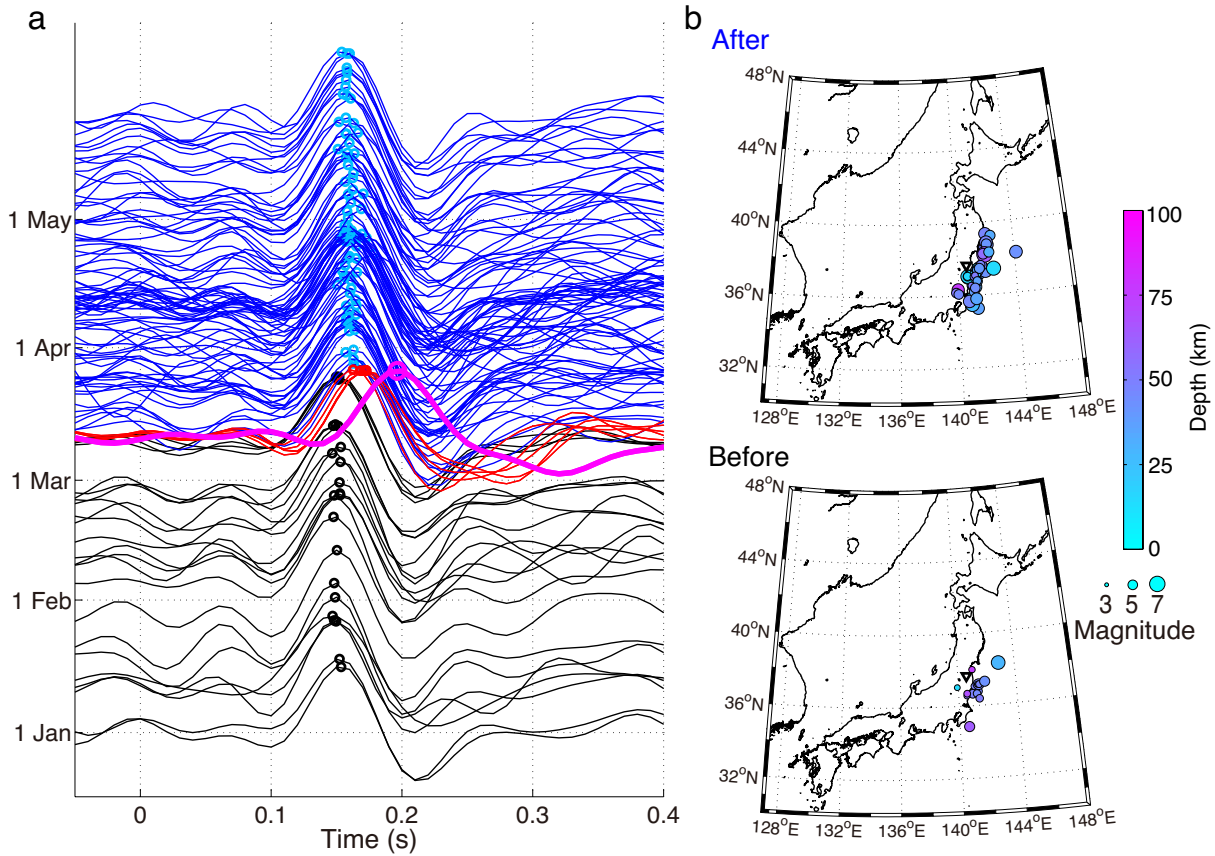


Figure 3.1. (a) Deconvolved waveforms of individual earthquakes from 1 January 2011 to 26 May 2011 at station FKSH18. This station recorded 25 earthquakes from 1 January 2011 to 10 March 2011 (black curves), the Tohoku-Oki earthquake of 11 March 2011 (magenta thick curve), 5 other earthquakes on 11 March 2011 (red curves), and 96 earthquakes from 12 March 2011 to 26 May 2011 (blue curves). Circles, marked by the same color as the waveforms (blue replaces cyan), represent the interpolated arrival times of waves. The waveforms are ordered by the origin times of earthquakes in the vertical axis. (b) Epicenters of two time intervals: 1 January 2011 to 10 March 2011 and 12 March 2011 to 26 May 2011. The size of each circle indicates the magnitude of each earthquake and the color denotes the depth. The white triangle points to the location of station FKSH18.

200 km from the epicenter of the Tohoku-Oki earthquake; Figure 3.1b shows the epicenters of the earthquakes that occurred during the periods before and after the event. The arrival times obtained by quadratic interpolation are shown with circles in Figure 3.1a. The average of  $\cos \theta$  (see section 3.4.3) over the events between 1 January 2011 and 10 March 2011 is 0.984, while between 12 March 2011 to 26 May 2011 this average is equal to 0.980. This implies that the bias in the estimated shear-wave velocity is only about 2%, but this bias is virtually identical in the periods before and after the Tohoku-Oki earthquake. Hence changes in the pattern of seismicity before and after the main shock are not responsible of the change in the shear-wave velocity that we present. To enhance the data quality, we discard some data which has a low signal-to-noise ratio based on a visual inspection.

The travel time measured during the main shock of the Tohoku-Oki earthquake (the large magenta circle in Figure 3.1a) is significantly later than that from the other earthquakes. This indicates a reduction of the shear-wave velocity of about 22% during the shaking caused by the Tohoku-Oki event. Note also the delay of the waves in the early aftershocks indicated in red in Figure 3.1a. The delay of the waveforms after the Tohoku-Oki earthquake relative to the waveforms recorded before the event indicates that the shear waves propagate with a reduced shear-wave velocity after the Tohoku-Oki earthquake (Figure 3.1a).

Figure 3.2 depicts the travel-time change during the shaking caused by the Tohoku-Oki earthquake by applying short-time moving-window seismic interferometry to the seismogram, in which we deconvolve 20-s time windowed borehole and surface records at station FKSH18. Since the time window moves with 10-s intervals, the windows have a 10-s overlap. The main delay occurs at 30-40 s, and it is increasing while the shaking increases. After the strongest shaking (at 130 s), the travel times recover and are fairly constant. Note that the delay, as well as the shear-wave velocity reduction, remains nonzero after 200 s compared to its values between 0-20 s. The velocity reduction at the time of strong shaking is likely to be influenced by several physical mechanisms including incipient liquefaction.

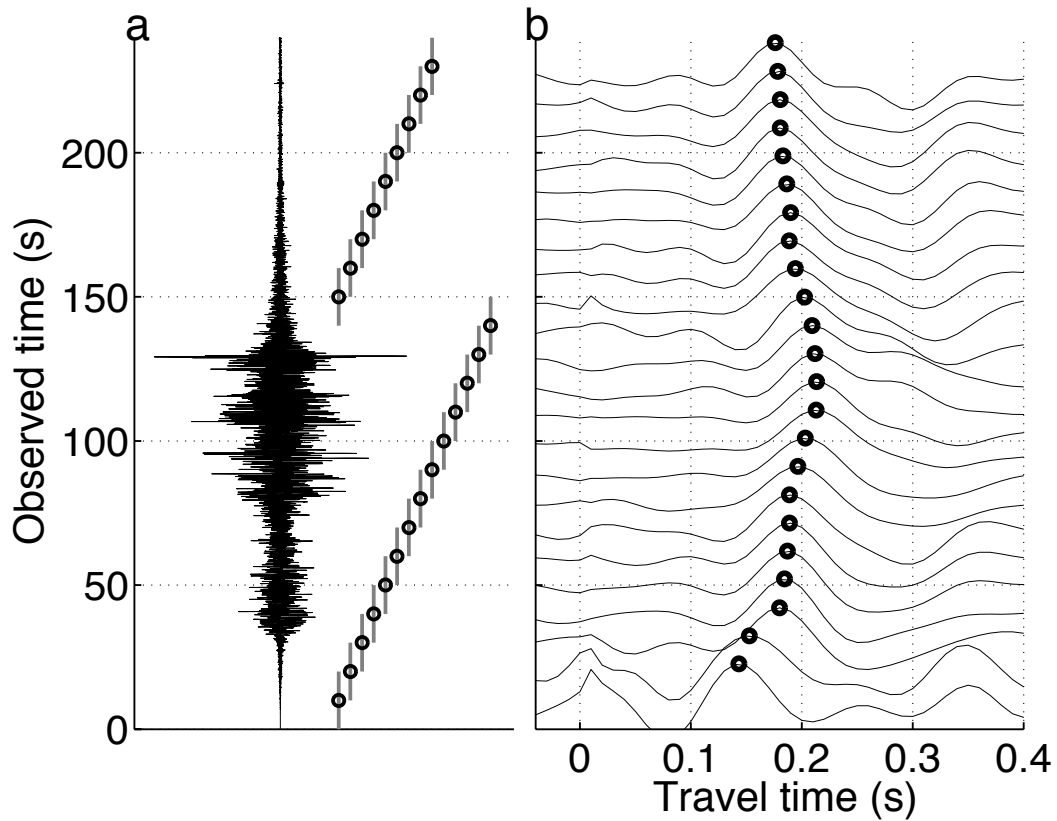


Figure 3.2. Short-time moving-window seismic interferometry of the ground motion caused by the Tohoku-Oki earthquake. (a) The earthquake record observed at the north-south horizontal component borehole seismometer of station FKSH18. Gray bars indicate the 20-s time windows for seismic interferometry with 10-s overlap. Black circles are the center of each window. (b) Deconvolved waveforms of each time window. Each waveform is aligned with the center time of the employed time window. Black circles illustrate the interpolated arrival times.

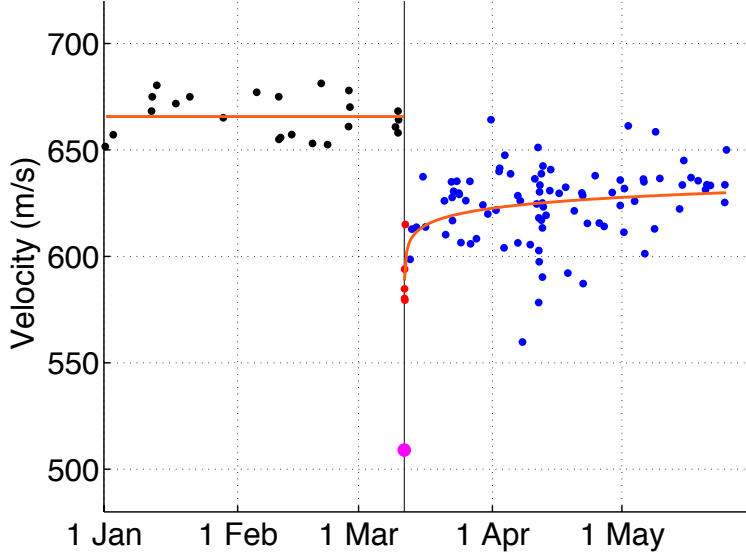


Figure 3.3. Shear-wave velocity variations in the upper 100 m at station FKSH18. By using the arrival times of waves (the circles in Figure 3.1), we compute the velocity variations from 1 January 2011 to 26 May 2011. The color of each dot is the same as in Figure 3.1. Black vertical line indicates the origin time of the Tohoku-Oki earthquake. Orange line depicts the average velocity (before the Tohoku-Oki earthquake) and the logarithm curve determined by least-squares fitting of the velocity after the earthquake. We do not include the Tohoku-Oki earthquake data point (magenta dot) in the data fit.

We compute the shear-wave velocity as a function of time from the interpolated travel times (the circles in Figure 3.1) using the known depth of the borehole. Figure 3.3 shows the shear-wave velocity estimated from each earthquake at station FSKH18. According to Figure 3.3, the velocity is reduced by almost 10% on the day after the Tohoku-Oki earthquake and the velocity recovers with about 5% in the 2 months after the earthquake. As shown by the orange curve in Figure 3.3, the shear-wave velocity after the Tohoku-Oki earthquake recovers logarithmically with time (Dieterich, 1972; Vidale and Li, 2003; Schaff and Beroza, 2004),  $v_s(t) = a \ln(t - t_0) + b$ , where  $t_0$  is the origin time of the Tohoku-Oki event, and  $t$  is time measured in days. We determine the parameters  $a$  and  $b$  by a linear least-squares fit of the data points shown by the red and blue dots in Figure 3.3. We exclude the data point of the Tohoku-Oki earthquake (the large magenta dot in Figure 3.3) in the estimation of the orange recovery curve in Figure 3.3 because the anomalously low velocity during the shaking by the

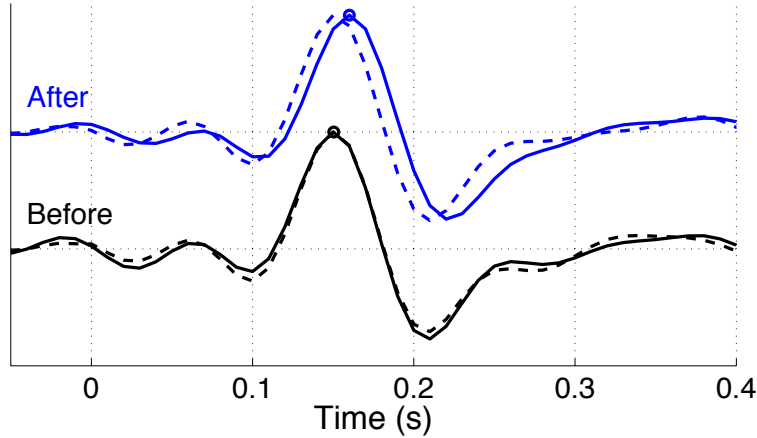


Figure 3.4. Averaged waveforms of Figure 3.1 before (from 1 January 2011 to 10 March 2011; black solid curve) and after (from 12 March 2011 to 26 May 2011; blue solid curve) the Tohoku-Oki earthquake at station FKSH18. Circles denote the interpolated arrival times of averaged waves. Black and blue dashed curves represent the averaged waveforms from 1 January to 10 March and from 12 March to 26 May over 11 years (from 2000 to 2010), respectively.

Tohoku-Oki event may be caused by a complex physical mechanism mentioned above.

We compute the average of the deconvolved waveforms for station FKSH18 over the periods 1 January - 10 March (before) and 12 March - 26 May (after) in 2011 of Figure 3.1. These average waveforms are shown by the solid lines in Figure 3.4. The shapes of the average deconvolved waveforms before and after the Tohoku-Oki earthquake are similar, but the average waveform after the Tohoku-Oki earthquake is delayed. We also determine the average shear-wave velocities before and after the Tohoku-Oki earthquake from the interpolated travel times (the circles in Figure 3.4). The average velocity in the time interval before the Tohoku-Oki earthquake is  $665 \pm 7$  m/s, and after the event it is  $625 \pm 14$  m/s, hence the average velocity reduction is about 6%. The uncertainty of the velocities is determined from the standard deviations of the travel times over all events in each time interval.

It has been documented that the shear-wave velocity in the near surface may exhibit seasonal changes associated with changes in precipitation (Sens-Schönfelder and Wegler, 2006). In order to investigate the influence of seasonal changes, we compute the mean shear-wave velocities in the periods 1 January - 10 March and 12 March - 26 May averaged over

all years from 2000 to 2010. The corresponding waveforms are shown by the dashed lines in Figure 3.4. The mean velocity over the period 1 January - 10 March averaged from 2000-2010 is  $664 \pm 6$  m/s, and the mean velocity for the interval 12 March - 26 May is  $661 \pm 6$  m/s. The difference between these values is statistically not significant, and it is much smaller than the measured velocity change associated with the Tohoku-Oki earthquake.

We average the deconvolved waves at each KiK-net station over earthquakes recorded in the time intervals before (from 1 January 2011 to 10 March 2011) and after (from 12 March 2011 to 26 May 2011) the Tohoku-Oki event to determine the arrival times of the average deconvolved waveforms at each KiK-net station that are the travel time of the shear wave that propagates between the seismometers in the borehole and at the surface of each station. These times thus constrain the near-surface shear-wave velocity between the seismometers. We convert this travel time to the shear-wave velocity in the near-surface at each station, and following spatial interpolation (Lawson, 1984) of the velocities between stations, we obtain near-surface shear-wave velocity maps before (the upper-left map in Figure 3.5) and after (the middle map in Figure 3.5) the Tohoku-Oki earthquake. In order to reduce the uncertainty in the velocity estimates, we use only stations that recorded more than 3 earthquakes during both time intervals. The average  $\cos \theta$  is greater than 0.975 but in the west side of the area  $\cos \theta \approx 0.94 - 0.96$ . These values are fairly constant in the time periods before and after the Tohoku-Oki earthquake. We use recorded data from 83 and 219 earthquakes, respectively, to create shear-wave velocity maps for the time intervals before and after the Tohoku-Oki earthquake. By subtracting the velocity measured before the main event from the velocity measured after the event, we obtain the map of the relative velocity change before and after the Tohoku-Oki earthquake shown in the lower-right map of Figure 3.5.

### 3.6 Discussion and Conclusions

It is known that large earthquakes can reduce seismic velocities close to the epicenter (e.g., Li et al., 1998; Vidale and Li, 2003; Schaff and Beroza, 2004; Wegler and Sens-Schönfelder, 2007; Brenguier et al., 2008; Sawazaki et al., 2009; Yamada et al., 2010). As shown in Figure

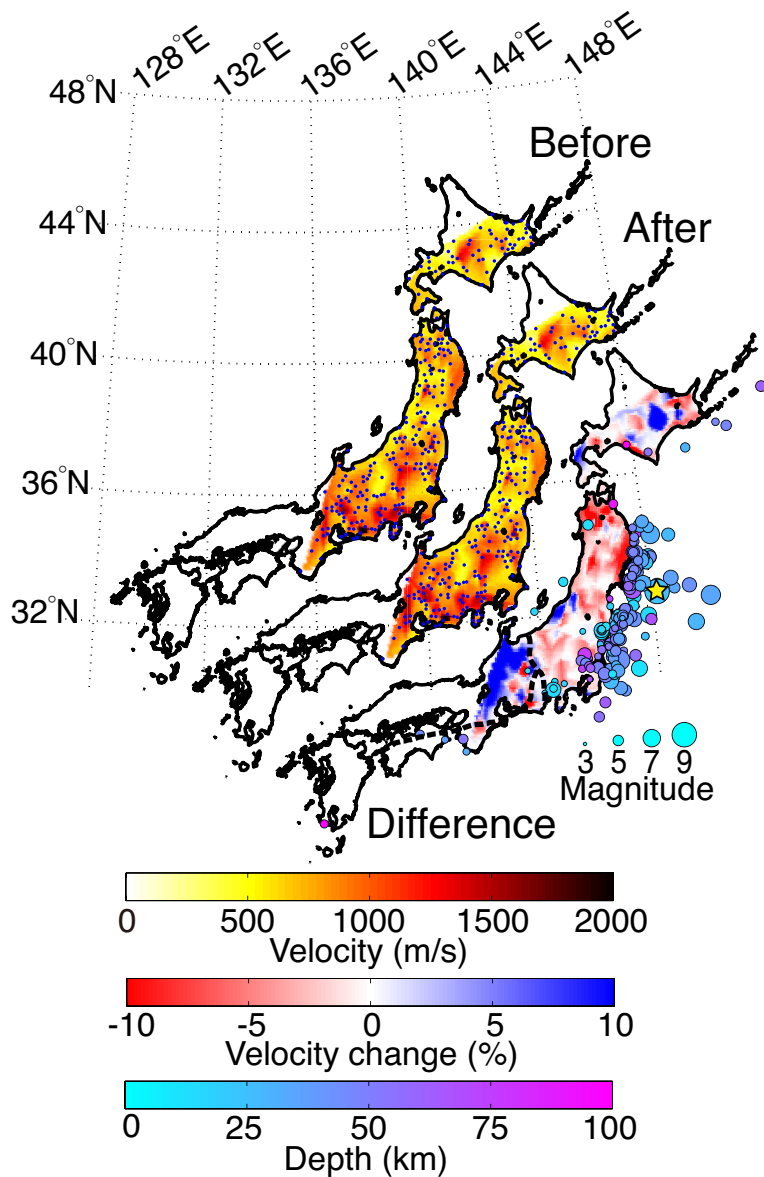


Figure 3.5. Shear-wave velocities estimated from deconvolved waveforms before (upper-left) and after (middle) the Tohoku-Oki earthquake. Blue dots on these two maps show the KiK-net stations used in this study. The map on the lower-right gives the relative change in shear-wave velocity before and after the event. The longitude and latitude belong to the map in the upper-left. Locations and magnitude of the earthquakes from 1 January 2011 to 26 May 2011 are shown as circles, relative to the map on the lower-right. The size of each circle indicates the magnitude of each earthquake and the color represents the depth. The yellow star denotes the location of the Tohoku-Oki earthquake. The dashed black lines show the locations of MTL and ISTL (Ito et al., 1996).

3.5, the shear-wave velocity was reduced by about 5% after the Tohoku-Oki earthquake over an area in northeastern Japan about 1,200 km wide, which is much larger than the region of velocity reduction after the earthquakes reported in earlier studies. We also measured the mean shear-wave velocity reduction in these time intervals over the period from 2000 to 2010 of the whole area shown in the maps in Figure 3.5. The seasonal change in the shear-wave velocity is only 0.2%, which is much smaller than the velocity reduction observed following the Tohoku-Oki earthquake (see the lower-right map of Figure 3.5). We conclude that the shear-wave velocity reduction in Figure 3.5 is caused by the Tohoku-Oki earthquake. The area with reduced shear-wave velocity is delimited on the western side by the Median Tectonic Line (MTL) and the Itoigawa-Shizuoka Tectonic Line (ISTL) (the dashed black lines on the lower-right map in Figure 3.5). Because the number of recorded earthquakes at the west side of these tectonic lines is small, between 3 and 5, and the average of  $\cos\theta$  is relatively low (around 0.94-0.96), the velocities in the western part are less reliable than those in other regions. The velocity reduction of Figure 3.5 does not correlate with the coseismic or postseismic displacements of the Tohoku-Oki earthquake (Ozawa et al., 2011) because the velocity reduction is also influenced by variations in local geology.

With seismic interferometry, we extract the waves that propagate between the borehole and surface seismometers at KiK-net stations, and find a significant reduction of the near-surface shear-wave velocity after the Tohoku-Oki earthquake that recovers logarithmically with time. By applying this analysis to all available seismograms, we detect a reduction of the shear-wave velocity in the upper few hundred meters throughout the eastern half of Japan. The shear-wave velocity is related to the shear modulus; hence the reduction of the shear-wave velocity over northeastern Japan implies that the Tohoku-Oki earthquake reduced the shear strength of the near surface throughout northeastern Japan.

### 3.7 Acknowledgments

We thank NIED for providing us with the KiK-net data. We are grateful to the editor, David Schaff, and one anonymous reviewer for suggestions, corrections, and discussions.

CHAPTER 4  
TIME-LAPSE CHANGE IN ANISOTROPY IN JAPAN'S NEAR SURFACE CAUSED  
BY THE 2011 TOHOKU-OKI EARTHQUAKE

Published in *Geophysical Research Letters* (2012): 39, L11313

Nori Nakata<sup>1</sup> and Roel Snieder<sup>1</sup>

#### 4.1 Summary

We apply seismic interferometry to strong-motion records to detect the near-surface (i.e., an upper few hundred meters deep) change in anisotropy caused by the  $M_W$  9.0 Tohoku-Oki earthquake on 11 March 2011. We show that the earthquake increased the difference between fast and slow shear-wave velocities arising from shear-wave splitting in most parts of northeastern Japan, but it did not significantly change fast shear-wave polarization directions in the near surface. Through monitoring of anisotropy and shear-wave velocity, we find that the changes in anisotropy and velocity partially recover with time; they are, however, still different from the pre-event values after nine months. The comparison of the spatial distribution between changes in anisotropy and velocity indicates the changes in anisotropy and velocity are generally correlated, especially in the northeastern Honshu (the main island in Japan). The change in the largest principal stress direction weakly correlates with the change in anisotropy.

#### 4.2 Introduction

The change in near-surface shear-wave velocity caused by the  $M_W$  9.0 Tohoku-Oki earthquake on 11 March 2011 is documented by Nakata and Snieder (2011). The earthquake, among the largest in recent history, resulted in a reduction in the near-surface velocity averaged over two months following the earthquake of about 5% throughout northeastern Japan

---

<sup>1</sup>Center for Wave Phenomena, Colorado School of Mines

(a region 1,200 km wide). In this study, we estimate the change in near-surface polarization anisotropy by applying seismic interferometry to seismograms recorded by KiK-net, a strong-motion recording network operated by the National Research Institute for Earth Science and Disaster Prevention (NIED).

Conventionally, shear-wave splitting is estimated by the cross-correlation method (e.g., Fukao, 1984). One can estimate the fast and slow shear-wave polarization directions and the delay time between the fast and slow shear waves, which are mean values along a ray path. Moreover, using a cluster of earthquakes, one can estimate the vertical variation of anisotropy (e.g., Okada et al., 1995).

Some studies discover that both the polarization directions and the splitting time change after large earthquakes (e.g., Tadokoro et al., 1999). In contrast, quite a few studies report no clear temporal change following major earthquakes (e.g., Cochran et al., 2003; Peng and Ben-Zion, 2005; Cochran et al., 2006). Other studies have found that the splitting time increases after intermediate or large earthquakes, but the polarization directions do not change (e.g., Saiga et al., 2003; Liu et al., 2004) because the splitting time is more sensitive to change in stress than the polarization direction is (Peacock et al., 1988). Since changes in splitting times have been observed prior to major earthquakes (e.g., Peacock et al., 1988; Crampin et al., 1990; Crampin and Gao, 2005), monitoring the splitting time has been proposed as a diagnostic for earthquake prediction (Crampin et al., 1984b).

We present the change in anisotropy based on shear-wave splitting caused by the Tohoku-Oki earthquake inferred from seismic interferometry. First, we show shear-wave splitting at one KiK-net station. Then we compute changes in polarization anisotropy after the main event for all available stations and compare with the changes in shear-wave velocity and the largest principal stress direction caused by the main shock.

### 4.3 Earthquake records and the analyzing method

#### 4.3.1 KiK-net

KiK-net, which includes about 700 stations all over Japan, has recorded strong motions continuously since the end of the 1990s (Okada et al., 2004). Each KiK-net station has a borehole a few hundred meters deep and two three-component seismographs, with a 0.01-s sampling interval, at the top and bottom of the borehole. In this study, we use the stations which have the borehole sensor at a depth between 100–337 m, and 91% of the receivers are at a depth less than 210 m. All the earthquakes used here are at a depth greater than 7 km, which is large compared to the depth of the boreholes. The velocity in the near surface is much slower than at greater depths. Since we consider events much deeper than the borehole, and because of the slow velocities at the near surface, we assume the waves propagate from the borehole to the surface receivers as plane waves in the vertical direction at each station.

To confirm this assumption, we compute the angle of incidence  $\theta$  by employing the procedure proposed by Nakata and Snieder (2012a) using ray tracing. All earthquake data used have  $\cos \theta > 0.975$ , which means the maximum of the estimated velocity bias is 2.5%. The bias is, in practice, much smaller because of the employed averaging over many earthquakes. This inaccuracy does not contribute to the estimated shear-wave splitting because  $\cos \theta$  is the same for the waves in all polarization directions.

#### 4.3.2 Seismic interferometry

By applying deconvolution-based seismic interferometry to the seismograms of each station, in which we deconvolve the seismogram at a surface receiver with that at a borehole receiver, we retrieve the wave propagating from the borehole receiver to the surface receiver (Nakata and Snieder, 2011), and then we apply a bandpass filter from 1 to 13 Hz to deconvolved waveforms. To estimate the fast and slow polarization directions resulting from shear-wave splitting, we follow the seismic-interferometry approach of Miyazawa et al. (2008). First, we rotate the seismograms recorded at the surface and borehole sensors in 10-

degree increments in polarization. We then deconvolve the waveforms for each polarization direction to extract the shear wave that propagates from the borehole receiver to the surface receiver. We chose to use an increment of 10 degrees because when we computed the shear-wave splitting for 10 stations with an increment of one degree, the estimated anisotropy was the same as we obtained using an increment of 10 degrees. Based on the travel times for the propagating waves, we calculate the shear-wave velocities in each polarization using the known depth of the borehole. To find the travel times, we pick the three adjacent samples that have the largest amplitude and interpolate using a quadratic function since the sampling interval is not small enough to estimate the changes in the travel time caused by an earthquake (Nakata and Snieder, 2012a).

Comparing the travel times as a function of polarization and interpolating the arrival time and the polarization direction using a quadratic function, we estimate the fast and slow shear-wave velocities and polarization directions at the near surface, and then separate the obtained shear-wave velocity into one velocity averaged over direction (i.e., isotropic velocity) and direction-dependent velocity (i.e., anisotropic velocity) using Fourier series (Nakata and Snieder, 2012a).

A part of the controversy that major earthquakes do or do not change anisotropy comes from the differences of ray paths of smaller earthquakes used for analyzing polarization anisotropy (Peng and Ben-Zion, 2005). By applying seismic interferometry, we estimate the polarization direction and the strength of anisotropy averaged over a top few-hundred meter (very shallow zone compared to other studies) for the fixed vertical path between the borehole and surface sensors.

The method proposed by Liu et al. (2004) can be also used to estimate the travel times of the fast and slow shear waves by using waves that reflect off the free surface and propagate back to the borehole receiver. However, because their method uses reflected waves recorded at the borehole sensor and computes the autocorrelation of the borehole record, one cannot eliminate the imprint of the power spectrum of the incoming wave; hence the autocorrelated

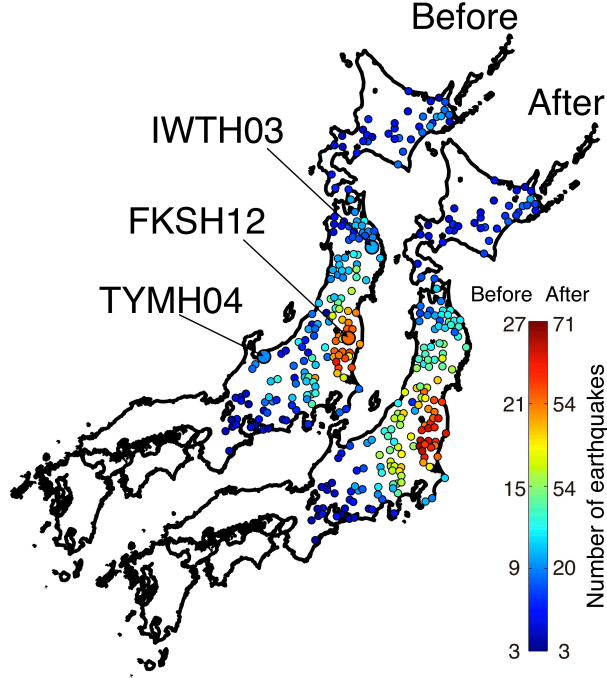


Figure 4.1. Number of earthquakes used in the study at each station before (left: 1 January 2011 to 10 March 2011) and after (right: 12 March 2011 to 26 May 2011) the Tohoku-Oki earthquake. The color represents the number of earthquakes. Three stations (FKSH12, IWTH03, and TYMH04) used in Figure 4.2 and Figure 4.3 are pointed.

waves can be contaminated by variations in the power spectrum of the incident waves. In contrast, our method uses the direct wave for the deconvolution, so that we can cancel the imprint of the incoming wave, thus allowing for more accurate measurements of the travel times of the fast and slow shear waves.

#### 4.4 The change in anisotropy caused by the Tohoku-Oki earthquake

We first present earthquake records of KiK-net station FKSH12, which is in the Fukushima prefecture (220 km west-southwest from the main-shock epicenter: Figure 4.1). Earthquakes used here were recorded from 1 May 2010 to 31 December 2011, the magnitude range is confined from 3.0 to 9.0. We compute the isotropic shear-wave velocities and the anisotropy coefficients,  $(v_{fast} - v_{slow})/v_{fast}$  (where  $v_{fast}$  and  $v_{slow}$  are the fast and slow velocities, respectively), of each earthquake (Figure 4.2). Figure 4.3 illustrates time variations of the velocities and the anisotropy coefficients at stations IWTH03 and TYMH04 from 1 January

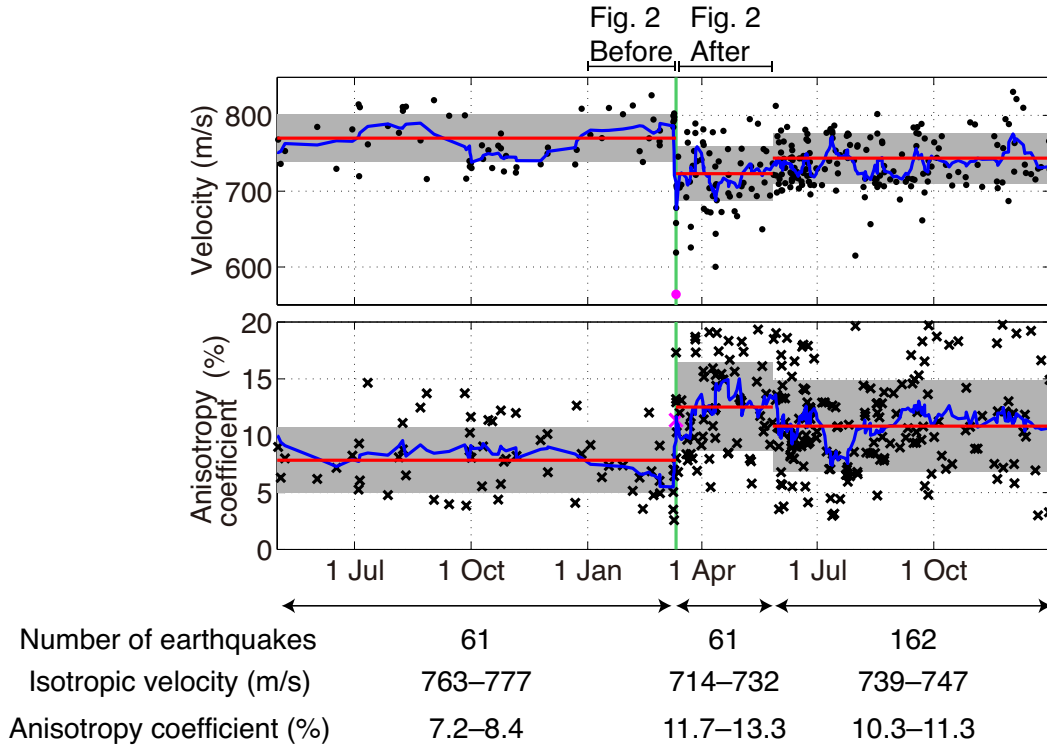


Figure 4.2. Variation in shear-wave velocity and anisotropy coefficient from 1 May 2010 to 31 December 2011 at station FKSH12. The top panel depicts the isotropic velocity of each earthquake (black dot) and its nine-point moving average (blue line). The bottom panel indicates the anisotropy coefficient computed from fast and slow shear-wave velocities (black cross) and its nine-point moving average (blue line). The velocity and the anisotropy coefficient estimated from the main event are illustrated by magenta symbols. Green vertical lines denote the origin time of the event. Red horizontal lines and gray shaded areas are the mean values and the mean values  $\pm$  the standard deviations of the measurements of all used earthquakes during each period. We show the number of earthquakes used and mean values of each period at the bottom. The range of each value is the 95% confidence interval of the mean. The bars at the top of the figure illustrate the time intervals used in Figure 4.4.

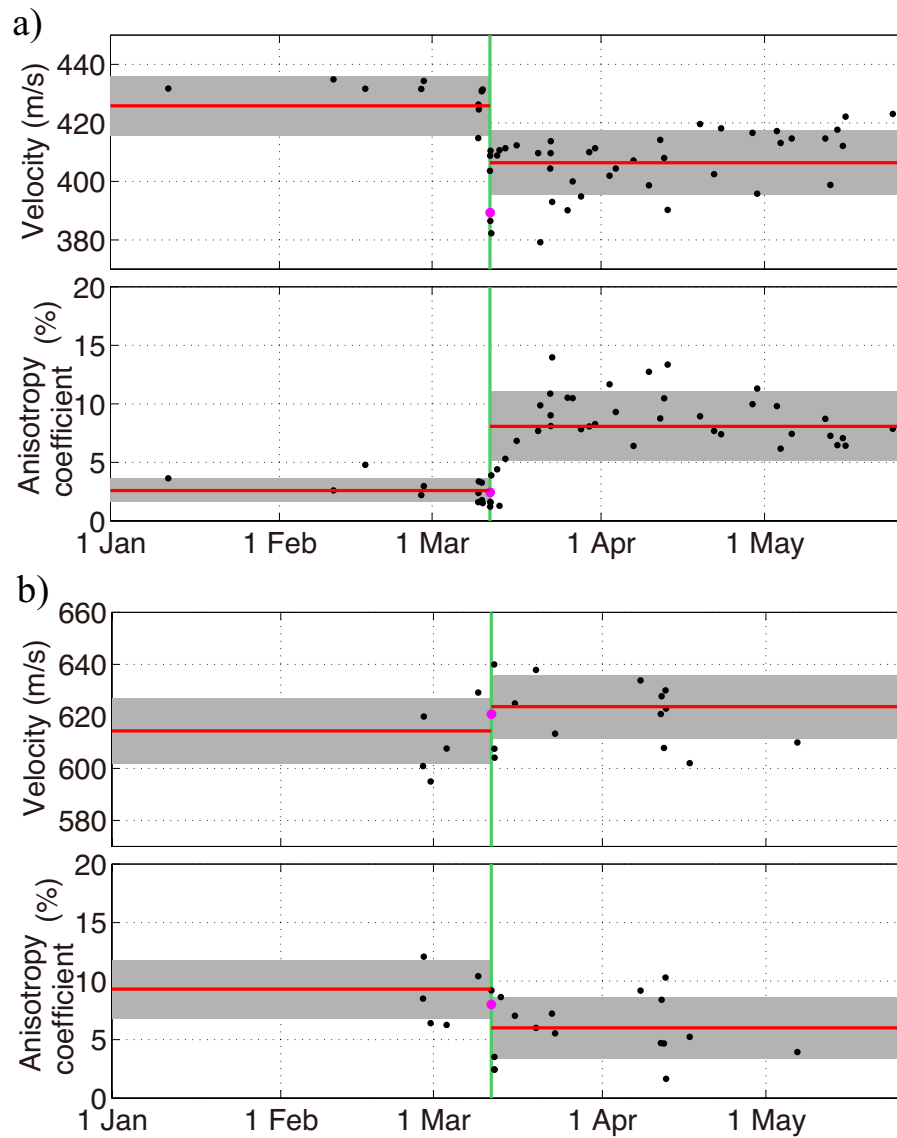


Figure 4.3. Variation in shear-wave velocity and anisotropy coefficient from 1 January 2011 to 26 May 2011 at (a) station IWTH03 and (b) station TYMH04 (see Figure 4.1 for locations of the stations). In each panel, the top and bottom subpanels illustrate the isotropic velocity (black dot) and the anisotropy coefficient (black cross) of each earthquake, respectively. The velocity and the anisotropy coefficient estimated from the main event are illustrated by magenta symbols. The green vertical lines denote the origin time of the event. The red horizontal lines are the mean values of all used earthquakes in each period.

2011 to 26 May 2011.

At the bottom of Figure 4.2, we show the mean values of isotropic shear-wave velocities and anisotropy coefficients during the periods of 1 May 2010–10 March 2011, 12 March 2011–26 May 2011, and 27 May 2011–31 December 2011. The range of each value is the 95% confidence interval of the mean, and it is different from the gray shaded areas in Figure 4.2. The gray shaded areas indicate the mean values  $\pm$  one standard deviation of the measurement. Based on Student's *t*-test (e.g., Bulmer, 1979), the mean velocities and mean anisotropy coefficients are significantly different between each consecutive pair of periods (Probability  $> 99.7\%$ ). After the main shock, the shear-wave velocity decreases (6%) and the anisotropy coefficient increases (60%), and these changes partially recover with time (mean velocity: 770 $\rightarrow$ 723 $\rightarrow$ 743 m/s and mean anisotropy coefficient: 7.8 $\rightarrow$ 12.5 $\rightarrow$ 10.8%). Nakata and Snieder (2011) discuss the change in the shear-wave velocity caused by the Tohoku-Oki earthquake. Because the fluid condition in cracks is one major cause of anisotropy (Crampin et al., 1984a), large and intermediate earthquakes, which induce a stress change to open or close cracks (Nur and Simmons, 1969) and extend cracks (Atkinson, 1984), can change the anisotropy coefficient.

As shown by the moving average of the anisotropy coefficient (the blue line in the bottom panel of Figure 4.2), the anisotropy coefficient continues to increase for more than one month after the main shock, which might be caused by several large aftershocks during that period; the gradual increase is, however, not statistically significant. In contrast, the velocity decreases suddenly at the time of the main shock (see the blue line in the top panel of Figure 4.2).

The moving average of the anisotropy coefficient decreases before the main shock (the blue line in the bottom panel of Figure 4.2), but it is not as significant as the changes between each pair of periods. Although some studies report changes in anisotropy before large earthquakes (e.g., Crampin et al., 1990; Crampin and Gao, 2005), we need to consider the influence of intermediate earthquakes that occur before the main shock; such events

may change the anisotropy as well. For example, the M6.2 earthquake on 13 June 2010 (a distance of 100 km and a depth of 40 km from station FKSH12) and the M5.7 earthquake on 29 September 2010 (a distance of 40 km and a depth of 8 km from the station) might both have been sources of elevated the anisotropy coefficient. The absence of such intermediate events in the nine weeks before the main earthquake near the station could have caused the observed reduction of the anisotropy coefficient in that period.

We estimate the fast polarization directions and the anisotropy coefficient for all available stations throughout Japan for a period before the main earthquake (1 January 2011–10 March 2011) and a period afterward (12 March 2011–26 May 2011) (Figure 4.4). To reduce uncertainty, we use only stations that have 1) more than three earthquake records during both time intervals, 2) travel times of interferometric waves greater than 0.1 s, 3) anisotropy coefficients greater than 1%, and 4) a standard deviation of velocity measurements smaller than 5%. The average change in the angles of the fast shear-wave polarization directions before and after the main event over all used stations is 17 degrees (Figure 4.5); this is close to the uncertainty, 15 degrees, computed from data over 11 years (Nakata and Snieder, 2012a). We conclude that the fast shear-wave polarization direction does not change significantly as a result of the main shock.

In contrast, the anisotropy coefficient in most parts of northeastern Japan increases after the earthquake. To evaluate the change in the anisotropy coefficient caused by the event, we define the change in anisotropy as  $(AC_{after} - AC_{before})/AC_{before}$ , where  $AC_{before}$  and  $AC_{after}$  are the anisotropy coefficients before and after the main shock, respectively. The change in the anisotropy coefficient is shown in the second map from right in Figure 4.4. In Figure 4.6, we show a crossplot of the changes in the shear-wave velocity and the anisotropy coefficient in four regions defined by the small map in Figure 4.4. The changes are reasonably well correlated in region II and poorly correlated in region I. Different from other regions, most measurements in region IV are in the lower-right quadrant where the velocity increases and the anisotropy coefficient decreases. Region IV is on the west side of the tectonic lines (the

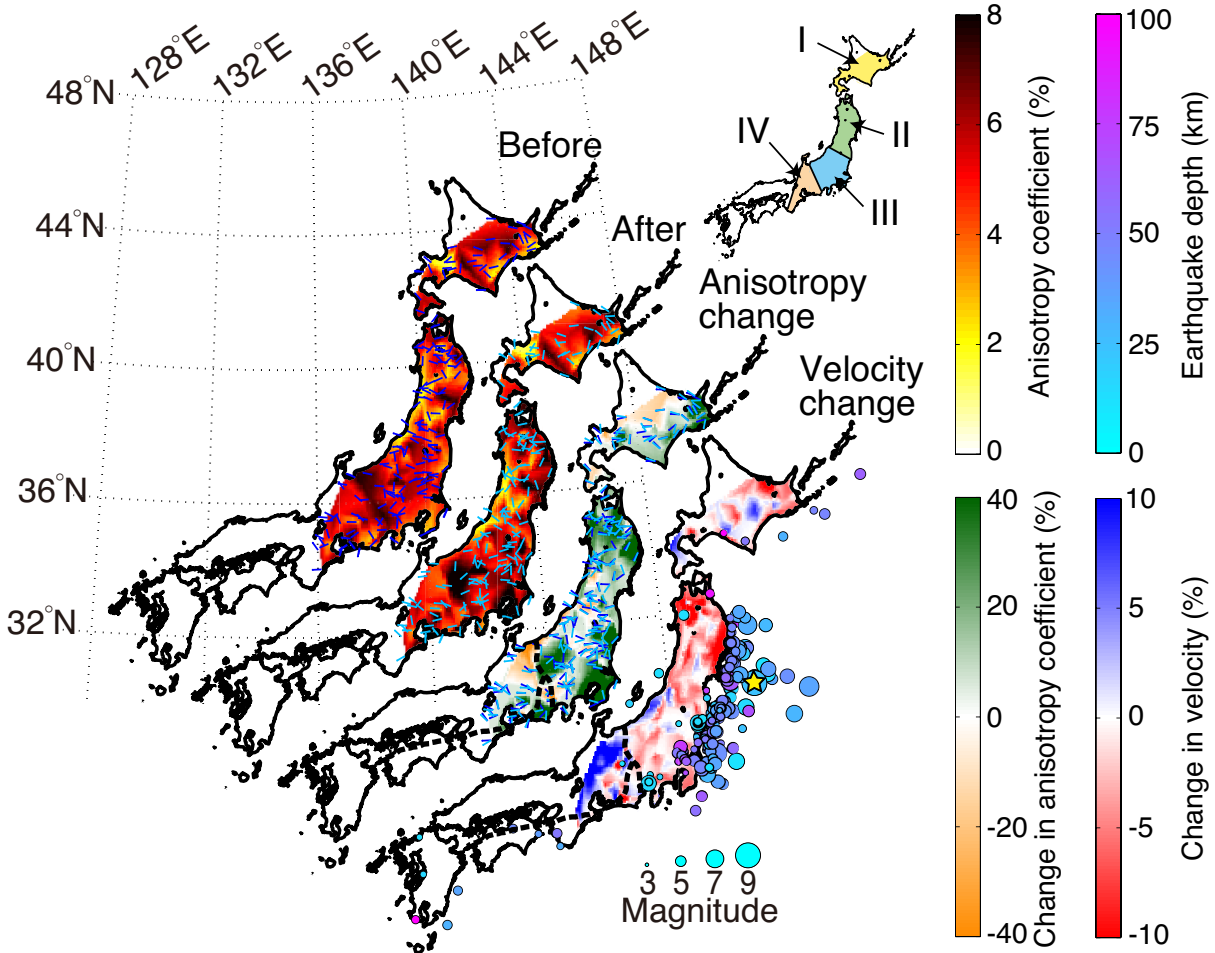


Figure 4.4. Changes in shear-wave velocity and anisotropy coefficient after the Tohoku-Oki earthquake. Each map has a label at upper-right: anisotropy coefficients before (Before: 1 January 2011 to 10 March 2011) and after (After: 12 March 2011 to 26 May 2011) the Tohoku-Oki earthquake, its change, defined as  $(AC_{after} - AC_{before})/AC_{before}$  (Anisotropy change), and the change in the isotropic shear-wave velocity (Velocity change). Dark blue (before) and light blue (after) arrows on the Before, After, and Anisotropy-change maps represent the direction of fast shear-wave polarization. We plot polarization-direction arrows without the change in the anisotropy coefficient in Figure 4.5. The longitude and latitude pertain to the leftmost map. The dashed black lines show the locations of major tectonic lines (the Median Tectonic Line and the Itoigawa-Shizuoka Tectonic Line) (Ito et al., 1996). Locations and magnitude of the earthquakes from 1 January 2011 to 26 May 2011 are shown as circles and relative to the rightmost map. The size of each circle indicates the magnitude of each earthquake and the color represents its depth. The yellow star denotes the epicenter of the Tohoku-Oki earthquake. The small Japanese map at the top shows four regions for interpretation in Figure 4.6.

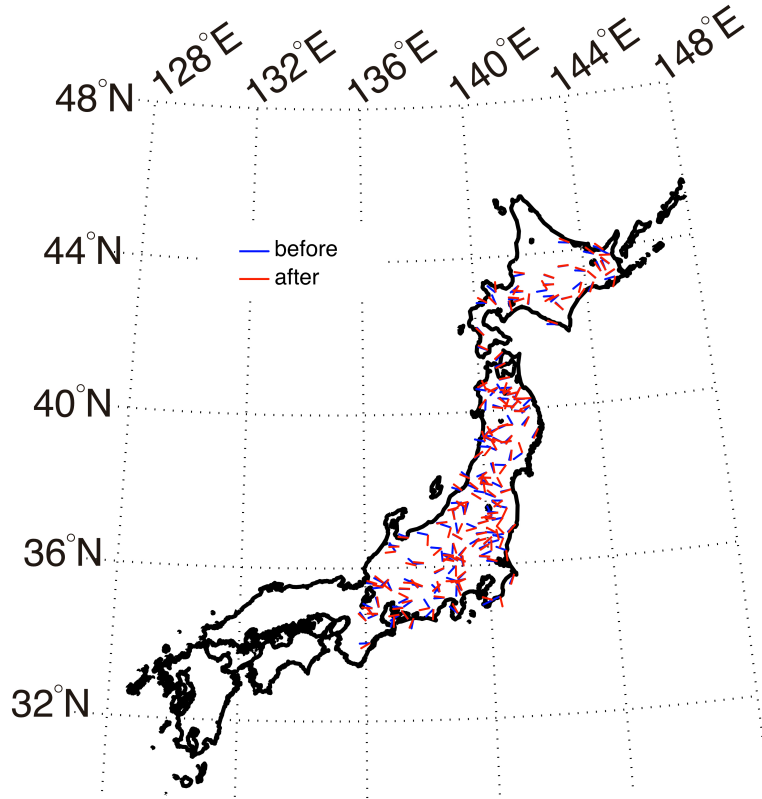


Figure 4.5. Directions of fast shear-wave polarization before (blue arrow: 1 January 2011 to 10 March 2011) and after (red arrow: 12 March 2011 to 26 May 2011) the Tohoku-Oki earthquake.

Median Tectonic Line and the Itoigawa-Shizuoka Tectonic Line: the black dashed lines in Figure 4.4), and the geologic age and the geomorphological classification both differ across these lines; the west side is an older mountain area and the east side consists of younger volcanics and sediments (Wakamatsu et al., 2006).

#### 4.5 Comparing the changes in anisotropy and static stress

Changes in stress caused by intermediate and large earthquakes have been studied for decades (e.g., Hanks, 1977; King et al., 1994; Baltay et al., 2010). The Tohoku-Oki earthquake changed the stress and strain conditions (Hasegawa et al., 2011). Changes in stress and strain induce changes in local permeability and pore pressure (Koizumi et al., 1996),

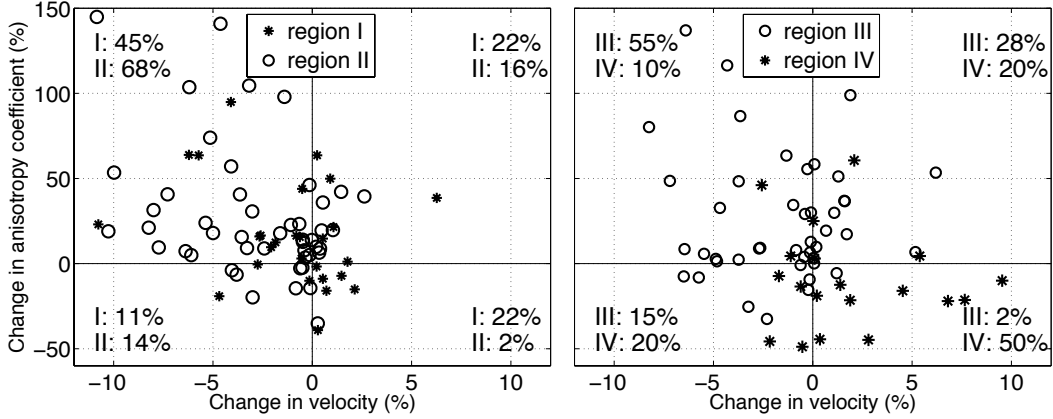


Figure 4.6. Crossplot of the changes in shear-wave velocity and anisotropy coefficient in the regions. Each symbol indicates the data of each station. The numbers in the corners of each panel show the fraction of stations in each quadrant of all stations in each region.

and thereby changes in the anisotropy coefficient (Zatsepin and Crampin, 1997). Fluid-filled microcracks, which cause shear-wave splitting (Zatsepin and Crampin, 1997), usually align with the direction of *in situ* stress (Crampin, 1978). Saiga et al. (2003) compare at two stations the time delays associated with shear-wave splitting with the change in the Coulomb stress, which is an indicator of how close a fault is to failure (e.g., King et al., 1994). Toda et al. (2011) and Yoshida et al. (2012) compute the change in stress in northeastern Japan caused by the Tohoku-Oki earthquake.

We compare the change in the anisotropy coefficient with the change in the largest principal stress direction computed by Yoshida et al. (2012) who used the damped stress tensor inversion method (Figure 4.7). We use this change as a proxy for changes in the stress. Since we do not know how the change in principal stress direction is related to the orientation of microfractures, which may either close or open in response to the change in stress, we cannot compute the change in anisotropy because of the change in stress. In Figure 4.7b, the changes in the largest principal stress direction and the anisotropy coefficient, which are both averaged over a  $0.5^\circ$  grid, indicate a weak positive correlation except for areas B, J, K, and L. A large change in the principal stress direction ( $> 20^\circ$ ) signifies that the stress condition before and after the main shock is significantly different; therefore a large change

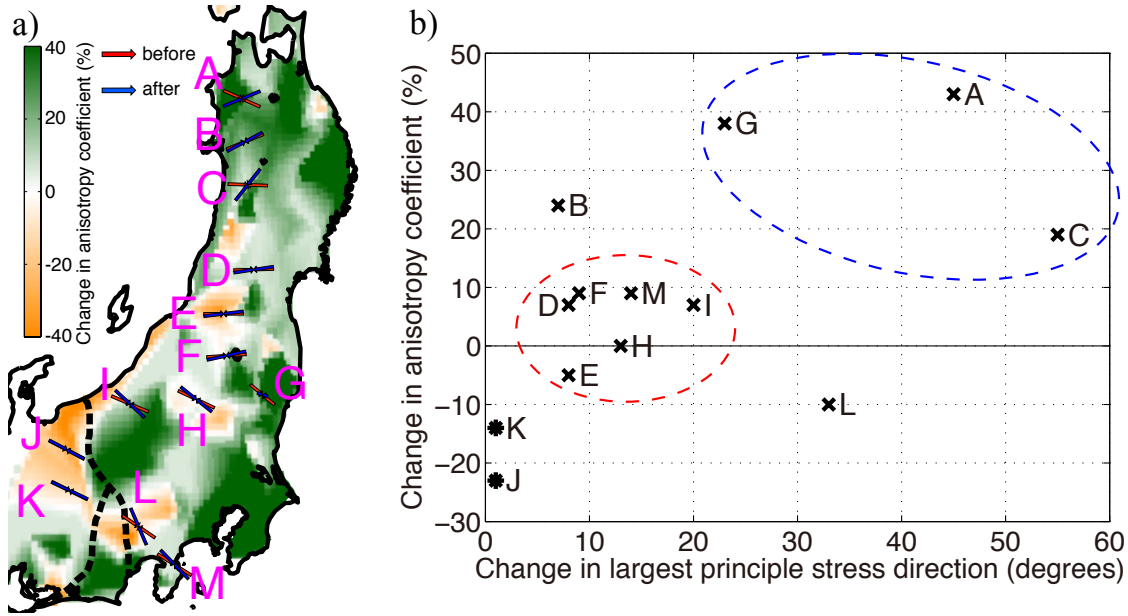


Figure 4.7. (a) Anisotropy change in Figure 4.4 with the largest principal stress direction (from Figure 3 in Yoshida et al. (2012)), before (red arrows) and after (blue arrows) the Tohoku-Oki earthquake. The arrows are estimated in each  $0.5^\circ$ -grid area. Black dashed lines indicate the locations of the major tectonic lines. A-M areas denote the interpreted regions in panel (b) as well as Yoshida et al. (2012). (b) Crossplot of the changes in the largest principal stress direction (Yoshida et al., 2012) and the anisotropy coefficient in each area shown in panel (a). The change in the anisotropy coefficient is the mean value for each  $0.5^\circ$  grid. Asterisk indicate the areas on the west side of the tectonic lines. The blue and red dashed circles indicate two groups which have a correlation between the changes in the largest principle stress direction and in the anisotropy coefficient.

in the principal stress direction might induce the large change in the anisotropy coefficient ( $> \pm 10\%$ ) in areas A, C, and G (the blue circle in Figure 4.7b). Likewise, a small change in the principal stress direction ( $< 20^\circ$ ) is coincident with the small change in the anisotropy coefficient ( $< \pm 10\%$ ) in areas D, E, F, H, I, and M (the red circle in Figure 4.7b).

Areas J and K (the asterisks in Figure 4.7b) are on the west side of the tectonic lines and area L is close to these lines, and the change in stress caused by the main event in the upper few hundred meters (the depth range of the boreholes) might be different on both sides of the tectonic lines. Kern (1978) found in rock-physics experiments that as the confining pressure increases, velocity increases and anisotropy decreases. We speculate that the increase in the velocity and the decrease in the anisotropy coefficient on the west side of the tectonic

lines could be explained by increase in the compressional stress, but since we cannot directly measure the compressional stress in this study, we cannot validate this hypothesis. Note that the model of Yoshida et al. (2012) does not include possible differences in compaction and in rheology across these lines. The change in the principal stress direction is only one proxy of changes in stress, and we cannot explain the change in the anisotropy coefficient in area B from the change in the principal stress direction.

#### **4.6 Conclusions**

By applying deconvolution-based seismic interferometry to KiK-net data, we measure changes in anisotropy caused by the Tohoku-Oki earthquake. The anisotropy coefficient increases in most parts of northeastern Japan after the Tohoku-Oki earthquake, but the fast polarization direction does not significantly change. The changes in shear-wave velocity and anisotropy both partly recover with time. Comparison of the changes in the shear-wave velocity and the anisotropy coefficient shows strong correlation in the northeastern half of Honshu. Also, the changes in the anisotropy coefficient and the largest principal stress direction are weakly correlated. On the west side of the tectonic lines, the increase in velocity and the decrease in anisotropy could be explained by a difference of the change in stress across the tectonic lines.

#### **4.7 Acknowledgments**

We are grateful to NIED for providing us with the KiK-net data. We thank Ken Larner, Elizabeth Cochran, Michael Wyssession, and an anonymous reviewer for valuable suggestions, correlations, edits, and discussions.

CHAPTER 5  
COMBINATION OF HI-NET AND KIK-NET DATA FOR DECONVOLUTION  
INTERFEROMETRY

Submitted to *Bulletin of the Seismological Society of America* (2013)

Nori Nakata<sup>1</sup>

## 5.1 Summary

Application of deconvolution interferometry to wavefields observed by KiK-net, a strong-motion recording network in Japan, is useful for estimating wave velocities and S-wave splitting in the near surface. At the location of the borehole accelerometer of each KiK-net station, a velocity sensor is also installed as a part of a high-sensitivity seismograph network (Hi-net). I present a technique that uses both Hi-net and KiK-net records for computing deconvolution interferometry. The deconvolved waveform obtained from the combination of Hi-net and KiK-net data is similar to the waveform computed from KiK-net data only. This similarity in the waveforms indicates that one can use Hi-net wavefields for deconvolution interferometry. Because Hi-net records have a high signal-to-noise ratio (S/N) and small dynamic resolution, the S/N and the quality of amplitude and phase of deconvolved waveforms can be improved with Hi-net data. These advantages are especially important for short-time moving-window seismic interferometry and deconvolution interferometry using coda waves.

## 5.2 Introduction

Data from a strong-motion recording network, *KiK-net*, have been used for estimating near-surface properties by computing spectral ratio and seismic interferometry based on deconvolution (e.g., Sawazaki et al., 2006, 2009). KiK-net has been operated by the National

---

<sup>1</sup>Center for Wave Phenomena, Colorado School of Mines

Research Institute for Earth Science and Disaster Prevention (NIED) since 1996 (Aoi et al., 2004); therefore, these data are useful for time-lapse studies. KiK-net includes about 700 stations distributed all over Japan, and each station has two three-component accelerometers: one at the surface and the other in a borehole. The depth of the boreholes is mostly 100–210 m, and some boreholes are more than 1000 m deep.

Applying seismic interferometry to KiK-net records, Sawazaki et al. (2009) and Yamada et al. (2010) estimated velocity reduction after 2000 Western-Tottori earthquake and 2008 Iwate-Miyagi Nairiku earthquake, respectively. Nakata and Snieder (2012a) found that S-wave velocity reductions after large earthquakes occurred at the Niigata prefecture in Japan, and Nakata and Snieder (2011) and Takagi and Okada (2012) discovered a reduction in S-wave velocity after the 2011 Tohoku-Oki earthquake. These reductions partly recover logarithmically with time (Nakata and Snieder, 2011, 2012b). Although Sawazaki and Snieder (2013) estimated P-wave velocities using this technique, computing P-wave velocities is more challenging than computing S-wave velocities because of the shallow depth of the boreholes. Wu and Peng (2011, 2012) found a reduction in peak frequencies of the spectral ratio and a recovery with time after the Tohoku-Oki earthquake. Nakata and Snieder (2012b), Takagi and Okada (2012), and Sawazaki and Snieder (2013) investigated time-lapse changes of shear-wave splitting due to the Tohoku-Oki earthquake, although their conclusions are different. One can also calculate the changes in S-wave velocities caused by precipitation with this technique (Nakata and Snieder, 2012a).

A high-sensitivity seismograph network, *Hi-net*, is also maintained by NIED to continuously record ground motion (Obara et al., 2005). Hi-net velocity meters are located at the same position as the KiK-net borehole receivers. Hi-net records, especially ambient-noise data, are used for estimating changes in velocity in deeper zones (e.g., Wegler et al., 2009; Minato et al., 2012). Although KiK-net and Hi-net receivers are co-located, no study has yet used combinations of KiK-net and Hi-net data for the techniques of spectral ratio or seismic interferometry. Because KiK-net and Hi-net have different targets (specifications are

Table 5.1. Specifications of KiK-net and Hi-net systems.

	KiK-net	Hi-net
Sensor type	accelerometer	velocity meter
Sensor location	surface and downhole	downhole
Sensor component	three components	three components
Recording system	event trigger	continuous
Sampling ratio	100 Hz <sup>I</sup>	100 Hz
Dynamic range	$\pm 40$ m/s <sup>2</sup>	$\approx 0.002$ m (sensitivity $\pm 200$ V/(m/s))
A/D resolution	24 bit	27 bit
Dynamic resolution <sup>II</sup>	$4.768 \times 10^{-6}$ m/s <sup>2</sup>	$1.023 \times 10^{-7}$ m/s

<sup>I</sup> Before 2007, the sampling ratio was 200 Hz.

<sup>II</sup> Dynamic resolution means the sampling interval of amplitude.

summarized in Table 5.1 and Okada et al. (2004)), the properties of the observed records are different; briefly, KiK-net has the large dynamic range, which prevents saturation of amplitudes for large earthquakes, and Hi-net has the high sensitivity to record small ground motions. Clinton and Heaton (2002) found some advantages of using strong-motion velocity meters compared with using strong-motion accelerometers; we are able to reduce numerical error to estimate displacement because we need only one integration, and the signal-to-noise ratio (S/N) is better especially for long periods.

One problem of using velocity meters instead of strong-motion accelerometers is the small dynamic range, which means that the amplitudes of records of the velocity meters may saturate when large earthquakes occur. Although Hi-net receivers are velocity meters, the dynamic range of the Hi-net sensors is much wider than that of conventional velocity meters. Therefore, we can use earthquake records observed by Hi-net when the earthquakes are relatively small. For large earthquakes, Shiomi et al. (2005) present criteria to detect amplitude saturation of Hi-net data (introduced later).

In this study, I propose a technique using both KiK-net and Hi-net data to improve the quality of correlograms obtained by deconvolution interferometry. I first compare observed records of Hi-net and KiK-net in the time and frequency domains. Then I briefly introduce

deconvolution interferometry and apply this interferometry to KiK-net and Hi-net data. Finally I compare deconvolved waveforms and present advantages of using both Hi-net and KiK-net data rather than only KiK-net records.

### 5.3 Comparison of observed waveforms of Hi-net and KiK-net

Figure 5.1 shows waveforms observed by Hi-net and KiK-net receivers at the same location in the Fukushima prefecture (Hi-net code: H.HTAH, KiK-net code: FKSH12). The waveforms in Figures 5.1a, 5.1e, and 5.1f are the unfiltered ground motion in the north-south (NS) horizontal component recorded by Hi-net, KiK-net borehole, and KiK-net surface sensors, respectively. Since borehole receivers do not align to the exact NS direction due to a technical limitation, I first rotate Hi-net and KiK-net borehole records to the NS direction (Shiomi et al., 2003). The amplitude of the waveform observed by the KiK-net surface receiver (Figure 5.1f) is greater than twice as large as the amplitude of the KiK-net borehole record (Figure 5.1e), which might be an indication of the site amplification (e.g., Héloïse et al., 2012), and is beyond the scope of this study.

I integrate and differentiate the waveform shown in Figure 5.1a using Fourier transforms to compute displacement and acceleration waveforms, respectively (Figures 5.1b and 5.1c). Theoretically, the waveform in Figure 5.1c is the same as that in Figure 5.1e because these waveforms are the recording of the same earthquake at the same station. I compare the wavefields in Figures 5.1c and 5.1e in the frequency domain (Figure 5.2). In the ideal case (where the waveform in Figure 5.1c is the same as that in Figure 5.1e), the amplitude ratio (the gray line in Figure 5.2b) and the phase difference (the gray dots in Figure 5.2c) are 1 and  $0^\circ$ , respectively. The main reason of deviation from the ideal cases is the difference in the receiver responses of Hi-net and KiK-net. Hi-net and KiK-net receivers have flat responses between 1–30 Hz and DC–20 Hz, respectively (Okada et al., 2004; Obara et al., 2005). The reduced values of the gray line in Figure 5.2b below 1.5 Hz are caused by the non-flat response of the Hi-net sensor, and the large values above 20 Hz are due to the response of the KiK-net sensor.

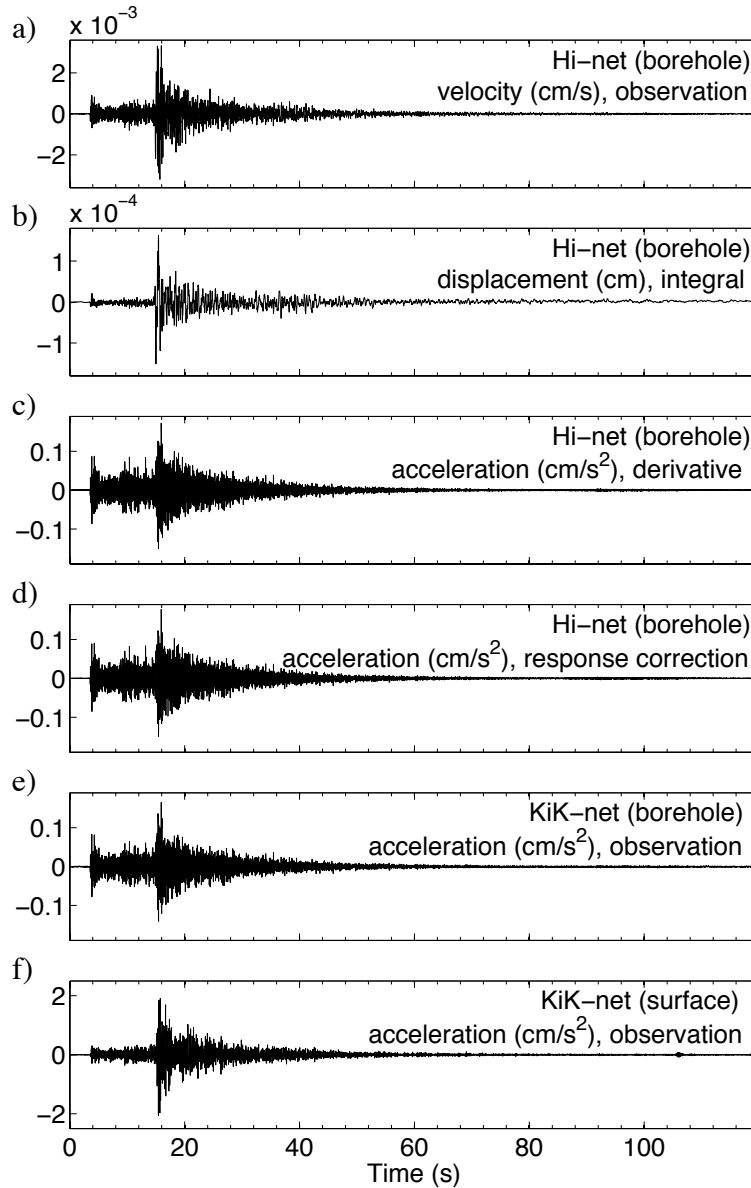


Figure 5.1. (a) Observed Hi-net waveform of one earthquake recorded in the NS horizontal component at H.HTAH ( $37.2139^{\circ}\text{N}$  and  $140.5736^{\circ}\text{E}$ ). This earthquake occurred at 18:17:59, 12 January 2012 (JST). The epicenter is at  $37.595^{\circ}\text{N}$  and  $141.616^{\circ}\text{E}$ , and the depth is 42.9 km. (b,c) Integral (displacement) and derivative (acceleration) of the waveform shown in panel (a). (d) Acceleration waveform computed from the waveform in panel (a) with the correction of the receiver response (equation 5.1). (e,f) Observed waveforms recorded by the co-located KiK-net receivers (FKSH12) in the borehole and at the surface. Units of each waveform are shown at top-right of each panel.

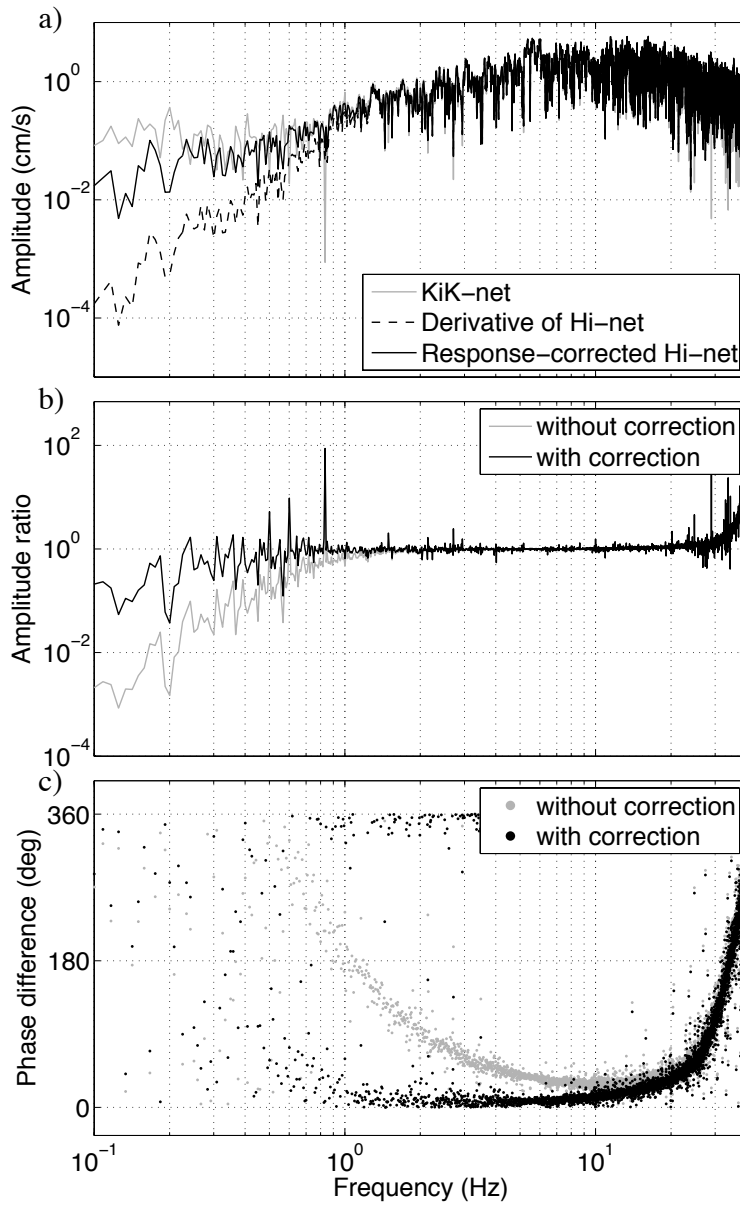


Figure 5.2. (a) Comparison of amplitude spectra computed from the waveforms in Figures 5.1c (derivative of Hi-net: dashed black), 5.1d (response-corrected Hi-net: solid black), and 5.1e (KiK-net: gray). (b) The ratios of amplitude spectra (Hi-net/KiK-net). The gray line is computed from the amplitude spectra of the waveforms in Figures 5.1c and 5.1e (the ratio of the gray and dashed black lines in panel (a)), and the black line from Figures 5.1d and 5.1e (the ratio of the gray and solid black lines in panel (a)). (c) The differences of phase spectra (Hi-net – KiK-net). The gray and black dots are computed from the waveforms used for the gray and black lines in panel (b). Because of the display, some dots are shown around  $360^\circ$ .

Because I use the frequency range of 1–13 Hz for deconvolution interferometry (Nakata and Snieder, 2012a), I correct the receiver response of the Hi-net sensor. Since phase information is important for deconvolution interferometry, I apply a correction for the receiver response to both amplitude and phase of the waveform in Figure 5.1a. I compute response-corrected acceleration waveforms as (Havskov and Ottemöller, 2010):

$$H_a(t) = \int_{-\infty}^{\infty} H_a(\omega)e^{-i\omega t}d\omega = \int_{-\infty}^{\infty} \frac{(i\omega - p_0)(i\omega - p_1)}{i\omega - z_0} H_v(\omega)e^{-i\omega t}d\omega, \quad (5.1)$$

where  $H_a(t)$  and  $H_a(\omega)$  are the response-corrected acceleration waveforms in the time and frequency domains, respectively,  $H_v(\omega)$  the Hi-net observed records (velocity data) after applying a Fourier transform,  $\omega$  the angular frequency,  $i$  the imaginary unit, and  $z_0 = 0.0 + 0.0i$ ,  $p_0 = -4.398230 + 4.487092i$ , and  $p_1 = -4.398230 - 4.487092i$  the complex zeros and poles of the Hi-net sensor (<http://www.hinet.bosai.go.jp/REGS/seed/>). The zeros and poles depend on the natural frequency, the damping coefficient, and the sensitivity of the Hi-net receiver.

Figure 5.1d shows the response-corrected acceleration waveform computed from the Hi-net observed record (Figure 5.1a). Although the time-domain waveforms in Figures 5.1c and 5.1d are almost the same based on a visual inspection, these wavefields are clearly different in the frequency domain (the dashed and solid black lines in Figure 5.2a). The black symbols of Figures 5.2b and 5.2c illustrate the amplitude ratio and the phase difference between this response-corrected acceleration waveform and the KiK-net record, respectively. As shown in Figure 5.2, the amplitude ratio and phase difference after the correction are close to 1 and  $0^\circ$ , respectively, in a wider frequency range, compared to the ratio and difference without the correction. Note that because of this correction, I successfully improve the similarity of the waveforms of KiK-net and Hi-net in the frequency range used in this study (1–13 Hz). Therefore, I use the response-corrected acceleration waveform for deconvolution interferometry. Another example of the amplitude ratio and the phase difference using another earthquake is shown in Figure 5.A1, and I can also recover the similarity by correcting

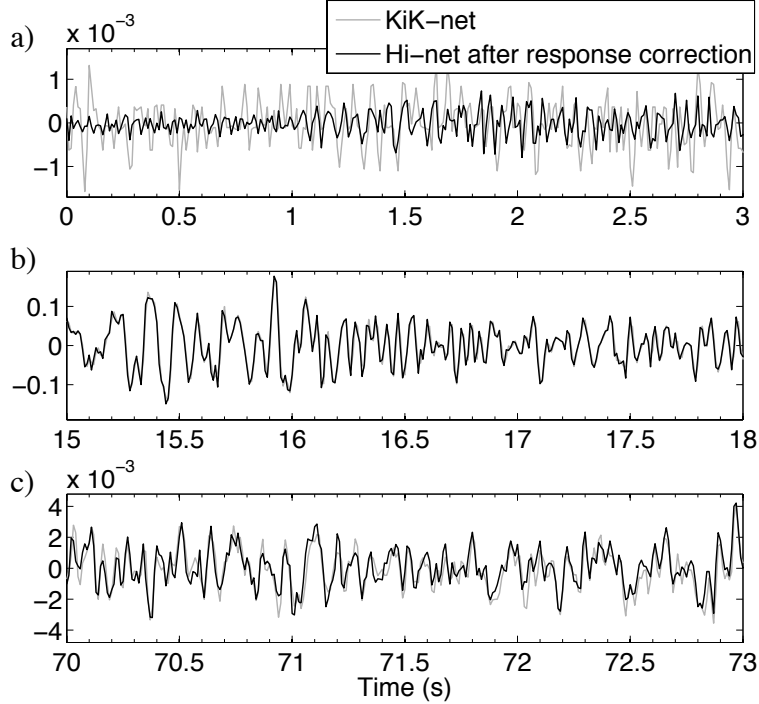


Figure 5.3. Comparison of the waveforms shown in Figures 5.1d (Hi-net: black) and 5.1e (KiK-net: gray) at different time intervals. Note that the amplitude scales of each panel are different. The unit of vertical axes is acceleration ( $\text{cm/s}^2$ ).

the receiver response.

Figure 5.3 shows the comparison of the waveforms shown in Figures 5.1d and 5.1e in three time intervals, which are before the P-wave arrival, at the maximum amplitude waves, and at later coda phases. The waveforms in Figure 5.3b are almost the same (correlation coefficient: 0.96), and those in Figure 5.3c are similar but some amplitudes are different (correlation coefficient: 0.86). These similarities indicate that I can use Hi-net data as strong-motion records. In contrast, the Hi-net waveform in Figure 5.3a is significantly different from the KiK-net record. One reason of this discrepancy is caused by the difference of S/N in Hi-net and KiK-net as mentioned in Clinton and Heaton (2002). The other reason is the difference of the dynamic resolutions. Here, the dynamic resolution means the sampling intervals of amplitude. Because the dynamic ranges and the A/D converters of KiK-net and Hi-net receivers are different due to the difference of their targets, the dynamic resolutions for KiK-

net and Hi-net records are different (Table 5.1). In KiK-net records, the dynamic resolution is approximately  $5 \times 10^{-4} \text{ cm/s}^2$ , which means that the KiK-net waveform in Figure 5.3a fluctuate over only one or two samples in amplitude. Note that the Hi-net system has a much higher dynamic resolution, and the resolution depends on the frequency (Obara et al., 2005). Figure 5.A2 shows comparisons of waveforms obtained from the other earthquake used in Figure 5.A1. The Hi-net waveform is also highly similar to the KiK-net waveform except for the time interval before the P waves arrive.

Although the Hi-net system has the higher S/N and the higher dynamic resolution, the dynamic range for the Hi-net system is smaller than that of the KiK-net system; therefore, the amplitude of Hi-net records can be saturated when a large earthquake occurs. I carefully examine to confirm that the records of the earthquakes used in this study are not saturated, but for dealing with large amounts of data, automatic methods for the examination are useful. Shiomi et al. (2005) propose several criteria to evaluate whether the amplitudes of Hi-net records are saturated or not. Based on Shiomi et al. (2005), when 1) the maximum amplitude of KiK-net borehole records is smaller than  $3.95 \text{ cm/s}^2$  and 2) the maximum displacement computed by the integration of Hi-net records is smaller than  $0.09 \text{ cm}$ , the Hi-net waveform of the earthquake is not likely to be saturated. The Hi-net records used in this study are much smaller than these criteria (Figure 5.1).

## 5.4 Deconvolution interferometry using Hi-net and KiK-net data

### 5.4.1 Deconvolution interferometry

Conventionally for deconvolution interferometry, one uses only KiK-net records (e.g., Nakata and Snieder, 2012a):

$$D_{KK}(S, B, t) = \int_{-\infty}^{\infty} \frac{K_a(S, \omega)}{K_a(B, \omega)} e^{-i\omega t} d\omega \approx \int_{-\infty}^{\infty} \frac{K_a(S, \omega) K_a^*(B, \omega)}{|K_a(B, \omega)|^2 + \epsilon \langle |K_a(B, \omega)|^2 \rangle} e^{-i\omega t} d\omega, \quad (5.2)$$

where  $S$  and  $B$  are the locations of receivers at the free surface and in the borehole,  $K_a$  the acceleration wavefields observed by a KiK-net receiver, the asterisk the complex conjugate,

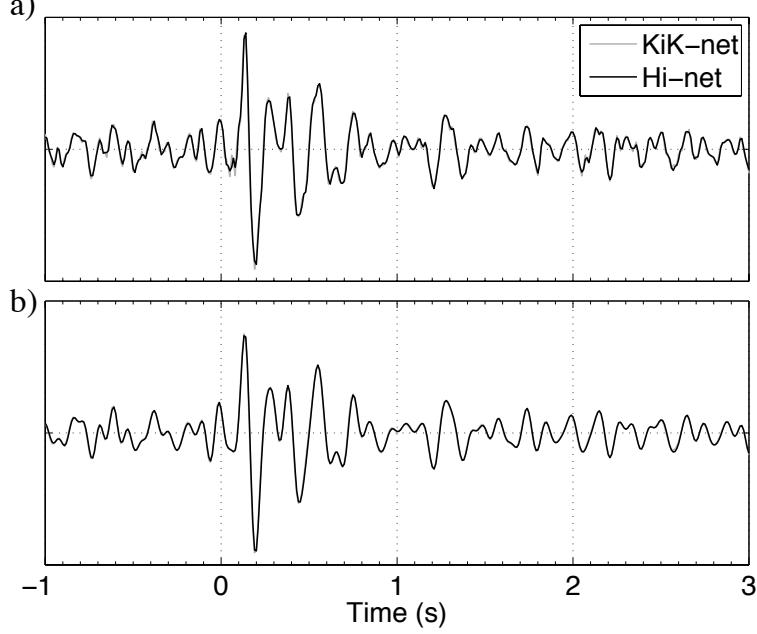


Figure 5.4. Comparison of deconvolved waveforms obtained from the earthquake shown in Figure 5.1 using only KiK-net records (gray: equation 5.2) and the combination of KiK-net and Hi-net records (black: equation 5.3). For the combination, I deconvolve the KiK-net record at the surface with the response-corrected Hi-net record at the borehole. Panel (a) is the unfiltered waveforms, and panel (b) the bandpass-filtered (1–13 Hz) waveforms. Note that panel (b) also shows black and gray lines.

$\langle \dots \rangle$  the average power spectrum, and  $\epsilon$  a regularization parameter to obtain stable deconvolved waveforms (Clayton and Wiggins, 1976). After the deconvolution interferometry, the borehole receiver behaves as a virtual source, and  $D_{KK}(S, B, t)$  corresponds to the wavefield propagating from the virtual source to the surface receiver (Nakata and Snieder, 2012a). Here, I replace the wavefield in the denominator of equation 5.2 by Hi-net data:

$$D_{KH}(S, B, t) = \int_{-\infty}^{\infty} \frac{K_a(S, \omega)}{H_a(B, \omega)} e^{-i\omega t} d\omega \approx \int_{-\infty}^{\infty} \frac{K_a(S, \omega) H_a^*(B, \omega)}{|H_a(B, \omega)|^2 + \epsilon \langle |H_a(B, \omega)|^2 \rangle} e^{-i\omega t} d\omega, \quad (5.3)$$

where  $H_a(\omega)$  is the response-corrected acceleration waveforms computed from Hi-net records (equation 5.1). In both expressions 5.2 and 5.3, I use  $\epsilon = 1\%$ .

In Figure 5.4, the gray and black lines depict  $D_{KK}(S, B, t)$  and  $D_{KH}(S, B, t)$ , respectively, obtained from the earthquake in Figure 5.1. These deconvolved waveforms are similar, and

the correlation coefficients of these waveforms in the time interval are 0.990 (Figure 5.4a) and 0.996 (Figure 5.4b). Note that this similarity indicates that one can use Hi-net data for applying deconvolution interferometry. In Figure 5.4a, some discrepancies of the waveforms are caused by the differences of the receiver responses of KiK-net and Hi-net in lower than 0.6 Hz and higher than 20 Hz (see Figure 5.2). The arrival times of the peak amplitudes in Figure 5.4b are slightly different: 0.132 s for the gray line and 0.134 s for the black line estimated by using the quadratic interpolation proposed by Nakata and Snieder (2012a). Because these times correspond to the arrival times of the traveling waves from the borehole receiver to the surface receiver (Nakata and Snieder, 2012a), this difference is related to the quality of the estimation of the S-wave velocities. Although a comparison of this small difference of the arrival times estimated from one earthquake is not practical, I speculate that this travel-time difference is caused by the dynamic resolution. In the next section, I use a numerical computation and show that the dynamic resolution changes the arrival times of the deconvolved waveforms.

#### 5.4.2 Discussion of dynamic resolution

In the simplest case, where I assume vertically propagating waves between receivers, constant amplitude and wavenumber, and no internal reflections above the borehole receiver, I can represent the observed wavefields at the borehole and surface receivers as (Nakata and Snieder, 2012a):

$$u(S, \omega) = 2W(\omega)e^{ikR}e^{-\gamma|k|R} \quad (5.4)$$

$$u(B, \omega) = W(\omega) \{1 + e^{2ikR}e^{-2\gamma|k|R}\}, \quad (5.5)$$

where  $W(\omega)$  is the incoming wavefield to the borehole receiver,  $R$  the distance between the borehole and surface receivers,  $k$  the wavenumber, and  $\gamma$  the attenuation coefficient. The incoming wavefield  $W(\omega)$  may include complicated wave propagation (e.g., scattering and attenuation) below the borehole receiver. By applying deconvolution interferometry to these

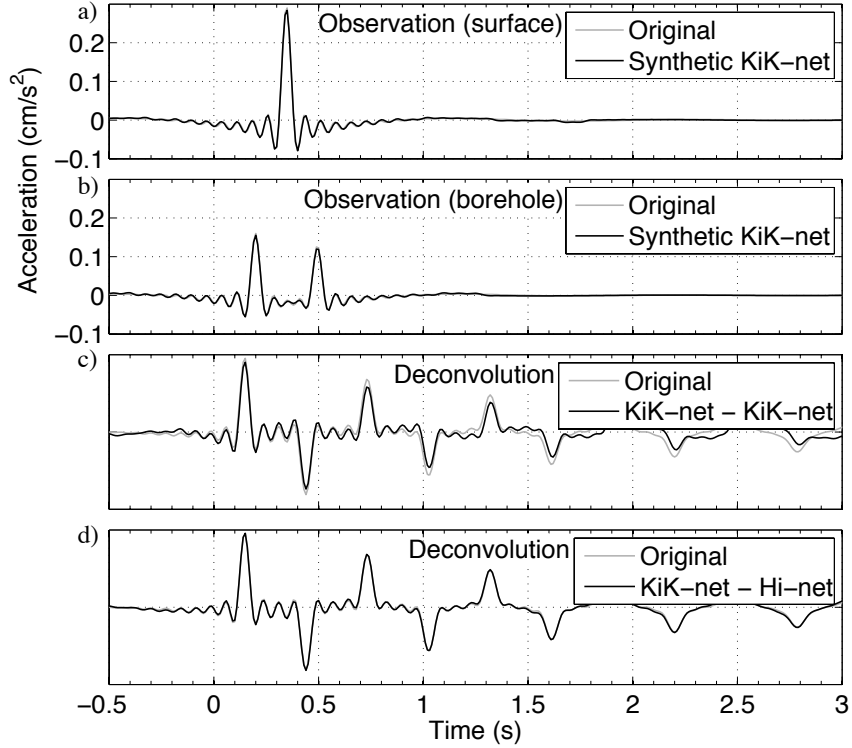


Figure 5.5. Synthetic observed waveforms recorded at the (a) surface and (b) borehole receivers. The gray and black lines show the original and synthetic KiK-net waveforms, respectively. (c) Deconvolved waveforms computed from the synthetic KiK-net records (simulated  $D_{KK}(S, B, t)$ ). (d) Deconvolved waveforms computed from the synthetic KiK-net (surface) and Hi-net (borehole) records (simulated  $D_{KH}(S, B, t)$ ). The gray lines in panels (c,d) are deconvolved waveforms computed from the original waveforms. The waveforms are applied the same bandpass filter used in Figure 5.4.

wavefields, in which I deconvolve  $u(S, \omega)$  with  $u(B, \omega)$ , I can cancel  $W(\omega)$ , and the computed deconvolved waveform is independent of the complexity below the borehole receiver.

I numerically compute expressions 5.4 and 5.5 with a 0.01-s time sampling, which is the same for KiK-net and Hi-net records (Table 5.1), and show the wavefields with the gray lines in Figures 5.5a and 5.5b. For this numerical computation, I employ  $R = 108$  m (which is the same as location H.HTAH),  $W(\omega) = 1$  (delta function in the time domain) for simplicity,  $\gamma = 1/60$ , and the velocity of traveling waves is 750 m/s. The earthquake wave arrives at around 0.2 s at the borehole receiver.

To simulate KiK-net observed records (low dynamic resolution: henceforth called synthetic KiK-net records), I discretize the amplitudes of  $u(S, t)$  and  $u(B, t)$  in the  $5 \times 10^{-4}$  cm/s<sup>2</sup> interval, which corresponds to the dynamic resolution of the KiK-net observation (Table 5.1). To synthetically compute Hi-net observed records (high dynamic resolution: henceforth called synthetic Hi-net records), I first integrate  $u(B, t)$  and discretize the amplitude of integrated waveforms in the  $1 \times 10^{-5}$  cm/s (Table 5.1). Then I differentiate the discretized waveform and create an acceleration waveform as the synthetic Hi-net record.

The black line in Figure 5.5c illustrates the deconvolved waveform computed by synthetic KiK-net records at both surface and borehole receivers (simulated  $D_{KK}(S, B, t)$ ). In Figure 5.5d, the black line depicts the waveform computed by the combination of synthetic Hi-net (borehole) and KiK-net (surface) records (simulated  $D_{KH}(S, B, t)$ ). The gray lines in Figures 5.5c and 5.5d illustrate the deconvolved waveform obtained from the original observed waveforms. The amplitudes and arrival times of deconvolved waveforms computed from only the synthetic KiK-net records (Figure 5.5c) deviate from the original deconvolved waveform. When I use the synthetic Hi-net record for the borehole wavefield, the deviations become small (Figure 5.5d). Therefore, I conclude that I obtain more correct deconvolved waveforms (more similar to the original deconvolved waveform in both phases and amplitudes) when I use Hi-net data for the borehole wavefield of the deconvolution interferometry. This conclusion is valid when Hi-net records are not saturated (section 5.3).

### 5.4.3 Short-time moving-window seismic interferometry

One advantage of using Hi-net records is that Hi-net data have the higher dynamic resolution than KiK-net data as discussed in the previous section. The other advantage is that Hi-net wavefields (velocity meter) have higher S/N than KiK-net recordings (accelerometer) (Clinton and Heaton, 2002). Here, I examine the advantage of the S/N using short-time moving-window seismic interferometry (SMSI). Nakata and Snieder (2011) found a nonlinear response caused by the 2011 Tohoku-Oki earthquake using SMSI. Because for SMSI we compute deconvolution in a short time segment, this technique is more sensitive for S/N than

normal deconvolution interferometry using entire earthquake records as shown in Figure 5.4.

Figure 5.6 shows the SMSI waveforms obtained from the earthquake used in Figure 5.1. In Figure 5.6, I compute deconvolution of the waveforms at each 20-s time interval with a 10-s overlap for SMSI. Using KiK-net records only (Figure 5.6b), I reconstruct the traveling waves, which have the prominent peaks at around 0.14 s, from the data during 0–70 s (first seven deconvolved waveforms). The last four waveforms (60–110 s) are noisy and have no coherent peaks at 0.14 s. In contrast, when I use both Hi-net and KiK-net data (Figure 5.6c), I obtain the deconvolved waveforms with explicit peaks throughout the time intervals. For example comparing the waveforms of the interval of 90–110 s, the peak of the waveform at 0.14 s in Figure 5.6c is clearer than that in Figure 5.6b. The coherent waves at around 0.5 s in Figure 5.6c are the first-order surface related multiple waves, which reflect between the free surface and the clamped boundary at the virtual source (Snieder et al., 2006a). One can also use these reflected waves for estimating S-wave velocities of the medium (Nakata et al., 2013).

Figure 5.6d shows S/N computed by the root-square-mean (RMS) amplitude at each time interval and an RMS amplitude of background noise. To obtain the stable RMS amplitude of background noise, I use data from approximately 100 earthquakes and look at the time intervals before P waves arrive. Figure 5.6d indicates that Hi-net data have higher S/N than KiK-net data at all time intervals, which is the main reason for the highly coherent deconvolved waveforms among different time intervals in Figure 5.6c. Therefore, by using Hi-net data, I obtain clear traveling wavefields even at later observed times due to the higher S/N. This advantage of the S/N is also important for deconvolved waveforms computed from coda waves (Sawazaki et al., 2009; Takagi and Okada, 2012) because the amplitudes of coda waves are usually smaller than those of direct waves, and the S/N at the time of coda waves is small. Deconvolved waveforms of SMSI using the other earthquake is shown in Figure 5.A3, where I also improve the coherency of the waveforms using the combination of Hi-net and KiK-net data.

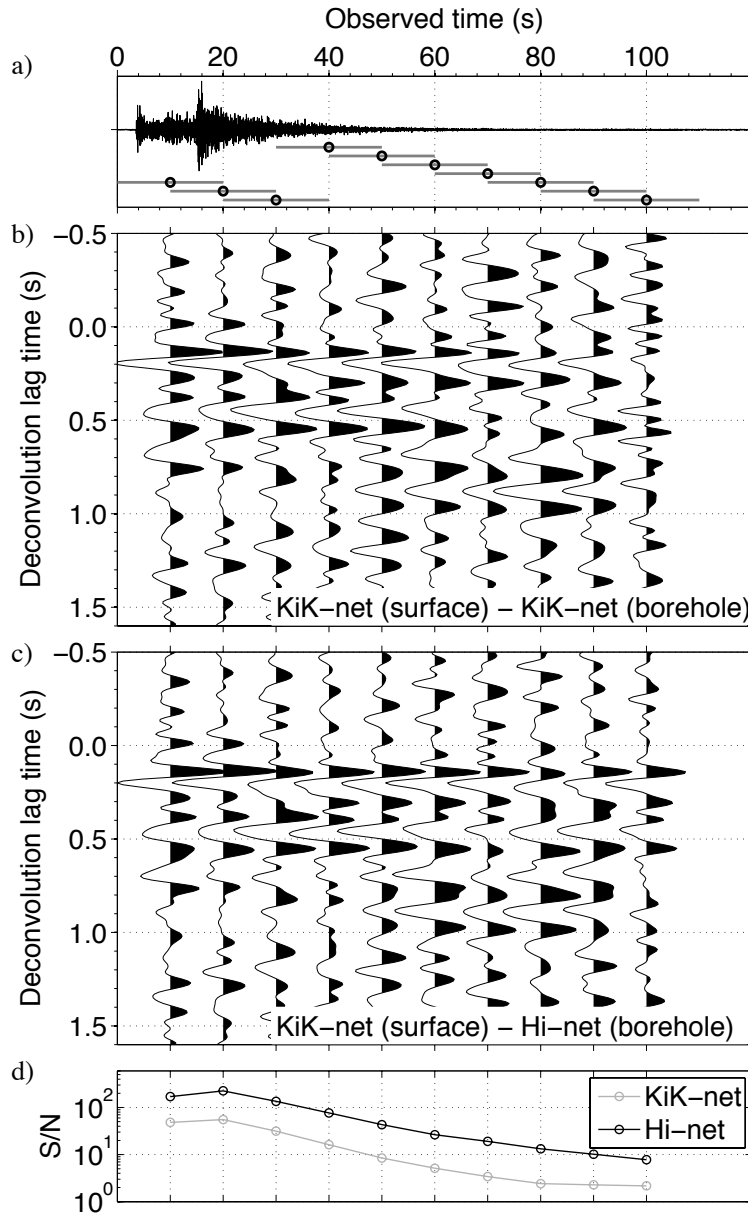


Figure 5.6. (a) Observed waveforms recorded at the KiK-net borehole receiver (the same waveforms shown in Figure 5.1e). Gray lines indicate the 20-s time windows for SMSI with a 10-s overlap. Black circles are the center of each time window. (b) Deconvolved waveforms at each time interval using only KiK-net records. (c) Deconvolved waveforms computed from the combination of KiK-net (surface) and Hi-net (borehole) records. (d) S/N of KiK-net (gray) and receiver-response corrected Hi-net records (black) computed by the RMS amplitude at each time interval divided by the RMS amplitude of background noise. Waveforms in panels (b) and (c) are applied the same bandpass filter used in Figure 5.4. Waveforms and circles in panels (b,c,d) are aligned with the center time of the employed time window shown in panel (a).

## 5.5 Conclusions

I propose the technique of using both Hi-net and KiK-net data for deconvolution interferometry. In this technique, I use Hi-net data as a borehole record and KiK-net data as a surface record to compute deconvolution. Because of the difference in receiver responses of Hi-net and KiK-net, I need to correct the response of the Hi-net records. After the correction, the waveform of Hi-net is similar to that of KiK-net especially in the frequency range used in this study (1–13 Hz). The deconvolved waveforms using the combination of Hi-net and KiK-net receivers are similar to those using only KiK-net receivers, which means that I can use Hi-net data for computing deconvolution. Because Hi-net wavefields have high S/N and high dynamic resolution, deconvolved waveforms computed by the combination have two advantages over the conventional deconvolved waveforms obtained by using only KiK-net data: higher S/N and better amplitude and phase information. These advantages are important for SMSI and deconvolution interferometry using coda waves. Note that Hi-net and KiK-net receivers are already installed at the same location, and this technique uses existing data to improve deconvolution interferometry.

## 5.6 Acknowledgments

I am grateful to sponsor companies of the Consortium Project on Seismic Inverse Methods for Complex Structures at the Center for Wave Phenomena. I thank NIED for providing me with the KiK-net and Hi-net data. I am grateful to Roel Snieder of Colorado School of Mines for his advice to improve this study. I also thank Shoichi Masuhara for his technical help, and Marine Denole of Stanford University for her insight and beneficial discussions to start this study.

### 5.A Example of another earthquake

In this appendix, I show the comparison of wavefields observed by Hi-net and KiK-net in the frequency (Figure 5.A1) and time domains (Figure 5.A2), and deconvolved waveforms after applying SMSI (Figure 5.A3) obtained from another earthquake recorded at the same

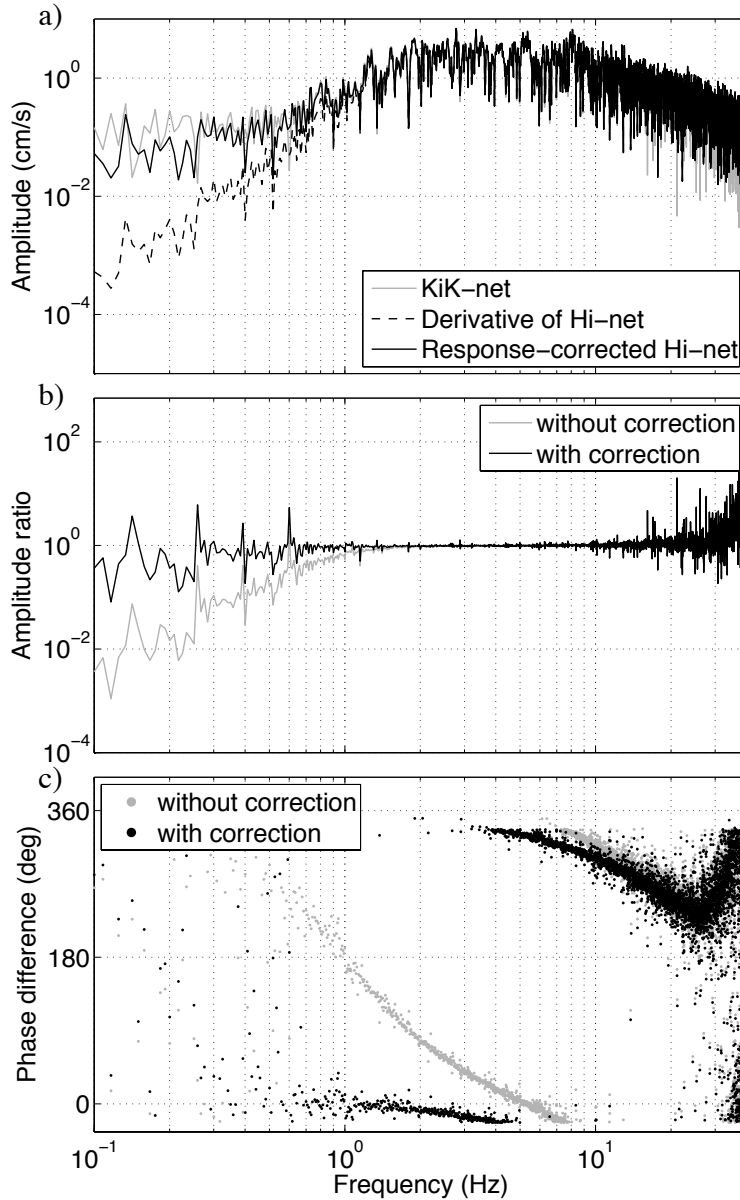


Figure 5.A1. (a) Comparison of amplitude spectra computed from waveforms generated by an earthquake, which occurred at 21:48:43, 4 January 2012 (JST). The epicenter is at  $36.574^{\circ}\text{N}$  and  $141.148^{\circ}\text{E}$ , and the depth is 32.9 km. The station is the same as used in Figure 5.1 (H.HTAH and FKSH12). The gray line illustrates the amplitude spectra of the KiK-net borehole record, the dashed black line the derivative of the Hi-net record, and the solid black line the response-corrected Hi-net record. (b) The ratios of amplitude spectra (Hi-net/KiK-net). The gray line is computed from the amplitude spectra shown in the gray and dashed black lines in panel (a), and the black line from the gray and solid black lines in panel (a). (c) The differences of phase spectra (Hi-net – KiK-net). The gray and black dots are computed from the waveforms used for the gray and black lines in panel (b). Because of the display, some dots are shown around  $360^{\circ}$ .

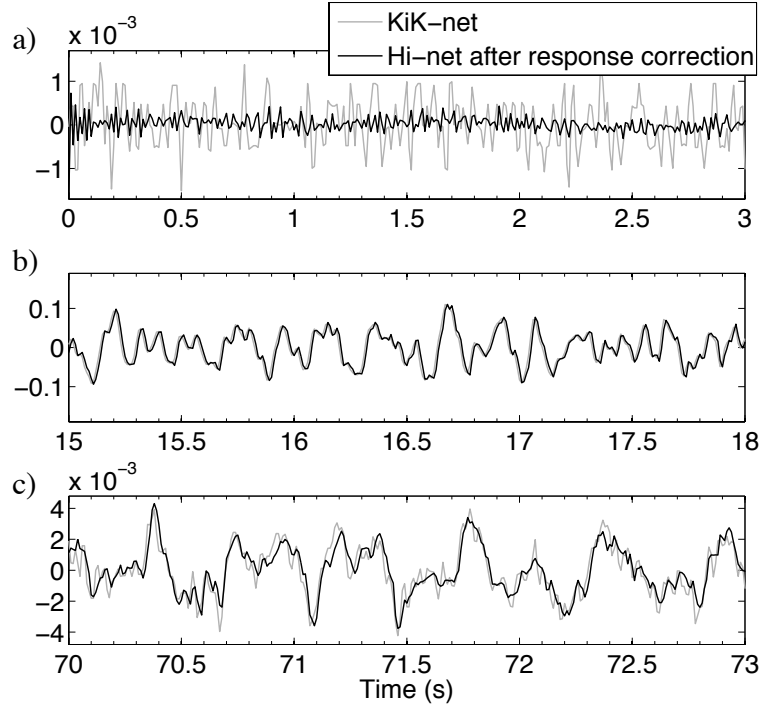


Figure 5.A2. Comparison of the waveforms between the response-corrected Hi-net records (black) and KiK-net records (gray) at different time intervals of the earthquake used in Figure 5.A1. Note that amplitude scales of each panel are different. The unit of vertical axes is acceleration ( $\text{cm/s}^2$ ).

station (H.HTAH and FKSH12). Based on Figures 5.A1–5.A3, the method proposed here to use the combination of Hi-net and KiK-net data is valid for other earthquakes.

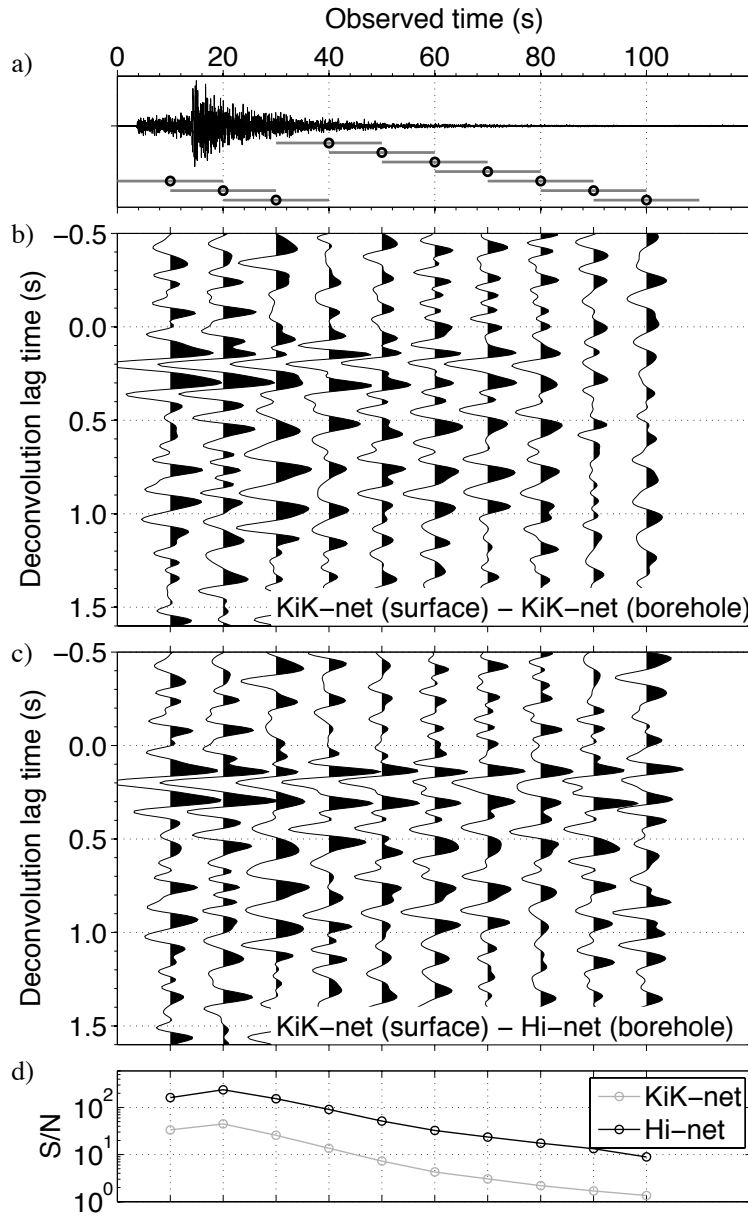


Figure 5.A3. (a) Observed waveforms recorded at the KiK-net borehole receiver obtained from the earthquake used in Figure 5.A1. Gray lines indicate the 20-s time windows for SMSI with a 10-s overlap. Black circles are the center of each time window. (b) Deconvolved waveforms at each time interval using only KiK-net records. (c) Deconvolved waveforms computed from the combination of KiK-net (surface) and Hi-net (borehole) records. (d) S/N of KiK-net (gray) and response-corrected Hi-net records (black) computed by the RMS amplitude at each time interval divided by the RMS amplitude of background noise. Waveforms in panels (b) and (c) are applied the same bandpass filter used in Figure 5.4. Waveforms and circles in panels (b,c,d) are aligned with the center time of the employed time window shown in panel (a).

CHAPTER 6  
MONITORING A BUILDING USING DECONVOLUTION INTERFEROMETRY. I:  
EARTHQUAKE-DATA ANALYSIS

*Accepted by Bulletin of the Seismological Society of America (2013)*

Nori Nakata<sup>1</sup>, Roel Snieder<sup>1</sup>, Seiichiro Kuroda<sup>2</sup>, Shunichiro Ito<sup>3</sup>, Takao Aizawa<sup>3</sup>, and  
Takashi Kunimi<sup>4</sup>

## 6.1 Summary

For health monitoring of a building, we need to separate the response of the building to an earthquake from the imprint of soil-structure coupling and from wave propagation below the base of the building. Seismic interferometry based on deconvolution, where we deconvolve the wavefields recorded at different floors, is a technique to extract this building response and hence estimate velocity of the wave which propagates inside the building. Deconvolution interferometry also allows us to estimate the damping factor of the building. Compared with other interferometry techniques, such as crosscorrelation and crosscoherence interferometry, deconvolution interferometry is the most suitable technique to monitor a building using earthquake records. For deconvolution interferometry, we deconvolve the wavefields recorded at all levels with the waves recorded at a target receiver inside the building. This receiver behaves as a virtual source, and we retrieve the response of a cut-off building, a short building which is cut off at the virtual source. Because the cut-off building is independent from the structure below the virtual source, the technique might be useful for estimating local structure and local damage. We apply deconvolution interferometry to

---

<sup>1</sup>Center for Wave Phenomena, Colorado School of Mines

<sup>2</sup>National Institute for Rural Engineering

<sup>3</sup>Suncoch Consultants Co., Ltd.

<sup>4</sup>Akebono Brake Industry Co., Ltd.

17 earthquakes recorded during two weeks at a building in Fukushima, Japan and estimate time-lapse changes in velocity and normal-mode frequency. As shown in a previous study, the change in velocity correlates with the change in normal-mode frequency. We compute the velocities from both traveling waves and the fundamental mode using coda-wave interferometry. These velocities have a negative correlation with the maximum acceleration of the observed earthquake records.

## 6.2 Introduction

The response of a building to an earthquake has been studied since the early 1900s (e.g., Biot, 1933; Sezawa and Kanai, 1935; Carder, 1936). We can estimate the frequencies of the fundamental and higher modes of buildings using ambient and forced vibration experiments (Trifunac, 1972; Ivanović et al., 2000; Kohler et al., 2005; Clinton et al., 2006; Michel et al., 2008). Due to the shaking caused by major earthquakes, the frequencies of normal modes decrease (Trifunac et al., 2001a; Kohler et al., 2005); the reduction is mostly temporary (a few minutes) and healing occurs with time, but some reduction is permanent (Clinton et al., 2006), who found more than 20% temporal reduction and 4% permanent reduction in the fundamental frequency of the motion of the Millikan Library located at the California Institute of Technology after the 1987 M6.1 Whittier Narrows earthquake. The reduction in the frequency logarithmically correlates with the maximum acceleration of observed records (Clinton et al., 2006). Precipitation, strong wind, temperature, reinforcement, and heavy weight loaded in a building also change the frequencies of normal modes (Kohler et al., 2005; Clinton et al., 2006). Because these frequencies are related to both the building itself and the soil-structure coupling, we have to consider soil-structure interactions (Şafak, 1995) and nonlinearities in the response of the foundation soil (Trifunac et al., 2001a,b). Normal-mode frequencies estimated from observed records are, therefore, not suitable for health monitoring of a building in isolation of its environment (Todorovska and Trifunac, 2008b).

Snieder and Şafak (2006) show that one can estimate an impulse response independent from the soil-structure coupling and the complicated wave propagation (e.g., attenuation and

scattering) below the bottom receiver by using seismic interferometry based on deconvolution. Seismic interferometry is a technique to extract the Green's function which accounts for the wave propagation between receivers (Lobkis and Weaver, 2001; Derode et al., 2003a; Snieder, 2004a; Paul et al., 2005; Snieder et al., 2006b; Wapenaar and Fokkema, 2006). Seismic interferometry can be based on crosscorrelation, deconvolution, and crosscoherence (Snieder et al., 2009; Wapenaar et al., 2010a). Deconvolution interferometry is a useful technique for monitoring structures especially in one dimension (Nakata and Snieder, 2011, 2012a,b). Because deconvolution interferometry changes the boundary condition at the base of the building, we are able to extract the pure response of the building regardless of its coupling to the subsurface (Snieder and Şafak, 2006; Snieder et al., 2006a).

Deconvolution interferometry has been applied to earthquake records observed in a building to retrieve the velocity of traveling waves and attenuation of the building (Oyunchimeg and Kawakami, 2003; Snieder and Şafak, 2006; Kohler et al., 2007; Todorovska and Trifunac, 2008a,b) (some studies call the method *impulse response function* or *normalized input-output minimization*). Todorovska and Trifunac (2008b) use 11 earthquakes occurring over a period of 24 years to monitor the fundamental frequency of a building after applying deconvolution interferometry. The fundamental frequencies they estimated from the interferometry are always higher than the frequencies obtained from the observed records because the frequencies computed from the observed records are affected by both the building itself and soil-building coupling, while the frequencies estimated using the interferometry are only related to the building itself. Oyunchimeg and Kawakami (2003) apply short-time moving-window seismic interferometry to an earthquake record to estimate the velocity reduction of a building during an earthquake. Prieto et al. (2010) apply deconvolution interferometry to ambient vibrations after normalizing amplitudes per frequency using the multitaper method (Thomson, 1982) to estimate the traveling-wave velocity and damping factor.

In this study, we apply deconvolution interferometry to 17 earthquakes observed at a building in Japan over a period of two weeks and monitor the changes in velocity of the

building. This study is based on the work of Snieder and Şafak (2006); furthermore, we extend the deconvolution interferometry as proposed by Snieder and Şafak (2006) to deconvolution with the waveforms recorded at an arbitrary receiver, compare this with crosscorrelation and crosscoherence interferometry, and use interferometry for monitoring a building in Japan. First, we introduce our data: geometry of receivers, locations of the building and epicenters of earthquakes used, observed waveforms, and shapes of the normal modes extracted from observed records. We also introduce the equations of interferometry based on deconvolution, crosscorrelation, and crosscoherence. We further indicate the deconvolved waveforms obtained from one earthquake and estimate a velocity as well as a quality factor ( $Q$ ). Next, we apply deconvolution interferometry to all observed earthquakes and monitor the change in velocity of the building using coda-wave interferometry (Snieder et al., 2002). In a companion paper, we apply the interferometry to ambient vibrations.

### 6.3 Building and earthquakes

The building (rectangle in Figure 6.1) in which we recorded vibrations is located in the Fukushima prefecture, Japan. Continuous seismic vibrations were recorded by Suncoch Consultants Co., Ltd. for two weeks using 10 microelectromechanical-systems (MEMS) accelerometers, which were developed by Akebono Brake Industry Co., Ltd., and 17 earthquakes were observed during the two weeks (Table 6.1 and Figure 6.1). In this study, we focus on processing of the earthquake records, and we analyze ambient vibrations in the companion paper. The building includes eight stories, a basement, and a penthouse (Figure 6.2). We installed receivers on the stairs, located 20 m from the east side and at the center between the north and south sides. The sampling interval of the records is 1 ms, and the receivers have three components. Here, we use two horizontal components which are aligned with the east-west (EW) and north-south (NS) directions.

Figures 6.3a–6.3d illustrate the observed waveforms and their power spectra of earthquake No. 5, which gives the greatest acceleration to the building. Figures 6.3e and 6.3f show the spectrogram of the motion at the fourth floor computed with the continuous-wavelet

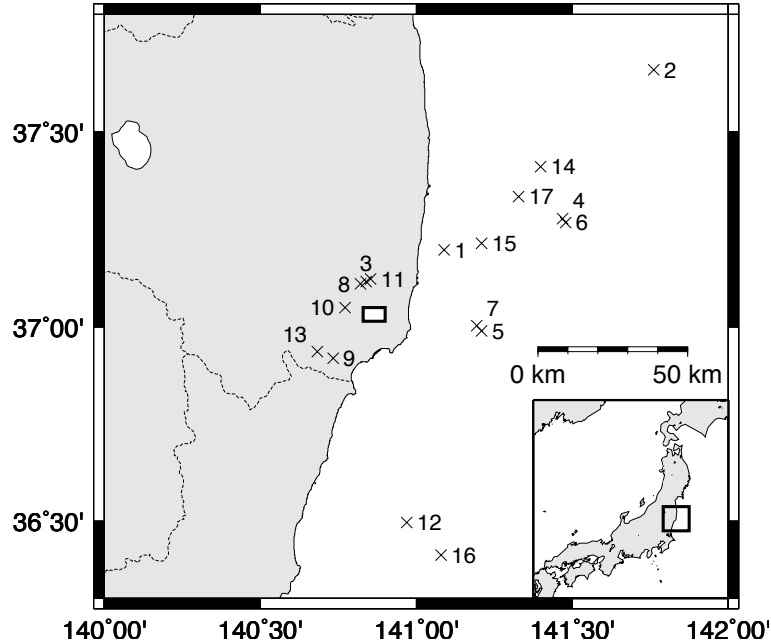


Figure 6.1. The building (rectangle, not to scale) and epicenters of earthquakes used (crosses). Numbers beside of crosses correspond to the sequential numbers in Table 6.1. The lower-right map indicates the location of the magnified area.

transform (Torrence and Compo, 1998). Higher frequencies quickly attenuate and the fundamental mode is dominant for later times in Figures 6.3e and 6.3f. The frequency of the fundamental mode in the EW component (1.17 Hz) is higher than the frequency in the NS component (0.97 Hz) because the EW side of the building is longer than the NS side. Both components have large amplitudes at around 0.5 Hz between 14 and 21 s. Since the 0.5-Hz component is localized in time (Figure 6.3e and 6.3f), it corresponds to a surface wave that moves the entire building. However, because the frequency of the surface wave is less than that of the fundamental mode of the building, it does not excite waves that propagate within the building.

Figure 6.4 illustrates the shapes of the normal-mode displacement computed from the real part of the Fourier spectra at different floors. We calculate displacement from acceleration using numerical integration (Schiff and Bogdanoff, 1967). Just as for the fundamental mode, the frequencies of overtones in the EW component are also higher than those in the NS

Table 6.1. Origin times, magnitudes, and hypocenter locations of recorded earthquakes estimated by the Japan Meteorological Agency (JMA). The earthquakes are numbered sequentially according to their origin times. Maximum acceleration is the observed maximum amplitude of the MEMS accelerometers at the first floor in the 120 s following the origin time of each earthquake.

No.	Origin time (yyyy/mm/dd hh:mm:ss.s)	$M_{JMA}$	Latitude	Longitude	Depth (km)	Maximum acceleration (m/s <sup>2</sup> )
1	2011/05/31 16:12:20.2	3.9	37.1983	141.0900	32	0.145
2	2011/06/01 01:41:19.6	4.2	37.6583	141.7617	44	0.088
3	2011/06/01 06:23:27.2	3.4	37.1167	140.8400	7	0.061
4	2011/06/03 21:44:38.7	4.2	37.2783	141.4683	36	0.040
5	2011/06/04 01:00:14.1	5.5	36.9900	141.2100	30	1.923
6	2011/06/04 09:03:33.7	4.3	37.2683	141.4783	36	0.147
7	2011/06/04 10:41:10.0	4.1	37.0033	141.1933	28	0.083
8	2011/06/05 17:32:38.9	3.5	37.1117	140.8217	7	0.281
9	2011/06/05 19:46:06.3	3.9	36.9200	140.7333	14	0.175
10	2011/06/05 20:16:37.0	4.4	37.0500	140.7717	11	0.843
11	2011/06/07 03:11:55.9	2.6	37.1233	140.8540	5	0.020
12	2011/06/09 19:38:32.9	5.7	36.4967	140.9700	13	0.358
13	2011/06/11 00:40:55.4	3.9	36.9367	140.6833	11	0.075
14	2011/06/11 01:41:19.6	3.9	37.4117	141.3983	46	0.087
15	2011/06/12 05:08:58.4	4.5	37.2150	141.2100	21	0.153
16	2011/06/12 17:09:45.4	4.6	36.4117	141.0800	47	0.270
17	2011/06/13 05:59:35.1	4.4	37.3350	141.3283	33	0.180

component. Although the displacements of both components in mode 1 (the fundamental mode) are almost the same, the NS-component displacement is larger than that of the EW component in modes 2 and 3. The amplitude of mode 1 is much larger than the amplitudes of other modes.

#### 6.4 Deconvolution with an arbitrary receiver

By deconvolving observed earthquake records, we obtain the impulse response of a building (Oyunchimeg and Kawakami, 2003; Snieder and Şafak, 2006; Kohler et al., 2007; Todorovska and Trifunac, 2008a). When the height of the building is  $H$ , the recorded signal of an earthquake in the frequency domain at an arbitrary receiver at height  $z$  is given by Snieder

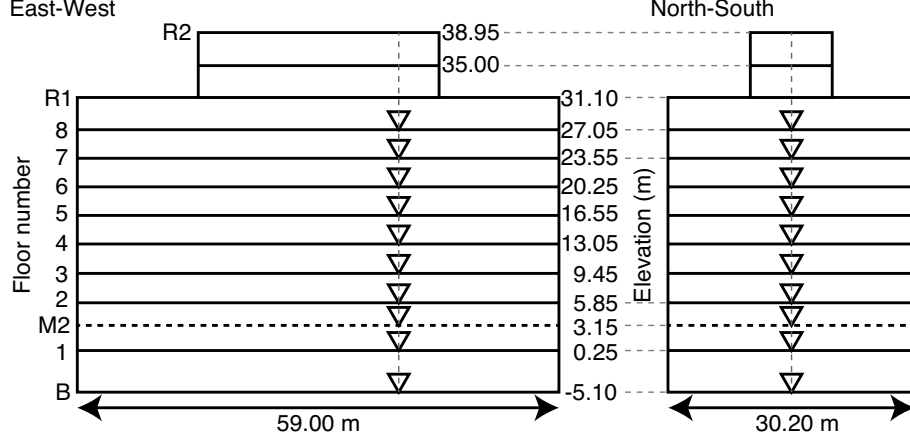


Figure 6.2. The (left) EW and (right) NS vertical cross sections of the building and the positions of receivers (triangles). Elevations denote the height of each floor from ground level. We put receivers on stairs 0.19 m below each floor except for the basement (on the floor) and the first floor (0.38 m below). Receiver M2 is located between the first and second floors. Horizontal-receiver components are aligned with the EW and NS directions.

and Şafak (2006):

$$\begin{aligned}
 u(z) &= \sum_{m=0}^{\infty} S(\omega) R^m(\omega) \{ e^{ik(2mH+z)} e^{-\gamma|k|(2mH+z)} + e^{ik(2(m+1)H-z)} e^{-\gamma|k|(2(m+1)H-z)} \} \\
 &= \frac{S(\omega) \{ e^{ikz} e^{-\gamma|k|z} + e^{ik(2H-z)} e^{-\gamma|k|(2H-z)} \}}{1 - R(\omega) e^{2ikH} e^{-2\gamma|k|H}},
 \end{aligned} \tag{6.1}$$

where  $S(\omega)$  is the incoming waveform to the base of the building,  $R(\omega)$  the reflection coefficient related to the coupling of the ground and the base of the building,  $k$  the wavenumber,  $\gamma$  the attenuation coefficient, and  $i$  the imaginary unit. We use the absolute value of wavenumbers in the damping terms because the waves attenuate regardless of whether the wavenumber is positive or negative. In expression 6.1, we assume the wave vertically propagates in the building (one-dimensional propagation) with constant amplitude and wavenumber, and without internal reflections. The constant wavenumber implies that we assume constant velocity  $c$  because  $k = \omega/c$ . The incoming waveform  $S(\omega)$  includes the source signature of the earthquake and the effect of propagation such as attenuation and scattering along the path from the hypocenter of the earthquake to the base of the building. The attenuation

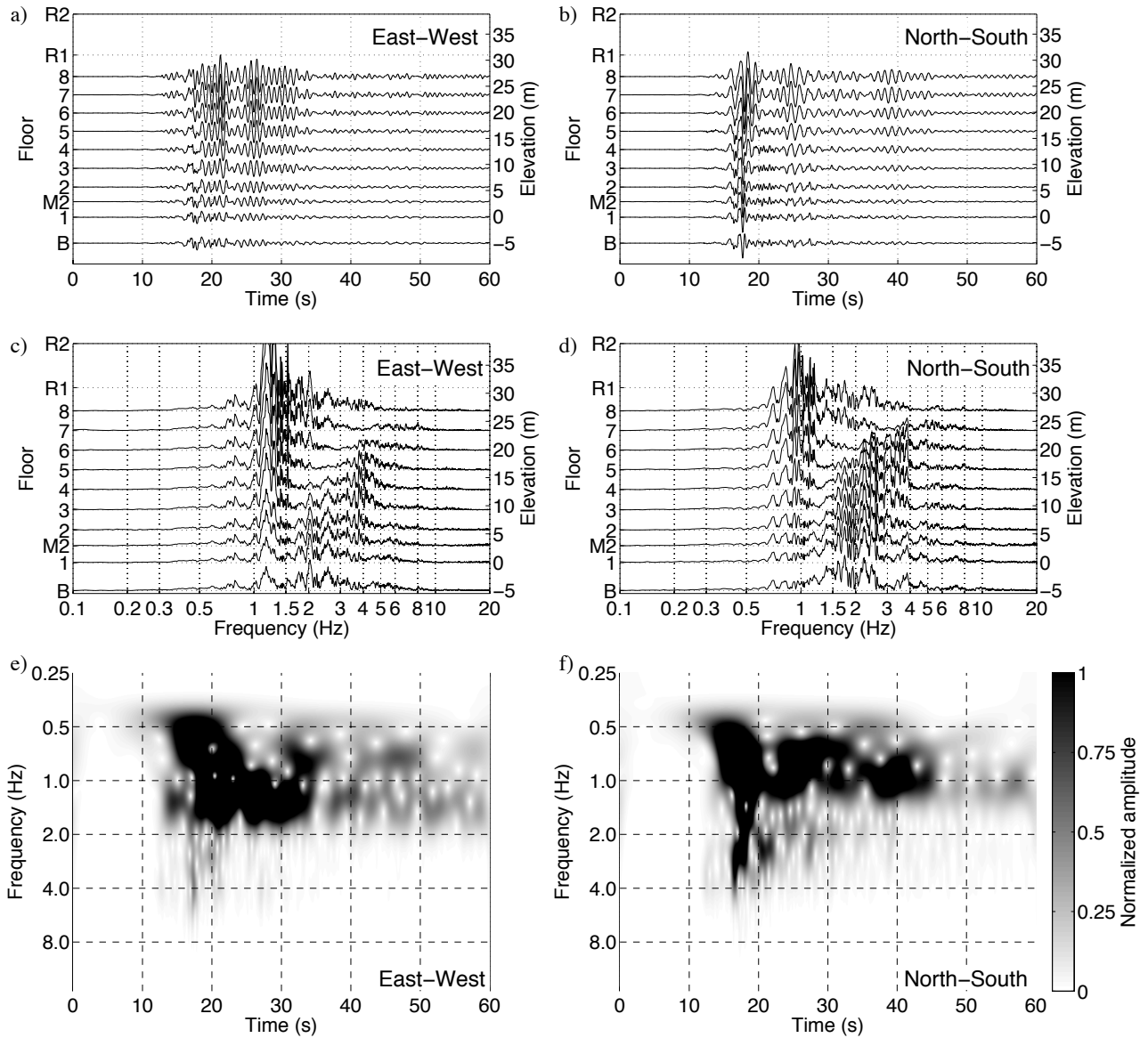


Figure 6.3. Unfiltered waveforms of earthquake No. 5 recorded at the building in (a) the EW component and (b) the NS component, and (c, d) their power spectra. (e, f) Spectrogram computed with continuous-wavelet transformed waveforms recorded at the fourth floor. Time 0 s represents the origin time of the earthquake. We preserve relative amplitudes of the EW and NS components.

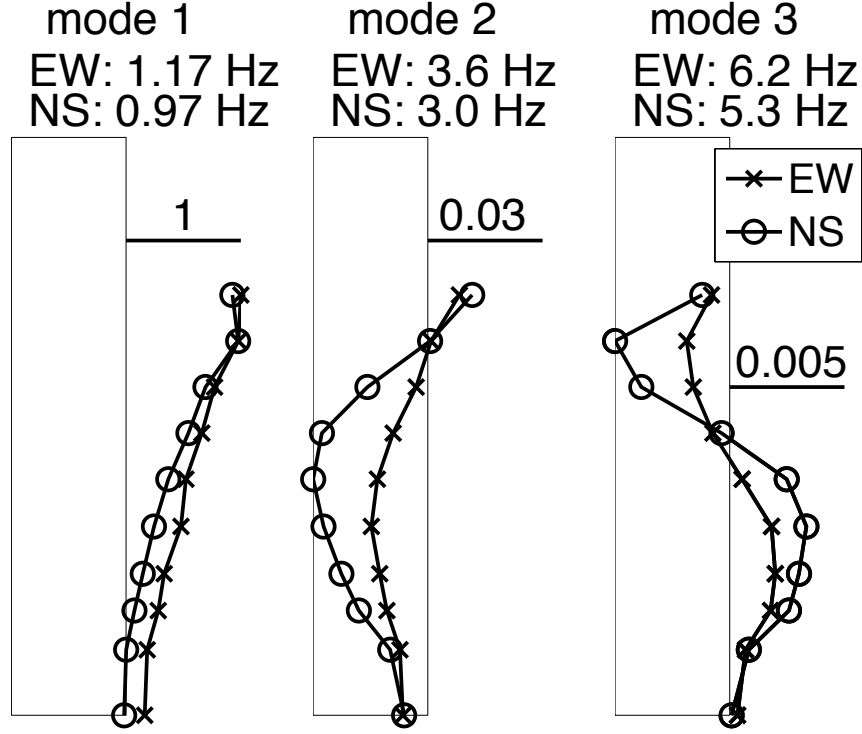


Figure 6.4. Displacement of the first three horizontal normal modes for earthquake No. 5 estimated from the real part of the Fourier spectra at different floors. Each mark indicates the displacement of a receiver. The center frequency of each mode is shown at the top of each panel. Black horizontal lines and the numbers on the lines show the amplitude ratio among modes, and the box depicts the height of the building (R2 in Figure 6.2). The zero displacement is at the right side of each box.

coefficient  $\gamma$  is defined as

$$\gamma = \frac{1}{2Q}, \quad (6.2)$$

with  $Q$  the quality factor (Aki and Richards, 2002).

For  $m = 0$  in the first line in expression 6.1, the first term  $S(\omega)e^{ikz}e^{-\gamma|k|z}$  indicates the incoming upgoing wave and the second term  $S(\omega)e^{ik(2H-z)}e^{-\gamma|k|(2H-z)}$  the downgoing wave, which is reflected off the top of the building. The index  $m$  represents the number of reverberations between the base and top of the building.

As we deconvolve a waveform recorded by a receiver at  $z$  with a waveform observed by another receiver at  $z_a$ , from expression 6.1 we obtain

$$\begin{aligned}
D(z, z_a, \omega) &= \frac{u(z)}{u(z_a)} \\
&= \frac{S(\omega)\{e^{ikz}e^{-\gamma|k|z} + e^{ik(2H-z)}e^{-\gamma|k|(2H-z)}\}}{S(\omega)\{e^{ikz_a}e^{-\gamma|k|z_a} + e^{ik(2H-z_a)}e^{-\gamma|k|(2H-z_a)}\}} \\
&= \sum_{n=0}^{\infty} (-1)^n \left\{ e^{ik(2n(H-z_a)+z-z_a)} e^{-\gamma|k|(2n(H-z_a)+z-z_a)} \right. \\
&\quad \left. + e^{ik(2n(H-z_a)+2H-z-z_a)} e^{-\gamma|k|(2n(H-z_a)+2H-z-z_a)} \right\}, \tag{6.3}
\end{aligned}$$

where we use a Taylor expansion in the last equality. In equation 6.3, the receiver at  $z_a$  behaves as a virtual source. Equation 6.3 may be unstable because of the spectral division. In practice we use a regularization parameter  $\epsilon$  (Yilmaz, 2001, Section 2.3):

$$\begin{aligned}
D(z, z_a, \omega) &= \frac{u(z)}{u(z_a)} \\
&\approx \frac{u(z)u^*(z_a)}{|u(z_a)|^2 + \epsilon\langle|u(z_a)|^2\rangle}, \tag{6.4}
\end{aligned}$$

where  $*$  is a complex conjugate and  $\langle|u(z_a)|^2\rangle$  the average power spectrum of  $u(z_a)$ . In this study we use  $\epsilon = 1\%$ .

Note that these deconvolved waves are independent of the incoming waveform  $S(\omega)$  and the ground coupling  $R(\omega)$ . When we consider substitutions  $S(\omega) \rightarrow 1$ ,  $R(\omega) \rightarrow -1$ ,  $H \rightarrow H - z_a$ , and  $z \rightarrow z - z_a$ , equation 6.1 reduces to equation 6.3. These conditions indicate the physical properties of the deconvolved waveforms: impulse response ( $S(\omega) \rightarrow 1$ ), perfect reflection at the virtual source ( $R(\omega) \rightarrow -1$ ), and a small building ( $H \rightarrow H - z_a$  and  $z \rightarrow z - z_a$ ) as we discuss later.

When  $z > z_a$ , equation 6.3 describes a wave that is excited at  $z_a$  and reverberates between  $z_a$  and the top of the building. Using a normal-mode analysis (equation 6.A4 in Appendix A), the fundamental mode of equation 6.3 in the time domain is given by

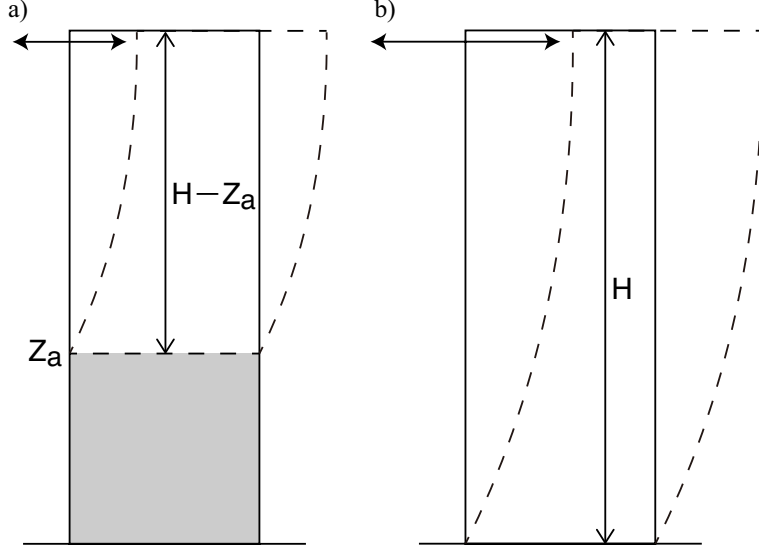


Figure 6.5. Schematic shapes of the fundamental mode retrieved by using seismic interferometry. (a) Fundamental mode retrieved by deconvolving wavefields with a motion recorded at  $z_a$  (equation 6.3). (b) Fundamental mode retrieved by deconvolving wavefields with a motion recorded at the first floor (equation 6.9).

$$D(z, z_a, t) = \frac{4\pi c}{H - z_a} e^{-\gamma\omega_0 t} \sin(\omega_0 t) \cos\left(\omega_0 \frac{H - z}{c}\right), \quad (6.5)$$

where  $\omega_0 = \pi c / \{2(H - z_a)\}$ . The period of the fundamental mode is, thus,

$$T_0 = \frac{4(H - z_a)}{c}, \quad (6.6)$$

which corresponds to the period of the fundamental mode of the building that is cut off at  $z_a$  (cut-off building: Figure 6.5a). According to equation 6.3 the polarity change resulting from reflection at  $z_a$  is given by  $(-1)^n$ , the reflection coefficient at the virtual source is  $-1$ . Therefore, the cut-off building is only sensitive to the properties of the building above  $z_a$ , and the reconstructed wave motion in the cut-off building has the potential to estimate local structure and local damage instead of structure and damage for the entire building.

When  $z < z_a$  and  $n = 0$  in equation 6.3, we obtain two waves: an acausal upgoing wave from  $z$  to  $z_a$  ( $e^{ik(z-z_a)} e^{-\gamma|k|(z-z_a)}$ ) and a causal downgoing wave from  $z_a$  to  $z$

$(e^{ik(2H-z-z_a)}e^{-\gamma|k|(2H-z-z_a)})$ . Waves for  $n \geq 1$  in equation 6.3 account for the reverberations between  $z_a$  and the top of the building. Because  $D(z_a, z_a, \omega) = 1$ , the deconvolved waveforms at  $z_a$  is a delta function in the time domain ( $D(z_a, z_a, t) = \delta(t)$ ); hence  $D(z_a, z_a, t) = 0$  for  $t \neq 0$  (clamped boundary condition (Snieder et al., 2006a, 2009)). The upgoing and downgoing waves interfere destructively at  $z_a$ .

Although we assume, for simplicity, a constant velocity in equation 6.1, we can apply deconvolution interferometry to wavefields observed at a building with smoothly varying velocities. When the velocity  $c$  varies with height, the local wavenumber does so as well, and using the WKBJ approximation for the phase, expression 6.1 generalizes to

$$u(z) = \frac{U}{1 - R(\omega) \exp\left(2i \int_0^H k(z) dz\right) \exp\left(-2\gamma \int_0^H |k(z)| dz\right)} \quad (6.7)$$

with

$$U = S(\omega) \left[ \exp\left(i \int_0^z k(z) dz\right) \exp\left(-\gamma \int_0^z |k(z)| dz\right) + \exp\left\{i \left(\int_0^H k(z) dz + \int_z^H k(z) dz\right)\right\} \exp\left\{-\gamma \left(\int_0^H |k(z)| dz + \int_z^H |k(z)| dz\right)\right\} \right],$$

and equation 6.3 generalizes in this case to

$$\begin{aligned} & D(z, z_a, \omega) \\ &= \sum_{n=0}^{\infty} (-1)^n \left[ \exp\left\{i \left(2n \int_{z_a}^H k(z) dz + \int_{z_a}^z k(z) dz\right)\right\} \exp\left\{-\gamma \left(2n \int_{z_a}^H |k(z)| dz + \int_{z_a}^z |k(z)| dz\right)\right\} \right. \\ &+ \exp\left\{i \left((2n+1) \int_{z_a}^H k(z) dz + \int_z^H k(z) dz\right)\right\} \\ &\left. \times \exp\left\{-\gamma \left((2n+1) \int_{z_a}^H |k(z)| dz + \int_z^H |k(z)| dz\right)\right\} \right]. \end{aligned} \quad (6.8)$$

As for equation 6.3, equation 6.8 represents the waves in a cut-off building at  $z_a$ , and the period of the fundamental mode of the cut-off building depends on the slowness averaged between  $z_a$  and  $H$ . Note that when  $z > z_a$ ,  $D(z, z_a, \omega)$  in equation 6.8 is only related to  $k(z)$

above  $z_a$ .

When  $z_a$  is at the first floor ( $z_a = 0$ ) or at the top of the building ( $z_a = H$ ), equation 6.3 corresponds to equations 26 or 21 in Snieder and Şafak (2006), respectively, which we rewrite here as

$$D(z, 0, \omega) = \sum_{n=0}^{\infty} (-1)^n \left\{ e^{ik(2nH+z)} e^{-\gamma|k|(2nH+z)} + e^{ik(2(n+1)H-z)} e^{-\gamma|k|(2(n+1)H-z)} \right\}, \quad (6.9)$$

$$D(z, H, \omega) = \frac{1}{2} \left\{ e^{ik(H-z)} e^{-\gamma|k|(H-z)} + e^{-ik(H-z)} e^{\gamma|k|(H-z)} \right\}. \quad (6.10)$$

Figure 6.5b illustrates a schematic shape of the fundamental mode as given in equation 6.9. The period of the mode in equation 6.9 is related to the structure of the entire building as if the building were placed on a rigid subsurface (i.e., the reflection coefficient at the base is  $-1$ ). When we put a receiver at the top floor (8 in Figure 6.2) of a building instead of the rooftop ( $R_1$  or  $R_2$  in Figure 6.2), we theoretically do not obtain the response in equation 6.10 because the traveling waves reflect at the top of the building rather than at the top floor. In this case, the deconvolved response follows equation 6.3. This difference may be insignificant when the wavelength of the traveling waves is much longer than the distance between the top floor and the top of the building.

## 6.5 Crosscorrelation and crosscoherence interferometry

In the previous section, we focused on seismic interferometry based on deconvolution. Let us consider seismic interferometry based on crosscorrelation (e.g., Schuster et al., 2004) and crosscoherence (e.g., Nakata et al., 2011); these two methods are the widest-applied technique and the earliest application (Aki, 1957), respectively.

### 6.5.1 Crosscorrelation

From equation 6.1, the crosscorrelation of  $u(z)$  and  $u(z_a)$  is

$$\begin{aligned}
C(z, z_a, \omega) &= u(z)u^*(z_a) \\
&= |S(\omega)|^2 \frac{\{e^{ikz}e^{-\gamma|k|z} + e^{ik(2H-z)}e^{-\gamma|k|(2H-z)}\} \{e^{-ikz_a}e^{-\gamma|k|z_a} + e^{-ik(2H-z_a)}e^{-\gamma|k|(2H-z_a)}\}}{1 - R(\omega)e^{2ikH}e^{-2\gamma|k|H} - R^*(\omega)e^{-2ikH}e^{-2\gamma|k|H} + |R(\omega)|^2e^{-4\gamma|k|H}}.
\end{aligned} \tag{6.11}$$

In contrast to the deconvolution (equation 6.3), equation 6.11 depends on the incoming wave  $S(\omega)$  and the ground coupling  $R(\omega)$ , and does not create a clamped boundary condition ( $C(z_a, z_a, \omega) \neq 1$ ). Because of the presence of the reflection coefficient  $R(\omega)$  and the power spectrum  $|S(\omega)|^2$ , it is much more complicated to estimate the properties (e.g., traveling-wave velocity and attenuation) of the building from crosscorrelation than from deconvolution.

When  $z_a = 0$  and  $z_a = H$ , equation 6.11 reduces to

$$C(z, 0, \omega) = |S(\omega)|^2 \frac{e^{ikz}e^{-\gamma|k|z} + e^{-ikz}e^{-\gamma|k|(4H-z)} + e^{ik(2H-z)}e^{-\gamma|k|(2H-z)} + e^{-ik(2H-z)}e^{-\gamma|k|(2H+z)}}{1 - R(\omega)e^{2ikH}e^{-2\gamma|k|H} - R^*(\omega)e^{-2ikH}e^{-2\gamma|k|H} + |R(\omega)|^2e^{-4\gamma|k|H}}, \tag{6.12}$$

$$C(z, H, \omega) = 2|S(\omega)|^2 \frac{e^{-2\gamma|k|H} \{e^{ik(H-z)}e^{-\gamma|k|(H-z)} + e^{-ik(H-z)}e^{\gamma|k|(H-z)}\}}{1 - R(\omega)e^{2ikH}e^{-2\gamma|k|H} - R^*(\omega)e^{-2ikH}e^{-2\gamma|k|H} + |R(\omega)|^2e^{-4\gamma|k|H}}, \tag{6.13}$$

respectively. If  $R(\omega) = 0$  (no reflection at the base), equation 6.13 is, apart from the prefactor  $2|S(\omega)|^2e^{-2\gamma|k|H}$ , the same as equation 6.10.

### 6.5.2 Crosscoherence

Crosscoherence is defined as frequency-normalized crosscorrelation:

$$CH(z, z_a, \omega) = \frac{u(z)u^*(z_a)}{|u(z)||u(z_a)|} \approx \frac{u(z)u^*(z_a)}{|u(z)||u(z_a)| + \epsilon' \langle |u(z)||u(z_a)| \rangle} \tag{6.14}$$

Similar to equation 6.4, we use a regularization parameter  $\epsilon'$  in the last equality in practice. In this study, we use  $\epsilon' = 0.1\%$ . For mathematical interpretation, using Taylor expansions of  $\sqrt{1+X}$  and  $1/\sqrt{1+X}$  for  $X < 1$ , the crosscoherence between  $u(z)$  and  $u(z_a)$  is given by

$$\begin{aligned}
CH(z, z_a, \omega) &= \frac{u(z)u^*(z_a)}{|u(z)||u(z_a)|} = \frac{u(z)u^*(z_a)}{\sqrt{u(z)u^*(z)}\sqrt{u(z_a)u^*(z_a)}} = \frac{\sqrt{u(z)}\sqrt{u^*(z_a)}}{\sqrt{u^*(z)}\sqrt{u(z_a)}} \\
&= \sqrt{\frac{\{e^{ikz}e^{-\gamma|k|z} + e^{ik(2H-z)}e^{-\gamma|k|(2H-z)}\} \{e^{-ikz_a}e^{-\gamma|k|z_a} + e^{-ik(2H-z_a)}e^{-\gamma|k|(2H-z_a)}\}}{\{e^{-ikz}e^{-\gamma|k|z} + e^{-ik(2H-z)}e^{-\gamma|k|(2H-z)}\} \{e^{ikz_a}e^{-\gamma|k|z_a} + e^{ik(2H-z_a)}e^{-\gamma|k|(2H-z_a)}\}}} \\
&= e^{ik(z-z_a)} \times \left[ 1 + \frac{1}{2} \sum_{n=1}^{\infty} \left\{ \frac{e^{2ink(H-z)}e^{-2n\gamma|k|(H-z)}}{n!} A_{n-1} \right\} \right] \\
&\quad \times \left[ 1 + \frac{1}{2} \sum_{n=1}^{\infty} \left\{ \frac{e^{-2ink(H-z_a)}e^{-2n\gamma|k|(H-z_a)}}{n!} A_{n-1} \right\} \right] \\
&\quad \times \left[ 1 + \sum_{n=1}^{\infty} \left\{ \frac{e^{-2ink(H-z)}e^{-2n\gamma|k|(H-z)}}{n!} A_n \right\} \right] \\
&\quad \times \left[ 1 + \sum_{n=1}^{\infty} \left\{ \frac{e^{2ink(H-z_a)}e^{-2n\gamma|k|(H-z_a)}}{n!} A_n \right\} \right], \tag{6.15}
\end{aligned}$$

where  $A_0 = 1$  and  $A_n = (2n-1)!!/(-2)^n$ . As for deconvolution interferometry, equation 6.15 does not depend on  $S(\omega)$  and  $R(\omega)$ . For a complex number  $z = re^{i\phi}$ , the square root is defined as  $\sqrt{z} = \sqrt{r}e^{i\phi/2}$ . Furthermore, the waveforms of crosscoherence interferometry satisfies a clamped boundary condition at  $z = z_a$  ( $CH(z_a, z_a, \omega) = 1$ , hence  $CH(z_a, z_a, t) = \delta(t)$ , and  $CH(z_a, z_a, t) = 0$  for  $t \neq 0$ ).

For  $z_a = 0$  and  $z_a = H$ , equation 6.15 simplifies to

$$\begin{aligned}
CH(z, 0, \omega) &= e^{ikz} \times \left[ 1 + \frac{1}{2} \sum_{n=1}^{\infty} \left\{ \frac{e^{2ink(H-z)}e^{-2n\gamma|k|(H-z)}}{n!} A_{n-1} \right\} \right] \\
&\quad \times \left[ 1 + \frac{1}{2} \sum_{n=1}^{\infty} \left\{ \frac{e^{-2inkH}e^{-2n\gamma|k|H}}{n!} A_{n-1} \right\} \right] \\
&\quad \times \left[ 1 + \sum_{n=1}^{\infty} \left\{ \frac{e^{-2ink(H-z)}e^{-2n\gamma|k|(H-z)}}{n!} A_n \right\} \right] \\
&\quad \times \left[ 1 + \sum_{n=1}^{\infty} \left\{ \frac{e^{2inkH}e^{-2n\gamma|k|H}}{n!} A_n \right\} \right], \tag{6.16}
\end{aligned}$$

$$\begin{aligned}
CH(z, H, \omega) = & e^{ik(z-H)} \times \left[ 1 + \frac{1}{2} \sum_{n=1}^{\infty} \left\{ \frac{e^{2ink(H-z)} e^{-2n\gamma|k|(H-z)}}{n!} A_{n-1} \right\} \right] \\
& \times \left[ 1 + \sum_{n=1}^{\infty} \left\{ \frac{e^{-2ink(H-z)} e^{-2n\gamma|k|(H-z)}}{n!} A_n \right\} \right], \tag{6.17}
\end{aligned}$$

respectively. Note that because of the complexity of crosscoherence interferometry, equations 6.15–6.17 contain pseudo events which propagate at slower velocities than the true velocity of the building. For example, equation 6.16 can be expanded into

$$\begin{aligned}
CH(z, 0, \omega) = & e^{ikz} \left\{ 1 - \frac{1}{4} e^{-4\gamma|k|(H-z)} - \frac{1}{4} e^{-4\gamma|k|H} \right\} + \frac{1}{4} e^{-ikz} e^{-2\gamma|k|(2H-z)} + \frac{1}{4} e^{3ikz} e^{-2\gamma|k|(2H-z)} \\
& - \frac{1}{2} e^{-ik(2H-3z)} e^{-2\gamma|k|(H-z)} - \frac{1}{2} e^{ik(2H+z)} e^{-2\gamma|k|H} \\
& + \frac{1}{2} e^{ik(2H-z)} e^{-2\gamma|k|(H-z)} + \frac{1}{2} e^{-ik(2H-z)} e^{-2\gamma|k|H} \\
& + \frac{3}{8} e^{-ik(4H-5z)} e^{-4\gamma|k|(H-z)} - \frac{1}{8} e^{-ik(4H-z)} e^{-4\gamma|k|H} - \frac{1}{4} e^{ik(4H-z)} e^{-2\gamma|k|(2H-z)} \\
& + \frac{3}{8} e^{-ik(4H-z)} e^{-4\gamma|k|H} - \frac{1}{8} e^{ik(4H-3z)} e^{-4\gamma|k|(H-z)} - \frac{1}{4} e^{-ik(4H-3z)} e^{-2\gamma|k|(2H-z)} \\
& + O(e^{-6\gamma|k|(H-z)}). \tag{6.18}
\end{aligned}$$

The terms  $e^{3ikz} e^{-2\gamma|k|(2H-z)}/4$  and  $-e^{-ik(2H-3z)} e^{-2\gamma|k|(H-z)}/2$  indicate waves that propagate at one third of the true velocity, and the term  $3e^{-ik(4H-5z)} e^{-4\gamma|k|(H-z)}/8$  at one fifth. These unphysical waves complicate the estimation of the velocity of traveling waves by applying crosscoherence interferometry to earthquake data.

### 6.5.3 Comparison of deconvolution, crosscorrelation, and crosscoherence

Each type of interferometry has different properties (e.g., amplitude or complexity). It follows from expressions 6.4, 6.11, and 6.14 that in the frequency domain the phases obtained by interferometry based on deconvolution, crosscorrelation, and crosscoherence are the same. The spectral amplitude is different, though, and this leads to different waveforms in the time domain. We list in Table 6.2 the amplitudes of the first four causal waves propagating at the true velocity of the building for observed record, deconvolution, crosscorrelation,

Table 6.2. Amplitudes of traveling waves obtained from observed records and computed by seismic interferometry based on deconvolution, crosscorrelation, and crosscoherence for  $z_a = 0$  (equations 6.1, 6.9, 6.12, and 6.16). We compute the amplitudes of crosscorrelation interferometry in Appendix B. For crosscoherence interferometry we ignore wavefields which attenuate faster than  $e^{-6\gamma|k|(H-z)}$ .

Phase	Observed record	Deconvolution	Crosscorrelation	Crosscoherence
$e^{ikz}$	$S(\omega)e^{-\gamma k z}$	$e^{-\gamma k z}$	$C_1$	$CH_1$
$e^{ik(2H-z)}$	$S(\omega)e^{-\gamma k (2H-z)}$	$e^{-\gamma k (2H-z)}$	$C_2$	$\frac{1}{2}e^{-2\gamma k (H-z)}$
$e^{ik(2H+z)}$	$S(\omega)R(\omega)e^{-\gamma k (2H+z)}$	$-e^{-\gamma k (2H+z)}$	$C_3$	$-\frac{1}{2}e^{-2\gamma k H}$
$e^{ik(4H-z)}$	$S(\omega)R(\omega)e^{-\gamma k (4H-z)}$	$-e^{-\gamma k (4H-z)}$	$C_4$	$-\frac{1}{4}e^{-2\gamma k (2H-z)}$

$$\begin{aligned}
C_1 &= |S(\omega)|^2 e^{-\gamma|k|z} \{1 + R(\omega)e^{-4\gamma|k|H}\} \left\{ \sum_{n=0}^{\infty} |R(\omega)|^{2n} e^{-4n\gamma|k|H} \right\} \\
C_2 &= |S(\omega)|^2 e^{-\gamma|k|(2H-z)} \{1 + R(\omega)e^{-4\gamma|k|H}\} \left\{ \sum_{n=0}^{\infty} |R(\omega)|^{2n} e^{-4n\gamma|k|H} \right\} \\
C_3 &= |S(\omega)|^2 R(\omega)e^{-\gamma|k|(2H+z)} \{1 + R(\omega)e^{-4\gamma|k|H}\} \left\{ \sum_{n=0}^{\infty} |R(\omega)|^{2n} e^{-4n\gamma|k|H} \right\} \\
C_4 &= |S(\omega)|^2 R(\omega)e^{-\gamma|k|(4H-z)} \{1 + R(\omega)e^{-4\gamma|k|H}\} \left\{ \sum_{n=0}^{\infty} |R(\omega)|^{2n} e^{-4n\gamma|k|H} \right\} \\
CH_1 &= 1 - \frac{1}{4}e^{-4\gamma|k|(H-z)} - \frac{1}{4}e^{-4\gamma|k|H}
\end{aligned}$$

and crosscoherence (equations 6.1, 6.9, 6.12, and 6.16, respectively). For crosscorrelation interferometry, we calculate the amplitudes of the traveling waves in Appendix B using Taylor expansions. Although the amplitudes of crosscorrelation are complicated due to the reflection coefficient  $R(\omega)$  and the power spectrum  $|S(\omega)|^2$ , the ratios of amplitudes for each pair of traveling waves are the same as those for observed records. The amplitudes of the waveforms obtained by crosscoherence are independent of incoming waveform  $S(\omega)$  and reflection coefficient  $R(\omega)$ , but the ratio of amplitudes varies between each pair of traveling waves. Therefore, estimating attenuation of the building using crosscoherence interferometry is problematic. Since the amplitudes of the deconvolved waveforms are independent of  $S(\omega)$  and  $R(\omega)$  and depend exponentially on the traveled distance, deconvolution interferometry

can be used to estimate attenuation of the building.

We numerically compute synthetic waveforms excited at 0 m by an impulsive source ( $S(\omega) = 1$ ) based on equation 6.1 shown in Figure 6.6a. In the computation, we use the following parameters:  $H = 100$  m,  $R(\omega) = 0.5$ ,  $Q = 3000$ , and  $c = 200$  m/s. In applying seismic interferometry, we compute deconvolution ( $\{u(z)u^*(0)\} / \{|u(0)|^2 + \epsilon\langle|u(0)|^2\rangle\}$ : Figure 6.6b), crosscorrelation ( $u(z)u^*(0)$ : Figure 6.6c), and crosscoherence ( $\{u(z)u^*(0)\} / \{|u(z)||u(0)| + \epsilon'\langle|u(z)||u(0)|\rangle\}$ : Figure 6.6d), where  $\epsilon = 1\%$  and  $\epsilon' = 0.1\%$ , using the synthetic waveforms shown in Figure 6.6a. In Figures 6.6b–6.6d, the virtual source is at  $z = 0$  m. Deconvolved waveforms (Figure 6.6b) arrive at the same time as the waves in the synthetic records, but the polarization is reversed when the wave is reflected at  $z = 0$  m due to the clamped boundary condition. In crosscorrelation interferometry (Figure 6.6c), the causal waves arrive at the same time as the waves in the synthetic records (Figure 6.6a), and the acausal waves are kinematically identical to the time-reversed causal waves. Although for simplicity we use  $S(\omega) = 1$  in Figure 6.6, the incoming wave complicates the crosscorrelated waveforms when we use real earthquake data, and picking the arrival times of the traveling waves may be difficult in that case. Crosscoherence interferometry creates traveling waves which propagate at slower velocities than true velocity  $c = 200$  m/s. In Figure 6.6d, the gray line highlights the wave  $-e^{-ik(2H-3z)}e^{-2\gamma|k|(H-z)}/2$ , which travels with one third of the true wave speed (66.7 m/s). To estimate the velocity of the traveling waves, therefore, deconvolution interferometry is useful.

We highlight the amplitudes of the waves in Figure 6.6 with the circles. A comparison of Figures 6.6a and 6.6b shows that the ratios of the amplitudes of the synthetic records and deconvolved waves within the first two circles are the same, but the ratios in the second and third circles are different. The reflection coefficient at 0 m of the synthetic records is  $R(\omega)$  while the reflection coefficient of waves obtained by deconvolution interferometry is  $-1$ ; see the numbers next to the arrows in Figures 6.6a and 6.6b. The difference between the reflection coefficients implies that deconvolved waveforms are independent from the ground

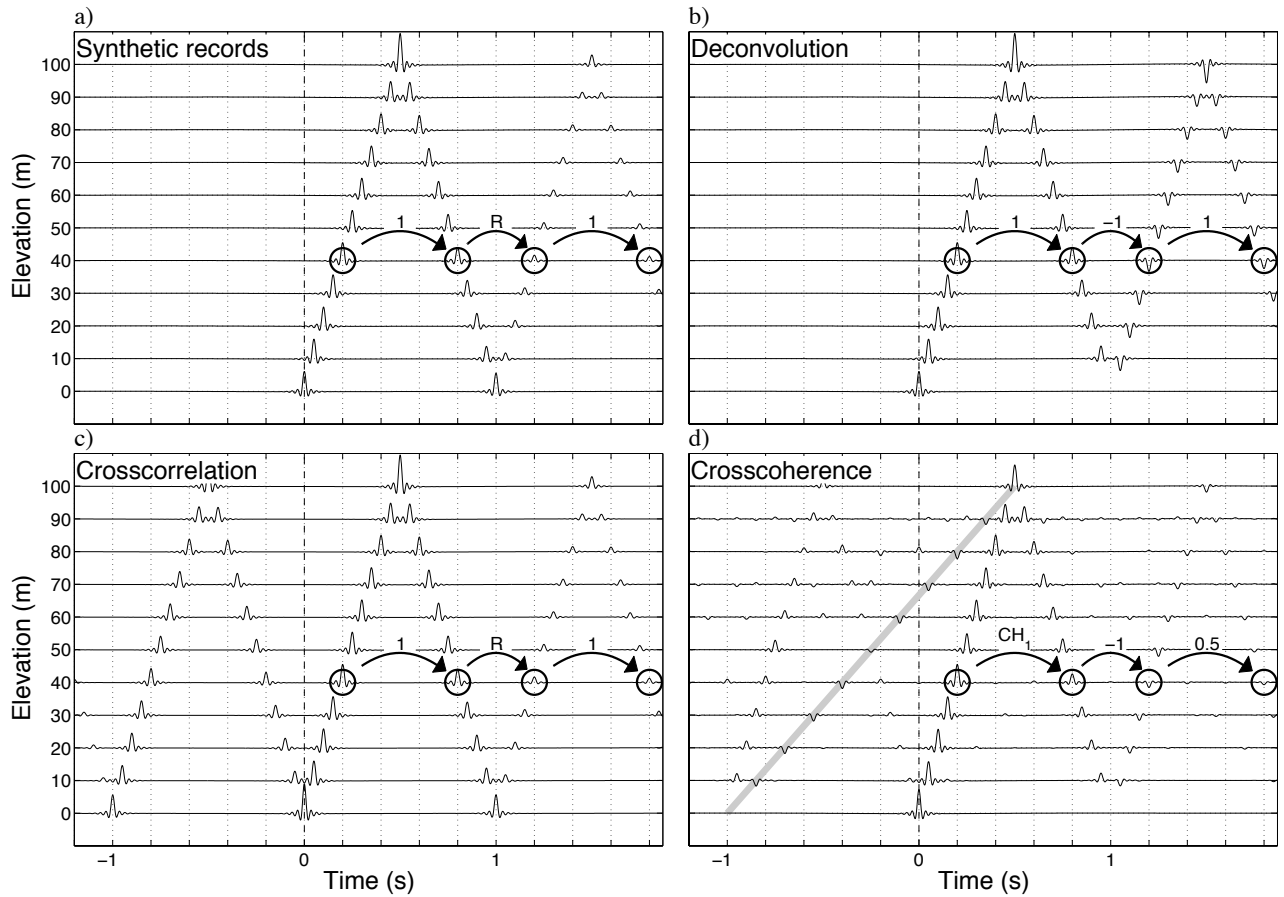


Figure 6.6. (a) Synthetic waveforms based on equation 6.1. We numerically calculate waveforms with an impulse response ( $S(\omega) = 1$ ) at  $t = 0$  s at 0 m,  $R(\omega) = 0.5$ ,  $Q = 3000$ ,  $H = 100$  m, and  $c = 200$  m/s. Interferometric waveforms by computing deconvolution (panel b: equation 6.9), crosscorrelation (panel c: equation 6.12), and crosscoherence (panel d: equation 6.16) using waveforms shown in panel (a). The virtual source for interferometry is at the 0-m receiver. We apply a bandpass filter 0.5-1-30-40 Hz after computing each waveform. The circles in each panel highlight four waves which are discussed in the main text. The numbers near each arrow indicate the ratio of the amplitude difference between two waves highlighted by the circles apart from the attenuation expected from the traveling distance at the correct velocity. To estimate the ratio of amplitude in panel (d), we ignore wavefields which attenuate faster than  $e^{-6\gamma|k|(H-z)}$ , and  $CH_1 = 2/(4 - e^{-4\gamma|k|(H-z)} - e^{-4\gamma|k|H})$  where  $z = 40$  m. Amplitudes in each panel are normalized by the amplitude of the first highlighted wave (at  $t=0.2$  s). The gray line in panel (d) shows the wave which propagates at 66.67 m/s.

coupling, and the decay of amplitudes of the waves are only related to the attenuation of the building. The ratios of the amplitudes of the waves highlighted by the circles in cross-correlation interferometry are the same as those in the synthetic records; see the numbers next to the arrows in Figures 6.6a and 6.6c. Hence, both the building and the soil-structure coupling influence the amplitudes of crosscorrelated waveforms. In crosscoherence interferometry (Figure 6.6d), the ratios of the amplitudes of the waves within the circles are different from either synthetic records or deconvolution interferometry. When we consider the amplitudes of each interferometry, deconvolution interferometry is useful for estimating the attenuation of the building.

Based on equations 6.11–6.18, Table 6.2, and Figure 6.6, we conclude that deconvolution interferometry is suitable for application to earthquake records to estimate the velocity and attenuation of the building. Crosscorrelated waveforms depend on the incoming wave  $S(\omega)$  and the ground coupling  $R(\omega)$ . Crosscoherence interferometry creates pseudo events, and the decay of amplitudes of waveforms reconstructed by crosscoherence is not exponentially depending on the traveled distances. Therefore, these types of interferometry are not appropriate to estimate velocity and attenuation.

Snieder et al. (2006a) show that the wavefields obtained from deconvolution interferometry satisfy the same wave equation as the wavefield of the real building for an external source. Using this idea, we explain why crosscoherence interferometry creates unphysical events. Following Snieder et al. (2006a), we denote the linear differential operator that defines the wave propagation by  $L(z)$  (e.g., for the one-dimensional wave equation  $L(z) = d^2/dz^2 + \omega^2/c^2(z)$ ). The operator acts on the space variable  $z$ . For an internal source at  $z_0$ , the wavefield  $u(z)$  (equation 6.1) satisfies  $L(z)u(z) = F(z_0)$  where  $F$  is the excitation at  $z_0$ . For an external source, on the other hand,  $u(z)$  satisfies  $L(z)u(z) = 0$ ; this homogeneous equation applies to earthquake data. Applying the operator  $L(z)$  to equations 6.3, 6.11, and 6.14, respectively, gives

$$L(z)D(z, z_a, \omega) = L(z) \frac{u(z)}{u(z_a)} = \frac{1}{u(z_a)} L(z)u(z) = 0, \quad (6.19)$$

$$L(z)C(z, z_a, \omega) = L(z)u(z)u^*(z_a) = \{L(z)u(z)\} u^*(z_a) = 0, \quad (6.20)$$

$$L(z)CH(z, z_a, \omega) = L(z) \frac{u(z)u^*(z_a)}{|u(z)||u(z_a)|} = \frac{u^*(z_a)}{|u(z_a)|} L(z) \left( \frac{u(z)}{|u(z)|} \right) \neq 0, \quad (6.21)$$

where we used that  $L(z)$  acts on the  $z$ -coordinate only. Crosscoherence interferometry (equation 6.21) does not produce a wavefield that satisfies the wave equation of the real building, but deconvolution and crosscorrelation interferometry do satisfy the wave equation. Equation 6.21 shows that crosscoherence interferometry creates unphysical internal sources that complicate wavefields obtained from crosscoherence.

## 6.6 Deconvolved waveforms generated from an earthquake

As an illustration of the data analysis, we first show the application of deconvolution interferometry to the records of earthquake No. 5. We first estimate whether the reflection point of the traveling wave is at R1 or R2 because the building has a penthouse (Figure 6.2). Figure waveforms deconvolved by the motion recorded at the first floor (equation 6.9) for the EW and NS components. We apply a 0.4-0.5-45-50 Hz sine-squared bandpass filter to the deconvolved waveforms. Because the physical property at the basement is different from the other floors, we do not deconvolve with the motion in the basement in this study. During the first several hundred milliseconds in Figure 6.7, the waveforms depict a traveling wave excited at the first floor at  $t = 0$  s. The wave is reflected off the top of the building and propagates down, and then reflects again at the first floor with the opposite polarization because the reflection coefficient of the deconvolved waves at the first floor is equal to  $-1$  (according to equation 6.9). While reverberating between the first floor and the top of the building, higher frequencies attenuate and the fundamental mode is dominant for later times.

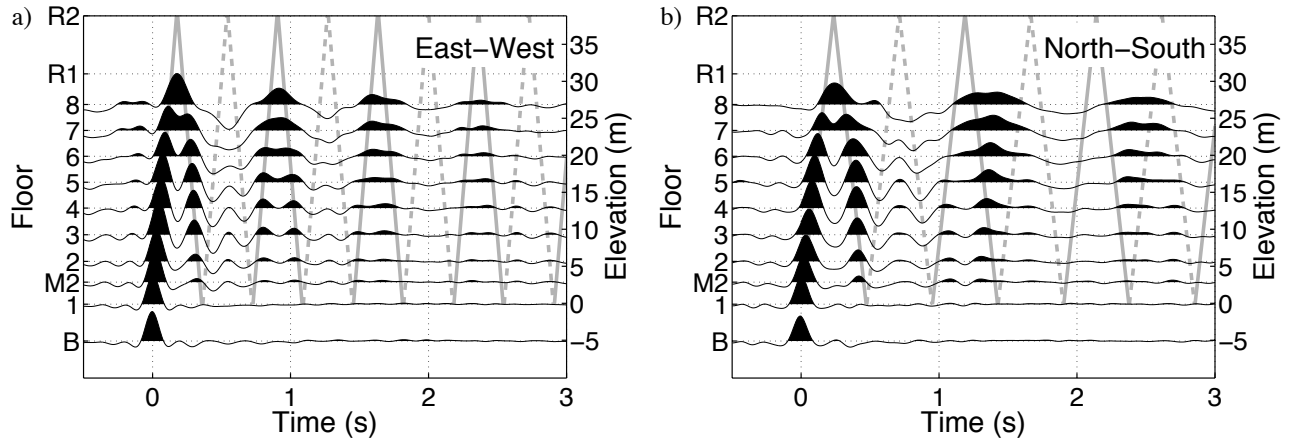


Figure 6.7. Deconvolved waveforms, in which the virtual source is at the first floor, of earthquake No. 5 after applying a bandpass filter 0.4-0.5-45-50 Hz in the (a) EW and (b) NS components. Gray lines indicate the arrival time of traveling waves with the velocity that is estimated from the least-squares fitting of the first upgoing and downgoing waves. We repeat the gray lines after the second traveling waves based on equation 6.9. Solid gray lines highlight the waves in the positive polarization and dashed gray lines the waves in the negative polarization.

To estimate the velocity of the traveling wave and the location of the reflection point, we compute the travel-time curve using a least-squares fitting of the picked travel times on the first upgoing and downgoing waves at each floor (the first two solid gray lines in Figure 6.7). For picking the travel times, we seek the maximum amplitude time in each traveling wave. We repeatedly draw the reverberating travel-wave paths based on equation 6.9 using the velocity estimated from the first upgoing and downgoing waves (in Figure 6.7). To avoid large uncertainties, we use the picked travel times between floors one through five in the EW component and between floors one through six in the NS component because at these floors the positive amplitudes of the upgoing and downgoing waves do not overlap. Both travel-time curves in the EW and NS components indicate that the waves reflect off the top of the penthouse (R2), and the velocity is  $214 \pm 9$  m/s in the EW direction and  $158 \pm 7$  m/s in the NS direction, respectively, where the uncertainties are one standard deviation of measurements. Because the NS side is shorter, the velocity in the NS component is slower. The deconvolved waveforms in the NS component show large deviation from expected arrival

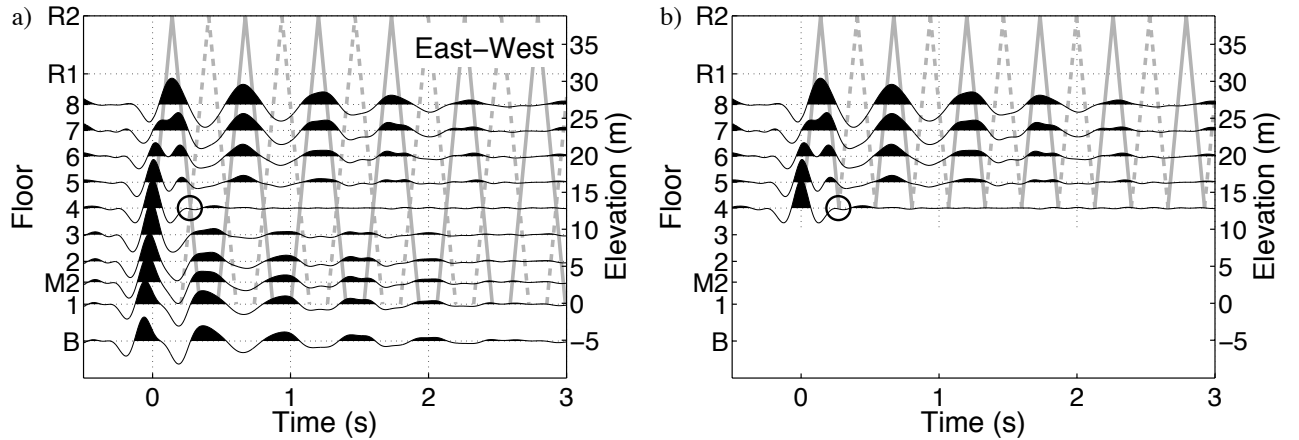


Figure 6.8. (a) Deconvolved waveforms, in which the virtual source is at the fourth floor, of earthquake No. 5 after applying a bandpass filter 0.4-0.5-45-50 Hz in the EW component. The gray lines indicate the travel paths expected from the velocity 195 m/s and equation 6.3. Solid gray lines highlight the waves in the positive polarization and dashed gray lines the waves in the negative polarization. The circle indicates the point where the positive and negative polarization waves cancel. (b) The same waveforms shown in panel (a) but omitting deconvolved waveforms lower than the fourth floor. When we focus on the cut-off building above the fourth floor, the reflection coefficient at the circle is  $-1$ .

times shown in the gray lines in Figure 6.7b, which indicates that the frequency dispersion in the NS component is larger than in the EW component. In the following, we focus on the EW-component analysis.

In Appendix C, we apply crosscorrelation and crosscoherence interferometry to records in the EW component. Because of the power spectrum of the incoming wave, we cannot obtain traveling waves using crosscorrelation interferometry (Figure 6.C1c). We can estimate the velocity of traveling waves from the waveforms created by crosscoherence interferometry, but cannot estimate attenuation because the fundamental mode is not reconstructed (Figure 6.C1d).

Next, we deconvolve the wavefields with the motion recorded by the receiver at the fourth floor (Figure 6.8), where the fourth-floor receiver behaves as a virtual source and satisfies a clamped boundary condition; then we apply the same bandpass filter as used in Figure 6.7. We can interpret waveforms in Figure 6.8 in two ways, which are explained using Figures

6.8a and 6.8b. We obtain upgoing and downgoing waves, which interfere at the fourth floor. At the circle in Figure 6.8a, the upgoing wave from the bottom and downgoing wave from the top cancel, and the deconvolved waveform at the fourth floor vanishes for nonzero time, which is due to the fact that the waveform at the virtual source is a band-limited delta function.

The fourth floor also behaves as the reflection point with reflection coefficient  $-1$  (equation 6.3), which means we can separate the building to two parts: above and below the virtual source. Figure 6.8b shows the building above the virtual source. At the circle in Figure 6.8b, the downgoing wave with positive polarization from the top is perfectly reflected as the negative-polarization upgoing wave. Since we obtain an upgoing wave from the virtual source and reverberations between the fourth floor and the top of the building, this example of interferometry creates the response of a cut-off building that is independent from the structure below the fourth floor (see equation 6.3 and Figure 6.8b). Similar to Figure 6.7, the fundamental mode for the cut-off building (equation 6.3 and Figure 6.5a) is dominant for later times in Figure 6.8b. Note the similarity between Figures 6.7a and 6.8b; both figures show traveling waves and fundamental mode. The period of the normal mode in Figure 6.8b is shorter than in Figure 6.7a as is expected from equation 6.6. Interestingly, because the cut-off building is independent from the structure below the fourth floor, this fictitious building is useful for detecting local structure and local damage of the building.

Applying a least-squares fit of the travel times of the first upgoing wave at the first to fourth floors ( $n = 0$  and  $0 \leq z \leq z_a$  in equation 6.3), we obtain the velocity of traveling waves to be  $195 \pm 25$  m/s. To avoid large uncertainties, we use the travel times at the first to fourth floors to estimate the velocity. At these floors, the upgoing waves are well separated from the downgoing waves. For the cut-off building, by estimating the velocity from the deconvolved waveforms at the floors only below or above the virtual source, we can obtain the velocity which is only related to the structure below or above the virtual source because the virtual source satisfies the clamped boundary conditions. The structure between the first

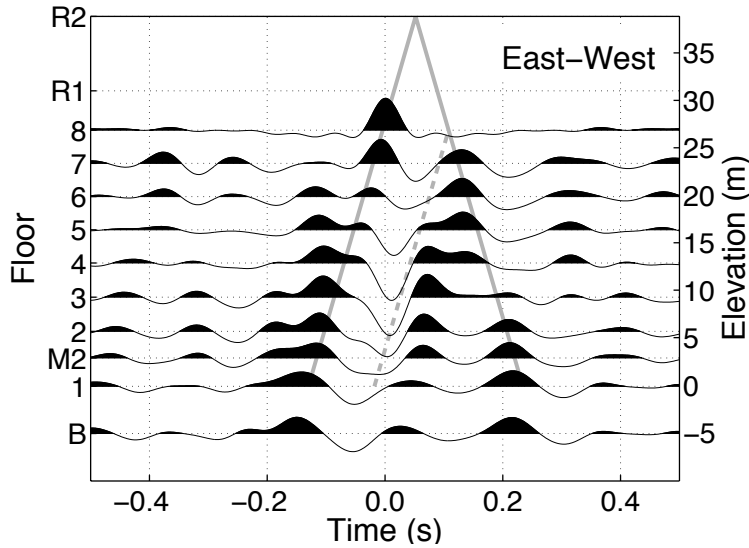


Figure 6.9. Deconvolved waveforms, in which the virtual source is at the eighth floor, of earthquake No. 5 after applying a bandpass filter 0.4-0.5-12-16 Hz in the EW component. The gray lines show the travel time of the waves propagating at 210 m/s. The positions of the lines are estimated from equation 6.3. The thick lines have positive polarization and the dashed line negative polarization.

and fourth floors (below the virtual source) contributes to the estimation of this velocity. This is the main reason why the mean velocities estimated from Figures 6.7 and 6.8 differ, but this discrepancy is not statistically significant.

We apply deconvolution interferometry to the motion recorded by the receiver at the eighth floor, which is the highest receiver in the building (Figure 6.9). Snieder and Şafak (2006) found that this procedure gives only one pair of upgoing and downgoing waves; however, since the eighth-floor receiver is about 12 m below the top of the building (R2), the deconvolved waveforms in Figure 6.9 satisfy equation 6.3 instead of equation 6.10. In Figure 6.9, we apply a 0.4-0.5-12-16 Hz sine-squared bandpass filter to deconvolved waveforms. Because the quality of the data is not enough to accurately pick travel times, we cannot estimate the wave velocity from Figure 6.9. The gray lines in Figure 6.9 indicate the arrival time of the traveling waves at 210 m/s as inferred from Figure 6.7a.

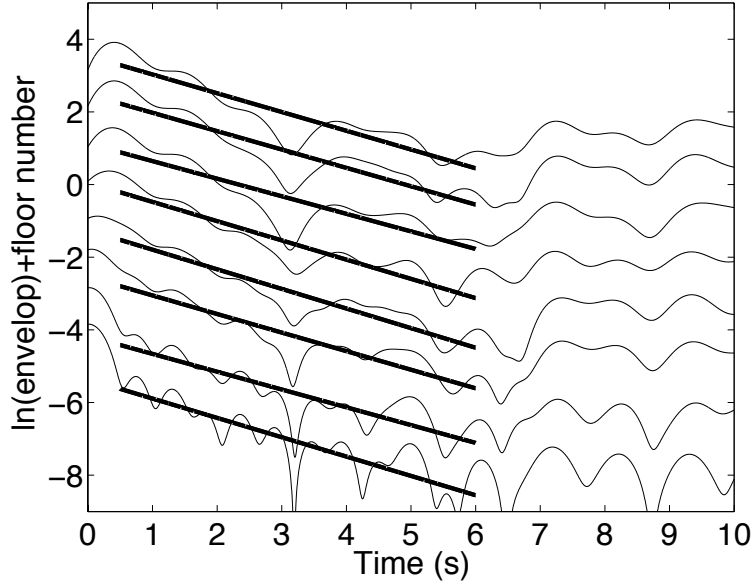


Figure 6.10. Natural logarithm of the envelopes (thin line) and linear fitting using the least-squares method (thick line). We show envelopes at only the middle-second to eighth floors because the first floor is a virtual source and the basement floor has a different physical condition.

From the resonant waves in Figures 6.7 and 6.8, we can estimate  $Q$  following the method proposed by Snieder and Şafak (2006). Figure 6.10 shows the logarithmic envelopes of the deconvolved waveforms in Figure 6.7a at each floor except the basement and the first floor (thin lines), and their least-squares linear fits (thick lines). Because we use the waveforms deconvolved with the first floor, the estimated  $Q$  is for the entire building. We assume  $Q$  is constant in the entire building because the wavelength in the frequency range used is much longer than the height of the building (the resonant frequency is 1.17 Hz). In Figure 6.10, the average slope of the fitting lines indicates that  $Q^{-1} = 0.098$  based on the fundamental-mode frequency 1.17 Hz.

## 6.7 Monitoring a building using 17 earthquakes

Using the 17 earthquakes recorded in the two weeks (Table 6.1 and Figure 6.2), we monitor the change in the shear-wave velocity of the building. Figure 6.11 illustrates the waveforms which are deconvolved by the wave recorded at the first floor of each earthquake

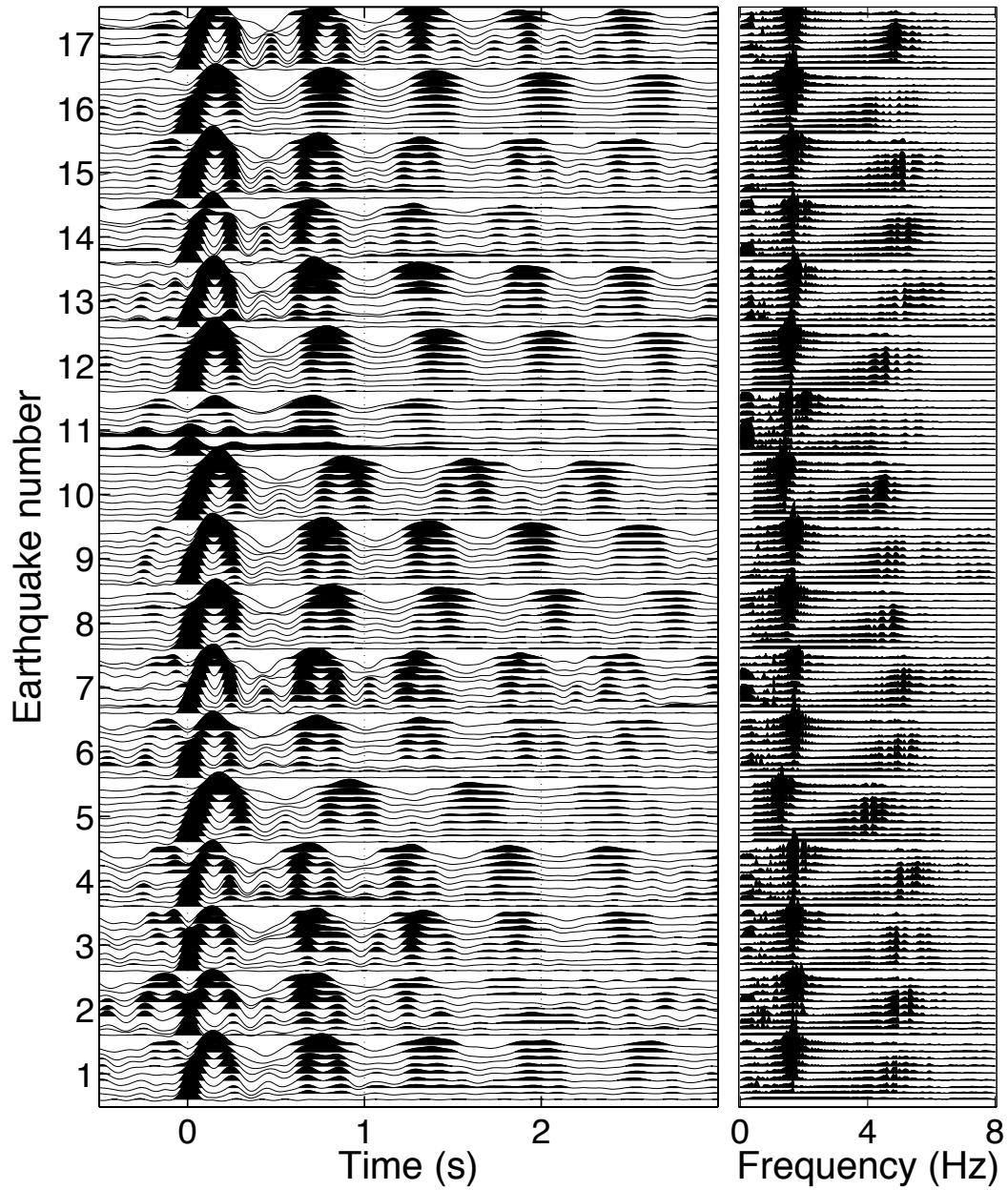


Figure 6.11. The waveforms of each earthquake in the EW component after deconvolution with the waves recorded on the first floor in the time domain (left panel), and the power spectra of the waveforms (right panel). We apply a bandpass filter 0.4-0.5-45-50 Hz. We show the traces from the first floor to the eighth floor in each earthquake.

(left panel) and the power spectra of the deconvolved waveforms (right panel). The virtual source is at the first floor (similar to Figure 6.7a). The frequency component around 1.5 Hz shows the fundamental mode and around 5 Hz the first overtone. From the bottom to top traces for each earthquake, the traces are aligned from the first to eighth floors, and the waves propagating between the bottom and the top are visible. Comparing the fundamental-mode waves for later times among earthquakes, we can roughly estimate changes in velocity from a visual inspection, e.g., the velocities in earthquakes 5, 8, 10, and 12 are slower. The earthquakes, which show slower velocity, indicate lower normal-mode frequencies as shown by Todorovska and Trifunac (2008b). The ratio of the reductions in velocity and frequency are almost the same.

The amplitude of each resonant wave provides an estimate of attenuation. For example, the attenuation is strong for earthquake No. 5 because the amplitude of the fundamental mode fades away at around 2.5 s. For some earthquakes, although the fundamental mode is dominant at later times, deconvolved waveforms still show upgoing and downgoing waves (e.g., at 2.5 s of earthquake No. 15), which implies either that the attenuation at higher frequency is relatively weak at the time these earthquakes occurred, or that the overtones are strongly excited. We estimate the velocity of traveling waves using the method that is the same as for Figure 6.7a (the black symbols in Figure 6.12). The black marks in Figure 6.12b illustrate a negative correlation between the velocities and the maximum acceleration of observed records.

To estimate velocities, we also apply coda-wave interferometry as developed by Snieder et al. (2002) to deconvolved waveforms. Coda-wave interferometry allows us to estimate a relative velocity change from two waveforms by computing crosscorrelation. Coda-wave interferometry has been applied to multiplets (e.g., Poupinet et al., 1984; Snieder and Vrijlandt, 2005) and to waveforms which are obtained by seismic interferometry (e.g., Sens-Schönfelder and Wegler, 2006). By using coda-wave interferometry, we estimate velocities from the deconvolved waves between 1-3 s in Figure 6.11. The waves in the time interval are mostly the

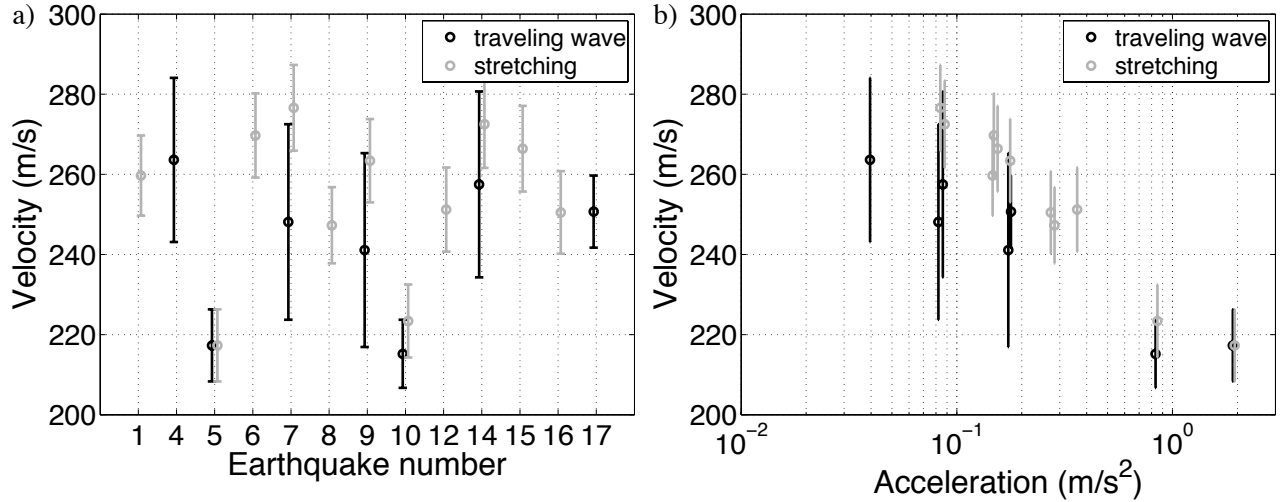


Figure 6.12. (a) Velocities estimated from traveling waves (black) and by coda-wave interferometry using the stretching method (gray) of each earthquake. The error bars of the velocities estimated from traveling waves (black) are one standard deviation of individual arrival times, and the bars in the stretching method are calculated by  $\sqrt{\sigma_5^2 + \sigma_{\delta v}^2}$ . We illustrate only velocities which have smaller than 10% velocity uncertainty (for traveling waves) or are estimated from more than three traces which have a correlation coefficient greater than 0.9 (for the stretching method). (b) Crossplot of estimated velocities with maximum acceleration observed at the first floor.

fundamental mode. We choose earthquake No. 5 as a reference and estimate the relative velocity for each earthquake from the reference earthquake. In coda-wave interferometry, we stretch and interpolate one waveform and compute a correlation coefficient (CC) with a reference waveform ( $u_{ref}$ ) in the time domain (Figure 6.13) (Lobkis and Weaver, 2003; Hadziioannou et al., 2009; Weaver et al., 2011):

$$CC(\alpha) = \frac{\int_{t_1}^{t_2} u(t(1-\alpha))u_{ref}(t)dt}{\sqrt{\int_{t_1}^{t_2} u^2(t(1-\alpha))dt \int_{t_1}^{t_2} u_{ref}^2(t)dt}}, \quad (6.22)$$

where  $t_1$  and  $t_2$  denote the time window, and in this study we use 1-3 s. At the maximum of  $CC(\alpha)$ ,

$$\alpha = \frac{v - v_{ref}}{v_{ref}}, \quad (6.23)$$

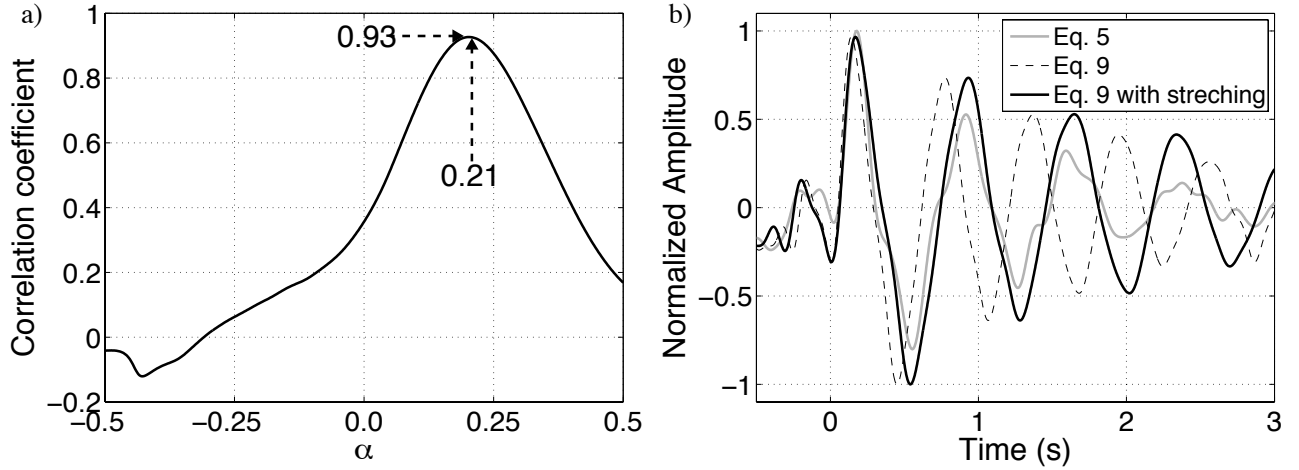


Figure 6.13. (a) Correlation coefficient (CC) as a function of  $\alpha$  (equation 6.22) between deconvolved waveforms computed from earthquakes No. 5 and No. 9 at the eighth floor. Dashed arrows point to the maximum CC value and its value of  $\alpha$ . For computing CC, we use only the waveforms from 1.0 s to 3.0 s. (b) Deconvolved waveforms at the eighth floor of earthquakes No. 5, No. 9, and No. 9 with stretching for  $\alpha = 0.21$  (see panel (a)).

where  $v$  and  $v_{ref}$  are the velocities at each earthquake and the reference earthquake, respectively. For computing CC, we apply the same bandpass filter as for Figure 6.11, and the waves are mostly the fundamental mode.

Note that even though we use the waves between 1-3 s for applying coda-wave interferometry, the origin time for stretching is at time 0 s. The gray symbols in Figure 6.12 are the velocities estimated by coda-wave interferometry using the stretching method. Because we use earthquake No. 5 as a reference ( $u_{ref}$ ), the estimated velocities of each earthquake using the stretching method (the gray symbols in Figure 6.12) are the relative velocities with respect to the velocity of earthquake No. 5. Therefore, the velocities estimated from traveling waves and by the stretching method in earthquake No. 5 are, by definition, the same. The standard deviation of the velocity change (the gray bars in Figure 6.12) for each earthquake is estimated by  $\sqrt{\sigma_5^2 + \sigma_{\delta v}^2}$ , where  $\sigma_5$  is the standard deviation of the velocity measurements estimated from traveling waves at different floors in earthquake No. 5, and  $\sigma_{\delta v}$  is the standard deviation of the relative velocity measurements between each earthquake and earthquake No. 5 estimated by the stretching method at different floors. The gray symbols

in Figure 6.12b indicate that the velocities obtained by the stretching method also have a negative correlation with the acceleration, but the slope is steeper than that for the traveling waves. Since the waves in 1-3 s are mostly fundamental mode and the main difference between the traveling waves and the fundamental mode is the frequency (the traveling waves contain higher frequencies than the fundamental mode), the difference in slopes indicates dispersion. The steeper slope of the gray symbols in Figure 6.12b indicates that the imprint of acceleration is stronger for lower frequencies than for higher frequencies.

## 6.8 Conclusions

We obtain impulse responses of the building and their changes in velocity by applying deconvolution interferometry to 17 earthquake records. We estimate the reflection point of the traveling wave, which is at the top of the penthouse, from the deconvolved waveforms. Since the shape of the ground plan of the building is rectangular, the velocities of the traveling wave in two orthogonal horizontal components are different. According to the properties of deconvolution, the responses are independent from the soil-structure coupling and the effect of wave propagation below the bottom receiver. Because the cut-off building is independent of the structure below the virtual source, one might be able to use the cut-off building to investigate local structure and local damage. Crosscorrelation interferometry cannot separate the building response from the soil-building coupling and the wave propagation below the virtual source. Crosscoherence interferometry produces unphysical wavefields propagating at slower velocity than the true wave speed of the real building, and the attenuation of the waveforms obtained from crosscoherence do not correspond to the travel distance of the waves. Hence, in contrast to deconvolution interferometry, these types of interferometry are not appropriate for applying to earthquake records for estimating velocities and attenuation of buildings. We estimate velocities from both traveling waves and the fundamental mode of deconvolved waveforms. The velocities estimated from each earthquake and maximum acceleration have a negative correlation.

## 6.9 Acknowledgments

We are grateful to the sponsors of the Center for Wave Phenomena at the Colorado School of Mines. We thank JMA for providing the earthquake catalog. We are grateful to Diane Witters for her help in preparing this manuscript. Seismograms used in this study were operated and maintained by Suncof Consultants Co., Ltd. Earthquake catalogs are listed at [www.jma.go.jp](http://www.jma.go.jp) (last accessed August 2012). Figure 6.1 is produced by using the Generic Mapping Tools (GMT: <http://gmt.soest.hawaii.edu>, last accessed August 2012).

### 6.A Normal-mode analysis of deconvolution interferometry

In equation 6.3, we analyze the deconvolution interferometry based on superposition of traveling waves using a Taylor expansion. Here, we analyze equation 6.3 based on summation of normal-mode waves while using contour integration as following the procedure proposed by Snieder and Şafak (2006). Applying the inverse Fourier transform to  $D(z, z_a, \omega)$  and using the relationship  $k = \omega/c$ , the deconvolved response in the time domain is given by

$$D(z, z_a, t) = \int_{-\infty}^{\infty} \frac{e^{-i\omega(t-\frac{z}{c})} e^{-\gamma|\omega|\frac{z}{c}} + e^{-i\omega(t-\frac{2H-z}{c})} e^{-\gamma|\omega|\frac{2H-z}{c}}}{e^{i\omega\frac{z_a}{c}} e^{-\gamma|\omega|\frac{z_a}{c}} + e^{i\omega\frac{2H-z_a}{c}} e^{-\gamma|\omega|\frac{2H-z_a}{c}}} d\omega. \quad (6.A1)$$

For  $t > (2H - z)/c$ , the locations of poles ( $\omega_{\dagger}$ ) of the integrand in equation 6.A1 are

$$\omega_{\dagger} = \omega_l(\pm 1 - i\gamma), \quad (l = 0, 1, 2, \dots) \quad (6.A2)$$

where the normal-mode frequencies are given by

$$\omega_l = \frac{(l + \frac{1}{2}) \pi c}{H - z_a} \quad (6.A3)$$

Using the residue theorem, equation 6.A1 can be written as the summation of normal-mode wavefields:

$$D(z, z_a, t) = \frac{4\pi c}{H - z_a} \sum_{l=0}^{\infty} (-1)^l e^{-\gamma\omega_l t} \sin(\omega_l t) \cos\left(\omega_l \frac{H - z}{c}\right). \quad (6.A4)$$

## 6.B Amplitude of crosscorrelation interferometry

In this appendix, we compute the amplitude of the crosscorrelated waveforms in equation 6.12. Using Taylor expansions, we rewrite the equation 6.12 as

$$C(z, 0, \omega) = |S(\omega)|^2 \left\{ e^{ikz} e^{-\gamma|k|z} + e^{-ikz} e^{-\gamma|k|(4H-z)} + e^{ik(2H-z)} e^{-\gamma|k|(2H-z)} + e^{-ik(2H-z)} e^{-\gamma|k|(2H+z)} \right\} \\ \times \left\{ \sum_{n=0}^{\infty} (R(\omega))^n e^{2inkH} e^{-2n\gamma|k|H} \right\} \left\{ \sum_{m=0}^{\infty} (R^*(\omega))^m e^{-2imkH} e^{-2m\gamma|k|H} \right\}. \quad (6.B1)$$

Here, we only focus on the waves with phases  $e^{ikz}$ ,  $e^{ik(2H-z)}$ ,  $e^{ik(2H+z)}$ , and  $e^{ik(4H-z)}$ , and define their amplitudes as  $C_1$ ,  $C_2$ ,  $C_3$ , and  $C_4$ , respectively. From equation 6.B1,  $C_1$  is obtained by

$$C_1 e^{ikz} = |S(\omega)|^2 \left[ e^{ikz} e^{-\gamma|k|z} \sum_{n=0}^{\infty} \left\{ (R(\omega))^n e^{2inkH} e^{-2n\gamma|k|H} (R^*(\omega))^n e^{-2inkH} e^{-2n\gamma|k|H} \right\} \right. \\ \left. + e^{-ik(2H-z)} e^{-\gamma|k|(2H+z)} \sum_{n=0}^{\infty} \left\{ (R(\omega))^{n+1} e^{2i(n+1)kH} e^{-2(n+1)\gamma|k|H} (R^*(\omega))^n e^{-2inkH} e^{-2n\gamma|k|H} \right\} \right] \\ C_1 = |S(\omega)|^2 e^{-\gamma|k|z} \left\{ 1 + R(\omega) e^{-4\gamma|k|H} \right\} \left\{ \sum_{n=0}^{\infty} |R(\omega)|^{2n} e^{-4n\gamma|k|H} \right\}. \quad (6.B2)$$

Similar to expression 6.B2, we obtain  $C_2$ ,  $C_3$ , and  $C_4$  as

$$C_2 = |S(\omega)|^2 e^{-\gamma|k|(2H-z)} \left\{ 1 + R(\omega) e^{-4\gamma|k|H} \right\} \left\{ \sum_{n=0}^{\infty} |R(\omega)|^{2n} e^{-4n\gamma|k|H} \right\}, \quad (6.B3)$$

$$C_3 = |S(\omega)|^2 R(\omega) e^{-\gamma|k|(2H+z)} \left\{ 1 + R(\omega) e^{-4\gamma|k|H} \right\} \left\{ \sum_{n=0}^{\infty} |R(\omega)|^{2n} e^{-4n\gamma|k|H} \right\}, \quad (6.B4)$$

$$C_4 = |S(\omega)|^2 R(\omega) e^{-\gamma|k|(4H-z)} \left\{ 1 + R(\omega) e^{-4\gamma|k|H} \right\} \left\{ \sum_{n=0}^{\infty} |R(\omega)|^{2n} e^{-4n\gamma|k|H} \right\}. \quad (6.B5)$$

## 6.C Applying crosscorrelation and crosscoherence interferometry to real data

In Figure 6.C1, we apply crosscorrelation and crosscoherence interferometry to real data to draw similar figures as Figure 6.7a. When we use the same bandpass filter as for Figure 6.7, crosscorrelation interferometry enhances the fundamental-mode frequency, and only the fundamental mode is visible (Figure 6.C1a). This is caused by the power spectrum of the incoming wave (equation 6.12). When we cut the fundamental-mode frequency, the first-higher mode is dominant in the crosscorrelated waveforms (Figure 6.C1c). Therefore, we cannot estimate the velocity of traveling waves.

Figure 6.C1b illustrates upgoing and downgoing waves from  $t = 0$  s, and the waves propagate at the same velocity as the traveling waves reconstructed by deconvolution interferometry (Figure 6.7a). However, these propagating waves may be affected by the wave which propagates at slower velocities. The fundamental mode is not clear in Figure 6.C1b. This is due to the spectral ratio used in crosscoherence interferometry, as a result the amplitude in later times is much smaller than the amplitude of deconvolution interferometry (Table 6.2). Because of the frequency we used, the wave propagating with slower velocity is not clear (the dashed gray line in Figure 6.C1d). The negative amplitudes around the dashed line might be related to the wave with slower velocity.

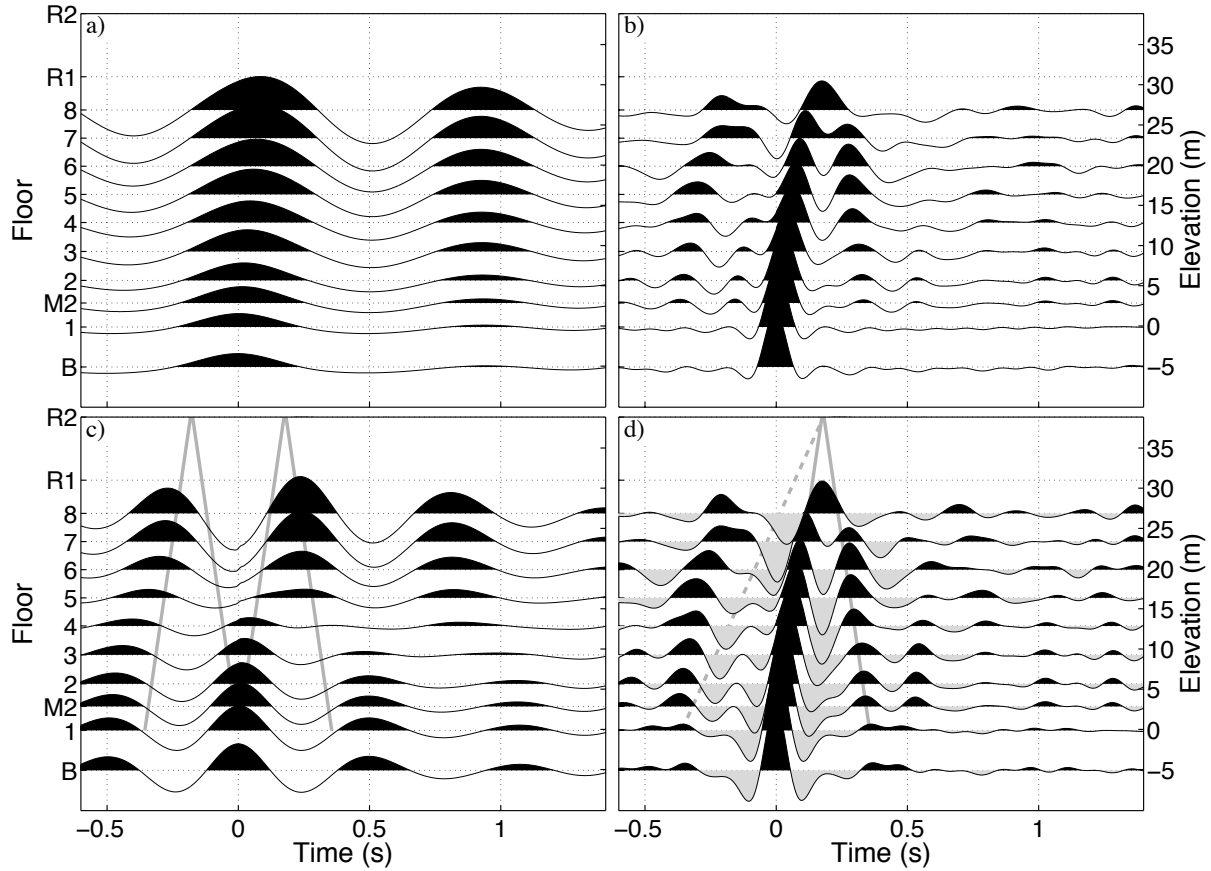


Figure 6.C1. Waveforms obtained by applying (a,c) crosscorrelation and (b,d) crosscoherence interferometry, in which the virtual source is at the first floor, to the records of earthquake No. 5 in the EW component. These waveforms are applied bandpass filters (a,b) 0.4-0.5-45-50 Hz, (c) 1.3-1.6-45-50 Hz, and (d) 1.4-2-45-50 Hz. Note that the bandpass filter for panels (a) and (b) is the same filter as for Figure 6.7. The amplitude scales in each panel are different. The solid gray lines in panel (c) and (d) are the positive-polarity traveling waves with the velocity estimated from Figure 6.7a based on equations 6.12 and 6.16. The dashed gray line in panel (d) indicates the wave that propagates at one third of the velocity of Figure 6.7a.

CHAPTER 7  
MONITORING A BUILDING USING DECONVOLUTION INTERFEROMETRY. II:  
AMBIENT-VIBRATION ANALYSIS

Submitted to *Bulletin of the Seismological Society of America* (2013)

Nori Nakata<sup>1</sup> and Roel Snieder<sup>1</sup>

### 7.1 Summary

Application of deconvolution interferometry to earthquake data recorded inside a building is a powerful technique for monitoring parameters of the building, such as velocities of traveling waves, frequencies of normal modes, and intrinsic attenuation. In this study, we apply interferometry to ambient-vibration data, instead of using earthquake data, to monitor a building. The time continuity of ambient vibrations is useful for temporal monitoring. We show that because multiple sources simultaneously excite vibrations inside the building, the deconvolved waveforms obtained from ambient vibrations are non-zero for both positive and negative times, unlike the purely causal waveforms obtained from earthquake data. We develop a string model to qualitatively interpret the deconvolved waveforms. Using the synthetic waveforms, we find that the traveling waves obtained from ambient vibrations propagate with the correct velocity of the building, and the amplitude decay of the deconvolved waveforms depends on both intrinsic attenuation and ground coupling. The velocities estimated from ambient vibrations are more stable than those computed from earthquake data. Since the acceleration of the observed earthquake records varies depending on the strength of the earthquakes and the distance from the hypocenter, the velocities estimated from earthquake data vary because of the nonlinear response of the building. From ambient vibrations, we extract the wave velocity due to the linear response of the building.

---

<sup>1</sup>Center for Wave Phenomena, Colorado School of Mines

## 7.2 Introduction

Spectral analysis using forced vibrations and/or earthquakes is a common technique to estimate frequencies of normal modes, mode shapes, and viscous damping parameters of a building (Kanai and Yoshizawa, 1961; Trifunac, 1972; Trifunac et al., 2001a,b; Clinton et al., 2006). These parameters are useful for risk assessment and for estimating the response of a building to earthquakes (Michel et al., 2008). The sources listed above are sometimes inappropriate to use for temporal monitoring a building because of the lack of data continuity. Ambient vibrations, caused by sources within the building, are more suitable for monitoring a building because of the quasi-continuous nature of these vibrations (Trifunac, 1972; Ivanović et al., 2000). In this study we use seismic interferometry to analyze ambient vibrations recorded inside a building in the Fukushima prefecture in Japan.

Using seismic interferometry, we can reconstruct waves that propagate from one receiver to another. Seismic interferometry was invented by Aki (1957) and Claerbout (1968), and has been well-developed over the last decade (e.g., Lobkis and Weaver, 2001; Derode et al., 2003; Snieder, 2004b; Wapenaar, 2004; Schuster, 2009; Snieder et al., 2009; Tsai, 2011). One can apply seismic interferometry to active sources (e.g., Bakulin and Calvert, 2006; Wegler et al., 2006; Mehta et al., 2008; van der Neut et al., 2011) or to earthquake data (e.g., Sawazaki et al., 2009; Yamada et al., 2010; Nakata and Snieder, 2011, 2012a,b). These latter studies used interferometry for monitoring purposes. One can also apply interferometry to noise caused by production (e.g., Miyazawa et al., 2008), drilling (e.g., Vasconcelos and Snieder, 2008a,b), and traffic (e.g., Nakata et al., 2011), and to non-specific vibrations (so-called *ambient vibration* or *ambient noise*) (e.g., Sens-Schönfelder and Wegler, 2006; Brenguier et al., 2008a,b; Draganov et al., 2009; Minato et al., 2012).

In a companion paper (henceforth called Part I: Nakata et al. (2013)), we analyze earthquake data, recorded over the same time period in the same building as in this study, using seismic interferometry. Although several studies apply interferometric approaches to earthquake data recorded in a building (e.g., Snieder and Şafak, 2006; Snieder et al., 2006; Kohler

et al., 2007; Todorovska and Trifunac 2008a,b), few studies apply this technique to ambient vibrations (Prieto et al., 2010). As we explain below, by applying seismic interferometry to ambient vibrations recorded in a building, we not only achieve continuous monitoring in time but also obtain information of the ground coupling and linear response of the building, which we cannot estimate from earthquake data.

We first introduce ambient-vibration data and deconvolved waveforms computed from the observed data. Next, we analytically and qualitatively interpret the deconvolved waveforms using traveling-wave and normal-mode analyses. Then we monitor the building using ambient vibrations based on the interpretation.

### **7.3 Deconvolution analysis using ambient vibration**

We present data acquisition, pre-processing for deconvolution interferometry, and the interferometry using ambient-vibration data in this section. Data are observed in the same building over the same time period as for the earthquake data in Part I (Figure 7.1). Pre-processing has an important role for obtaining reliable correlograms (Bensen et al., 2007), and here we focus on the pre-processing to exclude large amplitudes caused by earthquakes and human activities.

#### **7.3.1 Observed records**

The building we used is in the Fukushima prefecture, Japan (the rectangle in Figure 7.1). Continuous ambient seismic vibrations were recorded by SuncoH Consultants Co., Ltd. for two weeks (May 31–June 14, 2011) using 10 MEMS accelerometers developed by Akebono Brake Industry Co., Ltd. The building has eight stories, a basement, and a penthouse (Figure 7.2). Based on the analysis in Part I, the waves, which propagate vertically inside the building, reflect off the top of the penthouse (R2 in Figure 7.2). The sampling interval of the accelerometers is 1 ms, and the receivers have vertical, east-west (EW) horizontal, and north-south (NS) horizontal components. In this study we focus on the EW horizontal component to extract horizontal modes.

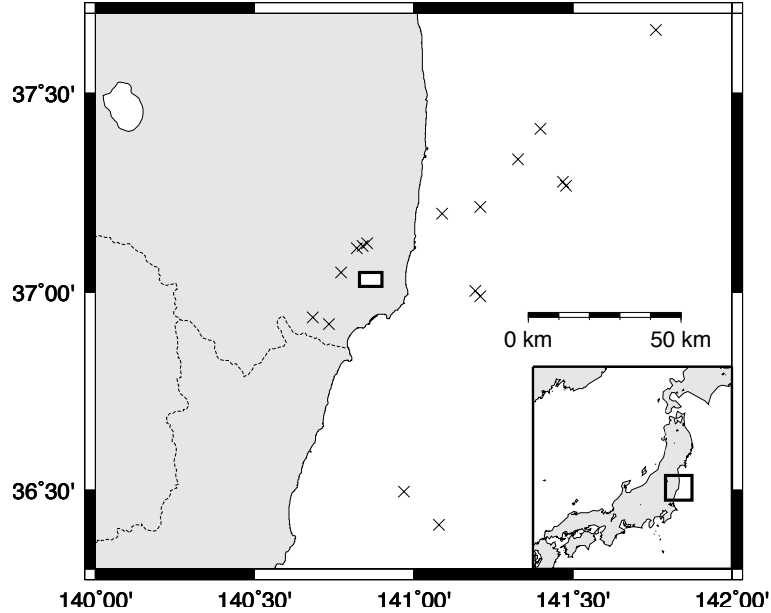


Figure 7.1. The building (rectangle, not to scale) and epicenters of earthquakes used in Part I (crosses). The lower-right map indicates the location of the magnified area.

Figure 7.3 illustrates the root-mean-square (RMS) amplitude computed over a moving window with a duration of 30 s of unfiltered seismic records observed for the two weeks. The hours of operation of the building are from 8AM to 6PM on weekdays, when the RMS amplitude is elevated. On the weekends we observe lower RMS amplitudes (June 4, 5, 11, and 12 are weekends). The vibrations are probably induced by human activities, elevators, air conditioners, computers, traffic near the building, and other sources. Amplitudes at the upper floors are stronger due to the shape of the fundamental mode of the building (see Figure 4 in Part I for the shape of the fundamental mode). Stronger amplitudes at the first floor compared with nearby floors may be caused by vibrations from traffic outside the building and/or many visitors to that floor. Because the amplitudes at the basement are much smaller than the other floors, we do not interpret the records at the basement in this study.

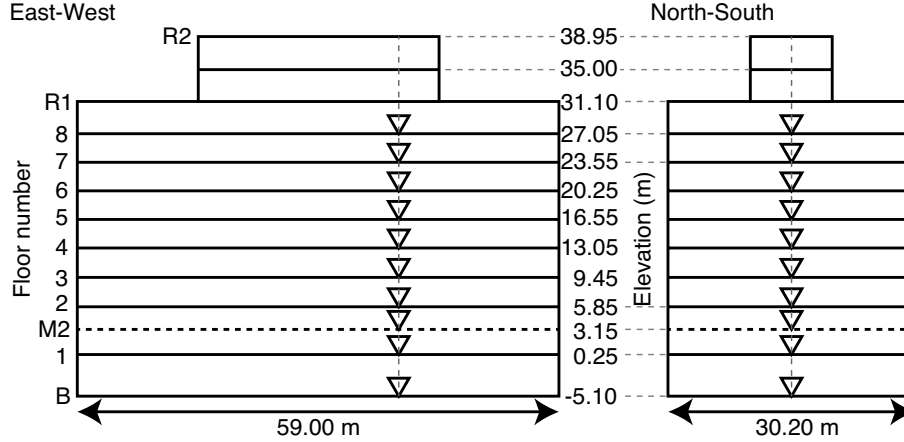


Figure 7.2. The (left) EW and (right) NS vertical cross sections of the building and the positions of receivers (triangles). Elevations denote the height of each floor from ground level. Receivers are located on stairs 0.19 m below each floor except for the basement (on the floor) and the first floor (0.38 m below). Receiver M2 is located between the first and second floors. Horizontal-receiver components are aligned with the EW and NS directions.

### 7.3.2 Pre-processing

Before applying deconvolution interferometry, we exclude large-amplitude intervals from the continuous records because we focus on ambient vibrations. Large amplitudes are excited by earthquakes and human interference, such as people touching the accelerometers. Since receivers are often located at places where people can touch them (e.g., on stairs), a technique proposed here to exclude the human interference is useful. To exclude large-amplitude waves, we apply a data-weighting procedure based on the standard deviation of data recorded for one hour in which the data do not include significant earthquakes or human interference (Wegler and Sens-Schönfelder, 2007). When one receiver records a larger amplitude than the threshold, the samples of all receivers at that time are set to zero since we need the waveforms at the same time at all sensors for the deconvolution analysis. After someone touches a receiver, the DC component on the seismograms may change. We subtract the DC component from the data of every 30 s and discard data when the DC component changes during that time interval. Similar to large amplitudes, we exclude time intervals when one receiver indicates a change in the DC component.

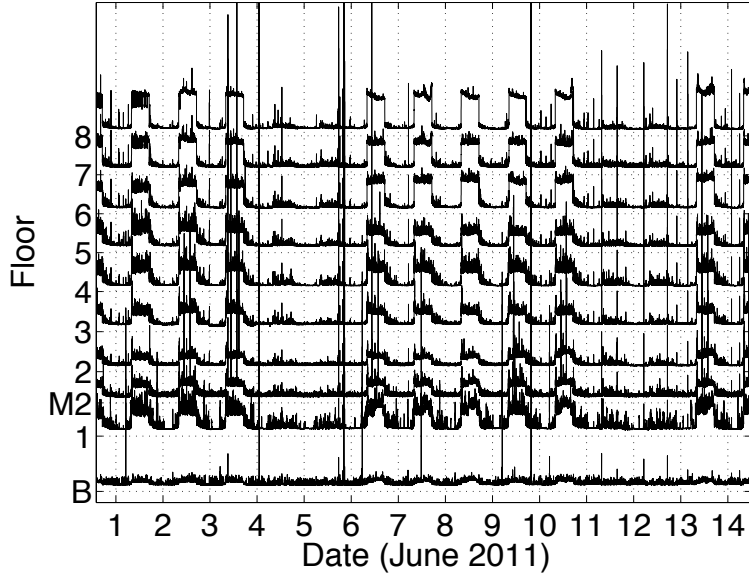


Figure 7.3. RMS amplitude of the records observed at each floor. The labels of the date are placed at the start of days (midnight). Each trace indicates the RMS amplitude, and the positive axis of amplitude for each trace is upward (dashed horizontal grids describe zero amplitude at each floor).

### 7.3.3 Deconvolution analysis using two-week ambient vibration

We apply deconvolution interferometry to ambient-vibration records observed inside the building. Here, we stack deconvolved waveforms over the two weeks in which data were collected. In the later section *Monitoring the building using ambient vibration*, we stack over four-day intervals for monitoring purposes. We deconvolve each 30-s ambient-vibration record with the first-floor record and then stack the waveforms over the two-week interval:

$$D(z, t) = \sum_{n=1}^N \left[ \mathcal{F}^{-1} \left\{ \frac{u_n(z, \omega)}{u_n(0, \omega)} \right\} \right] \approx \sum_{n=1}^N \left[ \mathcal{F}^{-1} \left\{ \frac{u_n(z, \omega) u_n^*(0, \omega)}{|u_n(0, \omega)|^2 + \alpha \langle |u_n(0, \omega)|^2 \rangle} \right\} \right], \quad (7.1)$$

where  $N$  is the number of 30-s intervals (40,080 in this study),  $u_n(z, \omega)$  the  $n$ th wavefield in the frequency domain recorded at  $z$  ( $z = 0$  is the first floor),  $\omega$  the angular frequency,  $t$  time,  $\mathcal{F}^{-1}$  the inverse Fourier transform,  $*$  the complex conjugate,  $\langle |u_n|^2 \rangle$  the average power spectrum of  $u_n$ , and  $\alpha = 0.5\%$  a regularization parameter stabilizing the deconvolution

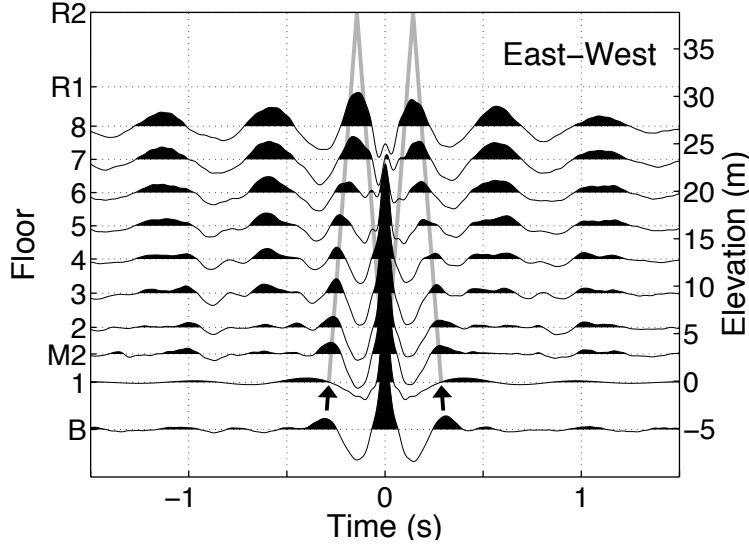


Figure 7.4. Deconvolved waveforms obtained from ambient vibrations in the EW component (expression 7.1). Ambient vibrations observed at Floor 1 is used for the denominator in expression 7.1. The waveforms are averaged over two weeks and applied a bandpass filter 1.3-1.5-15-20 Hz. The shear velocity is estimated from the downgoing waves in the positive time and the upgoing waves in the negative time marked by arrows. Gray lines show the arrival times of the waves propagating with a velocity equal to 270 m/s.

(Clayton and Wiggins, 1976). Our Fourier convention is  $f(t) = \int_{-\infty}^{\infty} F(\omega)e^{-i\omega t}d\omega$ . We apply a bandpass filter, 1.3-1.5-15-20 Hz, to the deconvolved waveforms (Figure 7.4).

In Figure 7.4, we obtain traveling waves and the fundamental mode for both positive and negative times, unlike the deconvolved waveforms obtained from earthquake data, which only contain the causal waves (Part I). Because deconvolution interferometry creates a virtual source exciting waves at  $t = 0$  (Snieder et al., 2006a), causal and acausal waves refer to the waves in the positive and negative times, respectively. The waveforms in Figure 7.4 are almost symmetric in time. We estimate the velocity from the downgoing wave in the positive time and the upgoing wave in the negative time (marked by the arrows in Figure 7.4) using the least-squares fitting of picked arrival times (see Part I for the detail of the method). The velocity thus obtained is  $270 \pm 5$  m/s, where the uncertainty is one standard deviation of the estimated velocities at each floor (the gray lines in Figure 7.4). We do not use the upgoing wave in the positive time and the downgoing wave in the negative time because these waves

overlap and we cannot accurately pick their arrival times.

If we estimate a quality factor ( $Q^{(ar)}$ ) from the amplitude decay of the waveforms in Figure 7.4 using the technique in Part I, where we time-reverse the waveforms to estimate  $Q^{(ar)}$  for the acausal part, the obtained values of  $Q^{(ar)}$  are 25.3 and 20.2 in the causal and acausal parts, respectively. We explain below that the amplitude decay does not only depend on the intrinsic attenuation in the building when we use ambient vibrations; the decay of the waveforms reconstructed from ambient vibrations is also affected by radiation losses due to the ground coupling. The superscripts of  $Q^{(ar)}$  indicate that the quality factor is effected by intrinsic attenuation ( $a$ ) and radiation damping ( $r$ ). Note that the quality factor estimated from earthquake data indicates only intrinsic attenuation ( $Q^{(a)}$ ). Hereafter, we use  $Q$  without a superscript to refer to the intrinsic attenuation ( $Q^{(a)}$ ).

## 7.4 Discussion of the deconvolved waveforms

In this section, we interpret the deconvolved waveforms in Figure 7.4 using a mathematical description and synthetic waveforms based on traveling waves and normal modes. The goal of this section is to understand why we obtain both causal and acausal waves after applying interferometry to ambient vibrations, to reconstruct the waveforms using synthetic computation, and to determine to what degree we can estimate the velocity of traveling waves and the quality factor from ambient vibrations. The main differences of deconvolved waveforms obtained from ambient vibrations and earthquakes are that for ambient vibrations, sources are inside the building and more than one source simultaneously excites inside and outside the building. We consider deconvolved waveforms computed from one source inside the building based on traveling waves and from multiple sources based on normal modes.

### 7.4.1 One source inside the building

To analyze deconvolved waveforms obtained from one source inside the building, we employ the same assumptions as equation 1 in Part I: vertically propagating waves in the

building, constant amplitude and wavenumber, no torsional waves, and no internal reflections. Based on Snieder and Şafak (2006) and Part I, when a source is at height  $z_s$ , the observed record at an arbitrary receiver at height  $z$  is

$$u(z > z_s, \omega) = S(\omega) \frac{X}{1 - Re^{2ikH} e^{-2\gamma|k|H}} \quad (7.2)$$

for  $z > z_s$ , and

$$u(z < z_s, \omega) = S(\omega) \frac{X'}{1 - Re^{2ikH} e^{-2\gamma|k|H}} \quad (7.3)$$

for  $z < z_s$ . Here,  $S(\omega)$  is the source function,  $R$  the reflection coefficient at the base of the building,  $k$  the wavenumber,  $\gamma$  the attenuation coefficient,  $H$  the height of the building, and  $i$  the imaginary unit. The attenuation coefficient is defined by  $\gamma = 1/(2Q)$  (Aki and Richards, 2002). The numerators  $X$  and  $X'$  are given by

$$\begin{aligned} X &= e^{ik(z-z_s)} e^{-\gamma|k|(z-z_s)} + e^{ik(2H-z-z_s)} e^{-\gamma|k|(2H-z-z_s)} \\ &\quad + R \left( e^{ik(z+z_s)} e^{-\gamma|k|(z+z_s)} + e^{ik(2H-z+z_s)} e^{-\gamma|k|(2H-z+z_s)} \right), \\ X' &= e^{ik(z_s-z)} e^{-\gamma|k|(z_s-z)} + e^{ik(2H-z-z_s)} e^{-\gamma|k|(2H-z-z_s)} \\ &\quad + R \left( e^{ik(z+z_s)} e^{-\gamma|k|(z+z_s)} + e^{ik(2H-z_s+z)} e^{-\gamma|k|(2H-z_s+z)} \right), \end{aligned}$$

respectively.

The waveforms recorded at height  $z$  deconvolved with the waveform recorded at the first floor ( $z = 0$ ) are

$$\begin{aligned} D(z > z_s, \omega) &= \frac{u(z > z_s)}{u(z = 0)} \\ &= \frac{\left\{ e^{ik(z-2z_s)} e^{-\gamma|k|(z-2z_s)} + Re^{ikz} e^{-\gamma|k|z} \right\} \left\{ 1 + e^{2ik(H-z)} e^{-2\gamma|k|(H-z)} \right\}}{1 + R} \\ &\quad \times \sum_{n=0}^{\infty} (-1)^n \left( e^{2ink(H-z_s)} e^{-2n\gamma|k|(H-z_s)} \right), \end{aligned} \quad (7.4)$$

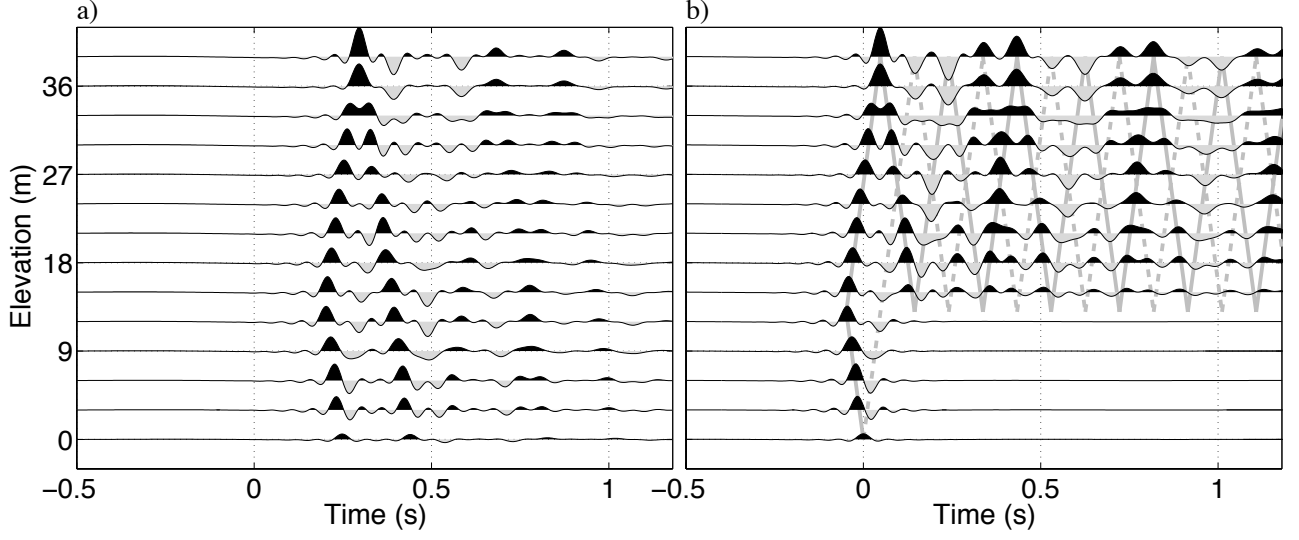


Figure 7.5. (a) Synthetic waveforms obtained from one source inside a building (expressions 7.2 and 7.3) and (b) waveforms of panel (a) after deconvolution with the waves observed at  $z = 0$  m. The source is located at  $z_s = 13$  m and excites waves at  $t = 0.2$  s. The gray lines in panel (b) show the arrival times of the traveling waves based on expressions 7.4 and 7.5. The solid and dashed gray lines respectively illustrate the terms  $e^{ik(z-2z_s)}e^{-\gamma|k|(z-2z_s)}$  and  $Re^{ikz}e^{-\gamma|k|z}$ , and their reverberations. The amplitudes of panels (a) and (b) are normalized after applying the same bandpass filter as used in Figure 7.4.

$$D(z < z_s, \omega) = \frac{u(z < z_s)}{u(z = 0)} = \frac{e^{-ikz}e^{\gamma|k|z} + Re^{ikz}e^{-\gamma|k|z}}{1 + R}. \quad (7.5)$$

From expressions 7.4 and 7.5, the deconvolved waveforms obtained from one source inside the building are dependent on the ground coupling; this is in contrast to the case when sources are outside the building (i.e., earthquakes). Interestingly, although the deconvolved waveforms retrieved from external sources are only related to the structure of the building (Part I), the waveforms from internal sources are governed by both the structure of the building and the ground coupling (through the reflection coefficient  $R$ ).

We numerically compute synthetic observed records based on expressions 7.2 and 7.3 (Figure 7.5a) and deconvolve these records with the waveform recorded at  $z = 0$  m (Figure 7.5b). The model parameters to compute the waveforms in Figure 7.5a are  $H = 39$  m,  $R = -0.6$ ,  $Q = 30$ , and  $c = 270$  m/s, where  $c$  is the velocity of the traveling wave in the

building. The waves are excited at  $z_s = 13$  m at  $t = 0.2$  s. The gray lines in Figure 7.5b indicate the arrival times of traveling waves estimated from expression 7.4 for above the source ( $z > z_s$ ) and expression 7.5 for below the source ( $z < z_s$ ). After deconvolution we obtain acausal waves in Figure 7.5b. These waves correspond to the term  $e^{ik(z-2z_s)}e^{-\gamma|k|(z-2z_s)}$  in expression 7.4 and  $e^{-ikz}e^{\gamma|k|z}$  in expression 7.5. Note that these acausal waves exist only for a time interval  $-z_s/c < t < 0$  ( $-0.05$  s  $< t < 0$  s in Figure 7.5b) and that the waves are not symmetric in time. Therefore, one source in the building does not explain the symmetry between the acausal and causal waves in Figure 7.4.

#### 7.4.2 Multiple sources

Using the normal-mode theory (Snieder, 2004b, Ch. 20), we compute the deconvolved waveforms obtained from multiple sources to qualitatively interpret the waveforms in Figure 7.4. We can express waves using either the summation of traveling waves or normal modes (Dahlen and Tromp, 1998, Ch. 4; Snieder and Şafak, 2006). Equations 7.2–7.5 are based on traveling waves, and these equations depend on the location of sources. We have to modify all terms in the numerators of equations 7.2 and 7.3, and choose equation 7.2 or 7.3 depending on the locations of receiver and source. On the other hand, the normal-mode analysis is suitable for multiple sources inside the building because source terms are separated from other terms (see for example equation 20.69 in Snieder (2004b)).

The model for our normal-mode analysis is a one-dimensional string model that includes radiation damping (Snieder, 2004b, Ch. 20.10). This model consists of an open-ended light string with mass density  $\rho$  connected to a heavy string with density  $\rho_g \gg \rho$  at  $z = 0$  (Figure 7.6). The wave propagation in the light and heavy strings represents the propagation in the building and the subsurface, respectively. Although the string model is primitive, the model qualitatively accounts for the wave propagation in the building because of three reasons; 1) we are only interested in the building, 2) the effect of the ground for the building is limited to the coupling at  $z = 0$ , and 3) we assume no waves return after the waves propagate to the ground. The ratio of the densities of the light and heavy strings is related to the reflection

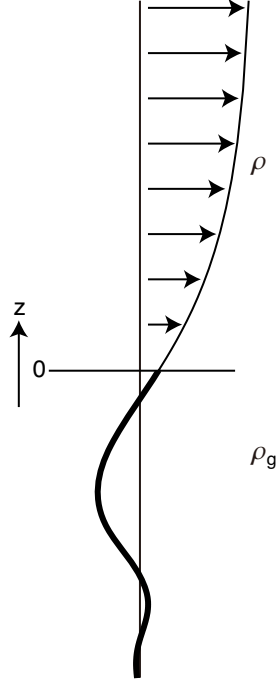


Figure 7.6. Displacement of radiation damping of the string model. The density of the light string ( $\rho$ ;  $z > 0$ ; thin line) is much smaller than that of the heavy string ( $\rho_g$ ;  $z < 0$ ; thick line).

coefficient at the connection of the strings (at the base of the building) (Coulson and Jeffrey, 1977, Ch. 2):

$$R = \frac{\sqrt{\rho} - \sqrt{\rho_g}}{\sqrt{\rho} + \sqrt{\rho_g}} = \frac{-1 + \epsilon}{1 + \epsilon}, \quad (7.6)$$

where

$$\epsilon = \sqrt{\rho/\rho_g}. \quad (7.7)$$

We carry out a perturbation analysis for this small dimensionless parameter.

The eigenfunctions and eigenfrequencies of this string model to first order in  $\epsilon$  for the mode  $m$  ( $m = 0, 1, \dots$ ) are given by

$$u_m(z) = \sin \left\{ \pm \left( m + \frac{1}{2} \right) \frac{\pi z}{H} \right\} - i\epsilon \frac{H-z}{H} \cos \left\{ \pm \left( m + \frac{1}{2} \right) \frac{\pi z}{H} \right\}, \quad (7.8)$$

$$\omega_m^{(r)} = \left\{ \pm \left( m + \frac{1}{2} \right) \pi - i\epsilon \right\} \frac{c}{H}, \quad (7.9)$$

respectively (see Appendix A). Because this string model does not include the intrinsic attenuation of the building, the eigenfrequency in expression 7.9 does not incorporate the attenuation. The superscript in expression 7.9 indicates that the complex eigenfrequency accounts only for the radiation loss. Snieder and Şafak (2006) derive the eigenfrequency ( $\omega_m^{(a)}$ ) with the intrinsic attenuation, but without radiation damping:

$$\omega_m^{(a)} = \left( m + \frac{1}{2} \right) \frac{\pi c}{H} (\pm 1 - i\gamma). \quad (7.10)$$

Comparing expressions 7.9 and 7.10, we account for the intrinsic attenuation and the radiation damping using the following eigenfrequency:

$$\omega_m^{(ar)} = \left\{ \pi \left( m + \frac{1}{2} \right) (\pm 1 - i\gamma) - i\epsilon \right\} \frac{c}{H}, \quad (7.11)$$

where we assume the intrinsic attenuation to be weak and ignore a cross term between the intrinsic attenuation and radiation damping. In expression 7.11, the first term ( $\pi(m + 1/2)c/H$ ) is the frequency in case there is no intrinsic attenuation ( $\gamma = 0$ ) and the building has a rigid boundary at the bottom ( $R = -1$ ). The second term ( $-i\gamma\pi(m + 1/2)c/H$ ) accounts for the intrinsic attenuation, and the third term ( $-i\epsilon c/H$ ) accounts for the radiation loss at the base of the building. The waveforms in this string model with the intrinsic attenuation are given by the summation of normal modes (Snieder, 2004b):

$$u(z, \omega) = \sum_{m=0}^{\infty} \frac{u_m(z) \int u_m^*(z') F(z') dz'}{(\omega_m^{(ar)})^2 - \omega^2}, \quad (7.12)$$

where  $F$  indicates the forces that excite the vibrations.

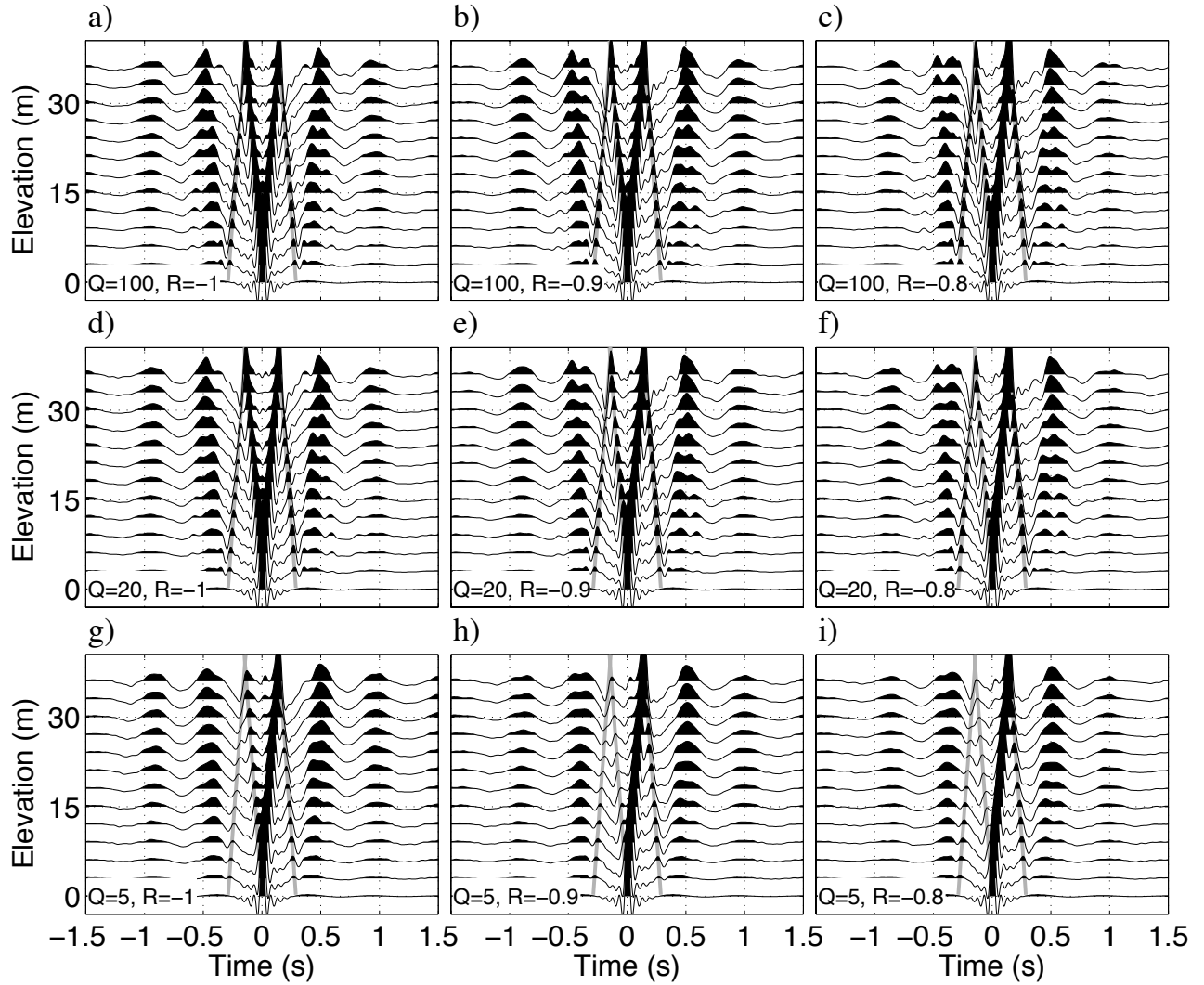


Figure 7.7. Synthetic deconvolved waveforms using three-hour random vibrations as sources after applying the same bandpass filter as in Figure 7.4. Panels (a)–(i) are computed by adopting different quality factors  $Q$  and reflection coefficients  $R$  (see lower-left of each panel). Gray lines indicate the arrival time of the traveling wave with the velocity used for the modeling ( $c = 270$  m/s). The scale of the amplitudes at each panel is the same.

We numerically compute the synthetic records using expression 7.12 for various values of the quality factor  $Q$  and the reflection coefficient  $R$  with fixed parameters:  $H = 39$  m and  $c = 270$  m/s. We use random sources (random amplitude, phase, and location) and compute three-hour random-source synthetic observed records. Then we deconvolve the waveforms with the records at the floor at  $z = 0$  (Figure 7.7). All panels in Figure 7.7 show waves for both positive and negative times, which is consistent with the deconvolved waveforms in Figure 7.4. Especially for  $|t| \gtrsim 1$  s, the waveforms in Figure 7.7 are similar in character to those in Figure 7.4. For  $|t| \lesssim 0.3$  s, we obtain the traveling waves, propagating with the same velocity as used for the modeling ( $c = 270$  m/s; compare the waveforms and the gray lines in Figure 7.7).

The waveforms are increasingly asymmetric in time as the reflection coefficient differs from  $R = -1$ , or as the anelastic damping increases (see for example Figures 7.7def or 7.7beh). From Figure 7.7, we learn that the amplitude decay of the waveforms is related to the intrinsic attenuation and the boundary condition. Based on the similarity of the waveforms in Figures 7.4 and 7.7, the reflection coefficient and the quality factor of the real building are likely close to those in Figures 7.7a–7.7e. Because we can estimate  $Q^{(a)}$  independent from the ground coupling using the earthquake data (Part I), the deconvolution using ambient vibrations is potentially useful for estimating  $R$ . However, to estimate  $R$ , we need a more quantitative analysis, which is a topic of future work. Also, for waveform matching this string model may be too simple. We conclude that the estimated velocity from the waveforms in Figure 7.4 indicates the true velocity of the traveling wave in the building, and the quality factor estimated from the amplitude decay of the waveforms is  $Q^{(ar)}$  not just  $Q^{(a)}$ . In the next section, we monitor the velocity of the building.

## 7.5 Monitoring the building using ambient vibration

For monitoring the velocity of the traveling waves, we need to know the minimum time length to obtain stable waveforms. To determine this time interval, we compute the convergence of the deconvolved waveforms as a function of the stacking duration  $h$  using a RMS

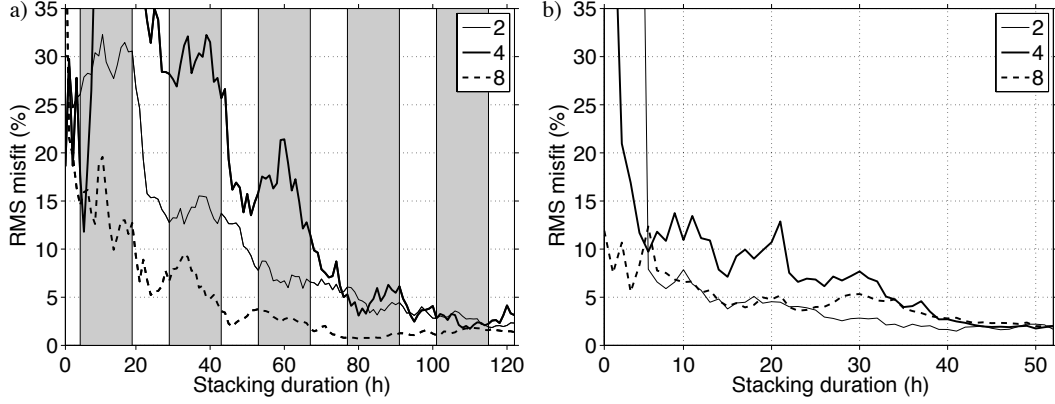


Figure 7.8. Convergence test of ambient-vibration interferometry based on RMS misfits (equation 7.13) as a function of the stacking duration. (a) RMS misfits with respect to the stacked waveform over two-week ambient vibrations recorded in both daytime (8AM–6PM) and nighttime (6PM–8AM). The shaded areas correspond to nighttimes. We show the misfits at second, fourth, and eighth floors. (b) RMS misfits with respect to the same waveforms as panel (a) but using only daytime data. We show the RMS misfits for 122 hours (52 hours of daytime and 70 hours of nighttime) in panel (a) and 52 hours in panel (b).

misfit as used by Prieto et al. (2010):

$$\text{Misfit}(z, h) = \sqrt{\frac{\int_{t_a}^{t_b} \{D_h(z, t) - D_{all}(z, t)\}^2 dt}{\int_{t_a}^{t_b} \{D_{all}(z, t)\}^2 dt}}, \quad (7.13)$$

where  $t_a$  and  $t_b$  define the time interval to compute the misfit (-1.5 s and 1.5 s in this study),  $h$  the stacking duration,  $D_h$  the deconvolved waves stacked over time period  $h$ , and  $D_{all}$  the deconvolved waveforms obtained from the entire data set recorded during the two weeks. If the RMS misfit is small, the deconvolved waveform  $D_h$  is similar to the deconvolved waveforms obtained from the entire data set.

Figure 7.8 indicates the convergence of deconvolved waveforms with respect to the stacking duration. In Figure 7.8a, we use both daytime (8AM–6PM) and nighttime (6PM–8AM) data. Since the RMS misfit is lower than 5% when we use the ambient-vibration data longer than 96 hours, we decide that stacking over 96 hours is sufficient to obtain stable deconvolved waveforms. The RMS misfit in Figure 7.8a increases during some nighttimes. However, since for example the RMS misfits at  $h = 66$  are smaller than the misfits at  $h = 52$  at all floors, the

vibrations in nighttime also contribute to the convergence. We also compute the waveforms using daytime data only and estimate the RMS misfit (Figure 7.8b). Interestingly, although Figure 7.8b shows rapid convergence to 10%, we need about 40 hours (equivalent to four days) to obtain the RMS misfit lower than 5%. In Figure 7.8, we show the RMS misfits for 122 hours (panel a) and for 52 hours (panel b), which are equivalent because 122 hours include 52 hours of daytime and 70 hours of nighttime.

Figure 7.9 shows the deconvolved waveforms using the data recorded during both daytime and nighttime (same data as used in Figure 7.8a), and Figure 7.10 using the data recorded daytime only (same data as used in Figure 7.8b). In Figure 7.9, we stack the data over four-day intervals (96 hours) and overlap these intervals over two days. From the waveforms in Figure 7.9, we estimate the velocity of the traveling waves using the same method as Figure 7.4. The estimated velocities are stable during the two weeks, and the uncertainty is about 6 m/s, which is smaller than the uncertainty in the velocity estimated from earthquake data (Figure 12 in Part I). For earthquakes, the estimated velocities vary more than for ambient vibrations, and the acceleration of the observed records also varies (Figure 12b in Part I). These variations indicate that the velocities estimated from earthquakes include nonlinear effects. The velocities estimated from ambient vibrations are not affected by nonlinearity because the acceleration of the observed records is small and does not vary much. Therefore, ambient vibration is appropriate for monitoring the velocity of traveling waves in the linear regime. Deconvolved waveforms in Figure 7.10 are similar to those in Figure 7.9, and the difference in estimated velocities are not statistically significant.

## 7.6 Conclusions

We retrieve traveling waves inside the building by applying seismic interferometry to ambient-vibration data. In contrast to the case when sources are only outside the building, deconvolved waves obtained from ambient vibrations are nonzero for both positive and negative times, which is explained by that multiple sources simultaneously excite inside the building. Based on the normal-mode analysis, we synthetically reconstruct waveforms

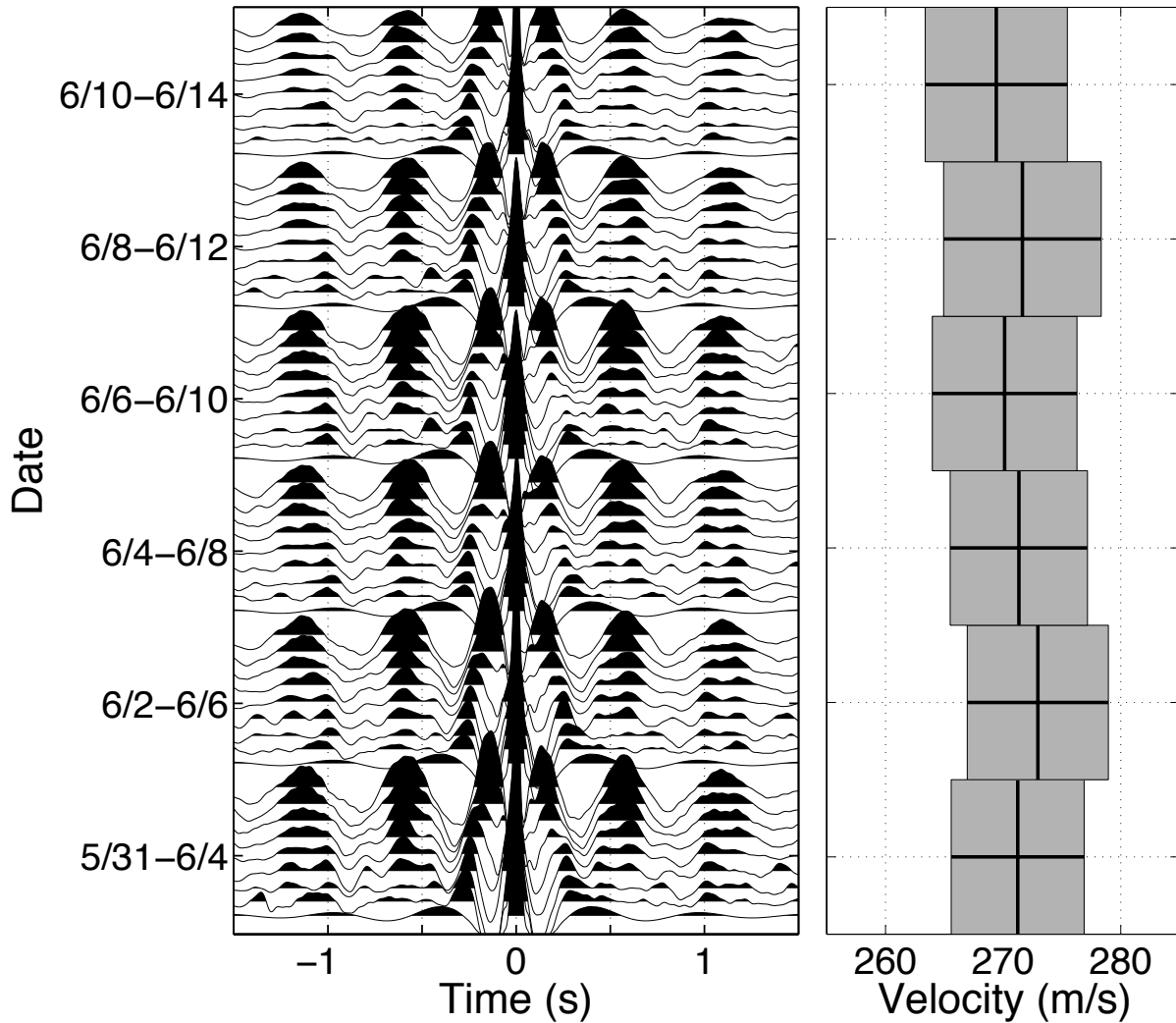


Figure 7.9. (Left) Time-lapse deconvolved waveforms averaged over 96 hours with a 48-hour overlap using ambient vibrations recorded in both daytime and nighttime. We have applied the same bandpass filter as used in Figure 7.4. (Right) Shear-wave velocities estimated from the traveling waves in the left panel. The width of each box indicates one standard deviation of estimated velocities at each floor.

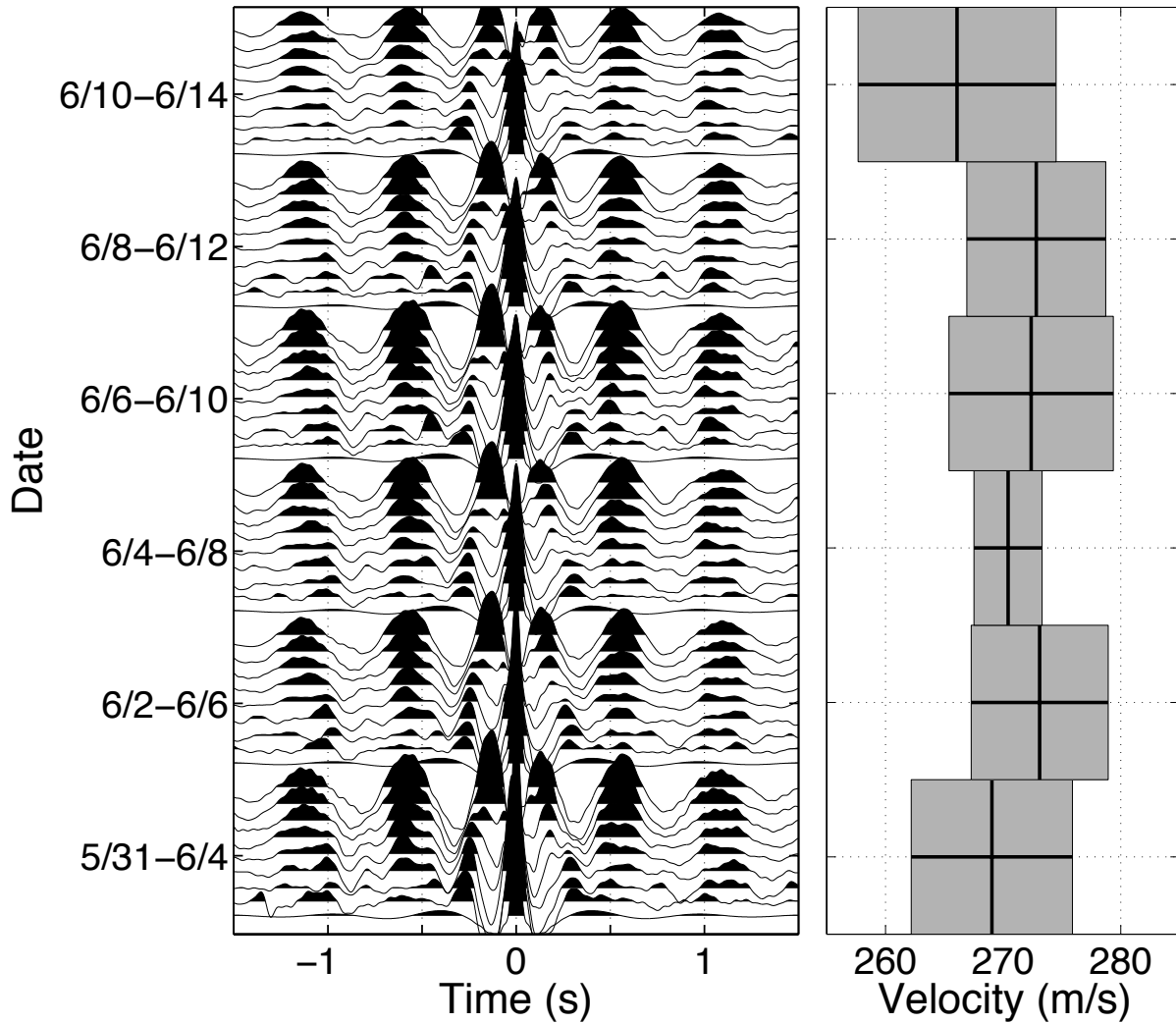


Figure 7.10. (Left) Time-lapse deconvolved waveforms averaged over 40 hours with a 20-hour overlap using ambient vibration recorded in daytime only. We have applied the same bandpass filter as used in Figure 7.4. (Right) Shear-wave velocities estimated from the traveling waves in the left panel. The width of each box indicates one standard deviation of estimated velocities at each floor.

that are qualitatively similar to the real data using the simple string model. The velocity estimated from the synthetic waveforms with this model is the same as the true velocity although the attenuation estimated from the decay of the amplitude with time is not equal to the intrinsic attenuation of the building. Since the amplitude decay is also influenced by radiation losses at the base of the building, we are, in principle, able to estimate both quality factors and reflection coefficients separately from the amplitude of the waveforms, which requires a more accurate model than the string model used here. For monitoring the building, we find the time interval to obtain stable waveforms using the convergence test, and we need deconvolved ambient vibrations averaged over four days to obtain stable waveforms for this building. The velocity estimated from ambient-vibration data is more stable than that from earthquake data because the ambient vibrations are due to the linear response of the building.

## 7.7 Acknowledgments

We want to thank Suncoch Consultant Co., Ltd. and Akebono Brake Industry Co., Ltd. for providing the data. We thank Seiichiro Kuroda for his professional comments to improve this work. N.N. thanks the instructor and classmates of the class *Academic Publishing* in Colorado School of Mines for their help in preparing this manuscript. This work was supported by the Consortium Project on Seismic Inverse Methods for Complex Structures at the Center for Wave Phenomena.

## 7.A Eigenfunctions and eigenfrequencies of the string model

In this appendix, we derive the eigenfunctions (expression 7.8) and eigenfrequencies (expression 7.9) of the string model (Figure 7.6) using a perturbation analysis in the small parameter  $\epsilon$  (expression 7.7). The normal modes of the unperturbed string ( $\epsilon = 0$ ,  $\rho_g = \infty$ , and  $R = -1$ ) are given by

$$u(z > 0) = \sin k^{(u)}z, \quad (7.A1)$$

$$u(z < 0) = 0, \quad (7.A2)$$

where  $k^{(u)}$  is the unperturbed wavenumber. The parameter  $\epsilon$  accounts for the coupling of the light string to the heavy string (expression 7.6). For the unperturbed model ( $\epsilon = 0$ ), the string has infinite mass for  $z < 0$ , and hence it does not move. When  $\epsilon \neq 0$ , the waveforms, which include perturbed waves, are expressed by

$$u(z > 0) = \sin kz + A \cos kz, \quad (7.A3)$$

$$u(z < 0) = B e^{-ik_g z}, \quad (7.A4)$$

respectively. The coefficients  $A$  and  $B$  depend on  $\epsilon$ . According to expression 7.A4, waves are radiated downward in the lower (heavy) part of the string (the thick line in Figure 7.6). The ratio of the wavenumbers in the light and heavy strings ( $k/k_g$ ) is given by Ch. 2 in Coulson and Jeffrey (1977):

$$k/k_g = \epsilon. \quad (7.A5)$$

The boundary conditions of the model are  $\partial u/\partial z = 0$  at  $z = H$ , and  $u$  and  $\partial u/\partial z$  are continuous at  $z = 0$ . From expressions 7.A3 and 7.A4 and the boundary conditions, we obtain

$$\frac{k}{k_g} \sin kH + i \cos kH = \frac{\epsilon}{2i}(e^{ikH} - e^{-ikH}) + \frac{i}{2}(e^{ikH} + e^{-ikH}) = 0, \quad (7.A6)$$

where we use expression 7.A5 for  $k/k_g$ . From expression 7.A6, we obtain

$$e^{2ikH} = -\frac{1 - \epsilon}{1 + \epsilon}. \quad (7.A7)$$

Applying a first-order Taylor expansion in  $\epsilon$  to the wavenumber in expression 7.A7, we obtain the wavenumber for mode  $m$ :

$$k_m = \left\{ \pm \left( m + \frac{1}{2} \right) \pi - i\epsilon \right\} \frac{1}{H}, \quad (7.A8)$$

where the real and imaginary of  $k_m$  are the unperturbed and perturbed parts of the wavenumber of mode  $m$ , respectively. The perturbation of the wavenumber caused by the radiation damping ( $-i\epsilon/H$ ) is constant for all modes. The eigenfrequency  $\omega_m$  that corresponds to this wavenumber is given by expression 7.9.

From expressions 7.A3 and 7.A8, the waveform (eigenfunction) for the mode  $m$  within the light string is given by

$$\begin{aligned} u_m(z) &= \sin(k_m z) + A \cos(k_m z) = \sin(k_m z) + \frac{\cos(k_m H)}{\sin(k_m H)} \cos(k_m z) \\ &= \frac{\cos\{k_m(H-z)\}}{\sin(k_m H)}, \end{aligned} \quad (7.A9)$$

where we use the boundary condition  $\partial u / \partial z = 0$  at  $z = H$  at the second equality. Using Taylor expansions to first order in  $\epsilon$  in the sine and cosine functions, we derive the eigenfunction shown in expression 7.8.

## CHAPTER 8

# BODY-WAVE INTERFEROMETRY USING REGIONAL EARTHQUAKES WITH MULTI-DIMENSIONAL DECONVOLUTION AFTER WAVEFIELD DECOMPOSITION AT FREE SURFACE

To be submitted to *Geophysical Journal International* (2013)

Nori Nakata<sup>1</sup>, Roel Snieder<sup>1</sup>, and Michael Behm<sup>1</sup>

### 8.1 Summary

Passive seismic methods using earthquakes can be applied for extracting body waves and obtaining information of subsurface structure. To analyze earthquake data, one uses receiver functions, tomography, and seismic interferometry. In this study, we retrieve reflected plane waves by applying seismic interferometry to the recorded ground motion from a cluster of earthquakes. We employ upgoing/downgoing P/S wavefield decomposition, time windows, time reversal, and multi-dimensional deconvolution to improve the quality of the extraction of reflected waves with seismic interferometry. The wavefield separation and seismic interferometry based on multi-dimensional deconvolution (MDD) allow us to reconstruct PP, PS, SP, and SS reflected waves without unwanted crosstalk between P and S waves. From earthquake data, we obtain PP, PS, and SS reflected plane waves that reflect off the same reflector, and estimate P- and S-wave velocities.

### 8.2 Introduction

Body waves obtained from earthquakes (especially teleseismic events) have been used for imaging deep structure (crust–mantle) (e.g., Bostock and Sacchi, 1997; Bostock and Rondey, 1999; Baig et al., 2005; Dasgupta and Nowack, 2006; Behm, 2013). The receiver function

---

<sup>1</sup>Center for Wave Phenomena, Colorado School of Mines

is one technique to obtain information of subsurface structure by estimating travel-time differences between P and PS converted waves (e.g., Langston, 1979; Li et al., 2000; Assumpção et al., 2002). Seismic interferometry (Aki, 1957; Claerbout, 1968; Wapenaar, 2004) is also used for analyses of passive seismic waves including earthquake records. One can apply seismic interferometry to body waves generated by earthquakes and obtain images of subsurface structure (e.g., Abe et al., 2007; Tonegawa et al., 2009; Ruigrok et al., 2010; Ruigrok and Wapenaar, 2012). Abe et al. (2007) found that the image obtained from seismic interferometry has higher resolution than retrieved from receiver functions, but seismic interferometry creates pseudo events, which can be suppressed by averaging over many earthquakes. Higher resolution Green's functions are also obtained by estimating and deconvolving source functions from earthquake data recorded by a receiver array (Bostock, 2004). The target for most body-wave seismic interferometry studies is deep structure, but a few studies create images in shallow zones (Ryberg, 2011; Yang et al., 2012). Seismic interferometry has been developed for analyzing data trace by trace, and Wapenaar et al. (2008a,b) improve seismic interferometry by using multi-dimensional deconvolution (MDD). Although MDD interferometry requires one to separate wavefields depending on the direction of wave propagation and to solve an inverse problem, MDD overcomes several limitations (e.g., attenuation, complicated incident waves, and source distribution) of trace-by-trace interferometry (see section 8.5.3).

In this study, we apply trace-by-trace and MDD seismic interferometry to earthquake data to retrieve direct and reflected plane waves. We first propose a technique of wavefield decomposition at the free surface. Using this decomposition, we can separate observed two-component wavefields into upgoing/downgoing P/S wavefields, which is necessary for MDD interferometry, and show why this is an improvement for seismic interferometry. Next, we introduce earthquake data observed over the LaBarge field in Wyoming. Then we show a mathematical description of seismic interferometry and improvement of interferometric wavefields by applying different techniques to the earthquake data.

### 8.3 Upgoing/Downgoing P/S wavefield decomposition

A number of studies propose different techniques for wavefield separation: using, for example, dual sensors (Loewenthal and Robinson, 2000), Helmholtz decomposition (Robertsson and Muyzert, 1999; Robertsson and Curtis, 2002), over/under towed-streamer acquisition (Moldoveanu et al., 2007), and two steps of acoustic and elastic decomposition (Schalkwijk et al., 2003). Wavefield separation improves interferometric gathers to focus on target reflections (Mehta et al., 2007a; Vasconcelos et al., 2008; van der Neut and Bakulin, 2009). When receivers are embedded in a medium (e.g., ocean-bottom sensors and borehole sensors), direct and reflected waves come from quasi-opposite directions. Therefore with decomposition, one can suppress some spurious multiples caused by crosstalk of direct-direct and reflected-reflected waves generated during the process of seismic interferometry (Snieder et al., 2006b; Mehta et al., 2007a). Because receivers are deployed at the free surface in our data, we cannot suppress the spurious multiples by separating wavefields based on the direction of wave propagation. We employ time windows to reduce the spurious multiples (Bakulin and Calvert, 2006), and apply wavefield decomposition for separating the direction of wave propagation, which is necessary for MDD (Wapenaar et al., 2011b), and for suppressing crosstalk of P and S waves.

We decompose wavefields into upgoing/downgoing P/S waves using the stress-free boundary condition at the free surface (similar to Wapenaar et al., 1990). Table 8.1 shows the notation used in this study, and Figure 8.1 defines the positive directions of  $x$ ,  $z$ , and each wavefield. Let us consider the reflection at the free surface within the vertical plane in which the wave propagates. The goal of this wavefield decomposition is to independently compute  $U_p$ ,  $D_p$ ,  $U_s$ , and  $D_s$  from observed data. We assume that a layer below the free surface is laterally homogeneous, which means  $\alpha$  and  $\beta$  are constant at the near surface. Based on the theory in Aki and Richards (2002, Table 5.1), the displacements of upgoing/downgoing P/S waves in the space-time domain using the Fourier convention  $f(x, t) = (1/2\pi)^2 \iint_{-\infty}^{\infty} F(k, \omega) e^{i(kx - \omega t)} dk d\omega$  are

Table 8.1. Notations of physical parameters and wavefields.

Notation	Description	Relationship with other parameters
$\omega$	Angular frequency <sup>1</sup>	
$\alpha$	P-wave velocity at the layer below the free surface	
$\beta$	S-wave velocity at the layer below the free surface	
$\rho$	Density	
$\sigma_{ij}$	Stress in the $ij$ component	
$\mu$	Lame's parameters	$\mu = \beta^2 \rho$
$\lambda$		$\lambda = (\alpha^2 - 2\beta^2)\rho$
$\theta_p$	Angle of the P incident wave with respect to the free surface	
$\theta_s$	Angle of the S incident wave with respect to the free surface	
$k$	Horizontal wavenumber	$k = \omega \sin \theta_p / \alpha = \omega \sin \theta_s / \beta$
$\nu_p$	Vertical wavenumber for P wave	$\nu_p = \omega \cos \theta_p / \alpha = \sqrt{\omega^2 / \alpha^2 - k^2}$
$\nu_s$	Vertical wavenumber for S wave	$\nu_s = \omega \cos \theta_s / \beta = \sqrt{\omega^2 / \beta^2 - k^2}$
$u_z$	Vertical component of the displacement of observed wavefields	
$u_x$	Horizontal component of the displacement of observed wavefields	
$\mathbf{U}_p$	Vector displacement of upgoing P waves	
$\mathbf{D}_p$	Vector displacement of downgoing P waves	
$\mathbf{U}_s$	Vector displacement of upgoing S waves	
$\mathbf{D}_s$	Vector displacement of downgoing S waves	
$U_p$	Scalar displacement of upgoing P waves at the free surface	
$D_p$	Scalar displacement of downgoing P waves at the free surface	
$U_s$	Scalar displacement of upgoing S waves at the free surface	
$D_s$	Scalar displacement of downgoing S waves at the free surface	
$U_p^d$	Direct upgoing P waves	
$U_p^r$	Surface-related reflected upgoing P waves	$U_p = U_p^d + U_p^r$
$G$	Green's function	

<sup>1</sup> We consider that the angular frequency is positive; therefore wavenumbers are also positive. For negative frequencies, we compute complex conjugate of a function in positive frequencies.

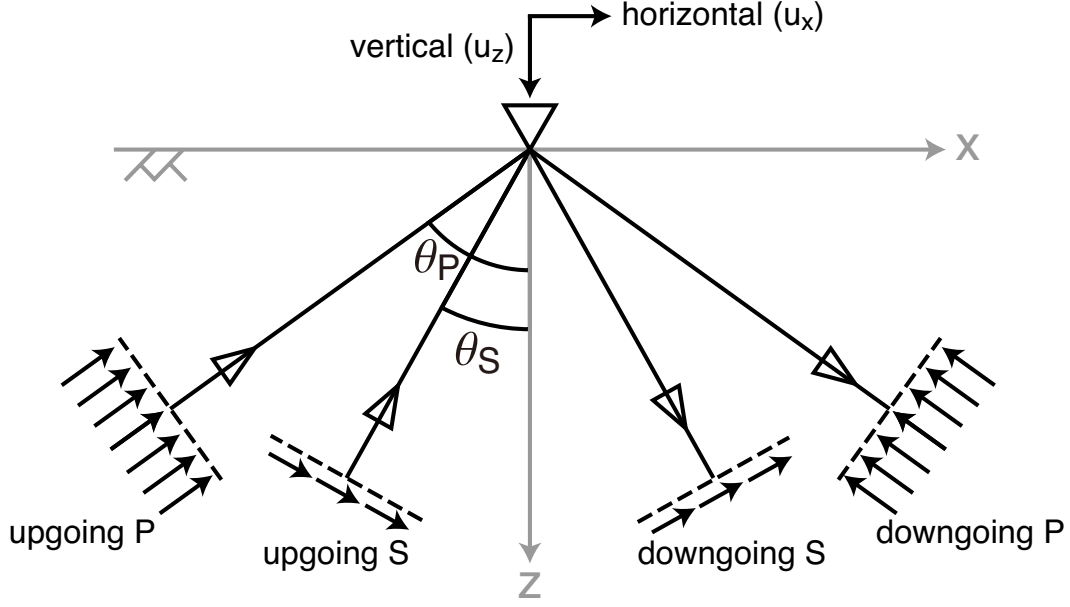


Figure 8.1. Plane-wave reflection system and coordinates for the wavefield decomposition in section 8.3. The horizontal gray line shows the free surface (indicated by  $\llcorner$ ), and the downward triangle on the line is a receiver. The black arrows near the receiver define the positive directions of observed records. The dashed lines illustrate portions of plane waves of upgoing/downgoing P/S waves. The black arrows near the dashed lines describe the positive directions of each vector wavefield. Solid black lines connected to dashed lines indicate the ray paths of each wavefield, and the triangles on the solid lines the direction of propagation. The angles  $\theta_P$  and  $\theta_S$  are the angles of incidence for P and S waves, respectively.

$$\begin{aligned}
 \mathbf{U}_p(x, z, t) &= \left(\frac{1}{2\pi}\right)^2 \iint_{-\infty}^{\infty} U_p(k, \omega) \frac{\alpha}{\omega} \begin{pmatrix} k \\ -\nu_p \end{pmatrix} e^{i(kx - \nu_p z - \omega t)} dk d\omega, \\
 \mathbf{D}_p(x, z, t) &= \left(\frac{1}{2\pi}\right)^2 \iint_{-\infty}^{\infty} D_p(k, \omega) \frac{\alpha}{\omega} \begin{pmatrix} k \\ \nu_p \end{pmatrix} e^{i(kx + \nu_p z - \omega t)} dk d\omega, \\
 \mathbf{U}_s(x, z, t) &= \left(\frac{1}{2\pi}\right)^2 \iint_{-\infty}^{\infty} U_s(k, \omega) \frac{\beta}{\omega} \begin{pmatrix} \nu_s \\ k \end{pmatrix} e^{i(kx - \nu_s z - \omega t)} dk d\omega, \\
 \mathbf{D}_s(x, z, t) &= \left(\frac{1}{2\pi}\right)^2 \iint_{-\infty}^{\infty} D_s(k, \omega) \frac{\beta}{\omega} \begin{pmatrix} \nu_s \\ -k \end{pmatrix} e^{i(kx + \nu_s z - \omega t)} dk d\omega,
 \end{aligned} \tag{8.1}$$

where the subscript  $s$  denotes SV waves. Since the scalar displacements are composed of constant amplitudes of upgoing waves and reflection coefficients at the free surface (see Table 5.1 in Aki and Richards, 2002), these scalar displacements are functions of wavenumber and

frequency but not of depth. In the wavenumber-frequency domain, expression 8.1 is written as

$$\begin{aligned}
\mathbf{U}_p(k, z, \omega) &= U_p(k, \omega) \frac{\alpha}{\omega} \begin{pmatrix} k \\ -\nu_p \end{pmatrix} e^{-i\nu_p z}, \\
\mathbf{D}_p(k, z, \omega) &= D_p(k, \omega) \frac{\alpha}{\omega} \begin{pmatrix} k \\ \nu_p \end{pmatrix} e^{i\nu_p z}, \\
\mathbf{U}_s(k, z, \omega) &= U_s(k, \omega) \frac{\beta}{\omega} \begin{pmatrix} \nu_s \\ k \end{pmatrix} e^{-i\nu_s z}, \\
\mathbf{D}_s(k, z, \omega) &= D_s(k, \omega) \frac{\beta}{\omega} \begin{pmatrix} \nu_s \\ -k \end{pmatrix} e^{i\nu_s z}.
\end{aligned} \tag{8.2}$$

The horizontal and vertical components of the displacement are, in the wavenumber-frequency domain, given by

$$u_x(k, z, \omega) = U_p(k, \omega) \frac{\alpha k}{\omega} e^{-i\nu_p z} + D_p(k, \omega) \frac{\alpha k}{\omega} e^{i\nu_p z} + U_s(k, \omega) \frac{\beta \nu_s}{\omega} e^{-i\nu_s z} + D_s(k, \omega) \frac{\beta \nu_s}{\omega} e^{i\nu_s z}, \tag{8.3}$$

$$u_z(k, z, \omega) = U_p(k, \omega) \frac{-\alpha \nu_p}{\omega} e^{-i\nu_p z} + D_p(k, \omega) \frac{\alpha \nu_p}{\omega} e^{i\nu_p z} + U_s(k, \omega) \frac{\beta k}{\omega} e^{-i\nu_s z} + D_s(k, \omega) \frac{-\beta k}{\omega} e^{i\nu_s z}. \tag{8.4}$$

When receivers are located at the free surface ( $z = 0$ ), expressions 8.3 and 8.4 simplify to

$$u_x(k, 0, \omega) = \frac{1}{\omega} [\alpha k \{U_p(k, \omega) + D_p(k, \omega)\} + \beta \nu_s \{U_s(k, \omega) + D_s(k, \omega)\}], \tag{8.5}$$

$$u_z(k, 0, \omega) = \frac{1}{\omega} [-\alpha \nu_p \{U_p(k, \omega) - D_p(k, \omega)\} + \beta k \{U_s(k, \omega) - D_s(k, \omega)\}]. \tag{8.6}$$

Because the stress condition at the free surface is

$$\sigma_{xz} = 0 \rightarrow \frac{\partial u_x}{\partial z} + \frac{\partial u_z}{\partial x} = 0, \tag{8.7}$$

$$\sigma_{zz} = 0 \rightarrow \lambda \left( \frac{\partial u_x}{\partial x} + \frac{\partial u_z}{\partial z} \right) + 2\mu \frac{\partial u_z}{\partial z} = 0, \tag{8.8}$$

the scalar displacements satisfy

$$2\alpha k\nu_p \{U_p(k, \omega) - D_p(k, \omega)\} - \beta (k^2 - \nu_s^2) \{U_s(k, \omega) - D_s(k, \omega)\} = 0, \quad (8.9)$$

$$\alpha (\lambda k^2 + \lambda\nu_p^2 + 2\mu\nu_p^2) \{U_p(k, \omega) + D_p(k, \omega)\} - 2\beta\mu k\nu_s \{U_s(k, \omega) + D_s(k, \omega)\} = 0, \quad (8.10)$$

where we inserted equations 8.3–8.4 into equations 8.7–8.8. To solve four unknowns ( $U_p$ ,  $D_p$ ,  $U_s$ , and  $D_s$ ), we have four equations (equations 8.5, 8.6, 8.9, and 8.10); therefore we can compute scalar wavefields:

$$\begin{aligned} U_p(k, \omega) &= \frac{\beta^2 k}{\alpha\omega} u_x(k, 0, \omega) - \frac{\omega^2 - 2\beta^2 k^2}{2\alpha\omega\nu_p} u_z(k, 0, \omega), \\ D_p(k, \omega) &= \frac{\beta^2 k}{\alpha\omega} u_x(k, 0, \omega) + \frac{\omega^2 - 2\beta^2 k^2}{2\alpha\omega\nu_p} u_z(k, 0, \omega), \\ U_s(k, \omega) &= \frac{\omega^2 - 2\beta^2 k^2}{2\beta\omega\nu_s} u_x(k, 0, \omega) + \frac{\beta k}{\omega} u_z(k, 0, \omega), \\ D_s(k, \omega) &= \frac{\omega^2 - 2\beta^2 k^2}{2\beta\omega\nu_s} u_x(k, 0, \omega) - \frac{\beta k}{\omega} u_z(k, 0, \omega). \end{aligned} \quad (8.11)$$

Finally, we apply inverse Fourier transforms to expression 8.11 to obtain upgoing/downgoing P/S waves in the space-time domain.

If we knew  $k$ ,  $\theta_p$ , or  $\theta_s$ , we could solve equation 8.11 with one receiver in the space-time domain; however the estimation is difficult because incoming waves are composed of a variety of angles of incidence. Therefore for this decomposition, we need a receiver array for the Fourier transform, which decomposes the wavefields into the different wavenumber components  $k$ , and the assumption, in which velocities just below the free surface in the region of this array are constant (laterally homogeneous in the near surface). In expression 8.11,  $u_x$  and  $u_z$  are observed after a double Fourier transform,  $k$  and  $\omega$  are given in the wavenumber-frequency domain, and  $\nu_p$  and  $\nu_s$  can be computed in the wavenumber-frequency domain when  $\alpha$  and  $\beta$  are given (Table 8.1). In conclusion, when we assume  $\alpha$  and  $\beta$ , we can compute  $U_p$ ,  $D_p$ ,  $U_s$ , and  $D_s$  using equation 8.11.

To estimate velocities, we use the fact that  $U_p$  and  $U_s$  do not include direct S and P waves, respectively. If we use correct velocities, the amplitudes of the direct P waves in  $U_s$

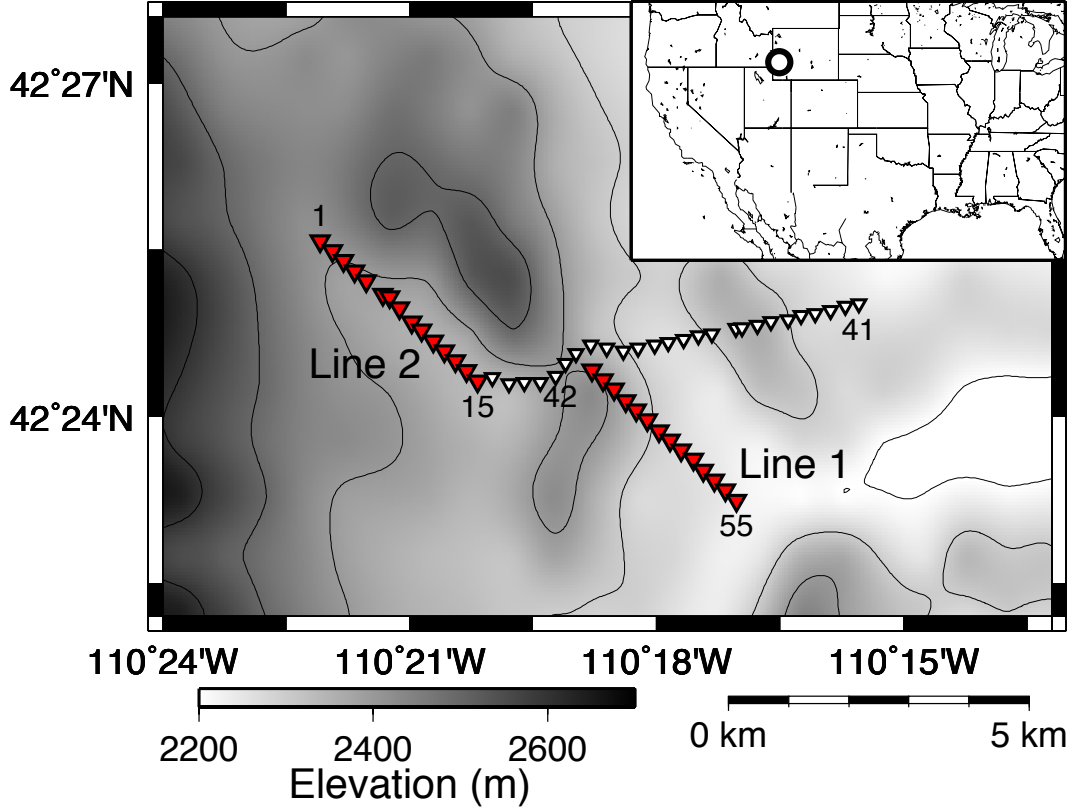


Figure 8.2. Geometry of receivers (triangles). We use records observed at the receivers shown by red triangles for this study. Survey lines 1 and 2 contain receivers 1–15 and 42–55, respectively. The circle on the top-right map shows the location of magnified area. The gray scale illustrates topography.

are zero and those of direct S waves in  $U_p$  are also zero. Therefore, we can estimate  $\alpha$  and  $\beta$  by minimizing amplitudes around arrival times of direct P waves in  $U_s$  and of direct S waves in  $U_p$ . Note that because  $U_s$  only depends on  $\beta$  (see equation 8.11), the estimation of  $\beta$  from  $U_s$  and then  $\alpha$  from  $U_p$  is computationally easier.

## 8.4 Earthquake data

### 8.4.1 Data set and previous studies

We analyze local earthquake data recorded at the LaBarge field in Wyoming (Figure 8.2) to extract subsurface information using seismic interferometry. A dense receiver network, which contained 55 three-component broadband seismometers with a 250-m average receiver interval, recorded more than 200 earthquakes (Figure 8.3) during a continuous recording pe-

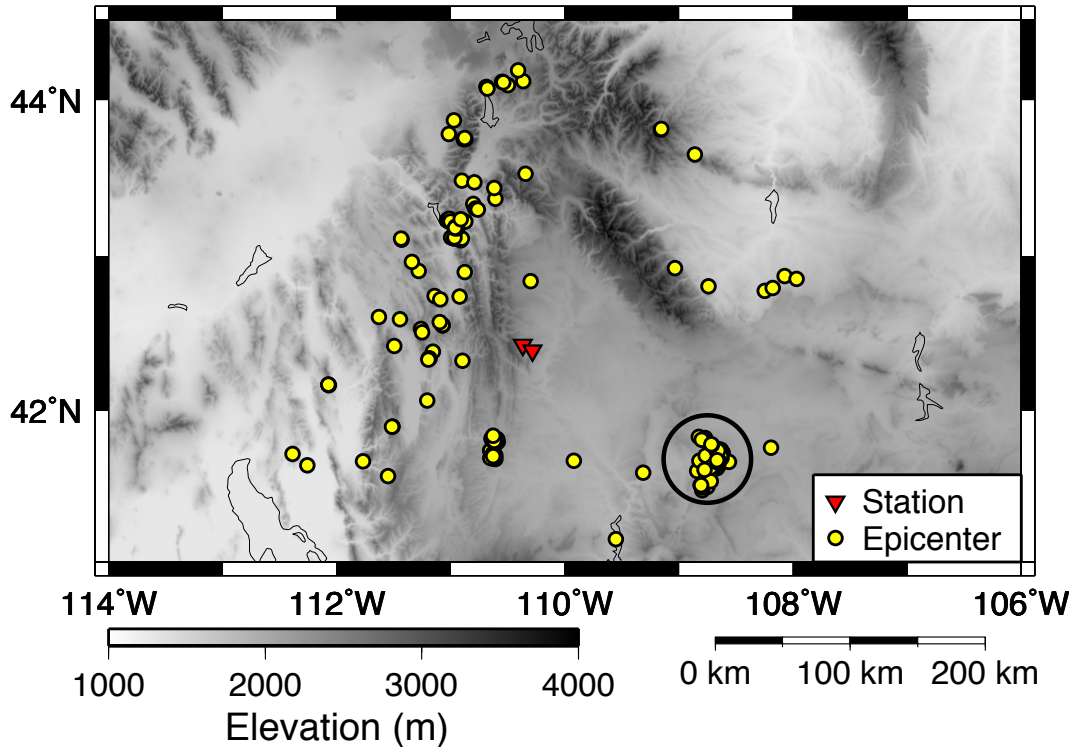


Figure 8.3. Geometry of earthquakes (yellow dots) and receivers (red triangles). We use an earthquake swarm (embraced by black circle) for the interferometry study. Triangles indicate the locations of receivers No. 1 and 55. The gray scale illustrates topography.

riod (November 2008–June 2009). With the dense receiver geometry, we have an opportunity to obtain relatively shallow structural information ( $\lesssim 5$  km). Based on the earthquake catalogs provided by U.S. Geological Survey (USGS) and the EarthScope Array Network Facility (ANF), the magnitudes and depths of observed earthquakes are smaller than 2 and shallower than 10 km, respectively. Using this data set, several studies obtain images or velocities of the subsurface in the survey area. Leahy et al. (2012) apply receiver function to teleseismic events to image the subsurface. Schmedes et al. (2012) and Biryol et al. (2013) apply earthquake tomography to teleseismic and local earthquake data, respectively. Behm et al. (2013) apply seismic interferometry to reconstruct surface waves using ambient-noise data and obtain Rayleigh- and Love-wave velocities. From teleseismic data, Behm (2013) obtains vertical-incident reflected waves by employing blind deconvolution based on a multichannel analysis.

### 8.4.2 Observed data

Because the wavefield decomposition in section 8.3 is valid for the wave propagation in a vertical plane, we restrict ourselves to hypocenters and receivers near that vertical plane. We use a cluster of earthquakes (represented by the black circle in Figure 8.3), which contains about 100 earthquakes and produces quasi-plane waves with nearly the same angles of incidence. This cluster of earthquakes is roughly 180 km away from the stations and located on the extensions of survey lines 1 and 2 in Figure 8.2. Therefore in this study, we use this cluster of earthquakes and receivers of survey lines 1 and 2 (the red triangles in Figure 8.2) to reconstruct direct and reflected plane waves with seismic interferometry.

Figure 8.4 shows sample observed wavefields excited by one earthquake. Direct P waves arrive around 28 s, S waves around 50 s, and surface waves around 70 s. Wavefields at receivers 29-30 are contaminated by traffic noise which is generated from a road close to these receivers. The high-energy waveforms contain frequencies up to 7 Hz. Because the aperture of the receiver array is small, we cannot estimate seismic phases of each arrival wave from the move out of travel times in Figure 8.4. The possible seismic phases of incoming waves are direct waves ( $Pg, Sg$ ), reflected waves from the crust-mantle boundary (Moho) ( $PmP, SmS$ ), and diving waves through the uppermost mantle ( $Pn, Sn$ ). Note that we can apply seismic interferometry to any type of phases and we do not have to specify the seismic phases although some studies use specific seismic phases to confine the angle of incident waves (Ruigrok et al., 2010; Ruigrok and Wapenaar, 2012). In this study, we estimate the travel times of each seismic phase to validate our interferometric wavefields, where we evaluate whether the reconstructed waves with seismic interferometry are reflected waves or later phases. To estimate travel times of each phase, we construct a three-dimensional (3D) local model based on Gans (2011) that includes crustal inhomogeneity and perform 3D ray tracing with the program ANRAY (Pšenčík, 1998). According to the ray tracing, travel-time differences are small for  $Pn/Pg$  as well as  $Sn/Sg$ , and  $PmP/SmS$  arrive 0.7/1.2 s later than  $Pn/Sn$ . Amplitudes of  $Pg/Sg$  are smaller than  $Pn/Sn$  and  $PmP/SmS$ . Although both

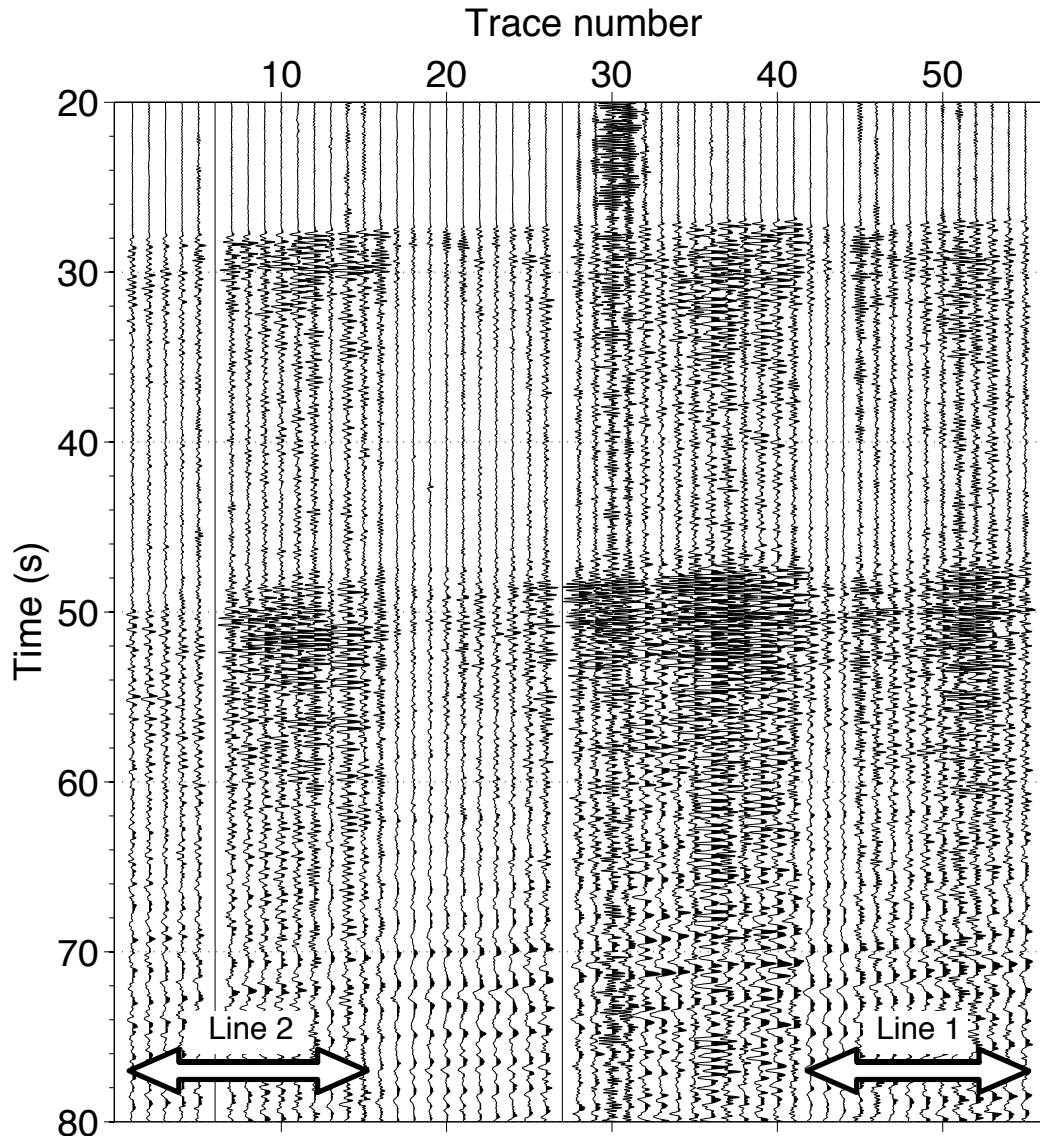


Figure 8.4. Example of observed records from an earthquake in the North-South horizontal component after applying a bandpass filter, 0.4–0.5–7–9 Hz. Time 0 s is the origin time of the earthquake. Trace numbers correspond with the receiver numbers in Figure 8.2. The white arrows show the receivers used for survey lines 1 and 2.

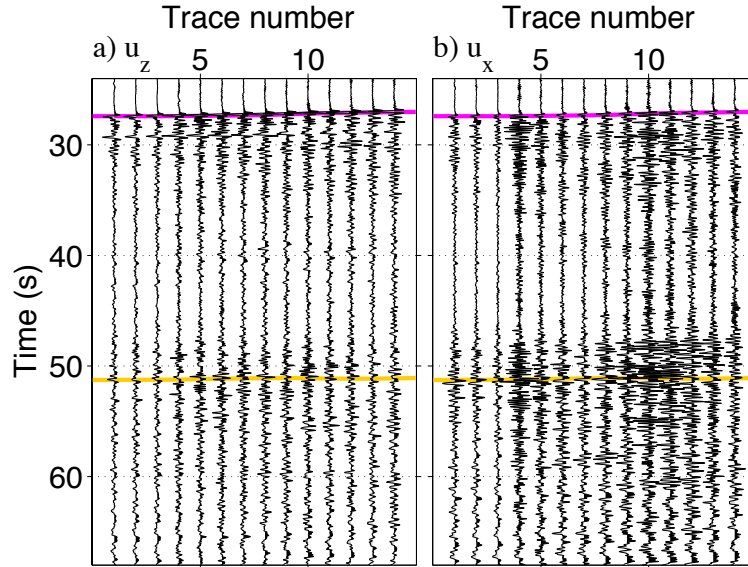


Figure 8.5. Space-interpolated observed record in (a) vertical and (b) radial components in line 1 (after rotating the horizontal components in the radial direction) from the same earthquake used in Figure 8.4. Trace number is assigned after the space interpolation, and traces 1–14 correspond to traces 42–55 in Figure 8.4. We apply the same bandpass filter used in Figure 8.4 to waveforms in all panels. The pink and yellow lines indicate the picked arrival times for the largest energy of direct P and S waves, respectively. Amplitudes are normalized separately at each panel.

travel times and, in particular, amplitudes still depend on the subsurface model, we conclude that the observed first arrivals are most likely  $P_n/S_n$  or  $P_mP/S_mS$  since their amplitudes are stronger.

### 8.4.3 Wavefield decomposition

To apply wavefield decomposition in the wavenumber-frequency domain using equation 8.11, we need traces at uniform spatial intervals. Therefore, we interpolate the observed data in space using a spline interpolation before the decomposition. Note that the receiver intervals in survey lines 1 and 2 are almost uniform and the interpolated distances are small. Figure 8.5 shows the interpolated wavefields after rotating the horizontal components in the radial direction (the same direction as the receiver lines).

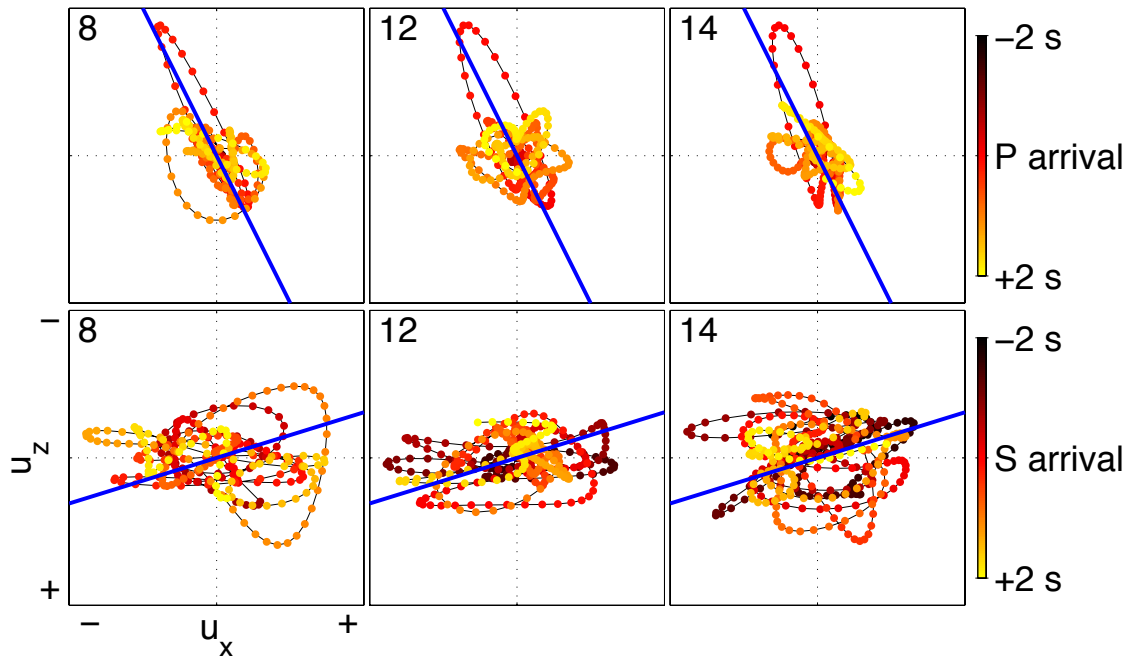


Figure 8.6. Particle motion of observed wavefields in the vertical and radial components (Figure 8.5) at around (top row) P- and (bottom row) S-wave arrivals after applying the same bandpass filter used in Figure 8.4. Red (0 s in the color bar) indicates the times at the pink line for P waves and the yellow line for S waves in Figure 8.5. Blue lines illustrate the particle motion based on the angle of incidence estimated by ray tracing. Top-left numbers at each panel describe trace numbers of each motion.

Figure 8.6 shows the particle motion around the P- and S-wave arrival times. We compute the angles of incident P and S waves by ray tracing with a velocity model based on Gans (2011) (shallow) and Kennett and Engdahl (1991) (deep); the angles of incidence in survey line 1 are  $35^\circ$  and  $18^\circ$  for P and S waves, respectively (the blue lines in Figure 8.6). The particle motions around P-wave arrivals correspond to the angle of incidence estimated by ray tracing, but the particle motions around S-wave arrivals do not. This anomalous particle motion for the S-wave arrivals may be caused by the fact that S waves overlap with the P-wave coda, the S-wave arrival time is less clear than the P-wave time (see Figure 8.5), and the subsurface may create strong PS converted waves (which we discuss later). Note that in both P and S waves, the particle motions do not have to perfectly align to the angle of incidence estimated by ray tracing because the incoming waves are not perfect plane waves.

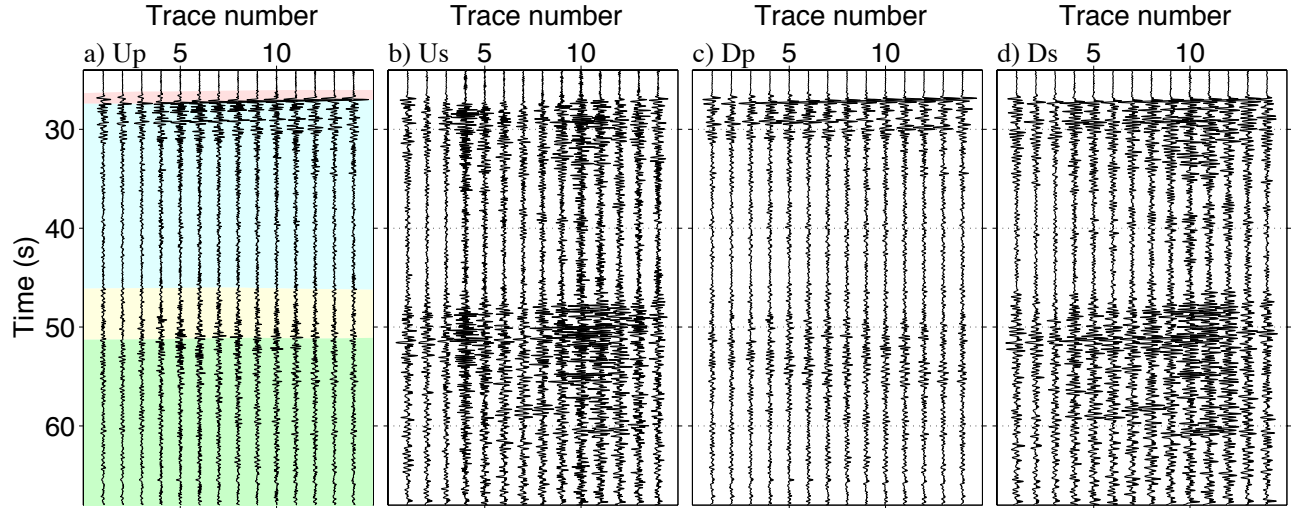


Figure 8.7. Upgoing/downgoing P/S waves after applying wavefield decomposition (equation 8.11) to the wavefields in Figure 8.5. We employ the same bandpass filter used in Figure 8.4 in all panels. The colors in panel (a) indicate the time windows we use in this study to separate direct (pink for P and yellow for S) and reflected waves (blue for P and green for S). The arrival times represented by the pink/yellow lines in Figure 8.5 locate the interfaces between pink/yellow and blue/green, respectively. Amplitudes are normalized separately at each panel.

Wavefield decomposition shown in equation 8.11 requires P- and S-wave velocities. We do not need to know the angle of incidence for the wavefield decomposition because we solve equation 8.11 in the wavenumber-frequency domain. To estimate velocities, we employ the method proposed in section 8.3 and minimize upgoing P-wave amplitude around S-wave arrival times as well as upgoing S-wave amplitude around P-wave arrival times. Figure 8.7 shows upgoing/downgoing P/S waves decomposed from waves in Figure 8.5 with estimated P- and S-wave velocities, which are 3.5 and 1.2 km/s, respectively. Based on these velocities, and an angle of  $35^\circ$  of the P incident wave, the reflection coefficients at the free surface are  $-0.905$  ( $\hat{P}\hat{P}$ ),  $0.665$  ( $\hat{P}\hat{S}$ ),  $0.273$  ( $\hat{S}\hat{P}$ ), and  $0.905$  ( $\hat{S}\hat{S}$ ) (Aki and Richards, 2002). In Figure 8.7a, the amplitudes in the pink/blue time intervals are larger than the yellow/green time intervals. In contrast in Figure 8.7b, amplitude differences between the pink/blue and yellow/green time intervals are not clear, which implies that the wavefields include strong PS converted waves in the pink/blue time interval. Since we normalize the amplitudes in Figure 8.7 for

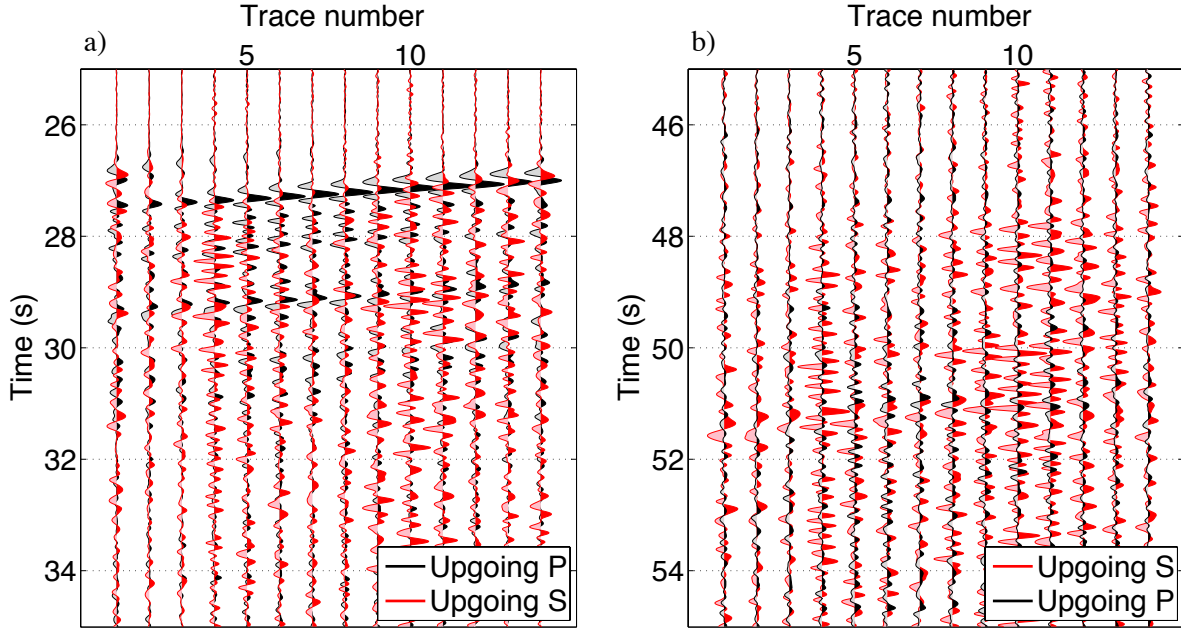


Figure 8.8. Comparison between upgoing P and S wavefields in Figures 8.7a and 8.7b at around (a) P-wave and (b) S-wave arrival times. Although in both panels upgoing P and S waves are shown in black and red, respectively, we change the order of wavefields; upgoing P is behind in panel (a) and upgoing S is behind in panel (b). Amplitude ratios between upgoing P/S waves are preserved.

each panel separately, we cannot directly compare the amplitudes between panels.

Figures 8.8 and 8.9 show comparisons of wavefields and particle motions between upgoing P and S waves. In Figure 8.8a, because direct P waves (at around 27–27.5 s) exist only in the upgoing P wavefields, we successfully separate observed waves into upgoing P and S waves (also see the top row of Figure 8.9). Strong upgoing S waves appearing just after the direct P waves in Figure 8.8a indicate that the observed waveforms include strong PS converted waves. Since Figure 8.8b is mostly red, upgoing S wavefields are dominant in this time interval, which implies that we can also separate wavefields in this interval. The particle motions in the bottom row of Figure 8.9 move along the horizontal blue lines, which denote that upgoing S wavefields are dominant in this interval. The anomalous particle motion in trace 14, which is at the edge of the array, may be caused by the space-wavenumber Fourier transform; therefore, we only use traces 3–12 for interferometry.

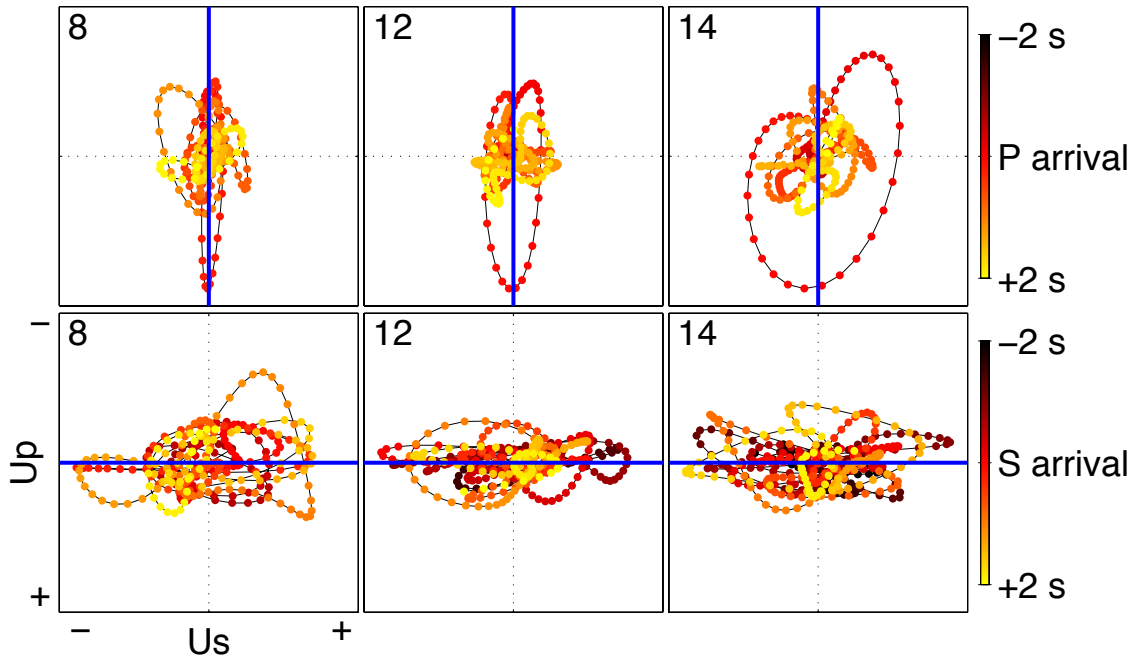


Figure 8.9. Particle motion of upgoing P and S wavefields at around (top row) P- and (bottom row) S-wave arrivals after applying the same bandpass filter used in Figure 8.4. Red (0 s in the color bar) indicates the times at the pink line for P wave and the yellow line for S waves in Figure 8.5. Blue lines illustrate the ideal particle motion of P (top row) and S (bottom row) waves in the case when wavefields are perfectly separated and no converted waves are generated. Top-left numbers at each panel describe trace numbers of each motion. Note that in contrast to Figure 8.6, the axes denote the upgoing P- and S-wave components.

## 8.5 Application of seismic interferometry to earthquake data

We introduce a mathematical description of seismic interferometry related to this study while assuming 2D wave propagation and show reconstructed waveforms from the earthquake data. More information on seismic interferometry is given by Snieder et al. (2009), Wapenaar et al. (2010a,b), and Wapenaar et al. (2011b), who summarize trace-by-trace and multi-dimensional interferometry. In this section, all equations are written in the space-frequency domain.

### 8.5.1 Trace-by-trace deconvolution

For trace-by-trace deconvolution interferometry, we compute deconvolution for each pair of traces at each earthquake. This method works well in the case of 1D wave propagation (Snieder and Şafak, 2006; Nakata and Snieder, 2012a) and can be applied to higher dimensions (e.g., Vasconcelos and Snieder, 2008b).

#### Deconvolution without wavefield decomposition

Deconvolution applied to the waveforms from one earthquake recorded by the vertical component of receivers  $A$  and  $B$  is given by

$$DI_{zz}(B, A) = \frac{u_z(B)}{u_z(A)} \approx \frac{u_z(B)u_z^*(A)}{|u_z(A)|^2 + \epsilon \langle |u_z(A)|^2 \rangle}, \quad (8.12)$$

where  $\epsilon$  is a regularization parameter (Clayton and Wiggins, 1976), the asterisk denotes the complex conjugate, and  $\langle \dots \rangle$  indicates the average power spectrum. In deconvolution interferometry, the receiver at the denominator in equation 8.12 (receiver  $A$ ) behaves as a virtual source (Vasconcelos and Snieder, 2008a). We can compute deconvolution for all combinations of the vertical and horizontal components, and each combination corresponds to different types of wave propagation between receivers  $A$  and  $B$ . For simplicity, we show only one combination in equation 8.12. In the 1D case,  $DI_{zz}(B, A)$  is equivalent to the wave propagation from receiver  $A$  to receiver  $B$  (Snieder et al., 2006a). In the 2D and 3D cases, we average  $DI_{zz}(B, A)$  over many sources around the receivers to reconstruct the wave propagation (Vasconcelos and Snieder, 2008a). Because  $u_z$  includes both P and S waves (equation 8.5),  $DI_{zz}(B, A)$  contains crosstalk between P and S waves.

In Figure 8.10, we apply trace-by-trace deconvolution to observed wavefields shown in Figure 8.5 (equation 8.12). Receiver  $A$  in equation 8.12 is at offset 0 km (virtual source). The deconvolved wavefields in Figure 8.10 are contaminated by noise around the zero-lag time; hence, trace-by-trace deconvolution using neither wavefield decomposition nor time windowing does not provide useful information about the subsurface.

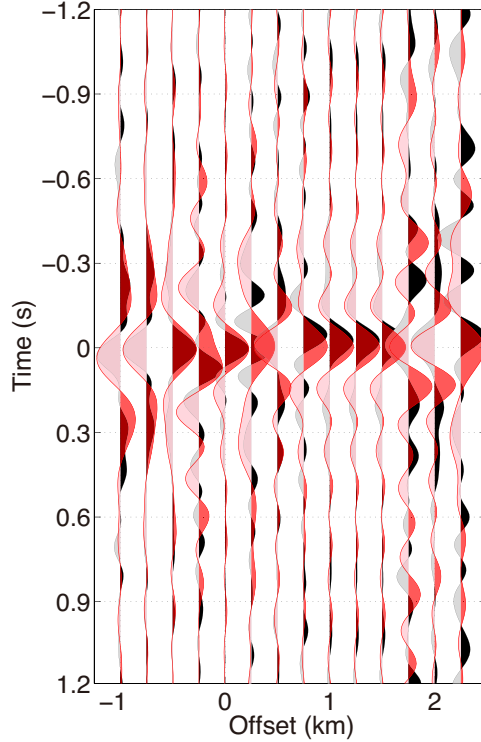


Figure 8.10. Wavefields at line 1 obtained by applying trace-by-trace deconvolution to observed vertical (black) and radial (red) components (equation 8.12). We apply a bandpass filter 0.4–0.5–7–9 Hz to wavefields in the vertical component and 0.4–0.5–4–6 Hz to wavefields in the radial component. Offset 0 km is the location of the virtual source.

### Direct-wave extraction

To improve interferometric wavefields, we decompose  $u_x$  and  $u_z$  into  $U_p$ ,  $D_p$ ,  $U_s$ , and  $D_s$  (Figure 8.7) using equation 8.11 before applying seismic interferometry. We represent the wavefield  $U_p$  at receiver  $B$  (the red triangle in Figure 8.11) with the wavefield  $U_p$  at receiver  $A$  (the blue triangle in Figure 8.11) as

$$U_p(B) = G_p U_p(A), \quad (8.13)$$

where we assume that all wavefields recorded at receiver  $B$  are also recorded at receiver  $A$ . The Green's function  $G_p$  accounts for the propagation of the direct waves from receiver  $A$  to receiver  $B$  (when the waves are plane waves, the Green's function relates to the distance  $h_d$  in Figure 8.11). Deconvolving equation 8.13 with  $U_p(A)$  gives  $G_p$ :

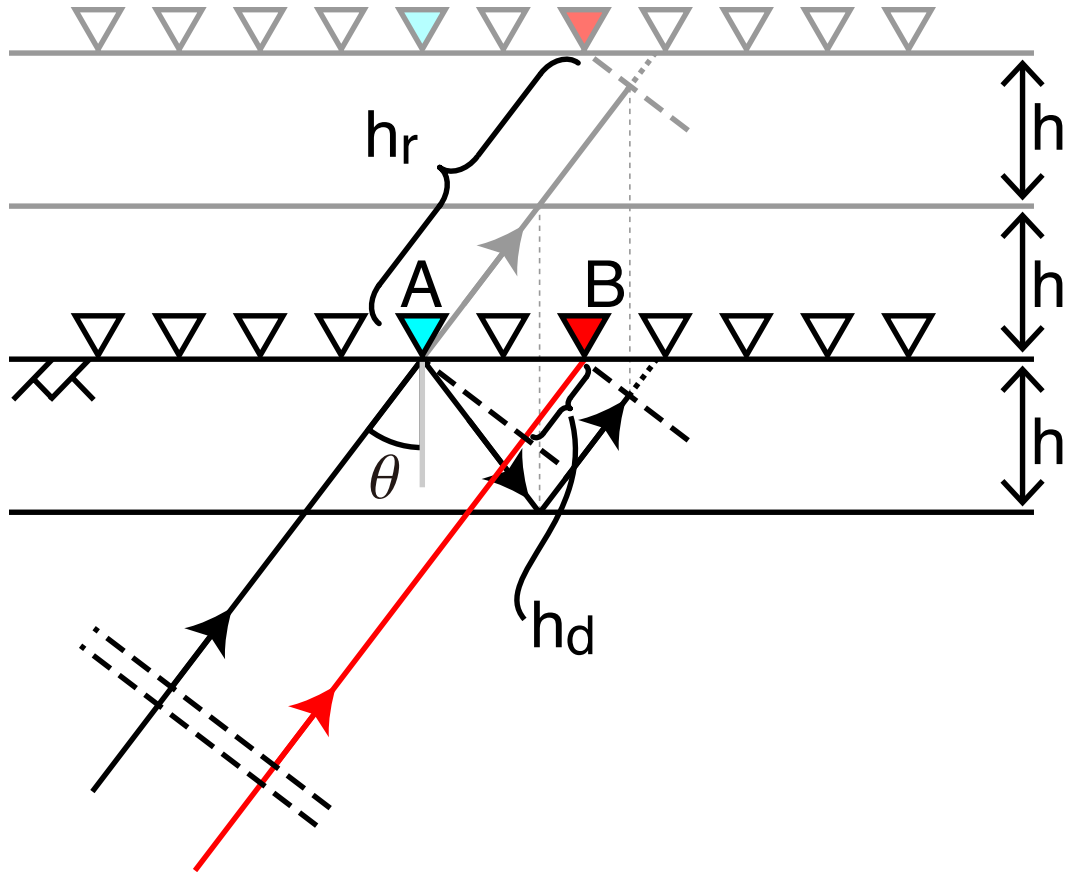


Figure 8.11. Schematic plane-wave propagation. Receivers (triangles) are deployed at the free surface (indicated by  $\llcorner$ ), and a plane wave (the black arrow at lower-left) propagates with angle  $\theta$  of the incidence. Dashed lines, all of which are parallel, indicate the portions of plane waves. The red arrow illustrates the ray path for the different portion of the same plane wave as the black arrow. The model contains one horizontal layer and a half space below the layer. The thickness of the layer is  $h$ . Gray lines and receivers show unfolded imaginary layers and receivers to understand reflected plane waves based on Snell's law. Distance  $h_d$  corresponds with the difference of the travel distance between direct upgoing waves to receivers  $A$  and  $B$ , and  $h_r$  is the travel distance of the reflected waves from  $A$  to  $B$ . We do not show converted waves in this figure.

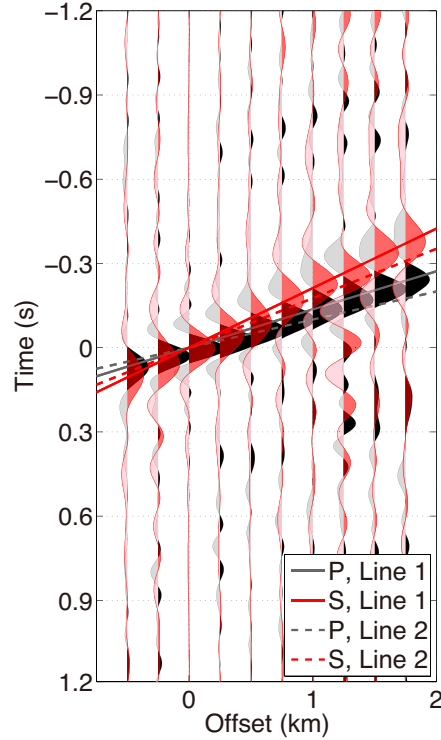


Figure 8.12. Wavefields in survey line 1 obtained by applying trace-by-trace deconvolution to upgoing P (black) and S (red) waves (equation 8.14). The solid lines show the dip of P (black) and S (red) plane waves in survey line 1, and the dashed lines in survey line 2. We apply the same bandpass filters used in Figure 8.10. Offset 0 km is the location of the virtual source.

$$\frac{U_p(B)}{U_p(A)} = G_p. \quad (8.14)$$

In practice, for computing this deconvolution, we use a regularization parameter introduced in equation 8.12.

We apply trace-by-trace deconvolution (equation 8.14), where we compute  $U_p(B)/U_p(A)$  and  $U_s(B)/U_s(A)$ , to decomposed wavefields obtained from each earthquake and average over all earthquakes used (Figure 8.12). The solid lines show the dips which maximize the amplitudes of slant-stacked waveforms. These dips depend on the angles of incidence and the wave velocities. Based on the angles of incidence estimated by ray tracing ( $35^\circ$  for P waves and  $18^\circ$  for S waves), the P- and S-wave velocities are 4.2 km/s and 1.5 km/s, respectively.

These velocities are average velocities over ray paths of the direct waves ( $h_d$  in Figure 8.11). We also apply this deconvolution to survey line 2 (dashed lines in Figure 8.12). The dips in line 2 are flatter than in line 1, which corresponds to the high-velocity layer under line 2 (Leahy et al., 2012). Note that without wavefield separation, we cannot clearly reconstruct direct waves (compare Figure 8.10 with Figure 8.12). The wavefield separation plays an important role for reconstructing waveforms with seismic interferometry.

### Reflected-wave extraction

Equation 8.13 indicates the relationship between upgoing waves recorded at different receivers. Next, we retrieve the reflected waves using upgoing and downgoing waves. Surface-related reflected upgoing P waves at receiver  $B$  are given by

$$U_p^r(B) = G_{pp}D_p(A) + G_{ps}D_s(A), \quad (8.15)$$

where  $G_{pp}$  and  $G_{ps}$  are the PP and PS reflected Green's function representing the wave propagation from receiver  $A$  to receiver  $B$  (Figure 8.13). In this study, we use time windows to separate direct and reflected waves. Equation 8.15 after deconvolving with  $D_p(A)$  is given by

$$\frac{U_p^r(B)}{D_p(A)} = G_{pp} + G_{ps} \frac{D_s(A)}{D_p(A)}. \quad (8.16)$$

Although we obtain the PP reflected Green's function ( $G_{pp}$ ) using equation 8.16, the deconvolved wavefield ( $U_p^r(B)/D_p(A)$ ) is contaminated by crosstalk of downgoing P and S waves. Note that we compute  $U_p^r(B)/D_p(A)$  to obtain  $G_{pp}$ , and  $G_{ps}D_s(A)/D_p(A)$  in equation 8.16 is an unwanted wave created by crosstalk. Therefore in the elastic-wave case, we cannot obtain pure (no crosstalk) reflected Green's function with trace-by-trace deconvolution.

To focus on the first surface-related multiples, which are the most coherent reflected waves, we use only direct downgoing P waves:

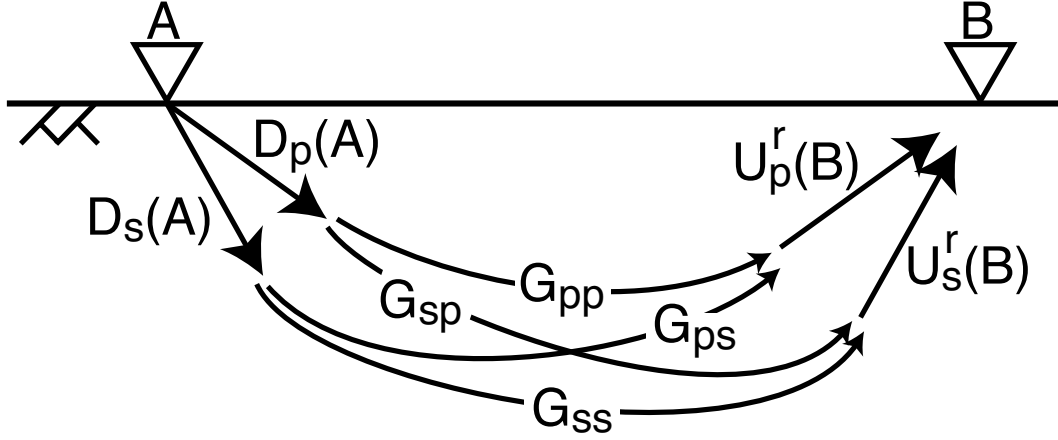


Figure 8.13. Relationship of upgoing/downgoing P/S wavefields and Green's functions between receivers  $A$  and  $B$ . The free surface is indicated by  $\sphericalangle$ . The direction of arrows represents the direction of causality. Upgoing waves are reflected waves (direct upgoing waves are not shown).

$$\frac{U_p^r(B)}{D_p^d(A)} = G_{pp} + G_{ps} \frac{D_s(A)}{D_p^d(A)}, \quad (8.17)$$

where we cannot apply a time window to  $D_s$  because this wavefield is contained in  $U_p^r$ . Reflected waves are less coherent between traces than direct waves due to multiple scattering. Therefore, when we show a virtual-shot gather (i.e., we fix receiver  $A$  and change receiver  $B$ ), which we use in this study, the gather created by equation 8.17 has little coherency between traces. To improve the coherency between traces in the virtual-shot gather, we use time reversal. Under time reversal,  $G \rightarrow G^*$ ,  $U \rightarrow D$ , and  $D \rightarrow U$ ; as a result, we rewrite equation 8.15 to

$$D_p(B) = G_{pp}^* U_p^r(A) + G_{ps}^* U_s^r(A) \quad (8.18)$$

and equation 8.17 to

$$\frac{D_p^d(B)}{U_p^r(A)} = G_{pp}^* + G_{ps}^* \frac{U_s^r(A)}{U_p^r(A)}. \quad (8.19)$$

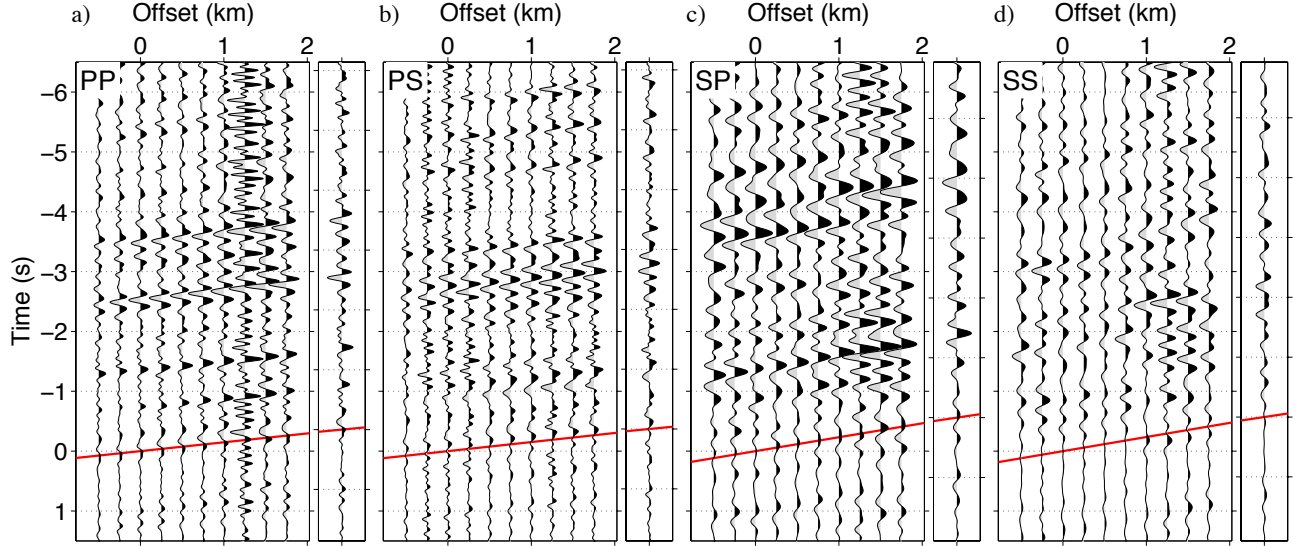


Figure 8.14. Reflected plane waves retrieved by trace-by-trace deconvolution after time windowing. We compute (a)  $D_p^d(B)/U_p^r(A) (\approx G_{pp}^*)$ , (b)  $D_p^d(B)/U_s^r(A) (\approx G_{ps}^*)$ , (c)  $D_s^d(B)/U_p^r(A) (\approx G_{sp}^*)$ , and (d)  $D_s^d(B)/U_s^r(A) (\approx G_{ss}^*)$ . We apply bandpass filters with (a,b) 0.4–0.5–7–9 Hz and (c,d) 0.4–0.5–4–6 Hz. Red lines indicate the dip for slant stacking, and the rightmost trace at each panel is the stacked trace. The reference trace for the deconvolution is the trace at offset 0 km (virtual source). The amplitudes in panels (c,d) are multiplied by a factor 2.5 compared with those in panels (a,b), and the amplitudes in panels (a,b) are the same .

Because the direct downgoing P waves  $D_p^d$  is more coherent than the reflected upgoing P waves  $U_p^d$ , expression 8.19 gives more coherent virtual-shot gathers than expression 8.17.

We compute equation 8.19 to obtain reflected waves while applying time windows for separating direct and reflected waves. We independently create time windows for each earthquake, and the time windows shown in Figure 8.7a are the windows for the earthquake in Figure 8.7. Figure 8.14 shows all P/S combinations of the trace-by-trace deconvolved waveforms after averaging over all earthquakes used. In Figures 8.14a and 8.14b, we employ the pink/blue time windows shown in Figure 8.7a (modified for each earthquake), respectively. Similarly, in Figures 8.14c and 8.14d, we use the yellow/green time windows shown in Figure 8.7a (modified for each earthquake). To mute truncation of waves, we apply cosine tapers at the edge of each time window. In Figure 8.14, offset 0 km is the location of the virtual source, which excites a quasi-plane wave at time 0 s. Although each panel in Figure

8.14 aims to show the target reflected Green's function (e.g.,  $G_{pp}$  for Figure 8.14a), each panel includes unwanted crosstalk caused by the last term in equation 8.19. Evaluating the amount of crosstalk is difficult, but we expect that the energy of SP reflected waves should be smaller than other reflected waves in the estimated angle of incidence (Aki and Richards, 2002). For example in the assumption of horizontal layers, when the P and S velocities in the first/second layers are 3.5/5.0 and 1.2/2.2 km/s (modified after Leahy et al., 2012) and the angle of P-wave incidence is  $35^\circ$ , the reflection coefficients at the interface are 0.189 ( $\dot{P}\dot{P}$ ), -0.135 ( $\dot{P}\dot{S}$ ), -0.055( $\dot{S}\dot{P}$ ), and -0.162 ( $\dot{S}\dot{S}$ ). Almost no P-wave energy is present in Figure 8.8b, which also indicates that  $G_{sp}$  is small. However, the amplitudes in Figure 8.14c are greater than those in Figure 8.14d, which might be caused by the crosstalk between upgoing waves in equation 8.19.

The right-most trace at each panel in Figure 8.14 shows slant-stacked wavefields, where the dip for stacking (the red lines in Figure 8.14) is chosen to maximize the peak amplitude of stacked waveforms. Since the dips are related to the wave velocities and the angles of incidence, the dips in Figures 8.14a and 8.14b as well as those in Figures 8.14c and 8.14d are almost the same. Stacked waveforms in Figure 8.14 are noisy and difficult to interpret.

### 8.5.2 Trace-by-trace crosscoherence

Because normalization in the frequency domain improves the signal-to-noise ratio of interferometric wavefields (Nakata et al., 2011), we apply the normalization before deconvolving waveforms, which is so-called crosscoherence interferometry. We normalize equation 8.18 with the amplitude of  $D_p(B)$ :

$$\frac{D_p(B)}{|D_p(B)|} = G_{pp}^* \frac{U_p^r(A)}{|D_p(B)|} + G_{ps}^* \frac{U_s^r(A)}{|D_p(B)|}. \quad (8.20)$$

By deconvolving equation 8.20 with  $U_p^r(A)/|D_p(B)|$ , we obtain the form of crosscoherence interferometry:

$$\begin{aligned} \frac{D_p(B)}{|D_p(B)|} \frac{|U_p^r(A)|}{|U_p^r(A)|} &= \frac{D_p(B)U_p^{r*}(A)}{|D_p(B)||U_p^r(A)|} \\ &= \frac{|U_p^r(A)|}{|D_p(B)|} \left\{ G_{pp}^* + G_{ps}^* \frac{U_s^r(A)}{U_p^r(A)} \right\}, \end{aligned} \quad (8.21)$$

where  $|U_p^r(A)|/|D_p(B)|$  is considered as an amplification term. Note that we still have crosstalk in equation 8.21 ( $G_{ps}^* U_s^r(A)/U_p^r(A)$ ). Similar to equation 8.17, we focus on the first surface-related multiples in equation 8.21 and compute

$$\frac{D_p^d(B)U_p^{r*}(A)}{|D_p^d(B)||U_p^r(A)|} = \frac{|U_p^r(A)|}{|D_p^d(B)|} \left\{ G_{pp}^* + G_{ps}^* \frac{U_s^r(A)}{U_p^r(A)} \right\}. \quad (8.22)$$

In practice, we use a regularization parameter to compute trace-by-trace crosscoherence (Nakata et al., 2013):

$$\frac{D_p^d(B)U_p^{r*}(A)}{|D_p^d(B)||U_p^r(A)|} = \frac{D_p^d(B)U_p^{r*}(A)}{|D_p^d(B)||U_p^r(A)| + \epsilon \langle |D_p^d(B)||U_p^r(A)| \rangle}. \quad (8.23)$$

When we apply trace-by-trace crosscoherence interferometry to earthquake data, we can suppress noise and compensate amplitude balance among traces (equation 8.22) as shown by Nakata et al. (2011) (Figure 8.15). Figure 8.15 shows more coherent waves than Figure 8.14 with the noise in traces around offset 1–1.5 km being suppressed. One criterion to evaluate the quality of the interferometric wavefields is given by using causality. Because we employ time reversal and apply time windows, the wavefields after applying interferometry should contain waves only for  $t < 0$ , and waves for  $t > 0$  are noise. Comparing Figures 8.14 and 8.15, the amplitudes in the causal time in Figure 8.15 are smaller than in Figure 8.14, which indicates that the wavefields constructed by trace-by-trace crosscoherence have the higher signal-to-noise ratio than trace-by-trace deconvolution. Although crosscoherence improves the signal-to-noise ratio, the waveforms in Figure 8.15 include unwanted crosstalk as indicated in equation 8.22. For example, a negative-amplitude wave exists at 4.6 s in both stacked waveforms of Figures 8.15c and 8.15d, which may be caused by the crosstalk

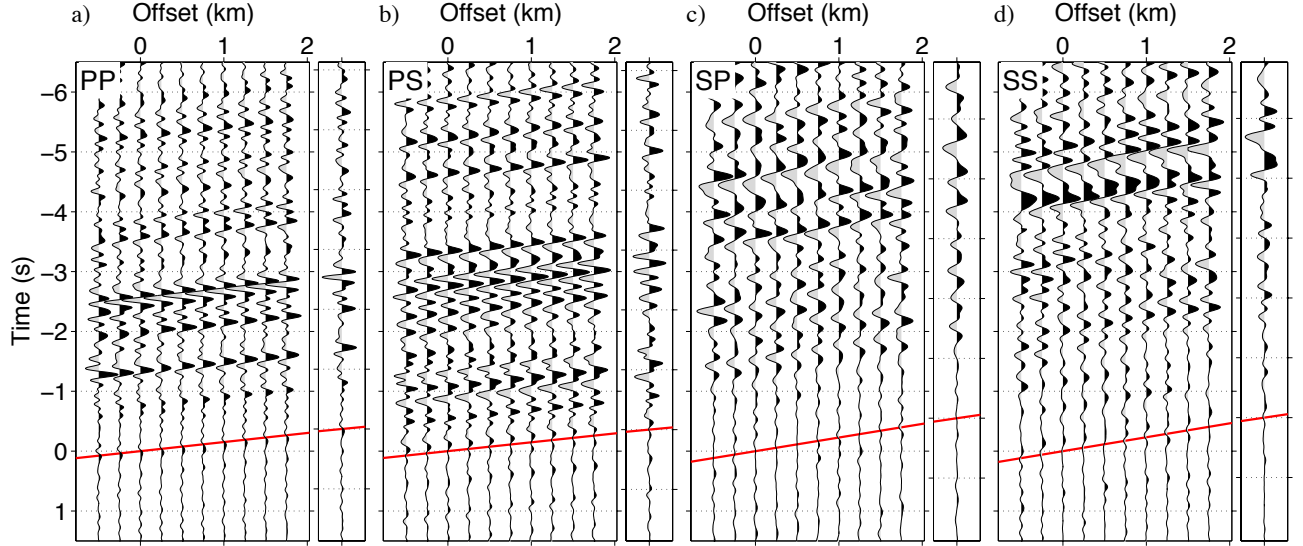


Figure 8.15. Reflected plane waves retrieved by trace-by-trace crosscoherence after time windowing. We compute (a)  $D_p^d(B)U_p^{r*}(A)/|D_p^d(B)||U_p^r(A)|$  ( $\approx G_{pp}^*$ ), (b)  $D_p^d(B)U_s^{r*}(A)/|D_p^d(B)||U_s^r(A)|$  ( $\approx G_{ps}^*$ ), (c)  $D_s^d(B)U_p^{r*}(A)/|D_s^d(B)||U_p^r(A)|$  ( $\approx G_{sp}^*$ ), and (d)  $D_s^d(B)U_s^{r*}(A)/|D_s^d(B)||U_s^r(A)|$  ( $\approx G_{ss}^*$ ). We apply the same bandpass filters as used in Figure 8.14. Red lines indicate the dip for slant stacking, and the rightmost trace at each panel is the stacked trace. The reference trace for the interferometry is the trace at offset 0 km (virtual source). The amplitudes in panels (c,d) are multiplied by a factor 2.5 compared with those in panels (a,b), and the amplitudes in panels (a,b) are the same.

because SP and SS waves rarely arrive at the same time.

### 8.5.3 Multi-dimensional deconvolution

In trace-by-trace interferometry, we solve the Green's functions of P and S reflected waves at each pair of traces for each combination of P/S waves separately. In MDD interferometry, we solve the Green's functions of all components for all traces simultaneously. From equation 8.18 and the similar notation for S waves, we obtain

$$\begin{pmatrix} D_p \\ D_s \end{pmatrix} = \begin{pmatrix} G_{pp}^* & G_{ps}^* \\ G_{sp}^* & G_{ss}^* \end{pmatrix} \begin{pmatrix} U_p^r \\ U_s^r \end{pmatrix}, \quad (8.24)$$

where each wavefield includes all traces (see Figure 8.13 to understand equation 8.24 schematically). Confining only direct downgoing waves (similar to equation 8.17), we obtain

$$\begin{pmatrix} D_p^d \\ D_s^d \end{pmatrix} = \begin{pmatrix} G_{pp}^* & G_{ps}^* \\ G_{sp}^* & G_{ss}^* \end{pmatrix} \begin{pmatrix} U_p^r \\ U_s^r \end{pmatrix}. \quad (8.25)$$

To solve equation 8.25, we first right-multiply  $(U_p^{r\dagger} \ U_s^{r\dagger})$ , where  $\dagger$  is the complex conjugate transpose (Wapenaar et al., 2011b):

$$\begin{pmatrix} D_P^d U_P^{r\dagger} & D_P^d U_S^{r\dagger} \\ D_S^d U_P^{r\dagger} & D_S^d U_S^{r\dagger} \end{pmatrix} = \begin{pmatrix} G_{PP}^* & G_{PS}^* \\ G_{SP}^* & G_{SS}^* \end{pmatrix} \begin{pmatrix} U_P^r U_P^{r\dagger} & U_P^r U_S^{r\dagger} \\ U_S^r U_P^{r\dagger} & U_S^r U_S^{r\dagger} \end{pmatrix} \quad (8.26)$$

and then add a damping parameter  $\epsilon \mathbf{I}$  to equation 8.26 to obtain a stable inverse matrix (van der Neut et al., 2011b):

$$\begin{pmatrix} D_P^d U_P^{r\dagger} & D_P^d U_S^{r\dagger} \\ D_S^d U_P^{r\dagger} & D_S^d U_S^{r\dagger} \end{pmatrix} \left\{ \begin{pmatrix} U_P^r U_P^{r\dagger} & U_P^r U_S^{r\dagger} \\ U_S^r U_P^{r\dagger} & U_S^r U_S^{r\dagger} \end{pmatrix} + \epsilon \mathbf{I} \right\}^{-1} = \begin{pmatrix} G_{PP}^* & G_{PS}^* \\ G_{SP}^* & G_{SS}^* \end{pmatrix}. \quad (8.27)$$

Employing equation 8.27, we can retrieve the Green's matrix from upgoing/downgoing P/S wavefields.

Because MDD treats the extraction of the Green's function as an inverse problem, MDD has several advantages compared with trace-by-trace interferometry. MDD can be applied to passive seismic data generated by uneven distributed sources in a dissipative medium (but MDD requires even distributed receivers) (van der Neut et al., 2011b; Wapenaar et al., 2011a,b). Snieder et al. (2009) suggest that one can retrieve Green's functions without estimating source spectra by using MDD. This method also removes complicated overburden without requiring a velocity model when receivers are embedded inside a medium (van der Neut et al., 2011a,b). Note that by comparing equations 8.19 and 8.27, MDD retrieves the Green's functions without unwanted crosstalk when we separate P and S waves.

Figure 8.16 shows wavefields reconstructed by MDD interferometry (expression 8.27). The amplitudes of causal waves are weaker than those in Figures 8.14 and 8.15, which indicates that based on the criterion of causality the quality of wavefields produced by MDD is better than trace-by-trace interferometry. Wavefields in Figure 8.16 do not include

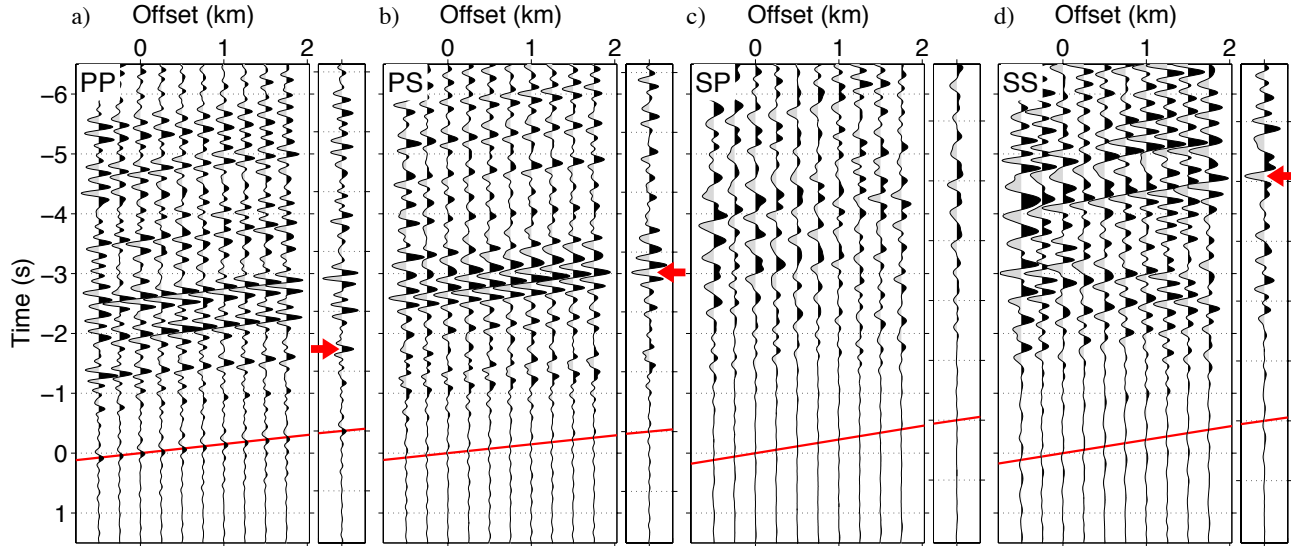


Figure 8.16. Reflected plane waves retrieved by multi-dimensional deconvolution after time windowing. (a)  $G_{pp}^*$ , (b)  $G_{ps}^*$ , (c)  $G_{sp}^*$ , and (d)  $G_{ss}^*$ . We apply the same bandpass filters as used in Figure 8.14. Red lines indicate the dip for slant stacking, and the rightmost trace at each panel is the stacked trace. The red arrows on the rightmost traces in panels (a,b,d) point at the waves that we interpret. The reference trace for the interferometry is the trace at offset 0 km (virtual source). The amplitudes in panels (c,d) are multiplied by a factor 2.5 compared with those in panels (a,b), and the amplitudes in panels (a,b) are the same.

unwanted crosstalk, which contaminates waveforms in Figures 8.14 and 8.15, because MDD solves the inverse problem (equation 8.27). As shown in Figure 8.8b, SP converted waves are weak (compare Figure 8.16c with the other panels in Figure 8.16). Also, the slant-stacked wavefields in Figures 8.16c and 8.16d are much dissimilar than the SP and SS waveforms in Figures 8.15c and 8.15d obtained by trace-by-trace crosscoherence. This is an indication that MDD successfully eliminate the crosstalk that contaminates Figures 8.15c and 8.15d.

Leahy et al. (2012) show that a reflector exists at about 3.8 km depth. The waves pointed by three arrows in Figure 8.16 are reflected waves from the reflector; their arrival times are 1.38 s (PP), 2.66 s (PS), and 4.10 s (SS). We do not pick the SP reflected wave because it is weak and noisy. These arrival times are much larger than the estimated travel-time differences between  $Pn/Sn$  and  $PmP/SmS$ , which are 0.7 s and 1.2 s. Although the differences of the travel times estimated by ray tracing include some uncertainties due to

the subsurface model used for the ray tracing, we conclude that the retrieved waves are reflected waves but not later direct arrivals based on two reasons explained below. First, the arrival times of these reflected waves highlighted by the arrows in Figure 8.16 are dependent. Using the arrival times of the PP and SS reflected waves, the arrival time of the PS reflected wave should be 2.74 s, which is a 3% discrepancy ( $\approx (2.74 - 2.66)/2.66$ ) from the observed time in Figure 8.16b. Second, the large difference of PP and SS arrival times in Figure 8.16 indicates large  $V_p/V_s$  ratio, which is the condition of near surface. Therefore, the arrival times obtained from Figure 8.16 include near-surface information. When we assume that the reflector is flat, the average P and S velocities over the raypaths of the reflected waves ( $h_r$  in Figure 8.11) are 4.5 km/s and 1.7 km/s, respectively, with the angles of incidence we estimated.

## 8.6 Discussion of velocities

The estimated velocities (4.2 and 1.5 km/s from direct waves and 4.5 and 1.7 km/s from reflected waves) and velocities used for the wavefield decomposition (3.5 and 1.2 km/s) are different. These differences indicate the depth variation of velocities. Gans (2011) and Leahy et al. (2012) show that the velocities in the region of survey line 1 monotonically increase with depth. The velocities estimated from direct (from Figure 8.12) and reflected waves (from Figure 8.16) are the average velocities over the distances  $h_d$  and  $h_r$  in Figure 8.11. Based on the estimated angles of incidence and the depth of the reflector, the velocities from the reflected waves include the information of deeper structure than the direct waves. Therefore, the fact that the estimated velocities from reflected waves are faster than those from direct waves is consistent with previous studies. The velocities used for decomposition are theoretically the velocities at the surface but practically the average velocities over a medium with some thickness depending on the wavelength we used. Since the velocities used for decomposition are slower than the velocities estimated from direct waves, the decomposition is sensitive for the velocities in the shallower structure than the distance  $h_d \cos(\theta)$  in Figure 8.11 for the used frequency range.

## 8.7 Conclusions

We apply seismic interferometry to plane waves excited by a cluster of earthquakes and obtain subsurface information. To improve the quality of interferometric wavefields, we employ several techniques such as upgoing/downgoing P/S wavefield decomposition, time windowing to separate direct and reflected waves, time reversal, and multi-dimensional analysis. The wavefield decomposition proposed here works well when the medium has no or weak lateral heterogeneity. For trace-by-trace interferometry, wavefield decomposition enhances coherence of interferometric wavefields between traces. We retrieve the Green's matrix without unwanted crosstalk of P and S waves with MDD interferometry. Although MDD interferometry requires wavefield separation, the computed waveforms follow causality and have the highest signal-to-noise ratio compared with trace-by-trace interferometry. The difference between the velocities estimated from direct waves and reflected waves retrieved by seismic interferometry is evidence of the depth variation of the velocities.

## 8.8 Acknowledgments

We are grateful to sponsor companies of the Consortium Project on Seismic Inverse Methods for Complex Structures at the Center for Wave Phenomena. We thank the IRIS data management center and Exxonmobil to provide the earthquake data, and USGS for managing the earthquake catalog. Figures 8.2 and 8.3 are produced by using the Generic Mapping Tools (GMT: <http://gmt.soest.hawaii.edu>, last accessed March 2013). We are grateful to Filippo Brogini for providing a code to implement MDD interferometry and Diane Witters for her professional help in preparing this manuscript.

## CHAPTER 9

### CONCLUSIONS

I extract traveling waves that propagate from one receiver to others with seismic interferometry, where the passive sources are either natural earthquakes or ambient noise. In contrast to crosscorrelation-based interferometry, deconvolution-based interferometry can separate the traveling waves between receivers from the complexity of the incident waves at the reference receiver, which acts as a virtual source. I use two types of deconvolution-based seismic interferometry, which are trace-by-trace deconvolution (TTD) and multi-dimensional deconvolution (MDD) interferometry. TTD interferometry is appropriate for one-dimensional (1D) applications to reconstruct propagating waves between two receivers. These traveling waves are useful for estimating physical properties between these receivers, such as velocities, anisotropy, and quality factors. MDD interferometry can be considered an extension of TTD interferometry to higher dimensions.

Deconvolution interferometry yields more repeatable and wider frequency-range wavefields than cross-correlation interferometry. This repeatability is important for temporal monitoring because our interests are estimating time-lapse changes of media that are not affected by uncertainties in the reconstructed waveforms. Convergence tests provide us with the information about the minimum time interval we need to retrieve stable waveforms (as I use in Chapter 7). These tests are beneficial for interferometry studies using both natural earthquakes and ambient noises to decide the time interval. The time interval for time-lapse seismic interferometry depends on the strength of sources and targets of the interferometry: for example, the intervals in one year in Chapter 2, two months in Chapter 3, a few minutes (duration of shaking caused by each earthquake) in Chapter 6, and four days in Chapter 7. A dilemma exists for determining the time interval. Although we would like to use shorter time intervals to improve the temporal resolution for monitoring, we need to minimize the

uncertainties of wavefield reconstruction. Therefore, techniques to improve the repeatability of deconvolved waveforms with more efficient ways than simple averaging over a time interval are important.

In Chapters 5 and 8, I propose techniques to enhance the repeatability of correlograms. The technique in Chapter 5 uses another sensor, which is already installed and operated by NIED, and I employ several signal-processing techniques (such as multi-dimensional analysis, wavefield decomposition, time windowing, and time reversal) in Chapter 8. In both cases, I improve the quality of retrieved waveforms with the proposed techniques compared to the quality of waveforms reconstructed by conventional techniques.

Besides the techniques proposed here, the discoveries of changes in shear-wave velocities and shear-wave splitting in this dissertation have significant impacts in the communities of earthquake seismology, earthquake engineering, and structural engineering. The work presented in Chapter 3 was the first to show the reduction in the near-surface shear-wave velocities caused by the Tohoku-Oki earthquake, and this result of velocity changes has stimulated other studies (e.g., Minato et al., 2012; Takagi and Okada, 2012; Wu and Peng, 2012; Sawazaki and Snieder, 2013; Tonegawa et al., 2013). The decrease in the shear-wave velocities is about 5% over an approximately 1200-km wide area in northeastern Japan, which is much larger than the region of velocity reduction after other large earthquakes. This near-surface change can be useful to interpret the strength and the character of the Tohoku-Oki earthquake. The area with reduced shear-wave velocity is delimited on the western side by the Median Tectonic Line and the Itoigawa-Shizuoka Tectonic Line. This confinement of the velocity reduction is not fully explained yet, and I will study this region with ambient-noise data as a future research project.

Changes in the strength and direction of shear-wave splitting after large earthquakes are controversial topics. Quite a few studies found changes in shear-wave splitting resulting from large earthquakes (Booth et al., 1990; Crampin et al., 1990; Crampin and Zatsepin, 1997; Gao et al., 1998; Tadokoro et al., 1999; Bokelmann and Harjes, 2000; Saiga et al., 2003; Liu

et al., 2004). In contrast for example, Cochran et al. (2003), Peng and Ben-Zion (2005), and Cochran et al. (2006) insist that no changes in splitting are caused by major earthquakes. In Chapter 3, I find a change in the strength but not in the direction of shear-wave splitting after the Tohoku-Oki earthquake. This change in the strength of splitting correlates with the change in shear-wave velocities, and the correlation could be explained by rock-physical models. Although Tonegawa et al. (2013) also found a change in anisotropy caused by the same earthquake, Takagi and Okada (2012) and Sawazaki and Snieder (2013) discovered no clear changes. These differences may partly arise from the evaluation of uncertainties of each technique and the selection of earthquakes used for the analyses.

The near-surface shear-wave velocities at the soft-rock sites also change because of precipitation (Chapter 2). Sens-Schönfelder and Wegler (2006) found a similar phenomenon with ambient-noise data. This discovery suggests that the technique proposed in Chapters 2–5 can be applied to interpretations of water tables and/or a degree of moisture in the near surface. In conclusion of Chapters 2-5, I emphasize that the shear-wave velocities in the near surface continuously change because of large earthquakes and precipitation, and these temporal fluctuations of velocities are detectable using deconvolution interferometry.

Estimation of nonlinear response is more challenging than that of linear response. I use short-time moving-window seismic interferometry to find the nonlinear response caused by the Tohoku-Oki earthquake (Chapter 3), and obtain nonlinear and linear responses of the building with earthquake and ambient-noise data, respectively (Chapters 6 and 7). In Chapters 6 and 7, because the strength of ambient noises is stable and much smaller than that of earthquakes, I successfully reconstruct the linear response of the building from ambient-noise records. Using the waveforms obtained in Chapters 6 and 7 to separately estimate linear and nonlinear responses of the building remains a topic for future study. Note that the shear motion in a building is different from the motion in a continuous elastic medium because a building consists of voids separated by structural elements. Although the shear-wave velocities vary about 30% (210–270 m/s) over the recorded range of peak-ground acceleration,

there is no indication of permanent damage because the velocity before and after the largest recorded event is comparable. Therefore, interpretation of the change in velocity in terms of a shear modulus is not appropriate.

In seismology, the number of stations for permanent observation has increased for monitoring, and in exploration geophysics, time-lapse measurements have become crucial during the production of reservoirs for enhanced oil recovery. Seismic interferometry is an important technique for monitoring, and the technique is still a topic of further research. Topics to be invested include estimating anisotropy and attenuation, and extending the methodology to electromagnetic or diffusion fields.

## REFERENCES CITED

- Abe, S., E. Kurashimo, H. Sato, N. Hirata, T. Iwasaki, and T. Kawanaka, 2007, Interferometric seismic imaging of crustal structure using scattered teleseismic waves: *Geophys. Res. Lett.*, **34**, L19305.
- Aki, K., 1957, Space and time spectra of stationary stochastic waves, with special reference to microtremors: *Bull. Earthq. Res. Inst.*, **35**, 415–456.
- , 1985, Theory of earthquake prediction with special reference to monitoring of the quality factor of lithosphere by the coda method: *Earthq. Predict. Res.*, **3**, 219–230.
- , 2004, A new view of earthquake and volcano precursors: *Earth Planets Space*, **56**, 689–713.
- Aki, K., and V. Ferrazzini, 2000, Seismic monitoring and modeling of an active volcano for prediction: *J. Geophys. Res.*, **105**, 16617–16640.
- Aki, K., and P. G. Richards, 2002, *Quantitative Seismology*, 2 ed.: Univ. Science Books.
- Alford, R. M., 1986, Shear data in the presence of azimuthal anisotropy: Dille, Texas: SEG Expanded Abstracts, **5**, 476–479.
- Allmann, B. P., and P. M. Shearer, 2009, Global variations of stress drop for moderate to large earthquakes: *J. Geophys. Res.*, **114**, B01310.
- Aoi, S., T. Kunugi, and H. Fujiwara, 2004, Strong-motion seismograph network operated by NIED: K-NET and KiK-net: *J. Japan Assoc. Earthq. Eng.*, **4**, 65–74.
- Arrowsmith, S. J., and L. Eisner, 2006, A technique for identifying microseismic multiplets and application to the valhall field, north sea: *Geophysics*, **71**, V31–V40.
- Arts, R., O. Eiken, A. Chadwick, P. Zweigel, L. van der Meer, and B. Zinszner, 2004, Monitoring of CO<sub>2</sub> injected at Sleipner using time-lapse seismic data: *Elsevier Energy*, **29**, 1383–1392.
- Assumpção, M., D. James, and A. Snoke, 2002, Crustal thicknesses in the Brazilian shield by receiver function analysis: Implications for isostatic compensation: *J. Geophys. Res.*, **107**, ESE2-1-2-15.

- Atkinson, B. K., 1984, Subcritical crack growth in geological materials: *J. Geophys. Res.*, **89**, 4077–4114.
- Baig, A. M., M. G. Bostock, and J. P. Mercier, 2005, Spectral reconstruction of teleseismic P Green’s functions: *J. Geophys. Res.*, **110**, B08306.
- Bakulin, A., and R. Calvert, 2004, Virtual source: new method for imaging and 4D below complex overburden: *SEG Expanded Abstracts*, **23**, 112–115.
- , 2006, The virtual source method: Theory and case study: *Geophysics*, **71**, S1139–S1150.
- Bakulin, A., and A. Mateeva, 2008, Estimating interval shear-wave splitting from multicomponent virtual shear check shots: *Geophysics*, **73**, A39–A43.
- Baltay, A., G. Prieto, and G. C. Beroza, 2010, Radiated seismic energy from coda measurements and no scaling in apparent stress with seismic moment: *J. Geophys. Res.*, **115**, B08314.
- Behm, M., 2013, Blind deconvolution of multichannel recordings by linearized inversion in the spectral domain: CWP report, **774**, 299–312.
- Behm, M., R. Snieder, and G. Leahy, 2013, Retrieval of local surface velocities from traffic noise – an example from the LaBarge basin (Wyoming): *Geophys. Prospect.* (submitted).
- Bensen, G. D., M. H. Ritzwoller, M. P. Barmin, A. L. Levshin, F. Lin, M. P. Moschetti, N. M. Shapiro, and Y. Yang, 2007, Processing seismic ambient noise data to obtain reliable broad-band surface wave dispersion measurements: *Geophys. J. Int.*, **169**, 1239–1260.
- Biot, M., 1933, Theory of elastic systems vibrating under transient impulse with an application to earthquake-proof buildings: *Proc. Natl. Acad. Sci.*, **19**, 262–268.
- Biryol, C. B., G. M. Leahy, G. Zandt, and S. L. Beck, 2013, Imaging the shallow crust with local and regional earthquake tomography: *J. Geophys. Res.* (in press).
- Bokelmann, G. H. R., and H.-P. Harjes, 2000, Evidence for temporal variation of seismic velocity within the upper continental crust: *J. Geophys. Res.*, **105**, 23879–23894.
- Booth, D. C., S. Crampin, J. H. Lovell, and J.-M. Chiu, 1990, Temporal changes in shear wave splitting during an earthquake swarm in Arkansas: *J. Geophys. Res.*, **95**, 11151–11164.
- Bostock, M. G., 2004, Green’s functions, source signatures, and the normalization of teleseismic wave fields: *J. Geophys. Res.*, **109**, B03303.

- Bostock, M. G., and S. Rondenay, 1999, Migration of scattered teleseismic body waves: *Geophys. J. Int.*, **137**, 732–746.
- Bostock, M. G., and M. D. Sacchi, 1997, Deconvolution of teleseismic recordings for mantle structure: *Geophys. J. Int.*, **129**, 143–152.
- Brenguier, F., M. Campillo, C. Hadziioannou, N. M. Shapiro, R. M. Nadeau, and E. Larose, 2008a, Postseismic relaxation along the San Andreas Fault at Parkfield from continuous seismological observations: *Science*, **321**, 1478–1481.
- Brenguier, F., N. M. Shapiro, M. Campillo, V. Ferrazzini, Z. Duputel, O. Coutant, and A. Nercessian, 2008b, Towards forecasting volcanic eruptions using seismic noise: *Nature Geosci.*, **1**, 126–130.
- Bulmer, M. G., 1979, *Principles of statistics*: Dover Publications.
- Campillo, M., and A. Paul, 2003, Long-range correlations in the diffuse seismic coda: *Science*, **299**, 547–549.
- Carder, D. S., 1936, Observed vibrations of buildings: *Bull. Seismol. Soc. Am.*, **26**, 245–277.
- Chadwick, A., G. Williams, N. Delepine, V. Clochard, K. Labat, S. Sturton, M.-L. Buddensiek, M. Dillen, R. Arts, F. Neele, and G. Rossi, 2010, Quantitative analysis of time-lapse seismic monitoring data at the Sleipner CO<sub>2</sub> storage operation: *The Leading Edge*, **29**, 170–177.
- Chapman, D., and O. Godin, 2001, Dispersion of interface waves in sediments with power-law shear speed profiles. II. Experimental observations and seismo-acoustic inversions: *J. Acoust. Soc. Am.*, **110**, 1908–1916.
- Claerbout, J. F., 1968, Synthesis of a layered medium from its acoustic transmission response: *Geophysics*, **33**, 264–269.
- Clayton, R. W., and R. A. Wiggins, 1976, Source shape estimation and deconvolution of teleseismic bodywaves: *Geophys. J. R. astr. Soc.*, **47**, 151–177.
- Clinton, J. F., S. C. Bradford, T. H. Heaton, and J. Favela, 2006, The observed wander of the natural frequencies in a structure: *Bull. Seismol. Soc. Am.*, **96**, 237–257.
- Clinton, J. F., and T. H. Heaton, 2002, Potential advantages of a strong-motion velocity meter over a strong-motion accelerometer: *Seismol. Res. Lett.*, **73**, 332–342.

- Cochran, E. S., Y.-G. Li, and J. E. Vidale, 2006, Anisotropy in the shallow crust observed around the San Andreas fault before and after the 2004 M 6.0 Parkfield earthquake: *Bull. Seismol. Soc. Am.*, **96**, S364–S375.
- Cochran, E. S., J. E. Vidale, and Y.-G. Li, 2003, Near-fault anisotropy following the Hector Mine earthquake: *J. Geophys. Res.*, **108**, 2436.
- Coulson, C. A., and A. Jeffrey, 1977, *Waves: A mathematical approach to the common types of wave motion*, 2 ed.: Longman.
- Crampin, S., 1978, Seismic-wave propagation through a cracked solid: polarization as a possible dilatancy diagnostic: *Geophys. J. R. astr. Soc.*, **53**, 467–496.
- , 1985, Evaluation of anisotropy by shear-wave splitting: *Geophysics*, **50**, 142–152.
- Crampin, S., D. C. Booth, R. Evans, S. Peacock, and J. B. Fletcher, 1990, Changes in shear wave splitting at Anza near the time of the North Palm Springs earthquake: *J. Geophys. Res.*, **95**, 11197–11212.
- Crampin, S., E. M. Chesnokov, and R. G. Hipkin, 1984a, Seismic anisotropy – the state of the art: II: *Geophys. J. R. astr. Soc.*, **76**, 1–16.
- Crampin, S., R. Evans, and B. K. Atkinson, 1984b, Earthquake prediction: a new physical basis: *Geophys. J. R. astr. Soc.*, **76**, 147–156.
- Crampin, S., and Y. Gao, 2005, Comment on "Systematic analysis of shear-wave splitting in the aftershock zone of the 1999 Chi-Chi, Taiwan, earthquake: Shallow crustal anisotropy and lack of precursory changes, by Yungfeng Liu, Ta-Liang Teng, and Yehuda Ben-Zion": *Bull. Seismol. Soc. Am.*, **95**, 354–360.
- Crampin, S., and S. Peacock, 2008, A review of the current understanding of seismic shear-wave splitting in the earth's crust and common fallacies in interpretation: *Wave Motion*, **45**, 675–722.
- Crampin, S., and S. V. Zatsepin, 1997, Modelling the compliance of crustal rock – II. Response to temporal changes before earthquakes: *Geophys. J. Int.*, **129**, 495–506.
- Şafak, E., 1995, Detection and identification of soil-structure interaction in buildings from vibration recordings: *J. Struct. Eng.*, **121**, 899–906.
- Curtis, A., H. Nicolson, D. Halliday, J. Trampert, and B. Baptie, 2009, Virtual seismometers in the subsurface of the earth from seismic interferometry: *Nature Geosci.*, **2**, 700–704.
- Dahlen, F. A., and J. Tromp, 1998, *Theoretical global seismology*: Princeton University Press.

- Das, B., 1993, Principles of soil dynamics: PWS-Kent Publishing Co.
- Dasgupta, S., and R. L. Nowack, 2006, Deconvolution of three-component teleseismic P waves using the autocorrelation of the P to SV scattered waves: *Bull. Seismol. Soc. Am.*, **96**, 1827–1835.
- DeMets, C., R. G. Gordon, and D. F. Argus, 2010, Geologically current plate motions: *Geophys. J. Int.*, **181**, 1–80.
- Derode, A., E. Larose, M. Campillo, and M. Fink, 2003a, How to estimate the Green's function of a heterogeneous medium between two passive sensors? Application to acoustic waves: *Applied Physics Letters*, **83**, 3054–3056.
- Derode, A., E. Larose, M. Tanter, J. de Rosny, A. Tourin, M. Campillo, and M. Fink, 2003b, Recovering the Green's function from field-field correlations in an open scattering medium (L): *J. Acoust. Soc. Am.*, **113**, 2973–2976.
- Dieterich, J. H., 1972, Time-dependent friction in rocks: *J. Geophys. Res.*, **77**, 3690–3697.
- Draganov, D., X. Campman, J. Thorbecke, A. Verdel, and K. Wapenaar, 2009, Reflection images from ambient seismic noise: *Geophysics*, **74**, A63–A67.
- Draganov, D., K. Wapenaar, W. Mulder, J. Singer, and A. Verdel, 2007, Retrieval of reflections from seismic background-noise measurements: *Geophys. Res. Lett.*, **34**, L04305.
- Farrar, C. R., and K. Worden, 2007, An introduction to structural health monitoring: *Philos. Trans. R. Soc. A*, **365**, 303–315.
- Forghani, F., and R. Snieder, 2010, Underestimation of body waves and feasibility of surface-wave reconstruction by seismic interferometry: *The Leading Edge*, **29**, 790–794.
- Fuhr, P. L., D. R. Huston, P. J. Kajenski, and T. P. Ambrose, 1992, Performance and health monitoring of the Stafford Medical Building using embedded sensors: *Smart Mater. Struct.*, **1**, 63–68.
- Fukao, Y., 1984, Evidence from core-reflected shear waves for anisotropy in the Earth's mantle: *Nature*, **309**, 695–698.
- Gans, C. R., 2011, Investigations of the crust and upper mantle of modern and ancient subduction zones, using Pn tomography and seismic receiver functions: PhD thesis, The university of Arizona.

- Gao, Y., P. Wang, S. Zheng, M. Wang, Y. Chen, and H. Zhou, 1998, Temporal changes in shear-wave splitting at an isolated swarm of small earthquakes in 1992 near Dongfang, Hainan Island, southern China: *Geophys. J. Int.*, **135**, 102–112.
- Hadziioannou, C., E. Larose, O. Coutant, P. Roux, and M. Campillo, 2009, Satability of monitoring weak changes in multiply scattering media with ambient noise correlation: Laboratory experiments: *J. Acoust. Soc. Am.*, **125**, 3688–3695.
- Hanks, T. C., 1977, Earthquakes stress drops, ambient tectonic stresses and stresses that drive plate motions: *Pure Appl. Geophys.*, **115**, 441–458.
- Hasegawa, A., K. Yoshida, and T. Okada, 2011, Nearly complete stress drop in the 2011  $M_w$  9.0 off the Pacific coast of Tohoku Earthquake: *Earth Planets Space*, **63**, 703–707.
- Havskov, J., and L. Ottemöller, 2010, Routine data processing in earthquake seismology with sample data, exercises and software: Springer.
- Héloïse, C., P.-Y. Bard, and A. Rodriguez-Marek, 2012, Site effect assessment using KiK-net data: Part 1. A simple correction procedure for surface/downhole spectral ratios: *Bull. Earthquake Eng.*, **10**, 421–448.
- Herwanger, J., and S. Horne, 2005, Predicting time-lapse stress effects in seismic data: *The Leading Edge*, **24**, 1234–1242.
- Hohl, D., and A. Mateeva, 2006, Passive seismic reflectivity imaging with ocean-bottom cable data: *SEG Expanded Abstracts*, **25**, 1560–1564.
- Ito, T., T. Ikawa, S. Yamakita, and T. Maeda, 1996, Gently north-dipping Median Tectonic Line (MTL) revealed by recent seismic reflection studies, southwest Japan: *Tectonophysics*, **264**, 51–63.
- Ito, Y., K. Obara, K. Shiomi, S. Sekine, and H. Hirose, 2007, Slow earthquakes coincident with episodic tremors and slow slip events: *Science*, **315**.
- Ivanović, S. S., M. D. Trifunac, and M. I. Todorovska, 2000, Ambient vibration tests of structures—a review: *ISER J. Earthq. Tech*, **37**, 165–197.
- Kanai, K., and S. Yoshizawa, 1961, On the period and the damping of vibration in actual buildings: *Bull. Earthq. Res. Inst.*, **39**, 477–489.
- Kato, A., K. Obara, T. Igarashi, H. Tsuruoka, S. Nakagawa, and N. Hirata, 2012, Propagation of slow slip leading up to the 2011  $M_w$  9.0 Tohoku-Oki Earthquake: *Science*, **335**, 705–708.

- Kennett, B. L. N., and E. R. Engdahl, 1991, Traveltimes for global earthquake location and phase identification: *Geophys. J. Int.*, **105**, 429–465.
- Kern, H., 1978, The effect of high temperature and high confining pressure on compressional wave velocities in quartz-bearing and quartz-free igneous and metamorphic rocks: *Tectonophysics*, **44**, 185–203.
- Kimura, H., T. Takeda, K. Obara, and K. Kasahara, 2010, Seismic evidence for active underplating below the megathrust earthquake zone in Japan: *Science*, **329**, 210–212.
- King, G. C. P., R. S. Stein, and J. Lin, 1994, Static stress changes and the triggering of earthquakes: *Bull. Seismol. Soc. Am.*, **84**, 935–953.
- Kohler, M. D., P. M. Davis, and E. Şafak, 2005, Earthquake and ambient vibration monitoring of the steel-frame UCLA Factor building: *Earthquake Spectra*, **21**, 715–736.
- Kohler, M. D., T. H. Heaton, and S. C. Bradford, 2007, Propagating waves in the steel, moment-frame Factor building recorded during earthquakes: *Bull. Seismol. Soc. Am.*, **97**, 1334–1345.
- Koizumi, N., Y. Kano, Y. Kitagawa, T. Sato, M. Takahashi, S. Nishimura, and R. Nishida, 1996, Groundwater anomalies associated with the 1995 Hyogo-ken Nanbu earthquake: *J. Phys. Earth*, **44**, 373–380.
- Koster, K., P. Gabriels, M. Hartung, J. Verbeek, G. Deinum, and R. Staples, 2000, Time-lapse seismic surveys in the north sea and their business impact: *The Leading Edge*, **19**, 286–293.
- Langston, C. A., 1979, Structure under Mount Rainier, Washington, inferred from teleseismic body waves: *J. Geophys. Res.*, **84**, 4749–4762.
- Larose, E., L. Margerin, A. Derode, B. van Tiggelen, M. Campillo, N. Shapiro, A. Paul, L. Stehly, and M. Ta, 2006, Correlation of random wavefields: An interdisciplinary review: *Geophysics*, **71**, S111–S121.
- Lawson, C. L., 1984,  $C^1$  surface interpolation for scattered data on a sphere: *Rocky Mountain J. Math.*, **14**, 177–202.
- Leahy, G. M., R. L. Saltzer, and J. Schmedes, 2012, Imaging the shallow crust with teleseismic receiver functions: *Geophys. J. Int.*, **191**, 627–636.
- Li, X., S. V. Sobolev, R. Kind, X. Yuan, and C. Estabrook, 2000, A detailed receiver function image of the upper mantle discontinuities in the japan subduction zone: *Earth Planet. Sci. Lett.*, **183**, 527–541.

- Li, Y.-G., J. E. Vidale, K. Aki, F. Xu, and T. Burdette, 1998, Evidence of shallow fault zone strengthening after the 1992 M7.5 Landers, California, earthquake: *Science*, **279**, 217–219.
- Lin, F.-C., M. H. Ritzwoller, and R. Snieder, 2009, Eikonal tomography: surface wave tomography by phase front tracking across a regional broad-band seismic array: *Geophys. J. Int.*, **177**, 1091–1110.
- Liu, Y., T.-L. Teng, and Y. Ben-Zion, 2004, Systematic analysis of shear-wave splitting in the aftershock zone of the 1999 Chi-Chi, Taiwan, earthquake: Shallow crustal anisotropy and lack of precursory variations: *Bull. Seismol. Soc. Am.*, **94**, 2330–2347.
- Lobkis, O. I., and R. L. Weaver, 2001, On the emergence of the Green’s function in the correlations of a diffuse field: *J. Acoust. Soc. Am.*, **110**, 3011–3017.
- , 2003, Coda-wave interferometry in finite solids: Recovery of P-to-S conversion rates in an elastodynamic billiard: *Phys. Rev. Lett.*, **90**, 254302.
- Loewenthal, D., and E. A. Robinson, 2000, On unified dual fields and Einstein deconvolution: *Geophysics*, **65**, 293–303.
- Lumley, D. E., 2001, Time-lapse seismic reservoir monitoring: *Geophysics*, **66**, 50–53.
- Ma, S., G. A. Prieto, and G. C. Beroza, 2008, Testing community velocity models for southern California using the ambient seismic field: *Bull. Seismol. Soc. Am.*, **98**, 2694–2714.
- Maxwell, S. C., J. Rutledge, R. Jones, and M. Fehler, 2010, Petroleum reservoir characterization using downhole microseismic monitoring: *Geophysics*, **75**, 75A129–75A137.
- Mehta, K., A. Bakulin, J. Sheiman, R. Calvert, and R. Snieder, 2007a, Improving the virtual source method by wavefield separation: *Geophysics*, **72**, V79–V86.
- Mehta, K., J. L. Sheiman, R. Snieder, and R. Calvert, 2008, Strengthening the virtual-source method for time-lapse monitoring: *Geophysics*, **73**, S73–S80.
- Mehta, K., R. Snieder, and V. Graizer, 2007b, Downhole receiver function: a case study: *Bull. Seismol. Soc. Am.*, **97**, 1396–1403.
- , 2007c, Extraction of near-surface properties for a lossy layered medium using the propagator matrix: *Geophys. J. Int.*, **169**, 271–280.
- Michel, C., P. Guéguen, and P.-Y. Bard, 2008, Dynamic parameters of structures extracted from ambient vibration measurements: An aid for the seismic vulnerability assessment of existing buildings in moderate seismic hazard regions: *Soil Dyn. Earthquake Eng.*, **28**, 593–604.

- Minato, S., T. Matsuoka, T. Tsuji, D. Draganov, J. Hunziker, and K. Wapenaar, 2011, Seismic interferometry using multidimensional deconvolution and crosscorrelation for crosswell seismic reflection data without borehole sources: *Geophysics*, **76**, SA19–SA34.
- Minato, S., T. Tsuji, S. Ohmi, and T. Matsuoka, 2012, Monitoring seismic velocity change caused by the 2011 Tohoku-oki earthquake using ambient noise records: *Geophys. Res. Lett.*, **39**, L09309.
- Miyazawa, M., and J. Mori, 2009, Test of seismic hazard map from 500 years of recorded intensity data in Japan: *Bull. Seismol. Soc. Am.*, **99**, 3140–3149.
- Miyazawa, M., R. Snieder, and A. Venkataraman, 2008, Application of seismic interferometry to extract P- and S-wave propagation and observation of shear-wave splitting from noise data at Cold Lake, Alberta, Canada: *Geophysics*, **73**, D35–D40.
- Moldoveanu, N., L. Combee, M. Egan, G. Hampson, L. Sydora, and W. Abriel, 2007, Over/under towed-streamer acquisition: A method to extend seismic bandwidth to both higher and lower frequencies: *The Leading Edge*, **26**, 41–58.
- Nakajima, J., and A. Hasegawa, 2004, Shear-wave polarization anisotropy and subduction-induced flow in the mantle wedge of northeastern Japan: *Earth Planet. Sci. Lett.*, **225**, 365–377.
- Nakajima, J., T. Matsuzawa, A. Hasegawa, and D. Zhao, 2001, Three-dimensional structure of  $V_p$ ,  $V_s$ , and  $V_p/V_s$  beneath northeastern Japan: Implications for arc magmatism and fluids: *J. Geophys. Res.*, **106**, 21843–21857.
- Nakajima, J., J. Shimizu, S. Hori, and A. Hasegawa, 2006, Shear-wave splitting beneath the southwestern Kurile arc and northeastern Japan arc: A new insight into mantle return flow: *Geophys. Res. Lett.*, **33**, L05305.
- Nakata, N., and R. Snieder, 2011, Near-surface weakening in Japan after the 2011 Tohoku-Oki earthquake: *Geophys. Res. Lett.*, **38**, L17302.
- , 2012a, Estimating near-surface shear-wave velocities in Japan by applying seismic interferometry to KiK-net data: *J. Geophys. Res.*, **117**, B01308.
- , 2012b, Time-lapse change in anisotropy in Japan’s near surface after the 2011 Tohoku-Oki earthquake: *Geophys. Res. Lett.*, **39**, L11313.
- Nakata, N., R. Snieder, S. Kuroda, S. Ito, T. Aizawa, and T. Kunimi, 2013, Monitoring a building using deconvolution interferometry. I: Earthquake-data analysis: *Bull. Seismol. Soc. Am.* (in press).

- Nakata, N., R. Snieder, T. Tsuji, K. Larner, and T. Matsuoka, 2011, Shear-wave imaging from traffic noise using seismic interferometry by cross-coherence: *Geophysics*, **76**, SA97–SA106.
- Nishimura, T., N. Uchida, H. Sato, M. Ohtake, S. Tanaka, and H. Hamaguchi, 2000, Temporal changes of the crustal structure associated with the M6.1 earthquake on September 3, 1998, and the volcanic activity of Mount Iwate, Japan: *Geophys. Res. Lett.*, **27**, 269–272.
- Nur, A., and G. Simmons, 1969, Stress-induced velocity anisotropy in rock: An experimental study: *J. Geophys. Res.*, **74**, 6667–6674.
- Obara, K., 2002, Nonvolcanic deep tremor associated with subduction in southwest Japan: *Science*, **296**, 1679–1681.
- Obara, K., K. Kasahara, S. Hori, and Y. Okada, 2005, A densely distributed high-sensitivity seismograph network in Japan: Hi-net by National Research Institute for Earth Science and Disaster Prevention: *Rev. Sci. Instrum.*, **76**, 021301.
- O’Connell, D. R. H., 2007, Concrete dams as seismic imaging sources: *Geophys. Res. Lett.*, **34**, L20307, doi:10.1029/2007GL031219.
- Okada, T., T. Matsuzawa, and A. Hasegawa, 1995, Shear-wave polarization anisotropy beneath the north-eastern part of Honshu, Japan: *Geophys. J. Int.*, **123**, 781–797.
- Okada, Y., K. Kasahara, S. Hori, K. Obara, S. Sekiguchi, H. Fujiwara, and A. Yamamoto, 2004, Recent progress of seismic observation networks in Japan — Hi-net, F-net, K-NET and KiK-net —: *Earth Planets Space*, **56**, 15–28.
- Oyunchimeg, M., and H. Kawakami, 2003, A new method for propagation analysis of earthquake waves in damaged buildings: evolutionary normalized input-output minimization (NIOM): *J. Asian. Archit. Build.*, **2**, 9–16.
- Ozawa, S., T. Nishimura, H. Suito, T. Kobayashi, M. Tobita, and T. Imakiire, 2011, Coseismic and postseismic slip of the 2011 magnitude-9 Tohoku-Oki earthquake: *Nature*, **475**, 373–376.
- Panakkat, A., and H. Adeli, 2008, Recent efforts in earthquake prediction (1990-2007): *Natural Hazards Rev.*, **9**, 70–80.
- Paul, A., M. Campillo, L. Margerin, and E. Larose, 2005, Empirical synthesis of time-asymmetrical Green functions from the correlation of coda waves: *J. Geophys. Res.*, **110**, B08302.

- Peacock, S., S. Crampin, and D. C. Booth, 1988, Shear wave splitting in the Anza seismic gap, southern California: Temporal variations as possible precursors: *J. Geophys. Res.*, **93**, 3339–3356.
- Peng, Z., and Y. Ben-Zion, 2005, Spatiotemporal variations of crustal anisotropy from similar events in aftershocks of the 1999 M7.4 İzmit and M7.1 Düzce, Turkey, earthquake sequences: *Geophys. J. Int.*, **160**, 1027–1043.
- Poupinet, G., W. L. Ellsworth, and J. Frechet, 1984, Monitoring velocity variations in the crust using earthquake doublets: An application to the Calaveras fault, California: *J. Geophys. Res.*, **89**, 5719–5731.
- Prieto, G. A., and G. Beroza, 2008, Earthquake ground motion prediction using the ambient seismic field: *Geophys. Res. Lett.*, **35**, L14304.
- Prieto, G. A., J. F. Lawrence, and G. C. Beroza, 2009, Anelastic earth structure from the coherency of the ambient seismic field: *J. Geophys. Res.*, **114**, B07303.
- Prieto, G. A., J. F. Lawrence, A. I. Chung, and M. D. Kohler, 2010, Impulse response of civil structures from ambient noise analysis: *Bull. Seismol. Soc. Am.*, **100**, 2322–2328.
- Pšenčík, I., 1998, Package anray, version 4.10: Technical Report Report 7, 403-404, Department of Geophysics, Charles University Prague.
- Reasenberg, P., and K. Aki, 1974, A precise, continuous measurement of seismic velocity for monitoring in situ stress: *J. Geophys. Res.*, **79**, 399–406.
- Robertsson, J. O. A., and A. Curtis, 2002, Wavefields separation using densely deployed three-component single-sensor groups in land surface-seismic recordings: *Geophysics*, **67**, 1624–1633.
- Robertsson, J. O. A., and E. Muyzert, 1999, Wavefield separation using a volume distribution of three component recordings: *Geophys. Res. Lett.*, **26**, 2821–2824.
- Roux, P., and M. Fink, 2003, Green’s function estimation using secondary sources in a shallow wave environment: *J. Acoust. Soc. Am.*, **113**, 1406–1416.
- Ruigrok, E., X. Campman, D. Draganov, and K. Wapenaar, 2010, High-resolution lithospheric imaging with seismic interferometry: *Geophys. J. Int.*, **183**, 339–357.
- Ruigrok, E., and K. Wapenaar, 2012, Global-phase seismic interferometry unveils P-wave reflectivity below the Himalayas and Tibet: *Geophys. Res. Lett.*, **39**, L11303.

- Ryberg, T., 2011, Body wave observations from cross-correlations of ambient seismic noise: A case study from the Karoo, RSA: *Geophys. Res. Lett.*, **38**, L13311.
- Sagiya, T., S. Miyazaki, and T. Tada, 2000, Continuous GPS array and present-day crustal deformation of Japan: *Pure appl. geophys.*, **157**, 2303–2322.
- Saiga, A., Y. Hiramatsu, T. Ooida, and K. Yamaoka, 2003, Spatial variation in the crustal anisotropy and its temporal variation associated with a moderate-sized earthquake in the Tokai region, central Japan: *Geophys. J. Int.*, **154**, 695–705.
- Sawazaki, K., H. Sato, H. Nakahara, and T. Nishimura, 2006, Temporal change in site response caused by earthquake strong motion as revealed from coda spectral ratio measurement: *Geophys. Res. Lett.*, **33**, L21303.
- , 2009, Time-lapse changes of seismic velocity in the shallow ground caused by strong ground motion shock of the 2000 western-Tottori earthquake, Japan, as revealed from coda deconvolution analysis: *Bull. Seismol. Soc. Am.*, **99**, 352–366.
- Sawazaki, K., and R. Snieder, 2013, Time-lapse changes of P- and S-wave velocities and shear wave splitting in the first year after the 2011 Tohoku earthquake, Japan: shallow subsurface: *Geophys. J. Int.*, **193**, 238–251.
- Schaff, D. P., and G. C. Beroza, 2004, Coseismic and postseismic velocity changes measured by repeating earthquakes: *J. Geophys. Res.*, **109**, B10302.
- Schalkwijk, K. M., C. P. A. Wapenaar, and D. J. Verschuur, 2003, Adaptive decomposition of multicomponent ocean-bottom seismic data into downgoing and upgoing P- and S-waves: *Geophysics*, **68**, 1091–1102.
- Schiff, A., and J. L. Bogdanoff, 1967, Analysis of current methods of interpreting strong-motion accelerograms: *Bull. Seismol. Soc. Am.*, **57**, 857–874.
- Schmedes, J., J. B. Roth, R. L. Saltzer, and G. M. Leahy, 2012, Imaging the shallow crust using teleseismic tomography: *Bull. Seismol. Soc. Am.*, **102**, 1276–1282.
- Schuster, G., 2009, *Seismic interferometry*: Cambridge Univ. Press.
- Schuster, G. T., J. Yu, J. Sheng, and J. Rickett, 2004, Interferometric/daylight seismic imaging: *Geophys. J. Int.*, **157**, 838–852.
- Sens-Schönfelder, C., and U. Wegler, 2006, Passive image interferometry and seasonal variations of seismic velocities at Merapi Volcano, Indonesia: *Geophys. Res. Lett.*, **33**, L21302.

- Sezawa, K., and K. Kanai, 1935, Energy dissipation in seismic vibrations of actual buildings: *Bull. Earthq. Res. Inst.*, **13**, 925–941.
- Shapiro, N. M., M. Campillo, L. Stehly, and M. H. Ritzwoller, 2005, High-resolution surface-wave tomography from ambient seismic noise: *Science*, **307**, 1615–1618.
- Shiomi, K., K. Obara, S. Aoi, and K. Kasahara, 2003, Estimation on the azimuth of the Hi-net and KiK-net borehole seismometers: *Zishin2* (in Japanese), **56**, 99–110.
- Shiomi, K., K. Obara, and K. Kasahara, 2005, Amplitude saturation of the NIED Hi-net waveforms and simple criteria for recognition: *Zishin2* (in Japanese), **57**, 451–461.
- Snieder, R., 2004a, Extracting the Green’s function from the correlation of coda waves: A derivation based on stationary phase: *Phys. Rev. E*, **69**, 046610.
- , 2004b, *A Guided Tour of Mathematical Methods for the Physical Sciences*: Cambridge Univ. Press.
- , 2006, The theory of coda wave interferometry: *Pure Appl. Geophys.*, **163**, 455–473.
- Snieder, R., and E. Şafak, 2006, Extracting the building response using seismic interferometry: Theory and application to the Millikan Library in Pasadena, California: *Bull. Seismol. Soc. Am.*, **96**, 586–598.
- Snieder, R., A. Grêt, H. Douma, and J. Scales, 2002, Coda wave interferometry for estimating nonlinear behavior in seismic velocity: *Science*, **295**, 2253–2255.
- Snieder, R., and M. Hagerty, 2004, Monitoring change in volcanic interiors using coda wave interferometry: application to Arenal volcano, Costa Rica: *Geophys. Res. Lett.*, **31**, L09608.
- Snieder, R., S. Hubbard, M. Haney, G. Bawden, P. Hatchell, A. Revil, and D. G. M. W. Group, 2007, Advanced noninvasive geophysical monitoring techniques: *Annu. Rev. Earth Planet. Sci.*, **35**, 653–683.
- Snieder, R., M. Miyazawa, E. Slob, I. Vasconcelos, and K. Wapenaar, 2009, A comparison of strategies for seismic interferometry: *Surveys in Geophysics*, **30**, 503–523.
- Snieder, R., J. Sheiman, and R. Calvert, 2006a, Equivalence of the virtual-source method and wave-field deconvolution in seismic interferometry: *Phys. Rev. E*, **73**, 066620.
- Snieder, R., and A. van den Beukel, 2004, The liquefaction cycle and the role of drainage in liquefaction: *Granular Matter*, **6**, 1–9.

- Snieder, R., and M. Vrijlandt, 2005, Constraining the source separation with coda wave interferometry: Theory and application to earthquake doublets in the Hayward fault, California: *J. Geophys. Res.*, **110**, B04301.
- Snieder, R., K. Wapenaar, and K. Larner, 2006b, Spurious multiples in seismic interferometry of primaries: *Geophysics*, **71**, SI111–SI124.
- Stehly, L., M. Campillo, B. Froment, and R. L. Weaver, 2008, Reconstruction Green's function by correlation of the coda of the correlation ( $C^3$ ) of ambient seismic noise: *J. Geophys. Res.*, **113**, B11306.
- Tadokoro, K., M. Ando, and Y. Umeda, 1999, S wave splitting in the aftershock region of the 1995 Hyogo-ken Nanbu earthquake: *J. Geophys. Res.*, **104**, 981–991.
- Takagi, R., and T. Okada, 2012, Temporal change in shear velocity and polarization anisotropy related to the 2011 M9.0 Tohoku-Oki earthquake examined using KiK-net vertical array data: *Geophys. Res. Lett.*, **39**, L09310.
- Thomsen, L., 1988, Reflection seismology over azimuthally anisotropic media: *Geophysics*, **53**, 304–313.
- Thomson, D. J., 1982, Spectrum estimation and harmonic analysis: *Proc. of the IEEE*, **70**, 1055–1096.
- Toda, S., R. S. Stein, and J. Lin, 2011, Widespread seismicity excitation throughout central Japan following the 2011 M=9.0 Tohoku earthquake and its interpretation by Coulomb stress transfer: *Geophys. Res. Lett.*, **38**, L00G03.
- Todorovska, M. I., and M. D. Trifunac, 2008a, Earthquake damage detection in the Imperial Country Services Building III: Analysis of wave travel times via impulse response functions: *Soil Dyn. Earthquake Eng.*, **28**, 387–404.
- , 2008b, Impulse response analysis of the Van Nuys 7-story hotel during 11 earthquakes and earthquake damage detection: *Struct. Control Health Monit.*, **15**, 90–116.
- Tonegawa, T., Y. Fukao, K. Nishida, H. Sugioka, and A. Ito, 2013, A temporal change of shear wave anisotropy within the marine sedimentary layer associated with the 2011 Tohoku-Oki earthquake: *J. Geophys. Res.*, **118**, 607–615.
- Tonegawa, T., K. Nishida, T. Watanabe, and K. Shiomi, 2009, Seismic interferometry of teleseismic S-wave coda retrieval of body waves: an application to the Philippine Sea slab underneath the Japanese Islands: *Geophys. J. Int.*, **178**, 1574–1586.

- Torrence, C., and G. P. Compo, 1998, A practical guide to wavelet analysis: *Bull. Am. Meteorol. Soc.*, **79**, 61–78.
- Trampert, J., M. Cara, and M. Frogneux, 1993, SH propagator matrix and  $Q_s$  estimates from borehole- and surface- recorded earthquake data: *Geophys. J. Int.*, **112**, 290–299.
- Trifunac, M. D., 1972, Comparisons between ambient and forced vibration experiments: *Earthquake Eng. and Structural Dynamics*, **1**, 133–150.
- Trifunac, M. D., S. S. Ivanović, and M. I. Todorovska, 2001a, Apparent periods of a building. I: Fourier analysis: *J. Struct. Eng.*, **127**, 517–526.
- , 2001b, Apparent periods of a building. II: Time-frequency analysis: *J. Struct. Eng.*, **127**, 527–537.
- Tsai, V. C., 2011, Understanding the amplitudes of noise correlation measurements: *J. Geophys. Res.*, **116**, B09311.
- van der Neut, J., and A. Bakulin, 2009, Estimating and correcting the amplitude radiation pattern of a virtual source: *Geophysics*, **74**, SI27–SI36.
- van der Neut, J., M. Tatanova, J. Thorbecke, E. Slob, and K. Wapenaar, 2011a, Deghosting, demultiple, and deblurring in controlled-source seismic interferometry: *International Journal of Geophysics*, **2011**, 870819.
- van der Neut, J., J. Thorbecke, K. Mehta, E. Slob, and K. Wapenaar, 2011b, Controlled-source interferometric redatuming by crosscorrelation and multidimensional deconvolution in elastic media: *Geophysics*, **76**, SA63–SA76.
- Vasco, D. W., A. Ferretti, and F. Novali, 2008, Reservoir monitoring and characterization using satellite geodetic data: Interferometric synthetic aperture radar observations from the krechba field, algeria: *Geophysics*, **73**, WA113–WA122.
- Vasconcelos, I., and R. Snieder, 2008a, Interferometry by deconvolution, Part 1 - Theory for acoustic waves and numerical examples: *Geophysics*, **73**, S115–S128.
- , 2008b, Interferometry by deconvolution: Part 2 - Theory for elastic waves and application to drill-bit seismic imaging: *Geophysics*, **73**, S129–S141.
- Vasconcelos, I., R. Snieder, and B. Hornby, 2008, Imaging internal multiples from subsalt VSP data - Examples of target-oriented interferometry: *Geophysics*, **73**, S157–S168.
- Verdon, J. P., J.-M. Kendall, and S. C. Maxwell, 2010, A comparison of passive seismic monitoring of fracture stimulation from water and CO<sub>2</sub> injection: *Geophysics*, **75**, MA1–MA7.

- Vidale, J. E., and Y.-G. Li, 2003, Damage to the shallow Landers fault from the nearby Hector Mine earthquake: *Nature*, **421**, 524–526.
- Wakamatsu, K., M. Matsuoka, and K. Hasegawa, 2006, GIS-based nationwide hazard zoning using the Japan engineering geomorphologic classification map: *Proc. U.S. Natl. Conf. on Earthq. Eng.*, **8**, 849.
- Wapenaar, C. P. A., P. Herrmann, D. J. Verschuur, and A. J. Berkhout, 1990, Decomposition of multicomponent seismic data into primary P- and S-wave responses: *Geophys. Prospect.*, **38**, 633–661.
- Wapenaar, K., 2003, Synthesis of an inhomogeneous medium from its acoustic transmission response: *Geophysics*, **68**, 1756–1759.
- , 2004, Retrieving the elastodynamic Green’s function of an arbitrary inhomogeneous medium by cross correlation: *Phys. Rev. Lett.*, **93**, 254–301.
- Wapenaar, K., D. Draganov, R. Snieder, X. Campman, and A. Verdel, 2010a, Tutorial on seismic interferometry: Part 1 - Basic principles and applications: *Geophysics*, **75**, 75A195–75A209.
- Wapenaar, K., and J. Fokkema, 2006, Green’s function representations for seismic interferometry: *Geophysics*, **71**, SI33–SI46.
- Wapenaar, K., E. Ruigrok, J. van der Neut, and D. Draganov, 2011a, Improved surface-wave retrieval from ambient seismic noise by multi-dimensional deconvolution: *Geophys. Res. Lett.*, **38**, L01313.
- Wapenaar, K., E. Slob, and R. Snieder, 2008a, Seismic and electromagnetic controlled-source interferometry in dissipative media: *Geophys. Prospect.*, **56**, 419–434.
- Wapenaar, K., E. Slob, R. Snieder, and A. Curtis, 2010b, Tutorial on seismic interferometry: Part 2 – Underlying theory and new advances: *Geophysics*, **75**, 75A211–75A227.
- Wapenaar, K., J. van der Neut, and E. Ruigrok, 2008b, Passive seismic interferometry by multidimensional deconvolution: *Geophysics*, **73**, A51–A56.
- Wapenaar, K., J. van der Neut, E. Ruigrok, D. Draganov, J. Hunziker, E. Slob, J. Thorbecke, and R. Snieder, 2011b, Seismic interferometry by crosscorrelation and by multidimensional deconvolution: a systematic comparison: *Geophys. J. Int.*, **185**, 1335–1364.
- Weaver, R. L., C. Hadziioannou, E. Larose, and M. Campillo, 2011, On the precision of noise correlation interferometry: *Geophys. J. Int.*, **185**, 1384–1392.

- Wegler, U., B.-G. Lühr, R. Snieder, and A. Ratdomopurbo, 2006, Increase of shear wave velocity before the 1998 eruption of Merapi volcano (Indonesia): *Geophys. Res. Lett.*, **33**, L09303.
- Wegler, U., H. Nakahara, C. Sens-Schönfelder, M. Korn, and K. Shiomi, 2009, Sudden drop of seismic velocity after the 2004  $M_w$  6.6 mid-Niigata earthquake, Japan, observed with passive image interferometry: *J. Geophys. Res.*, **114**, B06305.
- Wegler, U., and C. Sens-Schönfelder, 2007, Fault zone monitoring with passive image interferometry: *Geophys. J. Int.*, **168**, 1029–1033.
- Wu, C., and Z. Peng, 2011, Temporal changes of site response during the 2011  $M_w$  9.0 off the Pacific coast of Tohoku Earthquake: *Earth Planets Space*, **63**, 1–5.
- , 2012, Long-term change of site response after the  $M_w$  Tohoku earthquake in Japan: *Earth Planets Space*, **64**, 1259–1266.
- Wu, C., Z. Peng, and D. Assimaki, 2009, Temporal changes in site response associated with the strong ground motion of the 2004  $M_w$  6.6 Mid-Niigata earthquake sequences in Japan: *Bull. Seismol. Soc. Am.*, **99**, 3487–3495.
- Yamada, M., J. Mori, and S. Ohmi, 2010, Temporal changes of subsurface velocities during strong shaking as seen from seismic interferometry: *J. Geophys. Res.*, **115**, B03302.
- Yang, Z., A. F. Sheehan, W. L. Yeck, K. C. Miller, E. A. Erslev, L. L. Worthington, and S. H. Harder, 2012, Imaging basin structure with teleseismic virtual source reflection profiles: *Geophys. Res. Lett.*, **39**, L02303.
- Yilmaz, O., 2001, *Seismic data analysis*, 2 ed.: Society Of Exploration Geophysicists, volume **10** of *Investigations in Geophysics*.
- Yoshida, K., A. Hasegawa, T. Okada, T. Iinuma, Y. Ito, and Y. Asano, 2012, Stress before and after the 2011 great Tohoku-oki earthquake and induced earthquakes in inland areas of eastern Japan: *Geophys. Res. Lett.*, **39**, L03302.
- Zatsepin, S. V., and S. Crampin, 1997, Modelling the compliance of crustal rock – I. Response of shear-wave splitting to differential stress: *Geophys. J. Int.*, **129**, 477–494.

## APPENDIX - COPYRIGHT AND PERMISSIONS

### **A.1 Journals' permission and copyright information**

#### **A.1.1 Journal of Geophysical Research**

AUTHORS - If you wish to reuse your own article (or an amended version of it) in a new publication of which you are the author, editor or co-editor, prior permission is not required (with the usual acknowledgements). However, a formal grant of license can be downloaded free of charge from RightsLink if required.

<http://onlinelibrary.wiley.com/journal/10.1002/%28ISSN%292169-9356/homepage/Permissions.html>

#### **A.1.2 Geophysical Research Letters**

AUTHORS - If you wish to reuse your own article (or an amended version of it) in a new publication of which you are the author, editor or co-editor, prior permission is not required (with the usual acknowledgements). However, a formal grant of license can be downloaded free of charge from RightsLink if required.

<http://onlinelibrary.wiley.com/journal/10.1002/%28ISSN%291944-8007/homepage/Permissions.html>

#### **A.1.3 Bulletin of the Seismological Society of America**

Permissions policy

The Seismological Society of America (SSA) no longer requires that permission be obtained from SSA or the author(s) to reprint tables, figures, or short extracts of papers published in SSA journals, provided that the source be appropriately and accurately cited. However, the author's permission must be obtained for modifying the material in any way beyond simple redrawing.

<http://www.seismosoc.org/publications/permissions.php>

## A.2 Co-authors' permission

### A.2.1 Seiichiro Kuroda, *National Institute for Rural Engineering*

From: Seiichiro Kuroda <skuroda@affrc.go.jp>

Subject: Re: Authorization to publish co-authored material

Date: May 31, 2013, 2:50 AM

To: Nori Nakata <nnakata@mines.edu>

To whom it may concern,

I hereby authorize Nori Nakata to reproduce the content of the article "Monitoring a building using deconvolution interferometry. I: Earthquake-data analysis," currently submitted in fulfillment of his degree requirements at the Colorado School of Mines.

Please do not hesitate to contact me directly if there are any pending issues.

Best regards,

Seiichiro Kuroda

////////////////////////////////////

> Seiichiro KURODA, Ph.D

> Senior Researcher

> National Institute for Rural Engineering

> National Agriculture and Food Research Organization

> Email: skuroda@affrc.go.jp

> Zip Code: 305-8069

> Kannondai 2-1-6, Tsukuba-city, Ibaraki, Japan 305-8069

> TEL+81-29-838-7577FAX+81-29-838-7609

////////////////////////////////////

**A.2.2 Takao Aizawa and Shunichiro Ito, *Suncoh Consultants Co., Ltd.***

From: Takao Aizawa <aizawa@suncoh.co.jp>

Subject: Re: Copyright permission

Date: May 30, 2013, 5:20 AM

To: Nori Nakata <nnakata@mines.edu>

Hello Nori,

We hereby authorize Nori Nakata to reproduce the content of the article "Monitoring a building using deconvolution interferometry Earthquake-data analysis," currently submitted in fulfillment of his degree requirements at the Colorado School of Mines.

Best regards,

Takao AIZAWA and Shunichiro ITO

+++++

SUNCOH CONSULTANTS Co., Ltd.

Takao AIZAWA

1-8-9 Kameido Koto-ku Toyo, 136-8592, JAPAN

aizawa@suncoh.co.jp

Tel:+81-3-3683-7121 Fax:+81-3-3683-7222

Mobile:+81-9048418332

+++++

**A.2.3 Takashi Kunimi, *Akebono Brake Industry Co., Ltd.***

From: Kunimi Takashi <kunimi@akebono-brake.com>

Subject: Re: Copyright permission

Date: May 30, 2013, 7:25 PM

To: Nori Nakata <nnakata@mines.edu>

To whom it may concern,

I hereby authorize Nori Nakata to reproduce the content of the article "Monitoring a building using deconvolution interferometry. I: Earthquake-data analysis," currently submitted in fulfillment of his degree requirements at the Colorado School of Mines.

Best regards,

Takashi Kunimi